Die approbierte gedruckte Originalversion dieser Dissertation ist an der TU Wien Bibliothek verfügbar.
The approved original version of this doctoral thesis is available in print at TU Wien Bibliothek.

D I S S E R T A T I O N

Numerical Analysis and Simulation in Microelectronics by Vector Finite Elements

ausgeführt zum Zwecke der Erlangung des akademischen Grades
eines Doktors der technischen Wissenschaften

eingereicht an der Technischen Universität Wien
Fakultät für Elektrotechnik und Informationstechnik
von

Alexandre Nentchev

[redacted]

[redacted]

Wien, im Jänner 2008

Die approbierte gedruckte Originalversion dieser Dissertation ist an der TU Wien Bibliothek verfügbar.
The approved original version of this doctoral thesis is available in print at TU Wien Bibliothek.

Abstract

Modeling and simulation are a crucial aid for reducing development cycle time and costs in modern semiconductor technology. New modeling concepts increasingly require long-term research performed in an interdisciplinary manner, and new numerical methods and algorithms are needed to implement these concepts.

The three-dimensional interconnect structure in the integrated circuits represents a difficult electromagnetic system. It includes many metalization layers with links for typically more than one million transistors, which are characterized by resistance, capacitance, and inductance parameters governing the electric signal behavior and supply. To extract these parameters an electromagnetic analysis is performed which is actually a problem of solving a set of Maxwell equations in the domain of interest with given boundary conditions. Unfortunately such boundary-value problems can be solved analytically only for a few special cases. In general, for arbitrary shaped domains numerical approximation methods like the finite element method are used.

The presented thesis treats the numerical calculation of three-dimensional electromagnetic fields using the finite element method based on vector and scalar shape functions followed by consequent parameter extraction. It begins with an explanation of the boundary value problems, weighted residual and Galerkin's method. The Galerkin's method belongs to the classical methods forming the basis of modern finite element analysis. Subsequently the vector finite elements are introduced, which are particular suitable for the description of the electric field and the magnetic field vector functions. The formulated edge based triangular elements for two-dimensional applications and the edge based tetrahedral elements for the three-dimensional ones are the foundation for all calculations in this thesis derived and explained in detail. A special focus is the careful definition and analysis of the numerical schemes describing the dominant magnetic field case. The following complex diffusion models are handled by a partial differential equation system which is numerically calculated using a combination of vector and scalar shape functions.

The developed models are implemented in the three-dimensional finite element simulation software **SAP** (**S**mart **A**nalysis **P**rograms). The simulation results demonstrate the physical plausibility of the applied models and numerical methods as well as the necessity of three-dimensional simulations.

Die approbierte gedruckte Originalversion dieser Dissertation ist an der TU Wien Bibliothek verfügbar.
The approved original version of this doctoral thesis is available in print at TU Wien Bibliothek.
TU WIEN Bibliothek Your knowledge hub

Kurzfassung

Modellbildung und Simulation sind kritische Werkzeuge für die Minimierung von Entwicklungszeit und -kosten. Neue Modellierungskonzepte brauchen immer mehr langfristige fächerübergreifende Untersuchungen, die auf neuen numerischen Methoden und Algorithmen basieren.

Die dreidimensionale Verdrahtungsstruktur in integrierten Schaltkreisen stellt ein komplexes elektromagnetisches System dar. Sie enthält mehrere Metallisierungsschichten mit Verbindungen zu typisch mehr als einer Million Transistoren und ist charakterisiert durch Widerstands-, Kapazitäts- und Induktivitätsparameter, die das elektrische Signalverhalten und die elektrische Versorgung bestimmen. Die Extraktion dieser Parameter wird durch eine elektromagnetische Analyse durchgeführt, die schließlich zur Lösung der Maxwell-Gleichungen im interessierenden Gebiet bei vordefinierten Randbedingungen führt. Leider können solche Randwertaufgaben nur selten analytisch berechnet werden. Im Allgemeinen, wenn beliebige Geometrien berücksichtigt werden müssen, sollte man Approximationsmethoden wie z. B. die finite Elemente-Methode verwenden.

In der vorliegenden Arbeit wird die numerische Berechnung von dreidimensionalen elektromagnetischen Feldern unter der besonderen Verwendung von Vektorformfunkionen und der daraus resultierenden Parameterextraktion beschrieben. Zu Beginn werden die Randwertaufgabe, die Methode der gewichteten Residuen und die Methode von Galerkin eingeführt. Die Methode von Galerkin gehört zu den klassischen Methoden, die die Grundlage für die moderne finite Elemente-Analyse bilden. Anschließend werden die vektoriellen finiten Elemente eingeführt, die genau auf die Beschreibung von magnetischen und elektrischen Feldern im Definitionsbereich zugeschnitten sind. Die so formulierten Kantendreieckelemente für den zweidimensionalen und die Kantentetraederelemente für den dreidimensionalen Fall stellen die Grundlage für alle Berechnungen in dieser Arbeit dar und werden im Detail erklärt. Spezieller Wert wird auf die sorgsame Definition und Analyse der numerischen Schemata gelegt, die den Fall des dominant magnetischen Feldes beschreiben. Das davon resultierende komplexe Diffusionsmodell wird durch ein System von partiellen Differentialgleichungen beschrieben. Das System wird durch die finite Elemente-Methode mit einer Kombination aus vektoriellen und skalaren Formfunktionen gelöst.

Die entwickelten Modelle sind in das dreidimensionale Simulationspaket **SAP** (**S**mart **A**nalysis **P**rograms) implementiert. Die Simulationsergebnisse zeigen nicht nur die Plausibilität der verwendeten physikalischen Modelle und der numerischen Methoden, sondern auch die Notwendigkeit von dreidimensionalen Simulationen.

Die approbierte gedruckte Originalversion dieser Dissertation ist an der TU Wien Bibliothek verfügbar.
The approved original version of this doctoral thesis is available in print at TU Wien Bibliothek.

Acknowledgment

Without support of my colleagues and friends the creation of this work in this form would not have been possible. My thanks apply to all those who affected me positively during my work at the Institute for Microelectronics. First of all I like to express my thanks to Prof. Siegfried Selberherr and Prof. Erasmus Langer, who provided me with a perfect working environment. Their guidance and advise has been crucial for this work.

Especially I want to thank Prof. Herbert Haas. With his technical authority and experience in the numerical and analytical analysis of electromagnetic fields he helped me for the clear understanding of the theoretical part of this work.

Many thanks to Robert Bauer and Rainer Sabelka who created the basis for this work with their dissertations and their simulation software for resistance and capacitance extraction. I also extend my appreciation to Johann Cervenka and Hajdin Ceric for their ceaseless cooperation and for proofreading my thesis.

I owe gratitude to all my colleagues at the Institute for Microelectronics for the interesting discussions and their kind support.

And last but not least I want to thank my family and my relatives for supporting me during the whole time of my education.

Die approbierte gedruckte Originalversion dieser Dissertation ist an der TU Wien Bibliothek verfügbar.
The approved original version of this doctoral thesis is available in print at TU Wien Bibliothek.

Contents

1 Preface 1

2 Overview of Tools for Numerical Analysis of Electromagnetic Fields in Microelectronics 3

2.1 Ansoft 3
2.2 The COMSOL Group 4
2.3 CST 4
2.4 Magwel 5
2.5 Remcom 5
2.6 Synopsys 6
2.7 Institute for Microelectronics at the TU Wien 7

3 Introduction to the Finite Element Method 8

3.1 Boundary-Value Problems 9
3.2 The Weighted Residual Method 10
3.3 Galerkin's Method 11
  3.3.1 Galerkin's Method for the Scalar Differential Operator 12
  3.3.2 Galerkin's Method for the Vector Differential Operator 13

4 The Scalar Finite Element Method 16

4.1 Two-Dimensional Scalar Finite Element Method 17
  4.1.1 Domain Discretization 20
  4.1.2 Linear Shape Functions on Triangular Elements 21
  4.1.3 Introduction of Triangle Barycentric Coordinates 22
  4.1.4 Assembling 26
  4.1.5 Neumann Boundary Condition 29
4.2 Three-Dimensional Scalar Finite Element Method 33

4.2.1 Linear Shape Functions on Tetrahedral Elements 33
4.2.2 Tetrahedron Barycentric Coordinates 35
4.2.3 Assembling 37

5 The Vector Finite Element Method 40
5.1 Edge Elements Applications 41
5.1.1 The Wave Equation for the Electric Field 41
5.1.2 Equations for the Electrodynamic Potentials 41
5.1.3 Quasi-Magnetostatics 42
5.2 Three-Dimensional Vector Finite Element Method 43
5.2.1 Domain Discretization 48
5.2.2 Linear Vector Shape Functions on Tetrahedral Elements 49
5.2.3 Assembling 53
5.3 Two-Dimensional Vector Finite Element Method 60
5.3.1 Linear Vector Shape Functions on a Triangular Elements 61
5.3.2 Assembling 62

6 Applications 67
6.1 Inductance and Resistance of a Coaxial Structure 67
6.1.1 Analytical Inductance and Resistance Calculation 69
6.1.2 Numerical Inductance and Resistance Extraction 72
6.1.3 Simulated Fields Visualization and Results Comparison 75
6.2 Inductance and Resistance of On-Chip Inductors 77
6.2.1 Boundary Conditions 78
6.2.2 Domain Discretization 79
6.2.3 Examples and Results 79
6.3 Periodic Boundaries 83
6.3.1 Mesh Generation 84
6.3.2 Simulation Results 85

7 Outlook 87

A Integral Domain Transformation 88

B Two-Dimensional Neumann Boundary Term 91
B.1 Neumann Boundary for the Rotor-Rotor-Operator 91

Die approbierte gedruckte Originalversion dieser Dissertation ist an der TU Wien Bibliothek verfügbar.
The approved original version of this doctoral thesis is available in print at TU Wien Bibliothek.
TU WIEN Bibliothek Your knowledge hub

B.2 Neumann Boundary for Gauß's Law of Magnetism 94
  B.2.1 For the Scalar Function 94
  B.2.2 For the Vector Function 96

C Three-Dimensional Neumann Boundary Term Assembling 101

C.1 The Neumann Boundary for the Rotor-Rotor-Operator 101
C.2 Neumann Boundary for Gauß's Law of Magnetism 104
  C.2.1 For the Scalar Function 104
  C.2.2 For the Vector Function 105

Die approbierte gedruckte Originalversion dieser Dissertation ist an der TU Wien Bibliothek verfügbar.
The approved original version of this doctoral thesis is available in print at TU Wien Bibliothek.
TU WIEN Bibliothek Your knowledge hub

Die approbierte gedruckte Originalversion dieser Dissertation ist an der TU Wien Bibliothek verfügbar.
The approved original version of this doctoral thesis is available in print at TU Wien Bibliothek.

List of Tables

5.1 Tetrahedral Element Edge Definition. 54

6.1 Numerically simulated and analytically calculated R and L. 77
6.2 Calculated inductance and resistance. 80

List of Figures

4.1 Triangular element. 21
4.2 Barycentric coordinates outside a triangular element. 25
4.3 Two-dimensional domain transformation. 26
4.4 Node and element numbering in a discretized domain. 27
4.5 Homogeneous Neumann boundary conditions on the outer boundary. . . . 32
4.6 The outer region is cut off. 32
4.7 Tetrahedral element. 34
4.8 Three-dimensional domain transformation. 39

5.1 The inductor inside the simulation domain in Fig. <5.2>. 50
5.2 The entire simulation domain. 51
5.3 Inside view of the simulation domain in Fig. <5.2>. 52
5.4 The conductor entry. 53
5.5 The shape function along Edge 12. 55
5.6 The shape function along Edge 34. 56
5.7 The sum of all shape functions in the tetrahedron. 57
5.8 The shape function along Edge 12. 63
5.9 The sum of the shape functions in the triangle. 64

6.1 The simulated coaxial structure. 69
6.2 Current density distribution. 70
6.3 Magnetic field. 71
6.4 Current density distribution at low frequency. 75
6.5 Current density distribution at 3 GHz. 75
6.6 Current density distribution at 30 GHz. 75
6.7 Current density distribution at 300 GHz. 75
6.8 Magnetic field distribution at low frequency. 76

Die approbierte gedruckte Originalversion dieser Dissertation ist an der TU Wien Bibliothek verfügbar.
The approved original version of this doctoral thesis is available in print at TU Wien Bibliothek.
TU WIEN Bibliothek Your knowledge hub

6.9 Magnetic field distribution at 3 GHz. 76
6.10 Magnetic field distribution at 30 GHz. 76
6.11 Magnetic field distribution at 300 GHz. 76
6.12 The simulation domain. 81
6.13 The generated mesh. 81
6.14 Surface view of the current density [A/m^2] distribution at 100 MHz. . . . 81
6.15 Surface view of the current density [A/m^2] distribution at 10 GHz. 81
6.16 Current density distribution at 1 GHz. 82
6.17 Magnetic field distribution [A/m] at 1 GHz. 82
6.18 Current density distribution in the via at 100 MHz. 82
6.19 Current density distribution in the via at 10 GHz. 82
6.20 Current density [A/m^2] distribution in the substrate at 1 GHz. 82
6.21 Magnetic field [A/m] in the substrate at 1 GHz. 82
6.22 An interconnect bus. 86
6.23 The simulation area. 86
6.24 The electrodes in the simulation area. 86
6.25 The electric potential distribution with x periodicity. 86
6.26 The iso faces of the electric potential distribution with x periodicity. . . . 86
6.27 The electric potential distribution without periodicity. 86
6.28 The iso faces of the electric potential distribution without periodicity. . . 86

A.1 Two-dimensional domain transformation. 88

Die approbierte gedruckte Originalversion dieser Dissertation ist an der TU Wien Bibliothek verfügbar.
The approved original version of this doctoral thesis is available in print at TU Wien Bibliothek.

Die approbierte gedruckte Originalversion dieser Dissertation ist an der TU Wien Bibliothek verfügbar.
The approved original version of this doctoral thesis is available in print at TU Wien Bibliothek.
TU WIEN Bibliothek Your knowledge hub

Chapter 1

Preface

In modern microelectronics the interconnects represent a complicated electromagnetic system which is essentially characterized by parameters like capacitance, resistance, and inductance at different frequencies. These parameters are extracted from the electric and magnetic fields after solving the Maxwell equations. This is usually based on numerical methods like finite element analysis which is probably one of the most superior simulation techniques in electromagnetics. Inductive effects have been neglected in integrated circuit design for a long time. That is on one side, because they become noticeable only with very high frequencies, and on the other side probably, because its computation is much more complex than those of the capacitances or direct current (DC) resistances. Usually capacitance and DC resistance are obtained by finite element analysis with scalar interpolation functions. For three-dimensional inductance and high frequency resistance calculation another kind of interpolation functions, the so called edge or vector interpolation functions have to be introduced.

The procedures presented in this work bear mostly on the computation of inductance and resistance of arbitrarily shaped three-dimensional interconnect structures in microelectronics at frequencies at which skin effect can be observed. The extreme small dimensions of modern microelectronics topology give the opportunity to use the quasi-magnetostatic case, assuming the so-called dominant magnetic field model. The resulting partial differential equation system arising from the Maxwell equations is solved in the frequency domain and provides the time-harmonic magnetic field distribution and the current density distribution in the domain of interest at the given frequency. Thereby induction, skin effect, and proximity effect are taken into account. As a consequence the inductance and the resistance of the interconnect structure in the simulation domain at a specific frequency is extracted from the numerically calculated fields' distributions. Working in the frequency domain gives no disadvantage as it appears. Each time dependent function can be expressed in terms of time-harmonic parts using Fourier analysis.

In Chapter 3 a brief introduction to the finite element method is given. The basic principle is illustrated by the weighted residual and by Galerkin's method. Since the mathematical models in this work contain scalar and vector fields, both, the scalar and the vector finite element interpolation is addressed. A detailed explanation of the finite element assembling is discussed in Chapter 4, where the concept for scalar finite elements is presented. The governing mathematical expressions are derived and given for the two- and three-dimensional case. Chapter 5 is devoted to the formulation of vector finite element analysis. Some basic applications of electromagnetics for the vector interpolation are presented. Again the corresponding general algorithms and formulas for two- and three-dimensional assembling are explained. The simulation domain discretization is discussed to interfere the importance of the properties of the generated mesh for further analysis steps.

Typical three-dimensional applications occurring in microelectronics for vector and scalar finite element techniques are presented in Chapter 6. The theory from the previous chapters is used for magnetic field and current density or electrostatic potential distribution calculation in different regions for given electromagnetic problems. Consequently the parameters of interest are extracted. The fields are visualized to demonstrate the properness of the numerical analysis. This chapter starts with an inductance and resistance extraction example for a specific structure, which also provides analytical formulas for the parameters calculation. Thus the method is evaluated (at least for this structure) by comparison between the numerically simulated and analytically calculated results. This example addresses also the parameter extraction from the numerically calculated fields by the power in the simulation domain. After that an on-chip spiral inductor as typically used in microelectronics is analyzed. Another interesting application is the simulation of periodic structures. In such cases by applying so-called periodic boundary conditions it is possible to simulate only small substructures which represent the geometrical period of the entire structure. Thus the simulation resources and the computation time can be significantly optimized.

Related topics are covered in the appendices. In Appendix A the integration domain transformation is explained, which is commonly used for the derivation of the finite element assembling expressions. Appendix B and Appendix C describe a possible discretization of the Neumann boundary term naturally arising after the so called weak formulation in the finite element analysis. It corresponds with the Neumann boundary condition given on the Neumann boundary. Normally the Neumann boundary is a part of or the entire outer closure of the simulation domain and the corresponding Neumann condition is assumed to be zero — homogeneous Neumann boundary condition. This is almost legitimate also for open or infinite regions considering the fact that the field quantities decrease to zero with increasing distance to the source. However as discussed in Subsection 4.1.5 applying the homogeneous Neumann boundary to open regions distorts the results. In such cases hybrid techniques like a combination of finite elements and boundary integral methods can be addressed, where the discretization of the Neumann boundary term is required.

Die approbierte gedruckte Originalversion dieser Dissertation ist an der TU Wien Bibliothek verfügbar.
The approved original version of this doctoral thesis is available in print at TU Wien Bibliothek.

Die approbierte gedruckte Originalversion dieser Dissertation ist an der TU Wien Bibliothek verfügbar.
The approved original version of this doctoral thesis is available in print at TU Wien Bibliothek.

Chapter 2

Overview of Tools for Numerical Analysis of Electromagnetic Fields in Microelectronics

Over the past decades a large number of simulation tools for numerical analysis of the electromagnetic fields and for the subsequent parameter extraction has been developed. Parameter extraction based on the field calculation by the finite element method has a long tradition also in the Institute for Microelectronics at the Technical University in Vienna. In this chapter some of the most important commercial software packages for numerical analysis are discussed. At the end the interconnect simulation software package `Smart Analysis Programs` is introduced.

2.1 Ansoft

Ansoft [1] tools integrate electromagnetic, circuit, and system engineering in a complete design environment. Some of the most interesting applications are the following:

`HFSS` is a three-dimensional full-wave electromagnetic simulation tool for S-parameter, `SPICE` extraction, and field computation of high-frequency and high-speed components. It models on-chip embedded passive components, integrated circuit packages, printed circuit board interconnects, antennas, radio frequency and microwave components, and biomedical devices. It uses higher-order hierarchical shape functions and an iterative solver, which provides efficient and accurate field solutions at coarser meshes. A high-quality finite element mesher supports discretization of complex geometries.

`Q3D Extractor` provides high-performance three-dimensional and two-dimensional parasitic extraction of electronic components based on quasi-static electromagnetic-field simulation. The method of moments and the finite element method are used to obtain three-dimensional RLC and two-dimensional RLCG values. An equivalent `SPICE` circuit model can be automatically generated.

`TPA` (`Turbo Package Analyzer`) provides automated parasitic extraction for integrated circuit packages. Lumped or distributed RLC parameters in integrated circuit packages for analog radio frequency and high-speed digital applications are obtained automatically.

2.2 The COMSOL Group

The COMSOL Group [2] is an engineering software company providing solutions for multiphysics modeling.

`COMSOL Multiphysics` is a versatile simulation environment providing geometry modeling, physics specification, mesh generation, solving, and results post-processing. Predefined modeling modules and templates for a large number of applications like fluid flow and heat transfer, structural mechanics, and electromagnetic analyses guarantee quick problem description and solving. Excitation terms, boundary conditions, and material properties can be given by arbitrary functions. The researchers can define their own partial differential equations and interdependencies. The functionality can be extended by many auxiliary add-on interfaces. One of them is the *AC/DC Module* coupling electrostatics, magnetostatics, and quasi electro- and magnetostatics with different physical phenomenons, like thermal effects. Its `SPICE` interface allows to model circuit components for subsequent finite element analysis. The CAD import module provides easy handling of CAD formats. The radio frequency module is utilized in radio frequency, microwave and optical engineering simulations for easily modeling of antennas, waveguides, microwave and optical components.

`COMSOL SCRIPT` provides access to all `COMSOL Multiphysics` modeling capabilities.

2.3 CST

CST (Computer Simulation Technology) [3] offers solutions for static, stationary, low and high frequency problems.

`CST MWS` (`CST MICROWAVE STUDIO`) is an accurate and fast three-dimensional high frequency simulator for electromagnetic problems. Its frequency domain solver performs on tetrahedral as well as on hexahedral meshes. `CST MWS` can be linked with external simulators to a larger design environment through the open architecture `CST DESIGN STUDIO`. It can extract parameters ready for further `SPICE` analysis and provides filters for specific CAD input.

`CST DS` (`CST DESIGN STUDIO`) divides complex systems into smaller system parts, each described by its S-matrix. The particularly best suited simulator to each sub-system is applied. Thus the behaviour of the entire system is analysed more efficiently within a few seconds. Analytical models or measured components (e.g. transmission lines) can also be considered.

`CST EMS` (`CST EM STUDIO`) facilitates static and low frequency device simulation. `CST EMS` offers different solver techniques for electrostatics, magnetostatics, current flow, low

Die approbierte gedruckte Originalversion dieser Dissertation ist an der TU Wien Bibliothek verfügbar.
The approved original version of this doctoral thesis is available in print at TU Wien Bibliothek.

Die approbierte gedruckte Originalversion dieser Dissertation ist an der TU Wien Bibliothek verfügbar.
The approved original version of this doctoral thesis is available in print at TU Wien Bibliothek.
TU WIEN Bibliothek Your knowledge hub

frequency, and stationary temperature problems. In order to analyze coupled problems, the results obtained by one of the solvers can be transferred to another. The same three-dimensional electromagnetic simulator supports both, orthogonal and tetrahedral meshing. It chooses automatically the method (method on demand) and the mesh (mesh on demand) best suited to a particular problem and structure, respectively. If desired, different simulation technologies can be applied to a problem for cross-checking the results.

The electrostatic solver is utilized for static or quasi-static problems (for example to calculate the field between the electrodes of a capacitor). When eddy currents are negligible or when nonlinear materials are used, the magnetostatics solver is mostly used. Additionally it provides automated impedance extraction. Magnetostatic computation like current distributions in lossy materials are provided by the stationary current solver. The quasi-electrostatics solver applies for slowly varying fields in the presence of low conductivity materials. The low-frequency frequency domain solver has been developed for lossy low-frequency applications to calculate eddy currents, loss densities, and energy densities. Thereby, the wave propagation in a device can be also considered, because the displacement current is taken into account. For the thermal problems the thermal solver is used. Most solvers can be switched from orthogrid generation to tetrahedral meshing.

2.4 Magwel

Magwel [4] offers simulation software for designing integrated circuits.

`EditEM` is a very intuitive and versatile design editor. It can read CAD files, it is capable to check three-dimensional structures and the corresponding mesh. Layer based geometries are investigated layer-wise.

`SolvEM` is a powerful three-dimensional solver for electromagnetic problems. Its capabilities include Maxwell equations computation at high frequencies and drift-diffusion equations in semiconductor domains. Thereby skin effect, current crowding effect, eddy currents, and semiconductor junction space charges can be computed. It provides a coupling between interconnect simulation in conductors, insulators and semiconductors.

`ExtractEM` provides lumped or S-parameter extraction of the investigated structure. The researcher can inspect the computed field results and use the extracted parameters for further investigation as input for SPICE simulation.

2.5 Remcom

Remcom provides a large number of simulation software packages for electromagnetic analysis [5]. One of these products provided by Remcom is `XFdtd`. `XFdtd` is a full wave three-dimensional finite difference time domain electromagnetic solver. Models described by different CAD file formats can be easily imported, edited, and then exported to CAD format again. `XFdtd` offers a fast meshing algorithm and mesh preview before calculation. It can model complex nonlinear and frequency-dependent electric and magnetic materials, nonlinear devices, and anisotropic materials. Due to its parallelization capability huge applications can use computer clusters. `XFdtd` supports `XStream` hardware FDTD (another product of Remcom), which utilizes high speed graphics processors for increased calculation speed.

2.6 Synopsys

Synopsys [6] delivers software for semiconductor modeling, intellectual property, and design for manufacturing solutions. It provides professional tools for development of on-chip and electronic systems. Some of the very interesting extraction tools from the TCAD tool suite are `Raphael`, `Star-RCXT`, and `Raphael NXT`.

`Raphael` is a two-dimensional and three-dimensional field solvers collection for interconnect design and analysis. It calculates the electrical and thermal phenomena in complex on-chip interconnect structures. The graphical user interface allows process data to be easily incorporated and the critical interconnect geometries to be automatically generated. `Raphael` extracts capacitance, resistance, and inductance for optimizing multi-level interconnects and on-chip parasitics using its industry-standard field solvers and interfaces. It considers the effect of process variation by investigation of complex interconnect geometries and administrates a database to investigate the effect of design-rule changes. Its features include two- and three-dimensional capacitance and resistance extraction of interconnect structures by the finite difference method, two- and three-dimensional interconnect capacitance computation by the boundary element method, three-dimensional inductance and resistance calculation under consideration of skin effect, electric field and potential calculation, temperature and current density distribution simulation considering floating conductors and conformal dielectric layers with anisotropic permittivity.

`Star-RCXT` is accurate parasitic extraction tool, providing solution for ASIC, on-chip systems, digital and analog designs. Some of its features include three-dimensional parasitic computation with accurate process variation modeling, substrate extraction, automatic field solver flow, chemical-mechanical polishing simulation and litho-aware extraction.

`Raphael NXT` complements `Star-RCXT` by three-dimensional capacitance extraction of critical nets, cells, or blocks on the full-chip level. It considers conformal dielectrics, trapezoidal conductor cross sections, metal fill, and lithography effects to model accurately the complex interconnect geometries. `Raphael NXT` makes use of the floating random-walk method [7, 8], which allows parameter extraction in domains with a size well beyond the reach of mesh-based simulators. Usually `Raphael NXT` applies a $0\,\mathrm{V}$ Dirichlet boundary condition at the outer bounds of the simulation domain. However, reflecting Neumann boundary conditions and periodic boundary conditions for structures with repeated cells can be also specified explicitly. Due to the floating random-walk method `Raphael NXT` provides distributed computation even with different loads on different processors.

Die approbierte gedruckte Originalversion dieser Dissertation ist an der TU Wien Bibliothek verfügbar.
The approved original version of this doctoral thesis is available in print at TU Wien Bibliothek.
TU WIEN Bibliothek Your knowledge hub

Die approbierte gedruckte Originalversion dieser Dissertation ist an der TU Wien Bibliothek verfügbar.
The approved original version of this doctoral thesis is available in print at TU Wien Bibliothek.

TU WIEN Bibliothek Your knowledge hub

2.7 Institute for Microelectronics at the TU Wien

The scientists of the Institute for Microelectronics at the TU Wien develop software for device, process and interconnect simulation.

`Smart Analysis Programs` is a collection of tools for numerical simulations of electric, magnetic, and thermal phenomena occurring in interconnect lines of integrated circuits. It has been developed by Robert Bauer [9], Rainer Sabelka [10], and Christian Harlander [11]. The package contains preprocessing tools, a finite element simulator, and visualization software. The two- and three-dimensional finite element analysis program STAP is utilized for electric and magnetic field calculation and consequent RLC extraction. It can perform transient and static thermal analysis of interconnects under electrical stress. A transient electric or electro-quasistatic mode is supported for the simulation of delay times or crosstalk.

CUTGRID is the preprocessing tool for two-dimensional solid modeling and a mesh generation, well suited for cross-sectional two-dimensional planes. Its output is a triangular mesh which is used by the finite element simulator STAP as input. Another preprocessing software is the three-dimensional geometry specification and mesh generation tool LAYGRID. The interconnect lines in the integrated circuits build a layered structure. This allows the cumbersome problem of three-dimensional geometry description to be reduced to flat mask definitions and planar or non-planar layers. Thereby, the masks can easily be extracted from a layout description and layers can be derived from cross sections. LAYGRID generates a tetrahedral mesh suitable for further investigations with STAP.

For capacitance extraction STAP solves the Laplace equation for the electric potential in the simulation domain. It is assumed that the electrodes of the capacitor are ideal conductors and the dielectric is an ideal insulator. The surfaces of the electrodes represent Dirichlet boundary conditions. The capacitance is extracted from the electric field energy. STAP provides global grid refinement and quadratic shape scalar functions in order to increase the accuracy of the simulation. The finite element discretization leads often to a large linear equation system, which is solved by a preconditioned conjugate gradient method. Thereby a compressed matrix format for the sparsely occupied stiffness matrix is used in order to achieve an efficient utilization of computer memory.

For simulation of periodic structures STAP uses the so-called periodic boundary conditions. In this case the simulation is performed only in the geometrical period, which is usually much smaller than the entire structure. The periodic boundaries capability of the preprocessing tools CUTGRID and LAYGRID were developed and implemented by Wilfried Wessner [12].

The generated mesh and the resulting two- and three-dimensional distributions can be inspected with the visualisation tool SV.

Die approbierte gedruckte Originalversion dieser Dissertation ist an der TU Wien Bibliothek verfügbar.
The approved original version of this doctoral thesis is available in print at TU Wien Bibliothek.
TU WIEN Bibliothek Your knowledge hub

Chapter 3

Introduction to the Finite Element Method

Normally the problems arising from mathematical physics are described by partial differential equation systems [13, 14, 15, 16] defined in a given domain of interest. These boundary value problems represent the models of specific problems for further simulation and analysis [17] and are usually approximately solved by numerical procedures. One of these procedures is the finite element method. Originally this method has been successfully applied to mechanical problems [18, 19]. Today, the finite element method is the general technique widely used for mathematical and engineering numeric analysis. A lot of books and scripts have been issued to help understanding and applying this interesting and useful topic [20, 21, 22, 23, 24, 25, 26, 27, 28]. The method is also well suited for object-oriented treatment [29], which is essential for software implementation. Further enhancement of the finite element method can be achieved by formulating self-adapting procedures and techniques to solve open region problems [30] and by the analysis of the error in the computed finite element solution [31, 32]. There are two most widely used classical methods for approximation of boundary-value problems. One is the Ritz Method and the other is Galerkin's method [33, 34]. The Ritz method[1] is a variational method. It formulates the boundary value problem in terms of a variational expression, called functional. Galerkin's method belongs to the family of weighted residual methods. These two methods build the foundation of modern finite element analysis. In this work Galerkin's approach is preferred for the introduction of the finite element method.

In general an area $\mathcal{A}$ is enclosed in its boundary $\partial\mathcal{A}$ which usually consists of several closed curves. Closed surfaces have no boundary ($\partial\mathcal{A} = 0$). Analogously the boundary $\partial\mathcal{V}$ of a three-dimensional domain $\mathcal{V}$ can be represented by one or more closed surfaces. The unit normal vector to the boundary curve $\partial\mathcal{A}$ for the two-dimensional case or to the boundary surface $\partial\mathcal{V}$ for the three-dimensional case, respectively, is denoted as $\vec{n}$. It has the characteristic length one and points outward.

---

[1] The Ritz method is also known as Rayleigh-Ritz Method.

Die approbierte gedruckte Originalversion dieser Dissertation ist an der TU Wien Bibliothek verfügbar.
The approved original version of this doctoral thesis is available in print at TU Wien Bibliothek.

3.1 Boundary-Value Problems

The boundary-value problems can be described by the expression

$$\mathcal{L}\left[u\left(\vec{r}\right)\right] = f(\vec{r}) \tag{3.1}$$

in a domain $\mathcal{V}$ and by the boundary conditions applied on the boundary $\partial\mathcal{V}$ enclosing the domain $\mathcal{V}$. In (3.1) $\mathcal{L}$ is a differential operator, u is the unknown function, and f is the excitation or forcing term. The differential equations used in this thesis are linear. Therefore, $\mathcal{L}$ is assumed to be a linear differential operator.

Depending on the type of fields to be solved there are different kinds of linear differential operators $\mathcal{L}$. In this thesis the linear differential operator appears as scalar operator

$$\mathcal{L}[u] = \vec{\nabla} \cdot (\underset{\sim}{a} \cdot \vec{\nabla} u) + bu \tag{3.2}$$

or as vector operator

$$\vec{\mathcal{L}}[\vec{u}] = \vec{\nabla} \times \left[\underset{\sim}{a} \cdot (\vec{\nabla} \times \vec{u})\right] + \underset{\sim}{b} \cdot \vec{u}. \tag{3.3}$$

In (3.2) and (3.3) $\underset{\sim}{a} = \underset{\sim}{a}(\vec{r})$ and $\underset{\sim}{b} = \underset{\sim}{b}(\vec{r})$ are position dependent second order symmetric tensors and $b = b(\vec{r})$ is a position dependent scalar factor. The operator $\vec{\nabla}$ is the in the vector analysis widely used differential operator nabla. In Cartesian coordinates in the three-dimensional space $\vec{\nabla}$ has the following representation:

$$\vec{\nabla} = \vec{e}_x \partial_x + \vec{e}_y \partial_y + \vec{e}_z \partial_z.$$

The partial derivative, for example with respect to the variable x, is abbreviated as ∂_x instead of $\frac{\partial}{\partial x}$. The expressions (3.2) and (3.3) represent linear differential operators. In (3.2) $\mathcal{L}$ is a scalar differential operator which operates on the scalar function u. In (3.3) $\vec{\mathcal{L}}$ is a vector differential operator which operates on the vector function $\vec{u}$.

The boundary $\partial\mathcal{V}$ is divided as in [35] into a Dirichlet boundary $\mathcal{A}_D$ and a Neumann boundary $\mathcal{A}_N$, where

$$\partial\mathcal{V} = \mathcal{A}_D + \mathcal{A}_N.$$

For elliptical partial differential equations, like the Helmholtz equation $\vec{\nabla}\cdot\vec{\nabla}u + bu = f(\vec{r})$, the Dirichlet boundary condition (or the boundary condition of the first kind)

$$u(\vec{r}) = u_d \text{ on } \mathcal{A}_D$$

is given by the values of u on the Dirichlet boundary $\mathcal{A}_D$ and the Neumann boundary condition (or the boundary condition of the second kind)

$$\vec{n} \cdot \vec{\nabla} u(\vec{r}) = u_n \text{ on } \mathcal{A}_N.$$

Die approbierte gedruckte Originalversion dieser Dissertation ist an der TU Wien Bibliothek verfügbar.
The approved original version of this doctoral thesis is available in print at TU Wien Bibliothek.

by the normal derivative of u on the Neumann boundary $\mathcal{A}_N$, respectively [36]. For the more general case (3.2) the Neumann boundary condition has to be specified by the conormal derivative

$$\vec{n} \cdot \underset{\sim}{a} \cdot \vec{\nabla} u(\vec{r}) = u_n \text{ on } \mathcal{A}_N. \tag{3.4}$$

instead of the normal derivative [37].

The same can be written for two-dimensional problems. In this case the domain is an area denoted as $\mathcal{A}$ with the boundary $\partial\mathcal{A}$

$$\partial\mathcal{A} = \mathcal{C}_D + \mathcal{C}_N.$$

3.2 The Weighted Residual Method

The weighted residual method is demonstrated for the scalar function u and can be applied analogously to the vector one $\vec{u}$. Usually the unknown function u of (3.1) cannot be found analytically, therefore, it is approximated by

$$\tilde{u}(\vec{r}) = \sum_{j=1}^{n} c_j N_j(\vec{r}) + v(\vec{r}) \simeq u(\vec{r}). \tag{3.5}$$

In (3.5) $v(\vec{r})$ is a known function which fulfills exactly the Dirichlet boundary condition on $\mathcal{A}_D$

$$v(\vec{r}) = u(\vec{r}) \text{ on } \mathcal{A}_D. \tag{3.6}$$

The basis (also called form or shape) functions $N_j(\vec{r}),\ j \in [1;n]$ build a set of linear independent known functions which vanish on the Dirichlet boundary $\mathcal{A}_D$. Thus (3.6) is satisfied for each arbitrary set of coefficients $c_j,\ j \in [1;n]$. The coefficients c_j must be determined in such a way that the function $\tilde{u}$ approximates the solution of (3.1) as exactly as possible. The basis functions should be formulated in such way that each solution can be approximated with arbitrary accuracy, if a sufficiently large number of basis functions is used. After substitution of $\tilde{u}$ for u in (3.1) a nonzero residual is obtained in general

$$R(\vec{r}) = \mathcal{L}\left[\tilde{u}(\vec{r})\right] - f(\vec{r}) \neq 0. \tag{3.7}$$

To find a good approximation $\tilde{u}$ for u it is required to minimize the residual (3.7). The weighted residual method finds the unknown coefficients c_j by weighting the residual (3.7). This is performed by choosing a set of linear independent weighting (called test or trial) functions $W_i(\vec{r})$, $i \in [1;n]$ and by enforcing the condition

$$\int\limits_{\mathcal{V}} W_i(\vec{r}) R(\vec{r}) \,\mathrm{d}V = 0. \tag{3.8}$$

Die approbierte gedruckte Originalversion dieser Dissertation ist an der TU Wien Bibliothek verfügbar.
The approved original version of this doctoral thesis is available in print at TU Wien Bibliothek.

Insertion of (3.7) in (3.8) gives

$$\int_{\mathcal{V}} W_i(\vec{r}) \left\{ \mathcal{L}\left[\tilde{u}(\vec{r})\right] - f(\vec{r}) \right\} \mathrm{d}V = 0, \quad i \in [1;n], \tag{3.9}$$

which leads to the following expression to obtain the coefficients c_j

$$\int_{\mathcal{V}} W_i(\vec{r}) \left\{ \mathcal{L}\left[\sum_{j=1}^{n} c_j N_j(\vec{r}) + v(\vec{r}) \right] - f(\vec{r}) \right\} \mathrm{d}V = 0, \quad i \in [1;n]. \tag{3.10}$$

Since $\mathcal{L}$ is a linear differential operator (3.10) becomes

$$c_j \sum_{j=1}^{n} \int_{\mathcal{V}} W_i(\vec{r}) \mathcal{L}\left[N_j(\vec{r})\right] \mathrm{d}V = \int_{\mathcal{V}} W_i \left\{ f(\vec{r}) - \mathcal{L}\left[v(\vec{r})\right] \right\} \mathrm{d}V, \quad i \in [1;n], \tag{3.11}$$

which corresponds to a linear equation system

$$[K]\,\{c\} = \{d\}\,. \tag{3.12}$$

The Matrix $[K]$ and the right hand side vector $\{d\}$ are given by the expressions

$$\begin{aligned} K_{ij} &= \int_{\mathcal{V}} W_i(\vec{r}) \mathcal{L}\left[N_j(\vec{r})\right] \mathrm{d}V \\ d_i &= \int_{\mathcal{V}} W_i(\vec{r}) \left\{ f(\vec{r}) - \mathcal{L}\left[v(\vec{r})\right] \right\} \mathrm{d}V, \quad i \in [1;n], \; j \in [1;n]. \end{aligned} \tag{3.13}$$

3.3 Galerkin's Method

If the weighting functions W_i are chosen to be the same as those applied in the sum of the approximation ($W_i(\vec{r}) = N_i(\vec{r})$), the weighted residual method merges into Galerkin's method. If $\mathcal{L}$ is self-adjoint, the matrix from (3.12) is symmetric and Galerkin's method leads to the same linear equation system as those given by the Ritz method [38].

Die approbierte gedruckte Originalversion dieser Dissertation ist an der TU Wien Bibliothek verfügbar.
The approved original version of this doctoral thesis is available in print at TU Wien Bibliothek.
TU WIEN Bibliothek Your knowledge hub

3.3.1 Galerkin's Method for the Scalar Differential Operator

Equation (3.9) is written as

$$\int\limits_{\mathcal{V}} N_i \left[\vec{\nabla}\cdot(\underset{\sim}{a}\cdot\vec{\nabla}\tilde{u}) + b\tilde{u}\right]\,\mathrm{d}V - \int\limits_{\mathcal{V}} N_i f\,\mathrm{d}V = 0, \quad i\in[1;n], \tag{3.14}$$

where Galerkin's method ($W_i = N_i$) and the scalar differential operator (3.2) are used. After applying the first scalar Green's theorem

$$\int\limits_{\mathcal{V}} W\left[\vec{\nabla}\cdot(\underset{\sim}{a}\cdot\vec{u})\right]\,\mathrm{d}V = \int\limits_{\partial\mathcal{V}} W\,\vec{n}\cdot\underset{\sim}{a}\cdot\vec{u}\,\mathrm{d}A - \int\limits_{\mathcal{V}} \vec{\nabla}W\cdot\underset{\sim}{a}\cdot\vec{u}\,\mathrm{d}V \tag{3.15}$$

(3.14) is modified to read

$$\int\limits_{\partial\mathcal{V}} N_i\,\vec{n}\cdot\underset{\sim}{a}\cdot\vec{\nabla}\tilde{u}\,\mathrm{d}A - \int\limits_{\mathcal{V}} \vec{\nabla}N_i\cdot\underset{\sim}{a}\cdot\vec{\nabla}\tilde{u}\,\mathrm{d}V + \int\limits_{\mathcal{V}} bN_i\tilde{u}\,\mathrm{d}V - \int\limits_{\mathcal{V}} N_i f\,\mathrm{d}V = 0, \quad i\in[1;n]. \tag{3.16}$$

Since N_i vanishes on $\mathcal{A}_D$ for $i\in[1;n]$ the boundary integral from (3.16) reads

$$\int\limits_{\partial\mathcal{V}} N_i\,\vec{n}\cdot\underset{\sim}{a}\cdot\vec{\nabla}\tilde{u}\,\mathrm{d}A = \int\limits_{\mathcal{A}_N} N_i\,\vec{n}\cdot\underset{\sim}{a}\cdot\vec{\nabla}\tilde{u}\,\mathrm{d}A \simeq \int\limits_{\mathcal{A}_N} N_i\,u_n\,\mathrm{d}A. \tag{3.17}$$

In (3.17) the conormal derivative $\vec{n}\cdot\underset{\sim}{a}\cdot\vec{\nabla}\tilde{u}$ corresponds with the Neumann boundary condition on $\mathcal{A}_N$ (3.4) [35, 37]

$$\vec{n}\cdot\underset{\sim}{a}\cdot\vec{\nabla}\tilde{u} \simeq u_n = \vec{n}\cdot\underset{\sim}{a}\cdot\vec{\nabla}u \text{ on } \mathcal{A}_N. \tag{3.18}$$

Equation (3.16) leads with (3.5) and (3.17) to the linear equation system (3.12), where $[K]$ and $\{d\}$ are given by

$$\begin{aligned} K_{ij} &= -\int\limits_{\mathcal{V}} \vec{\nabla}N_i\cdot\underset{\sim}{a}\cdot\vec{\nabla}N_j\,\mathrm{d}V + \int\limits_{\mathcal{V}} bN_i\,N_j\,\mathrm{d}V \\ d_i &= \int\limits_{\mathcal{V}} N_i\,(f-\mathcal{L}\,[v])\,\mathrm{d}V - \int\limits_{\mathcal{A}_N} N_i\,u_n\,\mathrm{d}A, \quad i\in[1;n],\ j\in[1;n], \end{aligned} \tag{3.19}$$

with $\mathcal{L}[v]$ from (3.2).

Die approbierte gedruckte Originalversion dieser Dissertation ist an der TU Wien Bibliothek verfügbar.
The approved original version of this doctoral thesis is available in print at TU Wien Bibliothek.

3.3.2 Galerkin's Method for the Vector Differential Operator

If the vector differential operator $\vec{\mathcal{L}}$ from (3.3) is used the corresponding excitation function in (3.1) must be a vector function as well which is written as $\vec{f}\,(\vec{r})$.

$$\vec{\mathcal{L}}\,[\vec{u}\,(\vec{r})] = \vec{f}\,(\vec{r})\,. \tag{3.20}$$

The approximation (3.5) corresponds to

$$\tilde{\vec{u}}(\vec{r}) = \sum_{j=1}^{n} c_j \vec{N}_j(\vec{r}) + \vec{v}(\vec{r}) \simeq \vec{u}(\vec{r}), \tag{3.21}$$

where $\vec{v}(\vec{r})$ is a known function which exactly fulfills the Dirichlet boundary condition on $\mathcal{A}_D$. The basis functions $\vec{N}_j(\vec{r}),\ j \in [1;n]$ build a set of linear independent known functions. Their tangential components vanish on the Dirichlet boundary $\mathcal{A}_D$. The residual is given analogously to (3.7) by

$$\vec{R}(\vec{r}) = \vec{\mathcal{L}}\left[\tilde{\vec{u}}\,(\vec{r})\right] - \vec{f}(\vec{r}) \neq 0 \tag{3.22}$$

and does not vanish in general. In this case the weighting functions in Section 3.2 must also be merged into vector functions $\vec{W}_i$ and the dot product must be used instead of scalar multiplication.

$$\int\limits_{\mathcal{V}} \vec{W}_i(\vec{r}) \cdot \vec{R}(\vec{r}) = \int\limits_{\mathcal{V}} \vec{W}_i(\vec{r}) \cdot \left\{ \vec{\mathcal{L}}\left[\tilde{\vec{u}}(\vec{r})\right] - \vec{f}(\vec{r}) \right\} \mathrm{d}V = 0, \quad i \in [1;n] \tag{3.23}$$

or

$$\int\limits_{\mathcal{V}} \vec{W}_i(\vec{r}) \cdot \vec{\mathcal{L}}\left[\tilde{\vec{u}}(\vec{r})\right] \mathrm{d}V - \int\limits_{\mathcal{V}} \vec{W}_i(\vec{r}) \cdot \vec{f}(\vec{r})\,\mathrm{d}V = 0, \quad i \in [1;n]. \tag{3.24}$$

With these considerations the weighted residual method described in section 3.2 will also lead to the linear equation system (3.12) where the matrix $[K]$ and the right hand side $\{d\}$ are given by

$$\begin{aligned} K_{ij} &= \int\limits_{\mathcal{V}} \vec{W}_i(\vec{r}) \cdot \vec{\mathcal{L}}\left[\vec{N}_j(\vec{r})\right] \mathrm{d}V \\ d_i &= \int\limits_{\mathcal{V}} \vec{W}_i(\vec{r}) \cdot \left\{ \vec{f}(\vec{r}) - \vec{\mathcal{L}}\,[\vec{v}(\vec{r})] \right\} \mathrm{d}V, \quad i \in [1;n],\ j \in [1;n]. \end{aligned} \tag{3.25}$$

Die approbierte gedruckte Originalversion dieser Dissertation ist an der TU Wien Bibliothek verfügbar.
The approved original version of this doctoral thesis is available in print at TU Wien Bibliothek.
TU WIEN Bibliothek Your knowledge hub

After using the Galerkin approach $\vec{W}_i(\vec{r}) = \vec{N}_i(\vec{r})$, substituting the vector differential operator $[\vec{\mathcal{L}}]$ from (3.3), and applying the first vector theorem of Green

$$\begin{aligned}
&\int\limits_{\mathcal{V}} \vec{W}\cdot\left\{\vec{\nabla}\times\left[\underset{\sim}{a}\cdot(\vec{\nabla}\times\vec{u})\right]\right\}\,\mathrm{d}V = \\
&= \int\limits_{\mathcal{V}} (\vec{\nabla}\times\vec{W})\cdot\underset{\sim}{a}\cdot(\vec{\nabla}\times\vec{u})\,\mathrm{d}V - \int\limits_{\partial\mathcal{V}} \vec{n}\cdot\left\{\vec{W}\times\left[\underset{\sim}{a}\cdot(\vec{\nabla}\times\vec{u})\right]\right\}\,\mathrm{d}A
\end{aligned}\tag{3.26}$$

to the first integral from the left hand side of (3.24), the following is obtained:

$$\begin{aligned}
\int\limits_{\mathcal{V}} \vec{W}_i\cdot\vec{\mathcal{L}}\left[\tilde{\vec{u}}\right]\,\mathrm{d}V &= \int\limits_{\mathcal{V}} \vec{N}_i\cdot\left\{\vec{\nabla}\times\left[\underset{\sim}{a}\cdot(\vec{\nabla}\times\tilde{\vec{u}})\right]+\underset{\sim}{b}\cdot\tilde{\vec{u}}\right\}\,\mathrm{d}V = \\
&= \int\limits_{\mathcal{V}} (\vec{\nabla}\times\vec{N}_i)\cdot\underset{\sim}{a}\cdot(\vec{\nabla}\times\tilde{\vec{u}})\,\mathrm{d}V - \int\limits_{\partial\mathcal{V}} \vec{n}\cdot\left\{\vec{N}_i\times\left[\underset{\sim}{a}\cdot(\vec{\nabla}\times\tilde{\vec{u}})\right]\right\}\,\mathrm{d}A + \\
&\quad + \int\limits_{\mathcal{V}} \vec{N}_i\cdot\underset{\sim}{b}\cdot\tilde{\vec{u}}\,\mathrm{d}V.
\end{aligned}\tag{3.27}$$

Since the tangential component of $\vec{N}_i$ on the Dirichlet boundary $\mathcal{A}_D$ is zero the boundary integral of (3.27) can be written as

$$\begin{aligned}
&-\int\limits_{\partial\mathcal{V}} \vec{n}\cdot\left\{\vec{N}_i\times\left[\underset{\sim}{a}\cdot(\vec{\nabla}\times\tilde{\vec{u}})\right]\right\}\,\mathrm{d}A = -\int\limits_{\partial\mathcal{V}} \left(\vec{n}\times\vec{N}_i\right)\cdot\left[\underset{\sim}{a}\cdot(\vec{\nabla}\times\tilde{\vec{u}})\right]\,\mathrm{d}A = \\
&= -\int\limits_{\mathcal{A}_N} \left(\vec{n}\times\vec{N}_i\right)\cdot\left[\underset{\sim}{a}\cdot(\vec{\nabla}\times\tilde{\vec{u}})\right]\,\mathrm{d}A = \int\limits_{\mathcal{A}_N} \vec{N}_i\cdot\left\{\vec{n}\times\left[\underset{\sim}{a}\cdot(\vec{\nabla}\times\tilde{\vec{u}})\right]\right\}\,\mathrm{d}A.
\end{aligned}\tag{3.28}$$

Similarly to (3.18) for the scalar function u and its approximation $\tilde{u}$, the expression $\vec{n}\times\left[\underset{\sim}{a}\cdot(\vec{\nabla}\times\tilde{\vec{u}})\right]$ corresponds with the boundary condition $\vec{u}_n$ on $\mathcal{A}_N$ [35, 39, 40]

$$\vec{n}\times\left[\underset{\sim}{a}\cdot(\vec{\nabla}\times\tilde{\vec{u}})\right] \simeq \vec{u}_n = \vec{n}\times\left[\underset{\sim}{a}\cdot(\vec{\nabla}\times\vec{u})\right] \quad \text{on } \mathcal{A}_N. \tag{3.29}$$

Consequently for $[K]$ and $\{d\}$ it can be written

$$\begin{aligned}
K_{ij} &= \int\limits_{\mathcal{V}} (\vec{\nabla}\times\vec{N}_i)\cdot\underset{\sim}{a}\cdot(\vec{\nabla}\times\vec{N}_j)\,\mathrm{d}V + \int\limits_{\mathcal{V}} \vec{N}_i\cdot\underset{\sim}{b}\cdot\vec{N}_j\,\mathrm{d}V \\
d_i &= \int\limits_{\mathcal{V}} \vec{N}_i\cdot\left\{\vec{f}-\vec{\mathcal{L}}\left[\vec{v}\right]\right\}\,\mathrm{d}V - \int\limits_{\mathcal{A}_N} \vec{N}_i\cdot\vec{u}_n\,\mathrm{d}A, \quad i\in[1;n],\ j\in[1;n],
\end{aligned}\tag{3.30}$$

where $\vec{\mathcal{L}}$ is given by (3.3). For both, the scalar case (3.19) and the vector one (3.30), the matrix $[K]$ is symmetric.

The previous considerations are based on a three-dimensional domain. For the two-dimensional case similar formulas can be written. This will be explained by an example using Gauß's law:

$$\int\limits_{\mathcal{V}} \vec{\nabla} \cdot \vec{u} \, \mathrm{d}V = \int\limits_{\partial\mathcal{V}} \vec{n} \cdot \vec{u} \, \mathrm{d}A. \tag{3.31}$$

Let the three-dimensional domain $\mathcal{V}$ be a cylinder with an arbitrary basal plane $\mathcal{A}$ (with boundary $\partial\mathcal{A}$) and the height h.

The function $\vec{u}$ is only defined in the two-dimensional domain of the cylinder basal plane. Thus it has no normal component to the cylinder basal plane and does not depend on the height. Taking these considerations into account the left and the right hand side of (3.31) can be written as

$$\int\limits_{\mathcal{V}} \vec{\nabla} \cdot \vec{u} \, \mathrm{d}V = h \int\limits_{\mathcal{A}} \vec{\nabla} \cdot \vec{u} \, \mathrm{d}A$$

$$\int\limits_{\partial\mathcal{V}} \vec{n} \cdot \vec{u} \, \mathrm{d}A = \underbrace{\int\limits_{\mathcal{A}} \vec{n} \cdot \vec{u} \, \mathrm{d}A}_{=0} + \int\limits_{\mathcal{A}_{shell}} \vec{n} \cdot \vec{u} \, \mathrm{d}A + \underbrace{\int\limits_{\mathcal{A}} \vec{n} \cdot \vec{u} \, \mathrm{d}A}_{=0} = h \int\limits_{\partial\mathcal{A}} \vec{n} \cdot \vec{u} \, \mathrm{d}s,$$

which leads to Gauß's law for the two-dimensional case

$$\int\limits_{\mathcal{A}} \vec{\nabla} \cdot \vec{u} \, \mathrm{d}A = \int\limits_{\partial\mathcal{A}} \vec{n} \cdot \vec{u} \, \mathrm{d}s.$$

In a similar way the formulas for the three-dimensional case used in this work can be easily rewritten for two-dimensional regions. Thereby the three-dimensional domains $\mathcal{V}$ are replaced by two-dimensional ones $\mathcal{A}$. The boundaries $\partial\mathcal{V}$ of the three-dimensional regions are replaced by the boundaries $\partial\mathcal{A}$ of the corresponding two-dimensional ones. The integration variable must also be changed accordingly.

Die approbierte gedruckte Originalversion dieser Dissertation ist an der TU Wien Bibliothek verfügbar.
The approved original version of this doctoral thesis is available in print at TU Wien Bibliothek.

Die approbierte gedruckte Originalversion dieser Dissertation ist an der TU Wien Bibliothek verfügbar.
The approved original version of this doctoral thesis is available in print at TU Wien Bibliothek.

Chapter 4

The Scalar Finite Element Method

One typical application of the scalar finite element method is the numerical solution of a Poisson equation. Thus it is used for a detailed explanation of the basic concept of this method.

The Poisson equation is derived from the Maxwell equations [41, 42] for the static case — the field quantities do not vary with time. The differential form of the four Maxwell equations is usually given as

$$\vec{\nabla} \times \vec{E} = -\partial_t \vec{B} \qquad \text{(Faraday's law)} \tag{4.1}$$

$$\vec{\nabla} \cdot \vec{B} = 0 \qquad \text{(Gauß's law for magnetism)} \tag{4.2}$$

$$\vec{\nabla} \times \vec{H} = \vec{J} + \partial_t \vec{D} \qquad \text{(Maxwell–Ampère law)} \tag{4.3}$$

$$\vec{\nabla} \cdot \vec{D} = \rho \qquad \text{(Gauß's law)}, \tag{4.4}$$

where each variable has the following meaning and unit:

$\vec{E}$	electric field intensity	$\frac{\mathrm{V}}{\mathrm{m}}$
$\vec{H}$	magnetic field intensity	$\frac{\mathrm{A}}{\mathrm{m}}$
$\vec{D}$	electric flux density	$\frac{\mathrm{As}}{\mathrm{m}^2}$
$\vec{B}$	magnetic flux density	$\frac{\mathrm{Vs}}{\mathrm{m}^2}$
$\vec{J}$	electric current density	$\frac{\mathrm{A}}{\mathrm{m}^2}$
q	electric charge density	$\frac{\mathrm{As}}{\mathrm{m}^3}$.

In this work $\vec{E}$ and $\vec{H}$ will be also referred to as electric field and magnetic field, respectively. Applying the divergence operator to (4.3) and substitution by (4.4) give

$$\vec{\nabla} \cdot \vec{J} = -\partial_t \rho \qquad \text{(equation of continuity)}. \tag{4.5}$$

Die approbierte gedruckte Originalversion dieser Dissertation ist an der TU Wien Bibliothek verfügbar.
The approved original version of this doctoral thesis is available in print at TU Wien Bibliothek.

The macroscopic properties of the medium are described in terms of permittivity ϵ, permeability μ, and conductivity γ. These parameters are used for specifying the constitutive relations between the field quantities

$$\vec{D} = \epsilon \vec{E} \tag{4.6}$$

$$\vec{B} = \mu \vec{H} \tag{4.7}$$

$$\vec{J} = \gamma \vec{E}. \tag{4.8}$$

In general it is not necessary that the constitutive parameters ϵ, μ, and γ are simple constants. For example the relationship between $\vec{B}$ and $\vec{H}$ in (4.7) may by highly nonlinear for ferromagnetic materials. In this case μ depends on the field. For anisotropic media the directions of the flux densities differ from the directions of the corresponding field intensities and the constitutive parameters must be described by tensors. In inhomogeneous regions ϵ, μ, and γ are functions of position.

If the field values are invariant in time, the field is static. In this case the magnetic field and the electric field do not interact. For instance, the electrostatic case is given by (4.4) and

$$\vec{\nabla} \times \vec{E} = 0. \tag{4.9}$$

Equation (4.9) is satisfied by

$$\vec{E} = -\vec{\nabla} \varphi. \tag{4.10}$$

After substituting (4.10) in (4.6) and insertion in (4.4), the following second order partial differential equation for the electrostatic potential φ is obtained

$$\vec{\nabla} \cdot \left[\underset{\sim}{\epsilon}(\vec{r}) \cdot \vec{\nabla} \varphi(\vec{r}) \right] = f(\vec{r}), \text{ with } f(\vec{r}) = -\rho. \tag{4.11}$$

If assumed that $\underset{\sim}{\epsilon}(\vec{r})$ is a constant scalar, the expression (4.11) turns into the well known Poisson equation. If the charge density is zero allover the domain, (4.11) leads to

$$\vec{\nabla} \cdot \left[\underset{\sim}{\epsilon}(\vec{r}) \cdot \vec{\nabla} \varphi(\vec{r}) \right] = 0, \tag{4.12}$$

which corresponds for constant scalar permittivity ϵ to the Laplace equation. The most general presentation for the permittivity, which can be handled by the finite element method in the frequency domain is a position dependent tensor $\underset{\sim}{\epsilon}(\vec{r})$.

4.1 Two-Dimensional Scalar Finite Element Method

In this section the principle of the finite element method is demonstrated by solving the Poisson equation (4.11) in the two-dimensional domain $\mathcal{A}$. One part of the domain boundary $\partial\mathcal{A}$ represents the Dirichlet boundary $\mathcal{C}_D$ and the remaining part — the Neumann boundary $\mathcal{C}_N$, respectively ($\partial\mathcal{A} = \mathcal{C}_D + \mathcal{C}_N$).

Die approbierte gedruckte Originalversion dieser Dissertation ist an der TU Wien Bibliothek verfügbar.
The approved original version of this doctoral thesis is available in print at TU Wien Bibliothek.

As discussed in Chapter 3 the unknown function φ is approximated by $\tilde{\varphi}$ as in (3.5). The known basis functions will be notated with λ_j instead of N_j. The reason for this will became clear in the vector finite element chapter, where systems of partial differential equations appear, which require a combination of vector and scalar interpolation functions.

$$\varphi(\vec{r}) \simeq \tilde{\varphi}(\vec{r}) = \sum_{j=1}^{n} c_j \lambda_j(\vec{r}) + v(\vec{r}). \tag{4.13}$$

The function $v(\vec{r})$ complies with the Dirichlet boundary function on $\mathcal{C}_D$. The set of known functions λ_i, $i \in [1, n]$ builds a fundamental function system vanishing on the Dirichlet boundary $\mathcal{C}_D$. To find the numerically approximated solution of (4.11) for $\tilde{\varphi}$ it is necessary to determine the unknown multiplier coefficients c_i. This is performed by substituting φ in (4.11) by its approximation (4.13) and then weighting the resulting residual of (4.11) with the set of functions λ_i in the domain $\mathcal{A}$

$$\int\limits_{\mathcal{A}} [\vec{\nabla} \cdot (\underset{\sim}{\epsilon} \cdot \vec{\nabla}\tilde{\varphi})]\, \lambda_i \,\mathrm{d}A = \int\limits_{\mathcal{A}} f(\vec{r})\, \lambda_i \,\mathrm{d}A,\ \ i \in [1; n]. \tag{4.14}$$

Equation (4.14), using the first scalar theorem of Green (3.15) analogously to (3.16), leads to

$$\int\limits_{\partial\mathcal{A}} \lambda_i\ \vec{n} \cdot \underset{\sim}{\epsilon} \cdot \vec{\nabla}\tilde{\varphi} \,\mathrm{d}s - \int\limits_{\mathcal{A}} \vec{\nabla}\lambda_i \cdot \underset{\sim}{\epsilon} \cdot \vec{\nabla}\tilde{\varphi}(\vec{r}) \,\mathrm{d}A = \int\limits_{\mathcal{A}} f(\vec{r})\, \lambda_i \,\mathrm{d}A,\ \ i \in [1; n], \tag{4.15}$$

with the fact that all functions λ_i ($i \in [1; n]$) vanish on $\mathcal{C}_D$ to

$$\int\limits_{\mathcal{C}_N} \lambda_i\ \vec{n} \cdot \underset{\sim}{\epsilon} \cdot \vec{\nabla}\tilde{\varphi} \,\mathrm{d}s - \int\limits_{\mathcal{A}} \vec{\nabla}\lambda_i \cdot \underset{\sim}{\epsilon} \cdot \vec{\nabla}\tilde{\varphi}(\vec{r}) \,\mathrm{d}A = \int\limits_{\mathcal{A}} f(\vec{r})\, \lambda_i \,\mathrm{d}A,\ \ i \in [1; n]. \tag{4.16}$$

The Neumann boundary condition on $\mathcal{C}_N$ can be written analogously to (3.18) as

$$-D_n(\vec{r}) = -\vec{n} \cdot \vec{D}(\vec{r}) = \vec{n} \cdot \underset{\sim}{\epsilon} \cdot \vec{\nabla}\tilde{\varphi}(\vec{r}) \tag{4.17}$$

using $\vec{\nabla}\tilde{\varphi} = -\vec{E}$ and $\vec{D} = \underset{\sim}{\epsilon} \cdot \vec{E}$. After substitution of $\tilde{\varphi}$ in (4.16) by the approximation (4.13) and using the Neumann boundary condition (4.17) the following linear equation system for the unknown coefficients c_i ($i \in [1; n]$) is obtained

$$\int\limits_{\mathcal{A}} \vec{\nabla}\lambda_i \cdot \underset{\sim}{\epsilon} \cdot \vec{\nabla} \left[\sum_{j=1}^{n} c_j \lambda_j(\vec{r}) + v(\vec{r}) \right] \,\mathrm{d}A = -\int\limits_{\mathcal{A}} f(\vec{r})\, \lambda_i \,\mathrm{d}A - \int\limits_{\mathcal{C}_N} \lambda_i D_n \,\mathrm{d}s,\ \ i \in [1; n]. \tag{4.18}$$

Die approbierte gedruckte Originalversion dieser Dissertation ist an der TU Wien Bibliothek verfügbar.
The approved original version of this doctoral thesis is available in print at TU Wien Bibliothek.

The above equation can be converted to

$$\begin{aligned}\sum_{j=1}^{n} c_j \int\limits_{\mathcal{A}} \vec{\nabla}\lambda_i \cdot \underset{\sim}{\epsilon} \cdot \vec{\nabla}\lambda_j \,\mathrm{d}A = &-\int\limits_{\mathcal{A}} \vec{\nabla}\lambda_i \cdot \underset{\sim}{\epsilon} \cdot \vec{\nabla} v(\vec{r})\,\mathrm{d}A - \\ &-\int\limits_{\mathcal{A}} f(\vec{r})\,\lambda_i\,\mathrm{d}A - \int\limits_{\mathcal{C}_N} \lambda_i D_n \,\mathrm{d}s,\ \ i \in [1;n],\end{aligned} \tag{4.19}$$

which complies with the following linear equation system

$$[K]\{c\} = \{d\}. \tag{4.20}$$

The matrix $[K]$ and the right hand side vector $\{d\}$ are given by the expressions

$$\begin{aligned} K_{ij} &= \int\limits_{\mathcal{A}} \vec{\nabla}\lambda_i \cdot \underset{\sim}{\epsilon} \cdot \vec{\nabla}\lambda_j \,\mathrm{d}A \\ d_i &= -\int\limits_{\mathcal{A}} \vec{\nabla}\lambda_i \cdot \underset{\sim}{\epsilon} \cdot \vec{\nabla} v(\vec{r})\,\mathrm{d}A - \int\limits_{\mathcal{A}} f(\vec{r})\,\lambda_i\,\mathrm{d}A - \int\limits_{\mathcal{C}_N} \lambda_i D_n\,\mathrm{d}s, \\ &\quad i \in [1;n],\ \ j \in [1;n]. \end{aligned} \tag{4.21}$$

Let assume that $\mathcal{C}_N$ is a part of the outer boundary of the two-dimensional domain $\mathcal{A}$. Furthermore $\mathcal{A}$ is assumed sufficiently large to allow that D_n can be neglected on $\mathcal{C}_N$. Since the corresponding simulations are performed in finite domains, this assumption will lead to systematic error which became smaller with increasing domain size. This issue will be discussed in Subsection 4.1.5. It is also assumed that there is no electric charge density distribution ρ in the domain of interest. Thus the Neumann boundary term and the source term in (4.21) are set to zero. Otherwise, if $\vec{D}$ is perpendicular to $\vec{n}$ on $\mathcal{C}_N$, the boundary condition on $\mathcal{C}_N$ will be zero independently from the domain size.

The function $v(\vec{r})$, which satisfies the Dirichlet boundary $\mathcal{C}_D$ can be analogously to the solution approximation (4.13) written as a sum of known functions multiplied with coefficients

$$v(\vec{r}) = \sum_{j=n+1}^{m} c_j \lambda_j. \tag{4.22}$$

Now the coefficients c_j in (4.22) where $j \in [n{+}1;m]$ are known values. They are obtained easily from $v(\vec{r})$ for $m{-}n$ points on the Dirichlet boundary $\mathcal{C}_D$ by the following linear equation system

$$v(\vec{r}_i) = \sum_{j=n+1}^{m} c_j \lambda_j(\vec{r}_i), \quad i \in [1;m{-}n],\ \vec{r}_i \in \mathcal{C}_D. \tag{4.23}$$

Die approbierte gedruckte Originalversion dieser Dissertation ist an der TU Wien Bibliothek verfügbar.
The approved original version of this doctoral thesis is available in print at TU Wien Bibliothek.
TU WIEN Bibliothek Your knowledge hub

With (4.22) the right hand side vector $\{d\}$ from (4.21) can be rewritten as

$$
\begin{aligned}
d_i &= -\int\limits_{\mathcal{A}} \vec{\nabla}\lambda_i \cdot \underset{\sim}{\epsilon} \cdot \vec{\nabla} v(\vec{r})\, \mathrm{d}A = -\int\limits_{\mathcal{A}} \vec{\nabla}\lambda_i \cdot \underset{\sim}{\epsilon} \cdot \vec{\nabla} \left(\sum_{j=n+1}^{m} c_j \lambda_j \right) \mathrm{d}A = \\
&= -\sum_{j=n+1}^{m} c_j \int\limits_{\mathcal{A}} \vec{\nabla}\lambda_i \cdot \underset{\sim}{\epsilon} \cdot \vec{\nabla}\lambda_j \, \mathrm{d}A = -\sum_{j=n+1}^{m} K_{ij} c_j, \quad i \in [1; n].
\end{aligned}
\tag{4.24}
$$

In general the form functions λ_i can be defined in the entire simulation domain. For example, this is the case by the weighted residual method. In the case of the finite element method the domain $\mathcal{A}$ is divided into smaller sub-domains $\mathcal{A}_e$. This process is known as domain discretization and the resulting sub-domains $\mathcal{A}_e$ are called elements. The index ^{e} or $_e$ will be used in this work generally for quantities, which comply with an element. It can be considered as a numbering index. The shape functions λ_i are non-zero only in a few neighboring elements and vanish in the remaining simulation area. λ_i is a global shape function. Its local representation in each element, in which it is non-zero is termed as element shape function λ_i^e. Now ^{e} is written as a superscript index, because there is already another numbering index available — the subscript index $_i$. In each element usually many element shape functions are defined, which are part of different global shape functions. As it will be shown later for this purpose low order polynomials are used. It is very important to notice the difference in the indexing (index i) between the global and the element basis functions. In the global basis function λ_i i complies with the number of global functions in the whole region and with the number of unknown coefficients c_i, respectively. By the element basis function λ_i^e the index i corresponds to the number of the element basis functions in the element. In practice at first the element form functions are defined for each element in the domain and then the global ones are constructed by them.

In this work the area of interest is discretized on triangular elements. On these elements linear triangular element functions are employed.

4.1.1 Domain Discretization

As already mentioned the finite element method requires a discretized domain. By the discretization the two-dimensional domain $\mathcal{A}$ is divided into elements. Often the subdivision is treated as a preprocessing task to the finite element technique provided automatically for different and arbitrary shaped simulation regions [43, 44] from specific software. In this work the elements are triangles. The elements must not overlap and there must not be any gaps between them. A proper discretization avoids elements, which have a small inner angle (narrow elements). Such elements usually cause a larger simulation error. It can be shown that the relative deviation of the simulation result from the exact solution is inversely proportional to the sine of the smallest angle in the triangular element [45]. Thus, the best case will be, if all generated triangles were equilateral. Another important property of the discretization is the element size. Generally, smaller elements lead to higher precision of the numerical results. Otherwise, generation of smaller elements means generation of more elements, which gives more unknowns

Die approbierte gedruckte Originalversion dieser Dissertation ist an der TU Wien Bibliothek verfügbar.
The approved original version of this doctoral thesis is available in print at TU Wien Bibliothek.
TU WIEN Bibliothek Your knowledge hub

and a larger linear equation system, respectively. Thus longer simulation times and a higher memory demand must be taken into account. A good approach is to use smaller elements in the regions where it is expected that the field quantities will vary intensely. In the remaining regions, in which little variations are assumed, larger elements can be used. Such a method optimizes the number of elements and unknowns, respectively, for a desired solution accuracy. A number of algorithms and efficient techniques are developed to automate the mesh generation. Finite element mesh adaptation processes and mesh improvement techniques using posteriori error estimator guarantee the quality of the resulting mesh [46, 47].

4.1.2 Linear Shape Functions on Triangular Elements

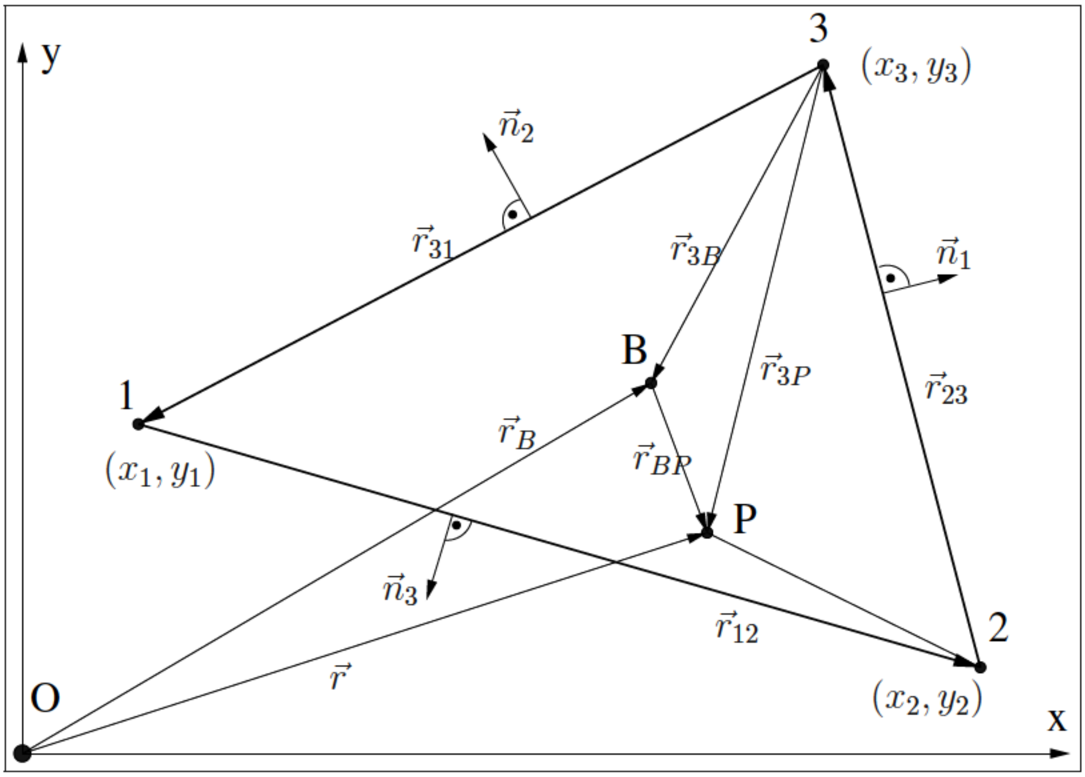

Figure 4.1: Triangular element.

The triangular element and the corresponding notations used in this work are shown in Fig. <4.1>. The well known linear approximation of an unknown function ϕ within a triangle is given by

$$\phi(x, y) = a + bx + cy. \tag{4.25}$$

The linear element form functions will be obtained from this approximation. Assume the values of ϕ on the nodes of the triangle are known. The nodes are numbered by 1, 2 and 3 as in Fig. <4.1>, and the corresponding field values are ϕ_1, ϕ_2 and ϕ_3. The coefficients

a, b and c are determined by the system

$$\begin{aligned}\phi_1 &= a + bx_1 + cy_1\\ \phi_2 &= a + bx_2 + cy_2\\ \phi_3 &= a + bx_3 + cy_3,\end{aligned} \tag{4.26}$$

where x_i and y_i are the coordinates of the i-th node in the element. Solving (4.26) for a, b, and c leads to

$$\begin{aligned}
a &= \frac{1}{J}\begin{vmatrix}\phi_1 & x_1 & y_1\\ \phi_2 & x_2 & y_2\\ \phi_3 & x_3 & y_3\end{vmatrix} = \frac{(x_2y_3 - x_3y_2)\phi_1 + (x_3y_1 - x_1y_3)\phi_2 + (x_1y_2 - x_2y_1)\phi_3}{J}\\
b &= \frac{1}{J}\begin{vmatrix}1 & \phi_1 & y_1\\ 1 & \phi_2 & y_2\\ 1 & \phi_3 & y_3\end{vmatrix} = \frac{(y_2 - y_3)\phi_1 + (y_3 - y_1)\phi_2 + (y_1 - y_2)\phi_3}{J}\\
c &= \frac{1}{J}\begin{vmatrix}1 & x_1 & \phi_1\\ 1 & x_2 & \phi_2\\ 1 & x_3 & \phi_3\end{vmatrix} = \frac{(x_3 - x_2)\phi_1 + (x_1 - x_3)\phi_2 + (x_2 - x_1)\phi_3}{J}.
\end{aligned} \tag{4.27}$$

J is the so called Jacobi determinant

$$J = \begin{vmatrix}1 & x_1 & y_1\\ 1 & x_2 & y_2\\ 1 & x_3 & y_3\end{vmatrix} = (\vec{r}_{12} \times \vec{r}_{23}) \cdot \vec{e}_z = (\vec{r}_{23} \times \vec{r}_{31}) \cdot \vec{e}_z = (\vec{r}_{31} \times \vec{r}_{12}) \cdot \vec{e}_z = 2F_e, \tag{4.28}$$

where F_e is the area of the triangular element and $\vec{r}_{ij} = \vec{r}_j - \vec{r}_i$ with $\vec{r}_i = x_i\vec{e}_x + y_i\vec{e}_y$. With back substituting of a, b, and c from (4.27) into (4.25) ϕ is written in the form

$$\begin{aligned}
\phi(x, y) = {} & \frac{x_2y_3 - x_3y_2 + (y_2 - y_3)x + (x_3 - x_2)y}{J}\,\phi_1 +\\
& + \frac{x_3y_1 - x_1y_3 + (y_3 - y_1)x + (x_1 - x_3)y}{J}\,\phi_2 +\\
& + \frac{x_1y_2 - x_2y_1 + (y_1 - y_2)x + (x_2 - x_1)y}{J}\,\phi_3 = \sum_{i=1}^{3} \lambda_i^e(x, y)\,\phi_i,
\end{aligned} \tag{4.29}$$

which gives the element shape functions λ_i^e.

4.1.3 Introduction of Triangle Barycentric Coordinates

For the following explanation of edge elements exclusively barycentric coordinates will be used, because they offer advantages in understanding the following calculations. A point

Die approbierte gedruckte Originalversion dieser Dissertation ist an der TU Wien Bibliothek verfügbar.
The approved original version of this doctoral thesis is available in print at TU Wien Bibliothek.

Die approbierte gedruckte Originalversion dieser Dissertation ist an der TU Wien Bibliothek verfügbar.
The approved original version of this doctoral thesis is available in print at TU Wien Bibliothek.

TU Bibliothek WIEN Your knowledge hub

P inside the triangle 123 (Fig. <4.1>) divides this triangle into three sub triangles, namely $P12$, $P23$, and $P31$, with the corresponding areas of these sub triangles F_3, F_1 and F_2. The barycentric coordinate λ_i^e is the ratio of the area F_i of the sub-face opposite to the i-th node to the whole area F. Thus the barycentric coordinates are given by the following definitions (see Fig. <4.1>)

$$\begin{aligned}\lambda_1^e(\vec{r}) = \frac{F_1}{F_e} &= \frac{(\vec{r}_{23} \times \vec{r}_{3P}) \cdot \vec{e}_z}{J} = \frac{(\vec{r}_{23} \times (\vec{r}_{3B} + \vec{r}_{BP})) \cdot \vec{e}_z}{J} = \\ &= \frac{(\vec{r}_{23} \times \vec{r}_{3B}) \cdot \vec{e}_z}{J} + \frac{(\vec{r}_{23} \times \vec{r}_{BP}) \cdot \vec{e}_z}{J} = \\ &= \frac{1}{3} - (\vec{r} - \vec{r}_B) \cdot \frac{\vec{r}_{23} \times \vec{e}_z}{J} = \frac{1}{3} - (\vec{r} - \vec{r}_B) \cdot \frac{l_{23} \cdot \vec{n}_1}{J}\end{aligned} \tag{4.30}$$

$$\lambda_2^e(\vec{r}) = \frac{F_2}{F_e} = \frac{1}{3} - (\vec{r} - \vec{r}_B) \cdot \frac{\vec{r}_{31} \times \vec{e}_z}{J} = \frac{1}{3} - (\vec{r} - \vec{r}_B) \cdot \frac{l_{31} \cdot \vec{n}_2}{J} \tag{4.31}$$

$$\lambda_3^e(\vec{r}) = \frac{F_3}{F_e} = \frac{1}{3} - (\vec{r} - \vec{r}_B) \cdot \frac{\vec{r}_{12} \times \vec{e}_z}{J} = \frac{1}{3} - (\vec{r} - \vec{r}_B) \cdot \frac{l_{12} \cdot \vec{n}_3}{J}, \tag{4.32}$$

where the following expressions have been used

$$\vec{r}_B = \frac{1}{3}(\vec{r}_1 + \vec{r}_2 + \vec{r}_3) \tag{4.33}$$

$$|\vec{r}_{12}| = l_{12}, \ |\vec{r}_{23}| = l_{23}, \ |\vec{r}_{31}| = l_{31} \tag{4.34}$$

$$\vec{r} = \vec{r}(x, y) = x\,\vec{e}_x + y\,\vec{e}_y. \tag{4.35}$$

F_1, F_2 and F_3 are the areas of the triangles $P23$, $P31$ and $P12$, respectively

$$F_1 = F_{P23}, \ F_2 = F_{P31}, \ F_3 = F_{P12}. \tag{4.36}$$

This definition is very helpful for understanding of some of the following properties of the barycentric coordinates or linear element form functions, respectively.

The reason for the introduction of the barycentric coordinates at this place is, that they are identical to the linear triangular element shape functions. For instance, the expression for the barycentric coordinate λ_1^e is given by

$$\begin{aligned}\lambda_1^e(\vec{r}) = \frac{F_1}{F} &= \frac{(\vec{r}_{23} \times \vec{r}_{3P}) \cdot \vec{e}_z}{J} = \\ &= \frac{\{[(x_3 - x_2)\vec{e}_x + (y_3 - y_2)\vec{e}_y] \times [(x - x_3)\vec{e}_x + (y - y_3)\vec{e}_y]\} \cdot \vec{e}_z}{J} = \\ &= \frac{[(x_3 - x_2)(y - y_3) - (y_3 - y_2)(x - x_3)]\,\vec{e}z \cdot \vec{e}_z}{J} = \\ &= \frac{x_2 y_3 - x_3 y_2 + (y_2 - y_3)x + (x_3 - x_2)y}{J},\end{aligned} \tag{4.37}$$

Die approbierte gedruckte Originalversion dieser Dissertation ist an der TU Wien Bibliothek verfügbar.
The approved original version of this doctoral thesis is available in print at TU Wien Bibliothek.

which complies with the first linear triangular element form function in (4.29). Thus the linear triangular barycentric coordinates and element shape functions use the same notation λ_i^e.

The barycentric coordinate λ_i^e is constant along a line parallel to the element edge opposite to the i-th node and is zero on the opposite edge. Two barycentric coordinates are sufficient to determine the position of the point P inside the triangle (see Fig. <4.1>). However, a third barycentric coordinate is introduced such that

$$\sum_{i=1}^{3} \lambda_i^e = 1. \tag{4.38}$$

Only two of the three linear element form functions are independent.

For the points inside the element and on the element edges it holds

$$0 \leq \lambda_1^e \leq 1,\ 0 \leq \lambda_2^e \leq 1,\ 0 \leq \lambda_3^e \leq 1. \tag{4.39}$$

For points outside the element the barycentric coordinates can take arbitrary values. Of coarse (4.38) must be fulfilled. At least one and at most two barycentric coordinates must have negative values. This is illustrated in the example (Fig. <4.2>), where λ_1^e and λ_2^e are negative and λ_3^e is greater than one. For instance, this relation can be used to determine, if a point lies inside or outside a given element. If there is at least one negative barycentric coordinate, the point lies outside. If one or two barycentric coordinates are zero, the point lies on the corresponding one or two edges of the element. Otherwise, if all are positive the point is inside.

Points located at a vertex of the element satisfy

$$\lambda_i^e(x_j, y_j) = \delta_{ij} = \begin{cases} 1 & i = j \\ 0 & i \neq j \end{cases} . \tag{4.40}$$

In the calculation of the finite elements also the gradients are needed. In barycentric coordinates the gradients are constant and expressed as

$$\begin{aligned}
\vec{\nabla}\lambda_1^e(\vec{r}) &= -\frac{\vec{r}_{23} \times \vec{e}_z}{J} = -\frac{l_{23} \cdot \vec{n}_1}{J} = const \\
\vec{\nabla}\lambda_2^e(\vec{r}) &= -\frac{\vec{r}_{31} \times \vec{e}_z}{J} = -\frac{l_{31} \cdot \vec{n}_2}{J} = const \\
\vec{\nabla}\lambda_3^e(\vec{r}) &= -\frac{\vec{r}_{12} \times \vec{e}_z}{J} = -\frac{l_{12} \cdot \vec{n}_3}{J} = const.
\end{aligned} \tag{4.41}$$

$$\sum_{i=1}^{3} \vec{\nabla}\lambda_i^e(\vec{r}) = \vec{0}. \tag{4.42}$$

Die approbierte gedruckte Originalversion dieser Dissertation ist an der TU Wien Bibliothek verfügbar.
The approved original version of this doctoral thesis is available in print at TU Wien Bibliothek.
TU WIEN Bibliothek Your knowledge hub

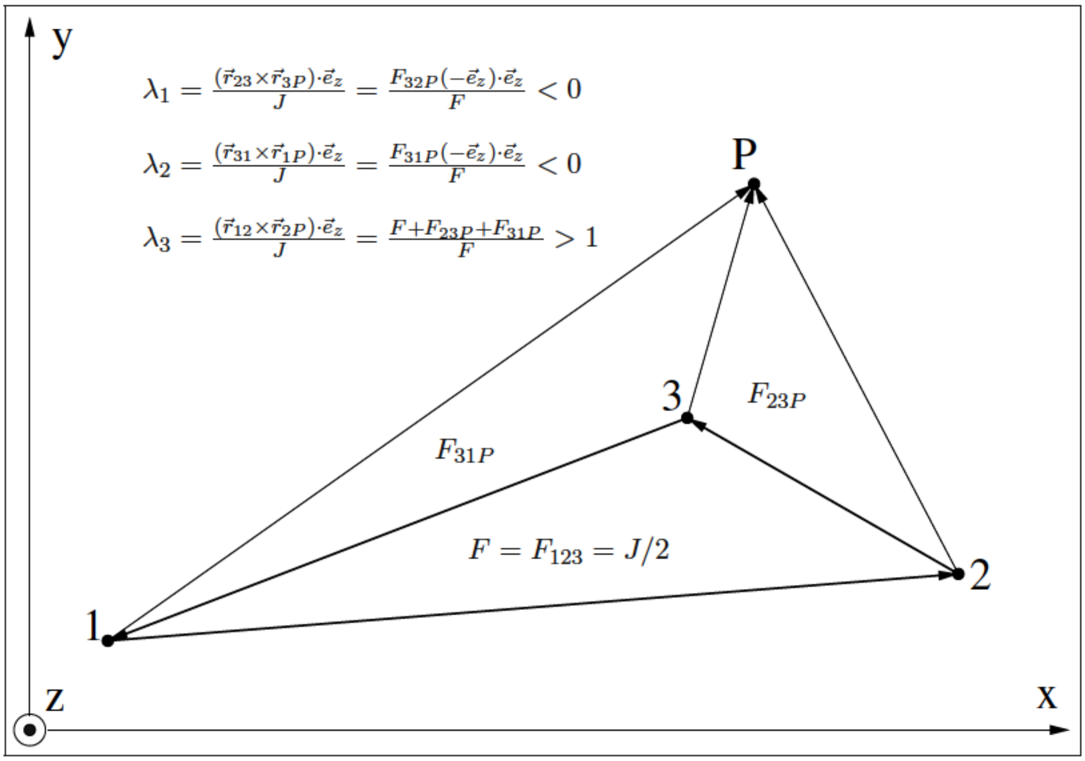
y
$\lambda_1 = \frac{(\vec{r}_{23}\times\vec{r}_{3P})\cdot\vec{e}_z}{J} = \frac{F_{32P}(-\vec{e}_z)\cdot\vec{e}_z}{F} < 0$
$\lambda_2 = \frac{(\vec{r}_{31}\times\vec{r}_{1P})\cdot\vec{e}_z}{J} = \frac{F_{31P}(-\vec{e}_z)\cdot\vec{e}_z}{F} < 0$
$\lambda_3 = \frac{(\vec{r}_{12}\times\vec{r}_{2P})\cdot\vec{e}_z}{J} = \frac{F+F_{23P}+F_{31P}}{F} > 1$
P
3
F_{23P}
F_{31P}
$F = F_{123} = J/2$
1
2
z
x

Figure 4.2: Barycentric coordinates outside a triangular element.

The coordinates of each point in the element are determined by

$$\vec{r} = \sum_{i=1}^{3} \lambda_i^e \vec{r}_i, \tag{4.43}$$

where λ_1^e, λ_2^e and λ_3^e are the barycentric coordinates of the point inside the triangle element and $\vec{r}_1$, $\vec{r}_2$ and $\vec{r}_3$ are the coordinates of the element vertices. Using (4.38) the expression (4.43) can be written as

$$\begin{aligned} x &= (x_1 - x_3)\lambda_1^e + (x_2 - x_3)\lambda_2^e + x_3 \\ y &= (y_1 - y_3)\lambda_1^e + (y_2 - y_3)\lambda_2^e + y_3. \end{aligned} \tag{4.44}$$

Equations (4.44) transform the local coordinates λ_1^e and λ_2^e to the global xy coordinate system. Reversely each global element is mapped to the unit triangle in the $\lambda_1^e \lambda_1^e$ plane (Fig. <4.3>).

With the properties mentioned above the barycentric coordinates guarantee the continuity of the element interpolation function (4.29) across the element sides. For instance, on the Side 23 the barycentric coordinates are restricted by

$$\lambda_1^e = 0 \text{ and } \lambda_3^e = 1 - \lambda_2^e \text{ (see Fig. <4.3>).}$$

TU Bibliothek Your knowledge hub WIEN
Die approbierte gedruckte Originalversion dieser Dissertation ist an der TU Wien Bibliothek verfügbar.
The approved original version of this doctoral thesis is available in print at TU Wien Bibliothek.

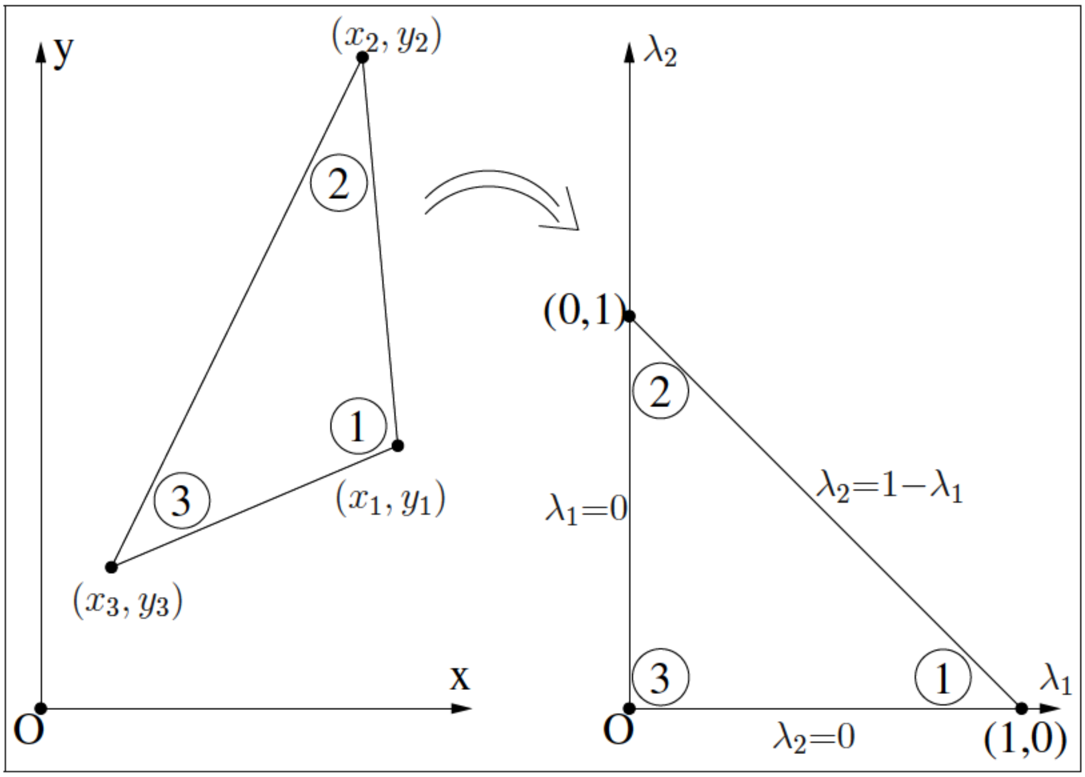

Figure 4.3: Two-dimensional domain transformation.

Thus the element interpolation function (4.29) on the Side 23 is given by

$$\phi^e = \lambda_2^e \, \phi_2 + (1 - \lambda_2^e) \, \phi_3. \tag{4.45}$$

$\lambda_2^e(\vec{r})$ depends only on the position of $\vec{r}$ on the Edge 23. Thus for the two neighbor elements, which share the Edge 23, the corresponding element interpolation functions will be equal for the same position on Edge 23.

4.1.4 Assembling

The assembling of the matrix $[K]$ and the right hand side vector $\{d\}$ from (4.20) is demonstrated in the discretized domain $\mathcal{A}$ from Fig. <4.4>. The entire domain is discretized and consists of the triangular elements $\mathcal{A}_1$ to $\mathcal{A}_{10}$. The Dirichlet boundary $\mathcal{C}_D$ is given by the curve elements $\mathcal{C}_1$, $\mathcal{C}_3$, $\mathcal{C}_6$, $\mathcal{C}_7$ and $\mathcal{C}_8$. The Neumann boundary $\mathcal{C}_N$ contains the curve elements $\mathcal{C}_2$, $\mathcal{C}_4$ and $\mathcal{C}_5$. In the entire domain $\mathcal{A}$ the nodes are numbered globally. In Fig. <4.4> the global node numbers are enclosed in circles. Since each element has three nodes, a local (element) number can be assigned to a node additionally to the global number. To map the local node number to the global one the so called connectivity array is used:

element	Node 1	Node 2	Node 3
1	2	10	1
2	2	3	10
3	3	4	9
4	4	5	9
5	9	5	6
6	9	6	7
7	10	7	8
8	8	1	10
9	3	9	10
10	10	9	7

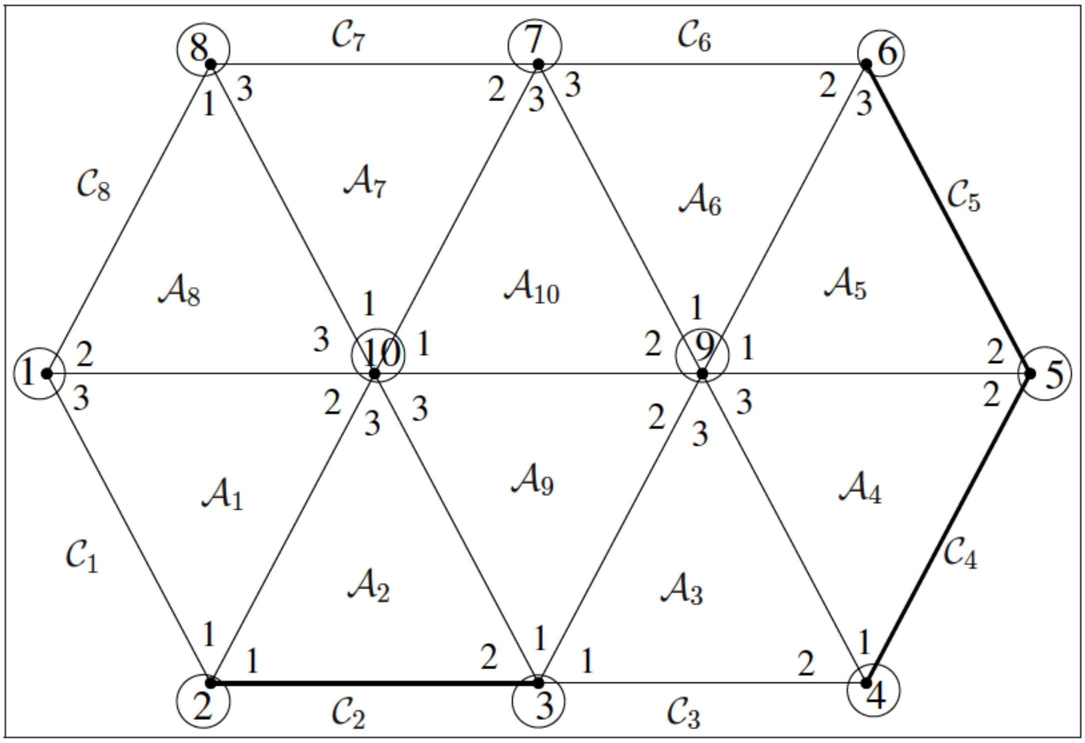

Figure 4.4: Node and element numbering in a discretized domain $\mathcal{A}$.

Considering (4.40) the global shape function λ_i is given by the union of all element (or local) shape functions, which are 1 for the global node i. From the local property (4.40) the global criterion follows

$$\lambda_i(\vec{r}_j) = \delta_{ij} = \begin{cases} 1 & i = j \\ 0 & i \neq j \end{cases} , \tag{4.46}$$

where $\vec{r}_j$ is the position vector of the node j. For example, the global trial function λ_1

Die approbierte gedruckte Originalversion dieser Dissertation ist an der TU Wien Bibliothek verfügbar.
The approved original version of this doctoral thesis is available in print at TU Wien Bibliothek.
TU WIEN Bibliothek Your knowledge hub

and λ_{10} (Fig. <4.4>) are given by

$$\begin{aligned}\lambda_1 &= \lambda_3^{e=\mathcal{A}_1} + \lambda_2^{e=\mathcal{A}_8}\\ \lambda_{10} &= \lambda_2^{e=\mathcal{A}_1} + \lambda_3^{e=\mathcal{A}_2} + \lambda_3^{e=\mathcal{A}_9} + \lambda_1^{e=\mathcal{A}_{10}} + \lambda_1^{e=\mathcal{A}_7} + \lambda_3^{e=\mathcal{A}_8}.\end{aligned}$$

The plus operators must be treated as union operators, because the element form functions must not overlap. Taking into account the continuity of the solution across the element edges, it can be seen, that the coefficients $c_j,\ j \in [1;n]$ comply with the values of the field approximation $\tilde{\varphi}(\vec{r}_j)$ (in the global node j). The notation $\lambda_j^{e=\mathcal{A}_i}$ means the j-th local (element) function λ_j in the i-th triangular element $\mathcal{A}_i$. The subscript index of the element form function (superscript expression $e = \mathcal{A}_i$) complies with the local node number in the i-th element. The corresponding global node number is taken from the connectivity array and is equal to the global trial function number. The global trial function λ_i is non-zero only in the elements which are attached to the node with global number i. As a consequence λ_i is non-zero in a very narrow area. With these considerations the matrix entry K_{ij} can be build piece wise in the elements sharing the global i-th and j-th nodes from the corresponding element form functions. For example the matrix element $K_{1,10}$ is given by

$$K_{1,10} = \int\limits_{\mathcal{A}} \vec{\nabla}\lambda_1 \cdot \underset{\sim}{\epsilon} \cdot \vec{\nabla}\lambda_{10}\,\mathrm{d}A = \int\limits_{\mathcal{A}_1^e} \vec{\nabla}\lambda_3^e \cdot \underset{\sim}{\epsilon} \cdot \vec{\nabla}\lambda_2^e\,\mathrm{d}A + \int\limits_{\mathcal{A}_8^e} \vec{\nabla}\lambda_2^e \cdot \underset{\sim}{\epsilon} \cdot \vec{\nabla}\lambda_3^e\,\mathrm{d}A. \qquad (4.47)$$

Analogously the remaining matrix entries are built. Most of the matrix entries correspond to global nodes, which do not belong to common elements and are zero for this reason. For instance, $K_{10,5}$ is such an entry. Thus $[K]$ is a sparse matrix.

Assembling $[K]$ like in (4.47) needs information of the neighbor nodes and the corresponding common elements. This information is contained in the connectivity array, unfortunately it cannot be obtained directly. Thus the assembling is performed in a different, reverse way. If the assembling of $[K]$ is performed as in (4.47), it can be seen that all possible variations of the element form functions

$$K_{ij}^e = \int\limits_{\mathcal{A}^e} \vec{\nabla}\lambda_i^e \cdot \underset{\sim}{\epsilon} \cdot \vec{\nabla}\lambda_j^e\,\mathrm{d}A, \quad i \in [1;3], j \in [1;3] \qquad (4.48)$$

in all elements can be found as a summand in an expression for a matrix entry K_{ij}. The assembling proceeds element by element. For each element all possible variations (4.48) are calculated and added to the corresponding global matrix entry K_{ij}. Instead of $e{=}\mathcal{A}_i$ now the superscript index e is used, since by the element wise assembling the current element number is known implicitly. Thus the superscript index e refers to the current element and notes that the indexes i and j are element (local) indexes. Otherwise, if no superscript index e is written, i and j are global indexes. The local indexes are transformed to the corresponding global ones by the connectivity array. The global matrix $[K]$ is built from the element matrices $[K]^e$ on a very efficient way. Thus the finite element formulation for a given problem is mostly solved by giving the general expressions for the entries of the element matrices [48, 49].

Die approbierte gedruckte Originalversion dieser Dissertation ist an der TU Wien Bibliothek verfügbar.
The approved original version of this doctoral thesis is available in print at TU Wien Bibliothek.

Die approbierte gedruckte Originalversion dieser Dissertation ist an der TU Wien Bibliothek verfügbar.
The approved original version of this doctoral thesis is available in print at TU Wien Bibliothek.

Let the permittivity $\underset{\sim}{\epsilon}$ be scalar ($\underset{\sim}{\epsilon} \rightarrow \epsilon$) and element wise constant for the further calculations. Thus using (4.41), the element matrix for the current problem is given by

$$
\begin{aligned}
K_{11}^e &= \int\limits_{\mathcal{A}_e} \epsilon \, \vec{\nabla}\lambda_1^e \cdot \vec{\nabla}\lambda_1^e \, \mathrm{d}A = \epsilon \, \vec{\nabla}\lambda_1^e \cdot \vec{\nabla}\lambda_1^e \int\limits_{\mathcal{A}_e} \mathrm{d}A = \epsilon \, \frac{\vec{r}_{23} \times \vec{e}_z}{2F_e} \cdot \frac{\vec{r}_{23} \times \vec{e}_z}{2F_e} \, F_e = \\
&= \frac{\epsilon}{4F_e} \left(\vec{r}_{23} \times \vec{e}_z\right) \cdot \left(\vec{r}_{23} \times \vec{e}_z\right) = \frac{\epsilon}{4F_e} \, \vec{r}_{23} \cdot \vec{r}_{23} \\
K_{12}^e = K_{21}^e &= \int\limits_{\mathcal{A}_e} \epsilon \, \vec{\nabla}\lambda_1^e \cdot \vec{\nabla}\lambda_2^e \, \mathrm{d}A = \frac{\epsilon}{4F_e} \, \vec{r}_{23} \cdot \vec{r}_{31} \\
K_{13}^e = K_{31}^e &= \int\limits_{\mathcal{A}_e} \epsilon \, \vec{\nabla}\lambda_1^e \cdot \vec{\nabla}\lambda_3^e \, \mathrm{d}A = \frac{\epsilon}{4F_e} \, \vec{r}_{23} \cdot \vec{r}_{12} \\
K_{22}^e &= \int\limits_{\mathcal{A}_e} \epsilon \, \vec{\nabla}\lambda_2^e \cdot \vec{\nabla}\lambda_2^e \, \mathrm{d}A = \frac{\epsilon}{4F_e} \, \vec{r}_{31} \cdot \vec{r}_{31} \\
K_{23}^e = K_{32}^e &= \int\limits_{\mathcal{A}_e} \epsilon \, \vec{\nabla}\lambda_2^e \cdot \vec{\nabla}\lambda_3^e \, \mathrm{d}A = \frac{\epsilon}{4F_e} \, \vec{r}_{31} \cdot \vec{r}_{12} \\
K_{33}^e &= \int\limits_{\mathcal{A}_e} \epsilon \, \vec{\nabla}\lambda_3^e \cdot \vec{\nabla}\lambda_3^e \, \mathrm{d}A = \frac{\epsilon}{4F_e} \, \vec{r}_{12} \cdot \vec{r}_{12}.
\end{aligned}
\tag{4.49}
$$

The Dirichlet boundary is considered by the coefficients c_j for $j \in [n{+}1; m]$, which are easily obtained from (4.23) taking (4.46) into account

$$c_j = v(\vec{r}_j).$$

The contributions of the Dirichlet boundary to the right hand side vector $\{d\}$ are assembled mutually with the global matrix $[K]$ using (4.24). The region $\mathcal{A}$ is proceeded element by element. For each element the element matrix (4.49) is calculated, the local indexes i and j of the element matrix entry K_{ij}^e are converted to the corresponding global indexes i and j of the global matrix entry K_{ij} by the connectivity array. The superscript e provides the distinction between i and j used as local or global nodes. By the global index j it is recognized, if K_{ij}^e is added to K_{ij} as a contribution to the matrix on the left side or if K_{ij}^e is multiplied by the known Dirichlet coefficient c_j and added to d_i, to the right hand side vector.

4.1.5 Neumann Boundary Condition

For the previous examination the Neumann boundary condition (4.17) on $\mathcal{C}_N$ is assumed to be zero (homogeneous Neumann boundary condition). This subsection discusses which consequences are drawn from this assumption. Furthermore, it presents specific models which require inhomogeneous (or non-zero) Neumann boundary conditions to be assigned to define the field quantities or even to preserve the physical consistence.

Die approbierte gedruckte Originalversion dieser Dissertation ist an der TU Wien Bibliothek verfügbar.
The approved original version of this doctoral thesis is available in print at TU Wien Bibliothek.
TU Bibliothek WIEN Your knowledge hub

For the electrostatic case using (4.5), (4.8), and (4.10) it is written

$$\vec{\nabla} \cdot \left(\underset{\sim}{\gamma} \cdot \vec{\nabla}\varphi \right) = 0. \tag{4.50}$$

Considering (3.18) the Neumann boundary condition is given by the conormal derivative of the electrostatic potential φ or by the normal component of the current density, respectively

$$J_n = \vec{n} \cdot \vec{J} = -\vec{n} \cdot \left(\underset{\sim}{\gamma} \cdot \vec{\nabla}\varphi \right) \text{ on } \mathcal{C}_N. \tag{4.51}$$

Thus, for a boundary value problems like (4.50) the normal current density or the corresponding total current forced in the simulation domain can be given by applying inhomogeneous Neumann boundary condition on $\mathcal{C}_N$ [50]. The same holds true for thermic problems. External sources impressing a normal heat flux density on an outer boundary part represent inhomogeneous Neumann boundary conditions [10].

However, the Neumann boundary condition cannot be arbitrarily chosen. For example, in the electrostatic case given by (4.11), Gauß's law (4.4) requires that the total electric flow through the boundaries must be equal to the electric charge inside the domain. For the two-dimensional case this is given the expression

$$\int\limits_{\mathcal{A}} \vec{\nabla} \cdot \vec{D} \, \mathrm{d}A = \int\limits_{\partial\mathcal{A}} \vec{n} \cdot \vec{D} \, \mathrm{d}s = -\int\limits_{\partial\mathcal{A}} \vec{n} \cdot \left(\underset{\sim}{\epsilon} \cdot \vec{\nabla}\varphi \right) \mathrm{d}s = \int\limits_{\mathcal{A}} \rho \, \mathrm{d}A. \tag{4.52}$$

According to (3.18) the Neumann boundary condition of (4.11) is (4.52). In this case, if the surface electric charge in the entire domain $\mathcal{A}$ does not vanish, physically it doesn't make sense to apply homogeneous Neumann boundary conditions allover the entire boundary $\partial\mathcal{A}$.

In this work for the approximation of the inhomogeneous Neumann boundary condition an extension of the sum (4.13) with (4.22) from Section 4.1 is used

$$\tilde{\varphi}(\vec{r}) = \sum_{j=m+1}^{l} c_j \lambda_j. \tag{4.53}$$

The coefficients are indexed in the following way: The entire discretized domain contains m nodes. The unknown coefficients numbered from 1 to n correspond to the nodes which do not lie on the Dirichlet boundary (the non-Dirichlet nodes). The known coefficients numbered from n+1 to m $(n < m)$ correspond to the nodes on the Dirichlet boundary (the Dirichlet nodes). The coefficients c_j from (4.53) $(m < l)$ must be obtained from the Neumann boundary condition (4.17) on the Neumann boundary $\mathcal{C}_N$. Thus, if $\vec{E}$ on the Neumann boundary is given

$$\vec{E} = -\vec{\nabla}\tilde{\varphi} = -\sum_{j=m+1}^{l} c_j \vec{\nabla}\lambda_j \quad \text{on} \quad \mathcal{C}_N. \tag{4.54}$$

Die approbierte gedruckte Originalversion dieser Dissertation ist an der TU Wien Bibliothek verfügbar.
The approved original version of this doctoral thesis is available in print at TU Wien Bibliothek.
TU WIEN Bibliothek Your knowledge hub

In an element (Fig. <4.1>), from which one or more edges are part of the Neumann boundary $\mathcal{C}_N$ $\vec{E}$ is given by

$$\begin{aligned}\vec{E}^e = -\vec{\nabla}\varphi^e = -\sum_{j=1}^{3} c_j \vec{\nabla}\lambda_j^e = c_1^e \frac{\vec{r}_{23}\times\vec{e}_z}{2F^e} + c_2^e \frac{\vec{r}_{31}\times\vec{e}_z}{2F^e} + c_3^e \frac{\vec{r}_{12}\times\vec{e}_z}{2F^e} = \\ = \frac{1}{2F^e}\left(c_1^e\, l_{23}\, \vec{n}_1 + c_2^e\, l_{31}\, \vec{n}_2 + c_3^e\, l_{12}\, \vec{n}_3\right).\end{aligned} \tag{4.55}$$

To express a given $\vec{E}$ on $\mathcal{C}_N$ some of the coefficients c_1^e, c_2^e and c_3^e can be set to zero. Let the Edge 23 in the element from Fig. <4.1> be part of the Neumann boundary. If $\vec{E}$ is normal to the Edge 23, then c_2^e and c_3^e can be set to zero. Otherwise c_1^e can be set to zero and c_2^e and c_3^e are calculated from $\vec{E}$ on $\mathcal{C}_N$.

Now the Neumann boundary integral from (4.21) is given by

$$\int\limits_{\mathcal{C}_N} \lambda_i D_n \,\mathrm{d}s = \sum_{j=m+1}^{l} c_j \int\limits_{\mathcal{C}_N} \lambda_i \left(\vec{n}\cdot \underset{\sim}{\epsilon} \cdot \vec{\nabla}\lambda_j\right) \mathrm{d}s = \sum_{j=m+1}^{l} c_j M_{ij},\ \ i \in [1; n]. \tag{4.56}$$

The corresponding element matrix $[M]^e$ for ϵ assumed as a constant scalar in each element, is given in the appendix in Subsection B.2.1, which also refers to the magnetic scalar potential and instead of ϵ and φ the tokens μ and ψ are used.

The acceptance of homogeneous Neumann boundary conditions is only an approximation, which is not generally valid. This will be demonstrated by an example. Let us consider the field generated by two electrodes with different electrostatic potential applied. Let there be no other potential or charge density distributions close to these electrodes to disturb this field. On the first electrode 0V and on the second one 1V is impressed as shown in Fig. <4.5>, which is given by Dirichlet boundary conditions for the boundaries $\mathcal{C}_{D1}$ and $\mathcal{C}_{D2}$ between the simulation domain $\mathcal{A}$ and the electrodes. The Laplace equation (4.12) for the electric potential is solved in $\mathcal{A}$. As usual, homogeneous Neumann boundary conditions are set to the outer boundary $\mathcal{C}_N$. This will not influence the result, if the Neumann boundary is infinitely far away from the electrodes and the corresponding Neumann boundary conditions can be neglected. In practice it is simulated with finite lengths which normally results in simulation error. To demonstrate this behavior the same electrode configuration is analyzed in a domain nine times larger than the domain in Fig. <4.5>. Then the domain is cut off to the same region size as in Fig. <4.5>. The corresponding electrostatic potential distribution is shown by equipotential lines in Fig. <4.6>. This is compared to the field in Fig. <4.5>. In contrast to Fig. <4.5> the field on Fig. <4.6> corresponds to the expected one for the given configuration. The homogeneous Neumann boundaries have distorted the simulation result in the small area on Fig. <4.5>. Of coarse this is a systematic error, it gets smaller with growing simulation domains. For simulation of open regions the finite element method can be combined with the boundary element method [51, 52, 53]. This can also be performed with the so called edge elements [54] introduced in Chapter 5.

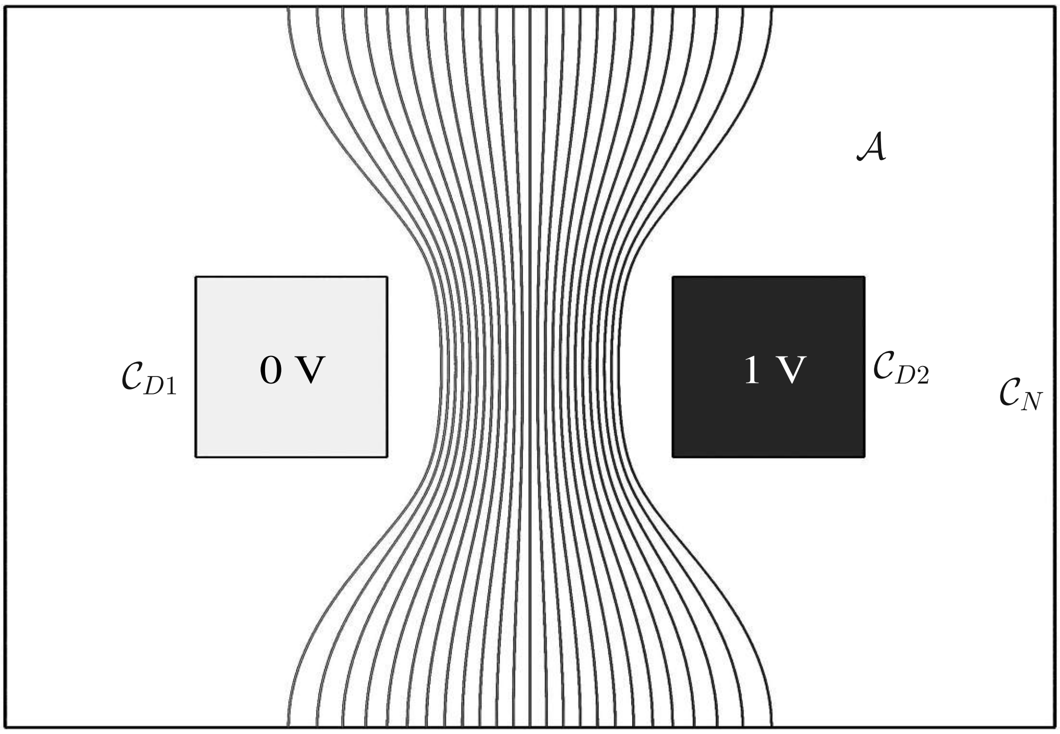

Figure 4.5: Homogeneous Neumann boundary conditions on the outer boundary $\mathcal{C}_N$.

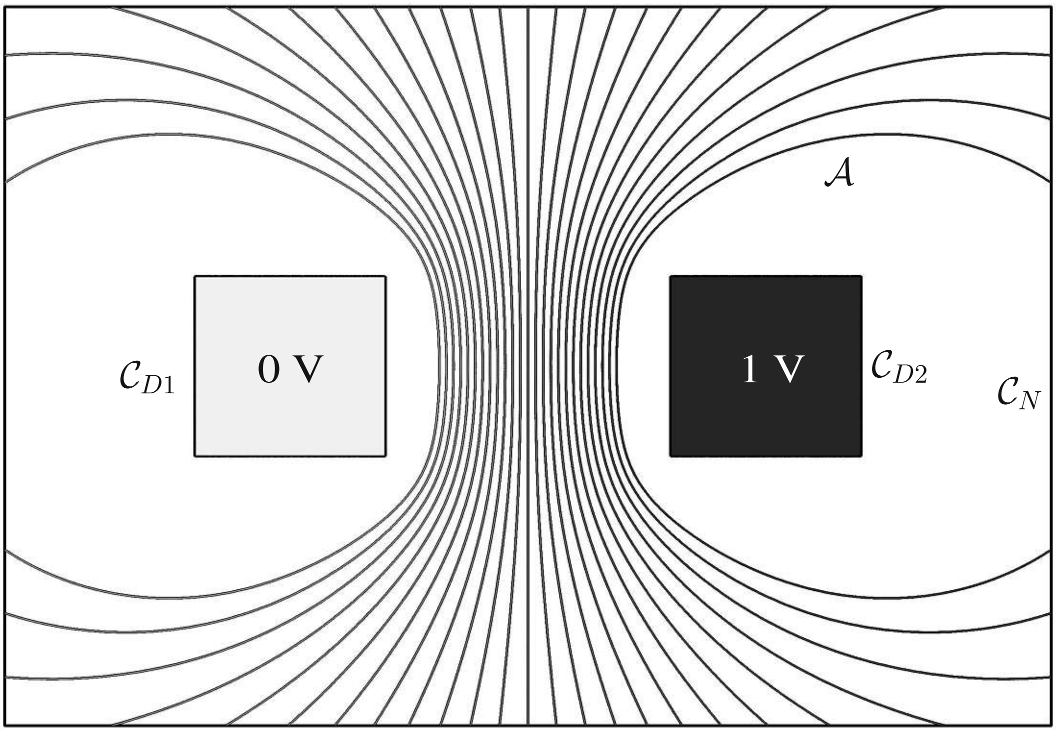

Figure 4.6: The outer region is cut off at $\mathcal{C}_N$.

Die approbierte gedruckte Originalversion dieser Dissertation ist an der TU Wien Bibliothek verfügbar.
The approved original version of this doctoral thesis is available in print at TU Wien Bibliothek.

Die approbierte gedruckte Originalversion dieser Dissertation ist an der TU Wien Bibliothek verfügbar.
The approved original version of this doctoral thesis is available in print at TU Wien Bibliothek.

4.2 Three-Dimensional Scalar Finite Element Method

Equation (4.11) is used again. The three-dimensional finite element method is very similar to the two-dimensional formulation. Now the analysis is performed in the three-dimensional domain $\mathcal{V}$ with its boundary $\partial\mathcal{V}$. It leads again to the linear equation system (4.20). The solution is approximated by (4.13). The global matrix $[K]$ and the right hand side vector $\{d\}$ are given analogously to (4.21) by

$$\begin{aligned} K_{ij} &= \int\limits_{\mathcal{V}} \vec{\nabla}\lambda_i \cdot \underset{\sim}{\epsilon} \cdot \vec{\nabla}\lambda_j \,\mathrm{d}V \\ d_i &= -\int\limits_{\mathcal{V}} \vec{\nabla}\lambda_i \cdot \underset{\sim}{\epsilon} \cdot \vec{\nabla}v(\vec{r}) \,\mathrm{d}V - \int\limits_{\mathcal{V}} f(\vec{r})\,\lambda_i \,\mathrm{d}V - \int\limits_{\mathcal{A}_N} \lambda_i D_n \,\mathrm{d}A, \\ & \quad i \in [1;n],\;\; j \in [1;n]. \end{aligned} \tag{4.57}$$

The expression (4.22) for $v(\vec{r})$ is governed by the Dirichlet boundary condition and D_n as in (4.17) complies with the Neumann boundary condition on $\mathcal{A}_N$. The global functions λ_i are constructed similarly as in the two-dimensional case from local ones λ^e defined only in a few neighbor elements.

As usual, the finite element procedure starts with the domain discretization. The three-dimensional volume $\mathcal{V}$ is broken into small tetrahedral elements $\mathcal{V}^e$. As a consequence the boundary $\partial\mathcal{V}$ is subdivided into triangular elements. This kind of elements are very well suited for discretizing of arbitrarily or irregularly shaped regions.

4.2.1 Linear Shape Functions on Tetrahedral Elements

The unknown field in the tetrahedral element (Fig. <4.7>) is approximated by the linear function

$$\phi(x, y, z) = a + bx + cy + dz. \tag{4.58}$$

Analogously to the two-dimensional case the four coefficients a, b, c and d are obtained assuming that the field values ϕ_1, ϕ_2, ϕ_3 and ϕ_4 on the four vertexes of the tetrahedron are known.

$$\begin{aligned} \phi_1 &= a + bx_1 + cy_1 + dz_1 \\ \phi_2 &= a + bx_2 + cy_2 + dz_2 \\ \phi_3 &= a + bx_3 + cy_3 + dz_3 \\ \phi_4 &= a + bx_4 + cy_4 + dz_4. \end{aligned} \tag{4.59}$$

Die approbierte gedruckte Originalversion dieser Dissertation ist an der TU Wien Bibliothek verfügbar.
The approved original version of this doctoral thesis is available in print at TU Wien Bibliothek.

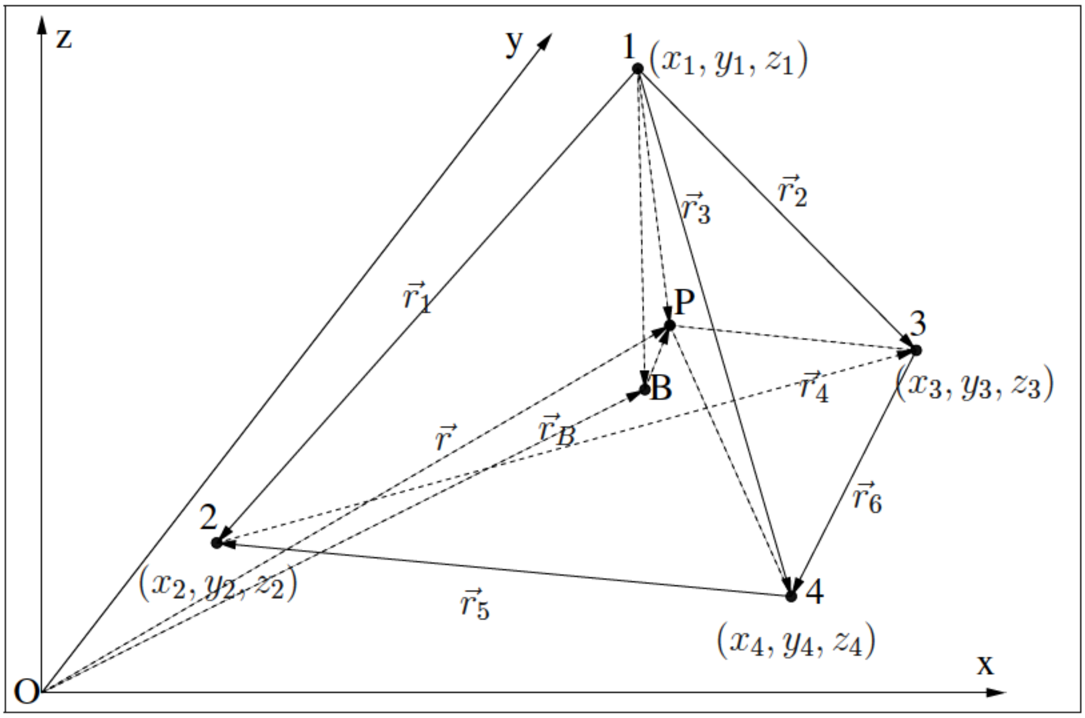

Figure 4.7: Tetrahedral element.

The coordinates x_i, y_i and z_i correspond to the vertex i. From (4.59) the coefficients a, b, c and d become

$$\begin{aligned} a = \frac{1}{J}\begin{vmatrix} \phi_1 & x_1 & y_1 & z_1 \\ \phi_2 & x_2 & y_2 & z_2 \\ \phi_3 & x_3 & y_3 & z_3 \\ \phi_4 & x_4 & y_4 & z_4 \end{vmatrix} &= \frac{1}{J}\begin{vmatrix} x_2 & y_2 & z_2 \\ x_3 & y_3 & z_3 \\ x_4 & y_4 & z_4 \end{vmatrix}\phi_1 - \frac{1}{J}\begin{vmatrix} x_1 & y_1 & z_1 \\ x_3 & y_3 & z_3 \\ x_4 & y_4 & z_4 \end{vmatrix}\phi_2 + \\ &\quad + \frac{1}{J}\begin{vmatrix} x_1 & y_1 & z_1 \\ x_2 & y_2 & z_2 \\ x_4 & y_4 & z_4 \end{vmatrix}\phi_3 - \frac{1}{J}\begin{vmatrix} x_1 & y_1 & z_1 \\ x_2 & y_2 & z_2 \\ x_3 & y_3 & z_3 \end{vmatrix}\phi_4 = \\ &= a_1\phi_1 + a_2\phi_2 + a_3\phi_3 + a_4\phi_4 \end{aligned} \tag{4.60}$$

$$\begin{aligned} b = \frac{1}{J}\begin{vmatrix} 1 & \phi_1 & y_1 & z_1 \\ 1 & \phi_2 & y_2 & z_2 \\ 1 & \phi_3 & y_3 & z_3 \\ 1 & \phi_4 & y_4 & z_4 \end{vmatrix} &= -\frac{1}{J}\begin{vmatrix} 1 & y_2 & z_2 \\ 1 & y_3 & z_3 \\ 1 & y_4 & z_4 \end{vmatrix}\phi_1 + \frac{1}{J}\begin{vmatrix} 1 & y_1 & z_1 \\ 1 & y_3 & z_3 \\ 1 & y_4 & z_4 \end{vmatrix}\phi_2 - \\ &\quad - \frac{1}{J}\begin{vmatrix} 1 & y_1 & z_1 \\ 1 & y_2 & z_2 \\ 1 & y_4 & z_4 \end{vmatrix}\phi_3 + \frac{1}{J}\begin{vmatrix} 1 & y_1 & z_1 \\ 1 & y_2 & z_2 \\ 1 & y_3 & z_3 \end{vmatrix}\phi_4 = \\ &= b_1\phi_1 + b_2\phi_2 + b_3\phi_3 + b_4\phi_4 \end{aligned} \tag{4.61}$$

$$
\begin{aligned}
c = \frac{1}{J}\begin{vmatrix} 1 & x_1 & \phi_1 & z_1 \\ 1 & x_2 & \phi_2 & z_2 \\ 1 & x_3 & \phi_3 & z_3 \\ 1 & x_4 & \phi_4 & z_4 \end{vmatrix} &= \frac{1}{J}\begin{vmatrix} 1 & x_2 & z_2 \\ 1 & x_3 & z_3 \\ 1 & x_4 & z_4 \end{vmatrix}\phi_1 - \frac{1}{J}\begin{vmatrix} 1 & x_1 & z_1 \\ 1 & x_3 & z_3 \\ 1 & x_4 & z_4 \end{vmatrix}\phi_2 + \\
&+ \frac{1}{J}\begin{vmatrix} 1 & x_1 & z_1 \\ 1 & x_2 & z_2 \\ 1 & x_4 & z_4 \end{vmatrix}\phi_3 - \frac{1}{J}\begin{vmatrix} 1 & x_1 & z_1 \\ 1 & x_2 & z_2 \\ 1 & x_3 & z_3 \end{vmatrix}\phi_4 = \\
&= c_1\phi_1 + c_2\phi_2 + c_3\phi_3 + c_4\phi_4
\end{aligned}
\tag{4.62}
$$

$$
\begin{aligned}
d = \frac{1}{J}\begin{vmatrix} 1 & x_1 & y_1 & \phi_1 \\ 1 & x_2 & y_2 & \phi_2 \\ 1 & x_3 & y_3 & \phi_3 \\ 1 & x_4 & y_4 & \phi_4 \end{vmatrix} &= -\frac{1}{J}\begin{vmatrix} 1 & x_2 & y_2 \\ 1 & x_3 & y_3 \\ 1 & x_4 & y_4 \end{vmatrix}\phi_1 + \frac{1}{J}\begin{vmatrix} 1 & x_1 & y_1 \\ 1 & x_3 & y_3 \\ 1 & x_4 & y_4 \end{vmatrix}\phi_2 - \\
&- \frac{1}{J}\begin{vmatrix} 1 & x_1 & y_1 \\ 1 & x_2 & y_2 \\ 1 & x_4 & y_4 \end{vmatrix}\phi_3 + \frac{1}{J}\begin{vmatrix} 1 & x_1 & y_1 \\ 1 & x_2 & y_2 \\ 1 & x_3 & y_3 \end{vmatrix}\phi_4 = \\
&= d_1\phi_1 + d_2\phi_2 + d_3\phi_3 + d_4\phi_4.
\end{aligned}
\tag{4.63}
$$

The Jacoby determinant for the three-dimensional case is given by

$$
J = \begin{vmatrix} 1 & x_1 & y_1 & z_1 \\ 1 & x_2 & y_2 & z_2 \\ 1 & x_3 & y_3 & z_3 \\ 1 & x_4 & y_4 & z_4 \end{vmatrix} = (\vec{r}_1 \times \vec{r}_2) \cdot \vec{r}_3 = 6V_e, \tag{4.64}
$$

where V_e is the volume of the tetrahedron. Equations (4.60) to (4.63) define the auxiliary coefficients a_i, b_i, c_i and d_i ($i \in [1;4]$), which are used to write (4.58) as

$$
\begin{aligned}
\phi(x,y,z) &= (a_1 + b_1x + c_1y + d_1z)\phi_1 + (a_2 + b_2x + c_2y + d_2z)\phi_2 + \\
&+ (a_3 + b_3x + c_3y + d_3z)\phi_3 + (a_4 + b_4x + c_4y + d_4z)\phi_4 = \sum_{i=1}^{4} \lambda_i^e\,\phi_i
\end{aligned}
\tag{4.65}
$$

to introduce the element shape functions λ_i^e.

4.2.2 Tetrahedron Barycentric Coordinates

Let P be a point inside the tetrahedral element as shown in Fig. <4.7>. It divides the tetrahedron in four sub-tetrahedrons

$$
V_1 = V_{P234},\ V_2 = V_{P134},\ V_3 = V_{P124},\ V_4 = V_{P123}.
$$

Die approbierte gedruckte Originalversion dieser Dissertation ist an der TU Wien Bibliothek verfügbar.
The approved original version of this doctoral thesis is available in print at TU Wien Bibliothek.
TU Bibliothek Your knowledge hub WIEN

Die approbierte gedruckte Originalversion dieser Dissertation ist an der TU Wien Bibliothek verfügbar.
The approved original version of this doctoral thesis is available in print at TU Wien Bibliothek.

The barycentric coordinates of the point P are given by

$$\lambda_1^e(\vec{r}) = \frac{V_1}{V_e} = \frac{1}{4} + (\vec{r} - \vec{r}_B) \cdot \frac{(\vec{r}_4 \times \vec{r}_5)}{J} = \frac{1}{4} - (\vec{r} - \vec{r}_B) \cdot \frac{F_1 \, \vec{n}_1}{3V_e} \tag{4.66}$$

$$\begin{aligned} \lambda_2^e(\vec{r}) = \frac{V_2}{V_e} &= \frac{\vec{r}_{1P} \cdot (\vec{r}_2 \times \vec{r}_3)}{J} = \frac{(\vec{r}_{1B} + \vec{r}_{BP}) \cdot (\vec{r}_2 \times \vec{r}_3)}{J} = \\ &= \frac{\vec{r}_{1B} \cdot (\vec{r}_2 \times \vec{r}_3)}{J} + \frac{\vec{r}_{BP} \cdot (\vec{r}_2 \times \vec{r}_3)}{J} = \\ &= \frac{1}{4} + (\vec{r} - \vec{r}_B) \cdot \frac{(\vec{r}_2 \times \vec{r}_3)}{J} = \frac{1}{4} - (\vec{r} - \vec{r}_B) \cdot \frac{F_2 \, \vec{n}_2}{3V_e} \end{aligned} \tag{4.67}$$

$$\lambda_3^e(\vec{r}) = \frac{V_3}{V_e} = \frac{1}{4} + (\vec{r} - \vec{r}_B) \cdot \frac{(\vec{r}_3 \times \vec{r}_1)}{J} = \frac{1}{4} - (\vec{r} - \vec{r}_B) \cdot \frac{F_3 \, \vec{n}_3}{3V_e} \tag{4.68}$$

$$\lambda_4^e(\vec{r}) = \frac{V_4}{V_e} = \frac{1}{4} + (\vec{r} - \vec{r}_B) \cdot \frac{(\vec{r}_1 \times \vec{r}_2)}{J} = \frac{1}{4} - (\vec{r} - \vec{r}_B) \cdot \frac{F_4 \, \vec{n}_4}{3V_e}, \tag{4.69}$$

where F_i ($i \in [1;4]$) is the area of the triangular face of the tetrahedron opposite to the vertex i

$$F_1 = F_{234}, \; F_2 = F_{134}, \; F_3 = F_{124}, \; F_4 = F_{123}.$$

The vector $\vec{n}_i$ ($i \in [1;4]$) is normal to its according face, has the length 1 and points outwards. The position vector is written as

$$\vec{r} = \vec{r}(x, y, z) = x \, \vec{e}_x + y \, \vec{e}_y + z \, \vec{e}_z \tag{4.70}$$

and $\vec{r}_i$ is the position of the vertex i.

Analogously to the two-dimensional case it can be shown that the barycentric coordinates are equal to the linear element shape functions in (4.65). Thus the same notation λ_i^e is used.

The gradient of the barycentric coordinates is a constant vector

$$\vec{\nabla} \lambda_1^e(\vec{r}) = \frac{(\vec{r}_4 \times \vec{r}_5)}{J} = -\frac{F_1 \, \vec{n}_1}{3V_e} \tag{4.71}$$

$$\vec{\nabla} \lambda_2^e(\vec{r}) = \frac{(\vec{r}_2 \times \vec{r}_3)}{J} = -\frac{F_2 \, \vec{n}_2}{3V_e} \tag{4.72}$$

$$\vec{\nabla} \lambda_3^e(\vec{r}) = \frac{(\vec{r}_3 \times \vec{r}_1)}{J} = -\frac{F_3 \, \vec{n}_3}{3V_e} \tag{4.73}$$

$$\vec{\nabla} \lambda_4^e(\vec{r}) = \frac{(\vec{r}_1 \times \vec{r}_2)}{J} = -\frac{F_4 \, \vec{n}_4}{3V_e}. \tag{4.74}$$

Die approbierte gedruckte Originalversion dieser Dissertation ist an der TU Wien Bibliothek verfügbar.
The approved original version of this doctoral thesis is available in print at TU Wien Bibliothek.
TU WIEN Bibliothek Your knowledge hub

Analogously to the two-dimensional case it is valid

$$\lambda_i^e(x_j, y_j, z_j) = \delta_{ij} = \begin{cases} 1 & i = j \\ 0 & i \neq j \end{cases} . \tag{4.75}$$

The barycentric coordinate λ_i^e is constant on a plane parallel to the element facet opposite to the i-th node and it is zero on this opposite facet, which ensures the inter-element continuity of the element interpolation function (4.58).

Only three of the four linear element form functions are independent

$$\sum_{i=1}^{4} \lambda_i^e = 1. \tag{4.76}$$

For points inside the element and on the element facets

$$0 \leq \lambda_1^e \leq 1,\ 0 \leq \lambda_2^e \leq 1,\ 0 \leq \lambda_3^e \leq 1,\ 0 \leq \lambda_4^e \leq 1 \tag{4.77}$$

is satisfied. Similar to the two-dimensional case some of the barycentric coordinates of a point outside the element can be negative or greater than 1.

Otherwise, the barycentric coordinates can be used to represent the coordinates of each point inside the tetrahedral element

$$\vec{r} = \sum_{i=1}^{4} \lambda_i^e \vec{r}_i. \tag{4.78}$$

Using (4.76), equation (4.78) leads to

$$\begin{aligned} x &= (x_1 - x_4)\lambda_1^e + (x_2 - x_4)\lambda_2^e + (x_3 - x_4)\lambda_3^e + x_4 \\ y &= (y_1 - y_4)\lambda_1^e + (y_2 - y_4)\lambda_2^e + (y_3 - y_4)\lambda_3^e + y_4 \\ z &= (z_1 - z_4)\lambda_1^e + (z_2 - z_4)\lambda_2^e + (z_3 - z_4)\lambda_3^e + z_4, \end{aligned} \tag{4.79}$$

which gives the coordinate transformation as shown in Fig. <4.8>.

4.2.3 Assembling

The assembling of the global matrix $[K]$ and the right hand side vector $\{d\}$ is done similarly to the two-dimensional method. The entire region is processed element wise. In each tetrahedron the element matrix $[K]^e$ is calculated. The local matrix entries K_{ij}^e are added to the global entries K_{ij} or are multiplied by the known coefficient c_j (obtained from the Dirichlet boundary condition) and added to the right hand side vector element d_i depending on the global index j, by which it is distinguished between Dirichlet or unknown node coefficients. The superscript ^{e} indicates that the indexes ij are local element indexes, which are converted to global ij indexes (without superscript ^{e}) by the

Die approbierte gedruckte Originalversion dieser Dissertation ist an der TU Wien Bibliothek verfügbar.
The approved original version of this doctoral thesis is available in print at TU Wien Bibliothek.
TU WIEN Bibliothek Your knowledge hub

connectivity array. In the three-dimensional case the connectivity array has four row entries for the four element nodes.

For the assembling of the element matrix it is assumed that the permittivity $\underset{\sim}{\epsilon}$ is a scalar and element wise constant. This assumption is not an essential restriction. It allows ϵ to change from one element to the next. Thus inhomogeneous materials (with respect to ϵ) can be easily simulated. The regions, in which ϵ changes substantially, must be discretized in appropriately small elements. Using the expressions for the gradient of the barycentric coordinates (4.71) to (4.74) the element matrix for the Laplace term is given by

$$\begin{aligned}
K^e_{11} &= \int\limits_{\mathcal{V}_e} \vec{\nabla}\lambda^e_1 \cdot \underset{\sim}{\epsilon} \cdot \vec{\nabla}\lambda^e_1 \,\mathrm{d}V = \epsilon\, \vec{\nabla}\lambda^e_1 \cdot \vec{\nabla}\lambda^e_1 \int\limits_{\mathcal{V}_e} \mathrm{d}V = \epsilon V_e\, \vec{\nabla}\lambda^e_1 \cdot \vec{\nabla}\lambda^e_1 = \\
&= \epsilon V_e \frac{\vec{r}_4 \times \vec{r}_5}{6V_e} \cdot \frac{\vec{r}_4 \times \vec{r}_5}{6V_e} = \frac{\epsilon}{36V_e}[(\vec{r}_4 \cdot \vec{r}_4)(\vec{r}_5 \cdot \vec{r}_5) - (\vec{r}_4 \cdot \vec{r}_5)(\vec{r}_4 \cdot \vec{r}_5)] && (4.80)\\
K^e_{12} = K^e_{21} &= \frac{\epsilon}{36V_e}[(\vec{r}_2 \cdot \vec{r}_6)(\vec{r}_4 \cdot \vec{r}_6) - (\vec{r}_2 \cdot \vec{r}_4)(\vec{r}_6 \cdot \vec{r}_6)] && (4.81)\\
K^e_{13} = K^e_{31} &= \frac{\epsilon}{36V_e}[(\vec{r}_3 \cdot \vec{r}_4)(\vec{r}_5 \cdot \vec{r}_5) - (\vec{r}_3 \cdot \vec{r}_5)(\vec{r}_4 \cdot \vec{r}_5)] && (4.82)\\
K^e_{14} = K^e_{41} &= \frac{\epsilon}{36V_e}[(\vec{r}_1 \cdot \vec{r}_6)(\vec{r}_4 \cdot \vec{r}_4) - (\vec{r}_1 \cdot \vec{r}_4)(\vec{r}_4 \cdot \vec{r}_6)] && (4.83)\\
K^e_{22} &= \frac{\epsilon}{36V_e}[(\vec{r}_2 \cdot \vec{r}_2)(\vec{r}_3 \cdot \vec{r}_3) - (\vec{r}_2 \cdot \vec{r}_3)(\vec{r}_2 \cdot \vec{r}_3)] && (4.84)\\
K^e_{23} = K^e_{32} &= \frac{\epsilon}{36V_e}[(\vec{r}_1 \cdot \vec{r}_6)(\vec{r}_3 \cdot \vec{r}_3) - (\vec{r}_1 \cdot \vec{r}_3)(\vec{r}_3 \cdot \vec{r}_6)] && (4.85)\\
K^e_{24} = K^e_{42} &= \frac{\epsilon}{36V_e}[(\vec{r}_1 \cdot \vec{r}_3)(\vec{r}_4 \cdot \vec{r}_6) - (\vec{r}_1 \cdot \vec{r}_6)(\vec{r}_3 \cdot \vec{r}_4)] && (4.86)\\
K^e_{33} &= \frac{\epsilon}{36V_e}[(\vec{r}_1 \cdot \vec{r}_1)(\vec{r}_3 \cdot \vec{r}_3) - (\vec{r}_1 \cdot \vec{r}_3)(\vec{r}_1 \cdot \vec{r}_3)] && (4.87)\\
K^e_{34} = K^e_{43} &= \frac{\epsilon}{36V_e}[(\vec{r}_1 \cdot \vec{r}_3)(\vec{r}_1 \cdot \vec{r}_4) - (\vec{r}_1 \cdot \vec{r}_1)(\vec{r}_3 \cdot \vec{r}_4)] && (4.88)\\
K^e_{44} &= \frac{\epsilon}{36V_e}[(\vec{r}_1 \cdot \vec{r}_1)(\vec{r}_4 \cdot \vec{r}_4) - (\vec{r}_1 \cdot \vec{r}_4)(\vec{r}_1 \cdot \vec{r}_4)]. && (4.89)
\end{aligned}$$

If inhomogeneous Neumann boundary conditions are used, the corresponding element matrix is depicted in Section C.2.1, which is also used for the quasi magnetostatic case. Thus the magnetic scalar potential ψ and the permeability $\underset{\sim}{\mu}$ are used instead φ and $\underset{\sim}{\epsilon}$. Additionally it is assumed that the permeability is a scalar and element wise constant ($\underset{\sim}{\mu} \to \mu$).

Die approbierte gedruckte Originalversion dieser Dissertation ist an der TU Wien Bibliothek verfügbar.
The approved original version of this doctoral thesis is available in print at TU Wien Bibliothek.

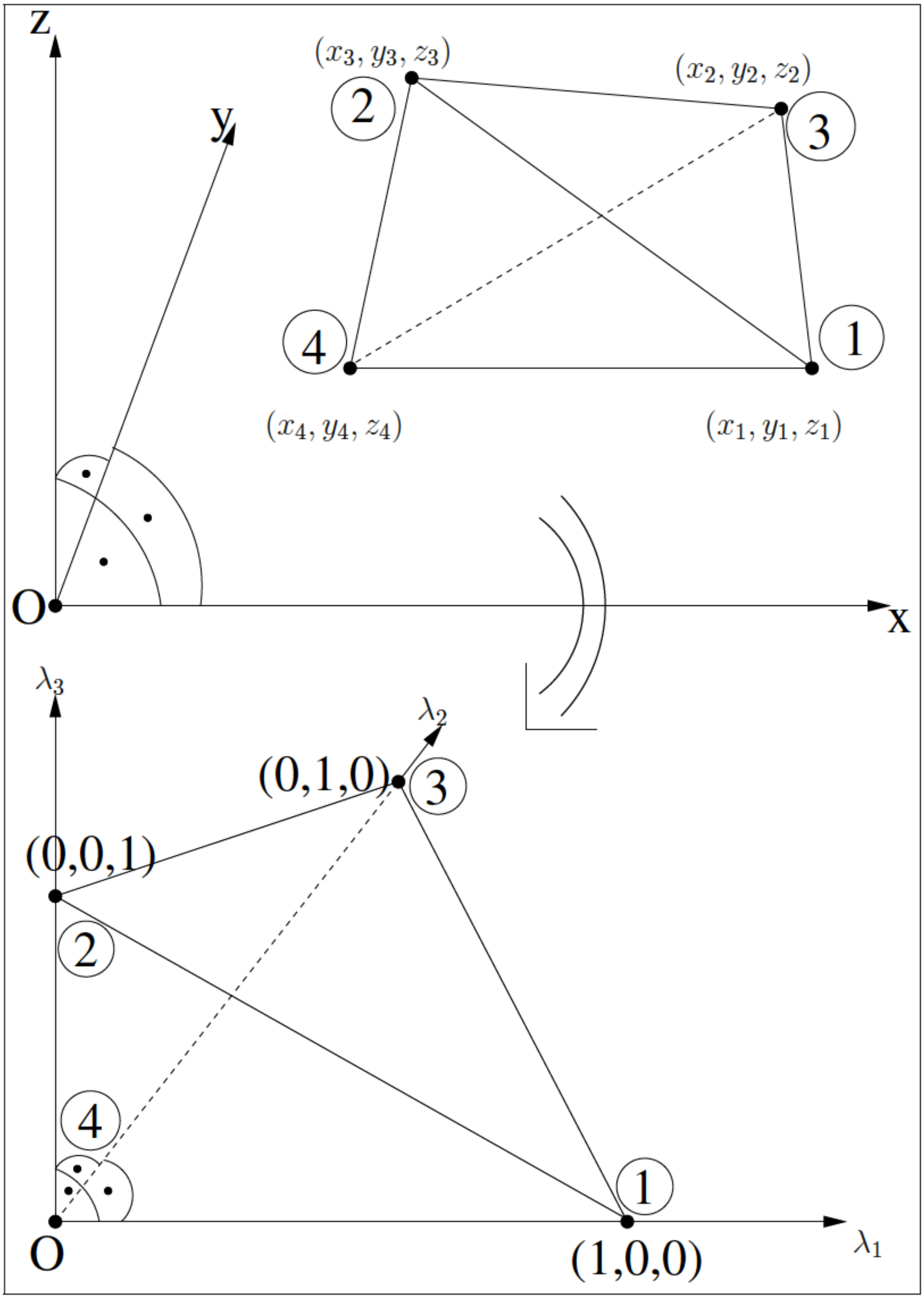

Figure 4.8: Three-dimensional domain transformation.

Die approbierte gedruckte Originalversion dieser Dissertation ist an der TU Wien Bibliothek verfügbar.
The approved original version of this doctoral thesis is available in print at TU Wien Bibliothek.

Chapter 5

The Vector Finite Element Method

Originally only the so called node finite element analysis has been used. By the node finite elements the unknown field values are assigned to the element vertexes. It is obvious that vector field quantities can be described with their components on the vertexes. Thus node elements can be used also for vector field calculations. In this case two or three scalars must be assigned to each vertex for the two- or three-dimensional case, respectively. Unfortunately using the coordinates of the vector gives problems. For example, the continuity requirements for the approximated vector fields cannot be easily fulfilled and also applying of the boundary conditions is very cumbersome [55]. To overcome these obstacles the so-called edge elements are used by the vector finite element analysis [56]. They are assigned to the edges of an element and are excellently suited for numerical solution of partial differential equations for the field intensities derived from the Maxwell equations (4.1) to (4.4). However the popular believe, that edge elements eliminate the problems with the so-called spurious modes is erroneous. Spurious solutions are avoided only by a proper finite element formulation [57].

In Chapter 4 at first the two-dimensional case is discussed, where the finite element assembling mechanism is explained in detail. In the three-dimensional case the method works analogously, actually only the element matrix is different. There is also no difference in the way of assembling between scalar and vector finite element analysis. Using the vector elements the assembling is performed in the same manner, namely element wise. The building of the element matrix is different and is discussed comprehensively. Since it is no longer necessary to explain the assembling process in detail, this chapter handles the three-dimensional case before the two-dimensional one. It starts with some typical applications for the edge elements.

Furthermore, it is assumed that the constitutive parameters are time invariant and scalars ($\underset{\sim}{\epsilon}\to\epsilon$, $\underset{\sim}{\mu}\to\mu$, and $\underset{\sim}{\gamma}\to\gamma$). If it is required that the constitutive parameters are tensors, just replace for example, $(\epsilon\vec{E})$ by $(\underset{\sim}{\epsilon}\cdot\vec{E})$, $(\epsilon\vec{\nabla}\varphi)$ by $(\underset{\sim}{\epsilon}\cdot\vec{\nabla}\varphi)$, or $[a\,\vec{\nabla}\times\vec{b}]$ by $[\underset{\sim}{a}\cdot(\vec{\nabla}\times\vec{b})]$.

Die approbierte gedruckte Originalversion dieser Dissertation ist an der TU Wien Bibliothek verfügbar.
The approved original version of this doctoral thesis is available in print at TU Wien Bibliothek.

5.1 Edge Elements Applications

In this chapter the emphasis is on reviewing of various differential equations and boundary conditions which define boundary-value problems to be numerically solved by finite element analysis with edge elements. Some basic methods and equations arising from the theory of electromagnetism are presented. A detailed explanation can be found in [58, 59, 60, 61, 62, 63, 64, 65, 66].

5.1.1 The Wave Equation for the Electric Field

Differentiation of (4.3) with respect to time and substituting $\vec{J}$ from (4.8) and $\vec{H}$ from (4.7) gives

$$\vec{\nabla} \times \frac{1}{\mu}\partial_t \vec{B} = \gamma\, \partial_t \vec{E} + \epsilon\, \partial_{tt} \vec{E}. \tag{5.1}$$

With $\vec{B}$ from (4.1) the wave equation for $\vec{E}$ in the frequency domain is given by the expression

$$\vec{\nabla} \times (\frac{1}{\mu}\vec{\nabla} \times \vec{E}) + (\jmath\omega\gamma - \omega^2\epsilon)\vec{E} = 0, \tag{5.2}$$

where ω is the angular frequency. The time convention $e^{\jmath\omega t}$ is used and suppressed.

5.1.2 Equations for the Electrodynamic Potentials

Equation (4.2) is satisfied by the expression

$$\vec{B} = \vec{\nabla} \times \vec{A}. \tag{5.3}$$

Thus (4.1) becomes

$$\vec{\nabla} \times \left(\vec{E} + \partial_t \vec{A}\right) = \vec{0} \Leftrightarrow \vec{E} + \partial_t \vec{A} = -\vec{\nabla}\varphi \tag{5.4}$$

and the electric field $\vec{E}$ can be given by the electrodynamic potentials — the magnetic vector potential $\vec{A}$ and the electric scalar potential φ

$$\vec{E} = -\partial_t \vec{A} - \vec{\nabla}\varphi. \tag{5.5}$$

Using (4.7) and (5.3) the left hand side of (4.3) is expressed as

$$\vec{\nabla} \times \vec{H} = \vec{\nabla} \times \frac{1}{\mu}\vec{B} = \vec{\nabla} \times (\frac{1}{\mu}\vec{\nabla} \times \vec{A}). \tag{5.6}$$

With (4.6), (4.8), and (5.5) the right hand side of (4.3) is given by

$$\vec{J} + \partial_t \vec{D} = \gamma\vec{E} + \epsilon\partial_t\vec{E} = -\gamma\partial_t\vec{A} - \gamma\vec{\nabla}\varphi - \epsilon\partial_{tt}\vec{A} - \epsilon\partial_t\vec{\nabla}\varphi. \tag{5.7}$$

Die approbierte gedruckte Originalversion dieser Dissertation ist an der TU Wien Bibliothek verfügbar.
The approved original version of this doctoral thesis is available in print at TU Wien Bibliothek.

Substituting (5.6) and (5.7) in (4.3) the following equation for $\vec{A}$ and φ in the frequency domain is obtained

$$\vec{\nabla} \times (\frac{1}{\mu}\vec{\nabla} \times \vec{A}) = (\omega^2\epsilon - \jmath\omega\gamma)\vec{A} - (\gamma + \jmath\omega\epsilon)\vec{\nabla}\varphi. \tag{5.8}$$

Analogously after partial differentiation of (4.4) with respect to time and using (4.5), (4.6), and (4.8) it can be written

$$\vec{\nabla} \cdot \epsilon\partial_t\vec{E} = \partial_t\rho = -\vec{\nabla} \cdot \left(\gamma\vec{E}\right), \tag{5.9}$$

which leads with (5.5) to

$$\vec{\nabla} \cdot \left\{(\omega^2\epsilon - \jmath\omega\gamma)\vec{A} - (\gamma + \jmath\omega\epsilon)\vec{\nabla}\varphi\right\} = 0. \tag{5.10}$$

Equation (5.10) can also be obtained by applying the divergence operator to (5.8). The unknown fields $\vec{A}$ and φ are obtained from the boundary value problem given by the partial differential equation system (5.8) and (5.10). A similar strategy can be found in [67, 68], where $\vec{B} = \vec{\nabla} \times (\vec{A} + \vec{\nabla}\chi)$ and the auxiliary arbitrary scalar field χ is conveniently termed as a ghost field.

5.1.3 Quasi-Magnetostatics

If the characteristic lengths of the analyzed structures are much smaller than the considered wave lengths and for conducting areas $\epsilon/\gamma \ll T$, the displacement current can be neglected [40, 69]. T is the characteristic period of the time change rate. In this case the Maxwell equations (4.1) to (4.4) can be simplified and the so called dominant magnetic field model is achieved:

$$\vec{\nabla} \times \vec{E} = -\mu\partial_t\vec{H} \tag{5.11}$$

$$\vec{\nabla} \cdot \vec{B} = 0 \tag{5.12}$$

$$\vec{\nabla} \times \vec{H} = \vec{J}. \tag{5.13}$$

After transforming (5.13)

$$\vec{\nabla} \times \vec{H} = \vec{J} = \gamma\vec{E} \Rightarrow \frac{1}{\gamma}\vec{\nabla} \times \vec{H} = \vec{E} \tag{5.14}$$

the rotor operator is applied and the right hand side is substituted by (5.11)

$$\vec{\nabla} \times \left(\frac{1}{\gamma}\vec{\nabla} \times \vec{H}\right) = \vec{\nabla} \times \vec{E} = -\partial_t\vec{B} = -\mu\partial_t\vec{H}. \tag{5.15}$$

Thus, in the frequency domain the quasi-magnetostatic case is described by the following partial differential equation for the magnetic field $\vec{H}$

$$\vec{\nabla} \times \left(\frac{1}{\gamma}\vec{\nabla} \times \vec{H}\right) + \jmath\omega\mu\vec{H} = \vec{0}. \tag{5.16}$$

Die approbierte gedruckte Originalversion dieser Dissertation ist an der TU Wien Bibliothek verfügbar.
The approved original version of this doctoral thesis is available in print at TU Wien Bibliothek.

5.2 Three-Dimensional Vector Finite Element Method

The vector finite element analysis will be demonstrated using the quasi magnetostatic case as described in Subsection 5.1.3. The Galerkin method is applied to (5.15) and the weak formulation for the vector differential operator, as discussed in Section 3.3, is used. This gives the following expression

$$\begin{aligned} &\int_{\mathcal{V}} \left(\vec{\nabla}\times\vec{N}_i\right)\cdot\left(\frac{1}{\gamma}\vec{\nabla}\times\vec{H}\right)\mathrm{d}V- \\ -&\int_{\partial\mathcal{V}} \vec{n}\cdot\left[\vec{N}_i\times\left(\frac{1}{\gamma}\vec{\nabla}\times\vec{H}\right)\right]\mathrm{d}A+\jmath\omega\int_{\mathcal{V}}\mu\vec{N}_i\cdot\vec{H}\,\mathrm{d}V=0. \end{aligned} \tag{5.17}$$

Adding an arbitrary gradient field (i. e. $\vec{\nabla}\psi$) to the magnetic field $\vec{H}$ does not alter (5.17), since the rotor operator of a gradient field is zero ($\vec{\nabla}\times\vec{\nabla}\psi{=}0$). The solution will remain unchanged like

$$\begin{aligned} &\int_{\mathcal{V}} \left(\vec{\nabla}\times\vec{N}_i\right)\cdot\left[\frac{1}{\gamma}\vec{\nabla}\times(\vec{H}+\vec{\nabla}\psi)\right]\mathrm{d}V- \\ -&\int_{\partial\mathcal{V}} \vec{n}\cdot\left\{\vec{N}_i\times\left[\frac{1}{\gamma}\vec{\nabla}\times(\vec{H}+\vec{\nabla}\psi)\right]\right\}\mathrm{d}A+\jmath\omega\int_{\mathcal{V}}\mu\vec{N}_i\cdot\vec{H}\,\mathrm{d}V=0. \end{aligned} \tag{5.18}$$

Applying the substitution

$$\vec{H}+\vec{\nabla}\psi=\vec{H}_1 \tag{5.19}$$

in (5.18) leads to the following equation

$$\begin{aligned} &\int_{\mathcal{V}} \left(\vec{\nabla}\times\vec{N}_i\right)\cdot\left(\frac{1}{\gamma}\vec{\nabla}\times\vec{H}_1\right)\mathrm{d}V- \\ -&\int_{\partial\mathcal{V}} \vec{n}\cdot\left[\vec{N}_i\times\left(\frac{1}{\gamma}\vec{\nabla}\times\vec{H}_1\right)\right]\mathrm{d}A+\jmath\omega\int_{\mathcal{V}}\mu\vec{N}_i\cdot(\vec{H}_1-\vec{\nabla}\psi)\,\mathrm{d}V=0. \end{aligned} \tag{5.20}$$

In the literature the vector potential $\vec{H}_1$ of the current density $\vec{J}$ is often denoted as **T** and the auxiliary scalar field ψ is denoted as Ω or ϕ, respectively. This gives the widely used names of the numerical procedure for handling the quasi-static method — **T**-Ω or **T**-ϕ method [70, 71, 72, 73, 74, 75, 76, 77, 78, 79]. Using this technique the finite element method can be combined with the boundary integral method to diminish the number of unknowns taking into account the unbounded regions [80]. Of coarse, the dominant magnetic field model can be also considered from the equations for the electrodynamic

TU WIEN Bibliothek Your knowledge hub
Die approbierte gedruckte Originalversion dieser Dissertation ist an der TU Wien Bibliothek verfügbar.
The approved original version of this doctoral thesis is available in print at TU Wien Bibliothek.

potentials from Subsection 5.1.2 to obtain expressions for the magnetic vector potential $\vec{A}$ and the electric scalar potential φ for the quasi-magnetostatic case [81].

In this chapter the finite element analysis with vector shape functions for the approximation of $\vec{H}_1$ and with scalar shape functions for the approximation of ψ is comprehensively explained. The same can be applied for the electric field $\vec{E}$ from Subsection 5.1.1 or for the electrodynamic potentials $\vec{A}$ and φ from Subsection 5.1.2.

De facto (5.20) corresponds to the partial differential equation

$$\vec{\nabla} \times \left(\frac{1}{\gamma} \vec{\nabla} \times \vec{H}_1 \right) + \jmath\omega\mu(\vec{H}_1 - \vec{\nabla}\psi) = \vec{0}. \tag{5.21}$$

Since there are two unknowns in (5.21) — the vector field $\vec{H}_1$ and the scalar field ψ, an additional relation between these two fields is required. Equation (5.20) (or the equivalent one (5.21)) is derived from (5.11) and (5.13), but (5.12) has not been used. With (4.7) it leads to

$$\vec{\nabla} \cdot \left[\mu(\vec{H}_1 - \vec{\nabla}\psi) \right] = 0. \tag{5.22}$$

Equation (5.22) provides the additional relation between $\vec{H}_1$ and ψ. Thus the magnetic field $\vec{H}$ is obtained by solving the boundary value problem, given by the partial differential equation system consisting of (5.21) and (5.22) for $\vec{H}_1$ and ψ

$$\vec{H} = \vec{H}_1 - \vec{\nabla}\psi. \tag{5.23}$$

In ideal dielectric regions (5.21) cannot be used, because $\gamma = 0$. In such regions the current density is zero and $\vec{H}$ can be expressed as gradient field like

$$\vec{\nabla} \times \vec{H} = \vec{0} \quad \Rightarrow \quad \vec{H} = \vec{\nabla}\psi. \tag{5.24}$$

Thus for the numerical analysis (5.24) can be used in the dielectric part of the simulation domain and (5.21), (5.22), and (5.23) can be applied in the remaining parts, respectively. However (5.24) is valid only for simply connected regions. For non-contiguous regions specific cutting algorithms have to be addressed [82, 83, 84, 85]. Unfortunately, these algorithms are quite expensive pre-processing steps for complex structures. In this work it is preferred to assume low conductivity of the dielectrics and to use (5.21), (5.22), and (5.23) in the entire simulation domain. The conductivity in the dielectric regions should be sufficiently low with respect to the conductivity of the conducting areas. However, it should not be very low, because the first summand of the right hand side of (5.21) would increase dramatically and would lead to an extremely ill conditioned linear equation system.

The boundary $\partial\mathcal{V}$ of the calculation domain $\mathcal{V}$ is divided into a Dirichlet boundary $\mathcal{A}_{D1}$ for $\vec{H}_1$ and a Neumann boundary $\mathcal{A}_{N1}$ for (5.21) and into a Dirichlet boundary $\mathcal{A}_{D2}$ for ψ and a Neumann boundary $\mathcal{A}_{N2}$ for (5.21).

$$\partial\mathcal{V} = \mathcal{A}_{D1} + \mathcal{A}_{N1} \quad \text{and} \quad \partial\mathcal{V} = \mathcal{A}_{D2} + \mathcal{A}_{N2}.$$

Die approbierte gedruckte Originalversion dieser Dissertation ist an der TU Wien Bibliothek verfügbar.
The approved original version of this doctoral thesis is available in print at TU Wien Bibliothek.

The weighting of the residual of (5.21) and the following weak formulation for the finite element analysis has been already dealt with (5.20). The same must be done for (5.22) as well. For this purpose the residual of (5.22) is weighted by a set of scalar functions λ_i

$$\int\limits_{\mathcal{V}} \vec{\nabla} \cdot \Big[\mu(\vec{H}_1 - \vec{\nabla}\psi)\Big]\, \lambda_i \, \mathrm{d}V = 0 \tag{5.25}$$

and then the first scalar Green's theorem is applied similarly as shown in Section 3.3 for the scalar differential operator. This leads to the equation

$$\int\limits_{\partial\mathcal{V}} \vec{n} \cdot \Big\{\lambda_i \Big[\mu(\vec{H}_1 - \vec{\nabla}\psi)\Big]\Big\} \, \mathrm{d}A - \int\limits_{\mathcal{V}} \vec{\nabla}\lambda_i \cdot \Big[\mu(\vec{H}_1 - \vec{\nabla}\psi)\Big] \, \mathrm{d}V = 0. \tag{5.26}$$

As usual for the finite element analysis the unknown vector function $\vec{H}_1$ is approximated by a sum of known vector functions multiplied by coefficients

$$\vec{H}_1 \simeq \sum_{j=1}^{m} c_j \vec{N}_j + \vec{v}, \quad \text{with} \quad \vec{v} = \sum_{j=n+1}^{M} c_j \vec{N}_j. \tag{5.27}$$

The same is done for the scalar function ψ

$$\psi \simeq \sum_{j=m+1}^{n} c_j \lambda_j + v, \quad \text{with} \quad v = \sum_{j=M+1}^{N} c_j \lambda_j. \tag{5.28}$$

The functions $\vec{v}$ and v comply with the Dirichlet boundary conditions for $\vec{H}_1$ and ψ, respectively. The tilde sign written over the approximated field quantity is not used any more. Of coarse it will be kept in mind that the sums (5.27) and (5.28) are approximations. As already mentioned the coefficients c_j in the scalar approximation (5.28) correspond to the scalar field values in the nodes of the discretized domain. It will be shown in Subsection 5.2.2 that the coefficient c_j in the vector approximation (5.27) complies with the tangential component of the field $\vec{H}$ along the global edge j of the discretized domain. Similarly to the nodes, the edges are numbered globally for the entire domain and locally in each element. Again there is a connectivity array which binds the local (element) edge index with the corresponding global one. The coefficients for both, nodes and edges lying at the Dirichlet boundary, can be obtained from the Dirichlet boundary condition and are arranged behind the unknown coefficients in the following way

$$j = \underbrace{\overbrace{1\ldots\ldots\ldots\ldots m}^{\textit{unknown edges}}\overbrace{\ldots\ldots\ldots\ldots n}^{\textit{unknown nodes}}}_{\textit{unknown coefficients}}\underbrace{\overbrace{\ldots\ldots\ldots\ldots M}^{\textit{Dirichlet edges}}\overbrace{\ldots\ldots\ldots N}^{\textit{Dirichlet nodes}}}_{\textit{known coefficients}}$$

The unknown coefficients associated with the edges are numbered from 1 to m and the unknown ones associated with the nodes count from m+1 to n, respectively. The known coefficients for the edges given by the Dirichlet boundary of (5.27) are numbered from $n{+}1$ till M and the known coefficients for the nodes on the Dirichlet boundary of (5.28) are numbered from $M{+}1$ to N. Thus the first n coefficients are unknown and are the solution of the finite element calculation and the remaining coefficients numbered from $n{+}1$ to N are given by the Dirichlet boundaries.

Each global vector function $\vec{N}_j$ corresponds to the global edge j and is constructed from element functions $\vec{N}_j^e$ similarly with the scalar functions λ_j. In Subsection 5.2.2 it will be demonstrated that $\vec{N}_j$ has no tangential component along other edges except edge j. Thus the boundary term in (5.20) can be given in a different form as

$$\begin{aligned}\int\limits_{\partial\mathcal{V}} \vec{n}\cdot\left[\vec{N}_i\times\left(\frac{1}{\gamma}\vec{\nabla}\times\vec{H}_1\right)\right]\,\mathrm{d}A &= \int\limits_{\partial\mathcal{V}} \vec{n}\cdot\left(\vec{N}_i\times\vec{E}\right)\,\mathrm{d}A = \\ = \int\limits_{\mathcal{A}_{N1}} \vec{E}\cdot\left(\vec{n}\times\vec{N}_i\right)\,\mathrm{d}A &= \int\limits_{\mathcal{A}_{N1}} \vec{N}_i\cdot\left(\vec{E}\times\vec{n}\right)\,\mathrm{d}A\end{aligned} \tag{5.29}$$

with

$$\vec{E} = \frac{1}{\gamma}\vec{J} = \frac{1}{\gamma}\,\vec{\nabla}\times\vec{H}_1.$$

Since the global edge functions $\vec{N}_i$ with $i\in[1;m]$ have no tangential component on the edges lying on the Dirichlet boundary $\mathcal{A}_{D1}$, they must be perpendicular to $\mathcal{A}_{D1}$ (or parallel to $\vec{n}$). As clearly shown by the third member of (5.29) the boundary integral in (5.20) has a contribution only for the Neumann boundary $\mathcal{A}_{N1}$. Furthermore the following is assumed: The electric field $\vec{E}$ is either perpendicular to $\mathcal{A}_{N1}$, which means that $\vec{E}\times\vec{n}$ is zero in the last term of (5.29), or the simulation domain is sufficiently large and allows that $\vec{E}\times\vec{n}$ can be neglected on $\mathcal{A}_{N1}$. Accepting this, the boundary term in (5.20) vanishes

$$\int\limits_{\partial\mathcal{V}} \vec{n}\cdot\left[\vec{N}_i\times\left(\frac{1}{\gamma}\vec{\nabla}\times\vec{H}_1\right)\right]\,\mathrm{d}A = \int\limits_{\partial\mathcal{V}} \vec{N}_i\cdot\left(\vec{E}\times\vec{n}\right)\,\mathrm{d}A = 0. \tag{5.30}$$

The boundary integral of (5.26) can be written in the following way

$$\int\limits_{\partial\mathcal{V}} \vec{n}\cdot\left\{\lambda_i\left[\mu(\vec{H}_1-\vec{\nabla}\psi)\right]\right\}\,\mathrm{d}A = \int\limits_{\mathcal{A}_{N2}} \lambda_i\,\vec{n}\cdot\vec{B}\,\mathrm{d}A \tag{5.31}$$

with

$$\mu(\vec{H}_1-\vec{\nabla}\psi) = \mu\vec{H} = \vec{B}.$$

The global node functions λ_i are non-zero only in the neighbor elements of the unknown nodes, which do not belong to the Dirichlet boundary $\mathcal{A}_{D2}$ and are indexed by $i\in[m{+}1;n]$. On the Dirichlet boundary $\mathcal{A}_{D2}$ the global functions λ_i are defined to zero. Thus the boundary integral (5.31) vanishes at the Dirichlet boundary $\mathcal{A}_{D2}$ and the integration domain is restricted to the Neumann boundary $\mathcal{A}_{N2}$. Additionally it is

TU WIEN Bibliothek Your knowledge hub
Die approbierte gedruckte Originalversion dieser Dissertation ist an der TU Wien Bibliothek verfügbar.
The approved original version of this doctoral thesis is available in print at TU Wien Bibliothek.

assumed that the magnetic flux $\vec{B}$ is perpendicular to $\vec{n}$ on the surface $\mathcal{A}_{N2}$ or that it can be neglected on this surface. Thus the boundary integral of (5.26) is also set to zero

$$\int\limits_{\partial\mathcal{V}} \vec{n}\cdot\left\{\lambda_i\left[\mu(\vec{H}_1-\vec{\nabla}\psi)\right]\right\}\,\mathrm{d}A=\int\limits_{\partial\mathcal{V}}\lambda_i\,\vec{n}\cdot\vec{B}\,\mathrm{d}A=0. \tag{5.32}$$

In such case it is often spoken of a homogeneous or zero Neumann boundary conditions. It will be shown in the application section that this is not a substantial restriction. Of coarse, it is important to use a suitable model which fulfills the assumed criteria as well as possible. For the sake of completeness a possible discretization of the element matrices arising from the boundary integrals over $\mathcal{A}_{N1}$ and $\mathcal{A}_{N2}$ are given in the appendix in Chapter B and Chapter C.

With the above considerations about the boundary integral terms the base equations used for the further finite element assembling can be written

$$\int\limits_{\mathcal{V}}\left(\vec{\nabla}\times\vec{N}_i\right)\cdot\left(\frac{1}{\gamma}\vec{\nabla}\times\vec{H}_1\right)\,\mathrm{d}V+\jmath\omega\int\limits_{\mathcal{V}}\mu\vec{N}_i\cdot\vec{H}_1\,\mathrm{d}V-\jmath\omega\int\limits_{\mathcal{V}}\mu\vec{N}_i\cdot\vec{\nabla}\psi\,\mathrm{d}V=0 \tag{5.33}$$

$$\int\limits_{\mathcal{V}}\vec{\nabla}\lambda_i\cdot\left(\mu\vec{H}_1\right)\,\mathrm{d}V-\int\limits_{\mathcal{V}}\vec{\nabla}\lambda_i\cdot\left(\mu\vec{\nabla}\psi\right)\,\mathrm{d}V=0. \tag{5.34}$$

$\vec{H}_1$ and ψ are substituted by their approximations (5.27) and (5.28) in (5.33) and (5.34)

$$\begin{aligned}
&\sum_{j=1}^{m}c_j\int\limits_{\mathcal{V}}\left(\vec{\nabla}\times\vec{N}_i\right)\cdot\left(\frac{1}{\gamma}\vec{\nabla}\times\vec{N}_j\right)\,\mathrm{d}V+\jmath\omega\sum_{j=1}^{m}c_j\int\limits_{\mathcal{V}}\mu\vec{N}_i\cdot\vec{N}_j\,\mathrm{d}V- \\
&-\jmath\omega\sum_{j=m+1}^{n}c_j\int\limits_{\mathcal{V}}\mu\vec{N}_i\cdot\vec{\nabla}\lambda_j\,\mathrm{d}V= \\
=&-\sum_{j=n+1}^{M}c_j\int\limits_{\mathcal{V}}\left(\vec{\nabla}\times\vec{N}_i\right)\cdot\left(\frac{1}{\gamma}\vec{\nabla}\times\vec{N}_j\right)\,\mathrm{d}V-\jmath\omega\sum_{j=n+1}^{M}c_j\int\limits_{\mathcal{V}}\mu\vec{N}_i\cdot\vec{N}_j\,\mathrm{d}V+ \\
&+\jmath\omega\sum_{j=M+1}^{N}c_j\int\limits_{\mathcal{V}}\mu\vec{N}_i\cdot\vec{\nabla}\lambda_j\,\mathrm{d}V\ ,\quad i\in[1;m]
\end{aligned} \tag{5.35}$$

$$\begin{aligned}
&\sum_{j=1}^{m}c_j\int\limits_{\mathcal{V}}\vec{\nabla}\lambda_i\cdot\left(\mu\vec{N}_j\right)\,\mathrm{d}V-\sum_{j=m+1}^{n}c_j\int\limits_{\mathcal{V}}\vec{\nabla}\lambda_i\cdot\left(\mu\vec{\nabla}\lambda_j\right)\,\mathrm{d}V= \\
=&-\sum_{j=n+1}^{M}c_j\int\limits_{\mathcal{V}}\vec{\nabla}\lambda_i\cdot\left(\mu\vec{N}_j\right)\,\mathrm{d}V+\sum_{j=M+1}^{N}c_j\int\limits_{\mathcal{V}}\vec{\nabla}\lambda_i\cdot\left(\mu\vec{\nabla}\lambda_j\right)\,\mathrm{d}V\ ,\quad i\in[m{+}1;n].
\end{aligned} \tag{5.36}$$

Die approbierte gedruckte Originalversion dieser Dissertation ist an der TU Wien Bibliothek verfügbar.
The approved original version of this doctoral thesis is available in print at TU Wien Bibliothek.
TU WIEN Bibliothek Your knowledge hub

Die approbierte gedruckte Originalversion dieser Dissertation ist an der TU Wien Bibliothek verfügbar.
The approved original version of this doctoral thesis is available in print at TU Wien Bibliothek.

The linear equation system consisting of (5.35) and (5.36) is written more conveniently in matrix form

$$\begin{bmatrix} [A] & [B] \\ [B]^T & [C] \end{bmatrix} \{c\} = \{b\}\,, \tag{5.37}$$

where (5.36) is multiplied by $-\jmath\omega$ to obtain a symmetric matrix. Thus, $[A]$, $[B]$, $[C]$ and $[b]$ are given by the expressions

$$A_{ij} = \int\limits_{\mathcal{V}} \left(\vec{\nabla} \times \vec{N}_i\right) \cdot \left(\frac{1}{\gamma}\vec{\nabla} \times \vec{N}_j\right) \mathrm{d}V + \jmath\omega \int\limits_{\mathcal{V}} \mu\vec{N}_i \cdot \vec{N}_j \,\mathrm{d}V,\ \ i \in [1;m],\ \ j \in [1;m] \tag{5.38}$$

$$B_{ij} = -\jmath\omega \int\limits_{\mathcal{V}} \mu\vec{N}_i \cdot \vec{\nabla}\lambda_j \,\mathrm{d}V,\ \ i \in [1;m],\ \ j \in [m{+}1;n] \tag{5.39}$$

$$C_{ij} = \jmath\omega \int\limits_{\mathcal{V}} \vec{\nabla}\lambda_i \cdot \left(\mu\vec{\nabla}\lambda_j\right) \mathrm{d}V,\ \ i \in [m{+}1;n],\ \ j \in [m{+}1;n] \tag{5.40}$$

$$\begin{aligned} b_i = &- \sum_{j=n+1}^{M} c_j \int\limits_{\mathcal{V}} \left(\vec{\nabla} \times \vec{N}_i\right) \cdot \left(\frac{1}{\gamma}\vec{\nabla} \times \vec{N}_j\right) \mathrm{d}V - \jmath\omega \sum_{j=n+1}^{M} c_j \int\limits_{\mathcal{V}} \mu\vec{N}_i \cdot \vec{N}_j \,\mathrm{d}V + \\ &+ \jmath\omega \sum_{j=M+1}^{N} c_j \int\limits_{\mathcal{V}} \mu\vec{N}_i \cdot \vec{\nabla}\lambda_j \,\mathrm{d}V\ ,\quad i \in [1;m] \end{aligned} \tag{5.41}$$

$$\begin{aligned} b_i = &\ \jmath\omega \sum_{j=n+1}^{M} c_j \int\limits_{\mathcal{V}} \vec{\nabla}\lambda_i \cdot \left(\mu\vec{N}_j\right) \mathrm{d}V - \\ &- \jmath\omega \sum_{j=M+1}^{N} c_j \int\limits_{\mathcal{V}} \vec{\nabla}\lambda_i \cdot \left(\mu\vec{\nabla}\lambda_j\right) \mathrm{d}V\ ,\quad i \in [m{+}1;n]. \end{aligned} \tag{5.42}$$

Obviously the right hand side vector $\{b\}$ can be calculated by (5.37) where $[A]$, $[B]$, and $[C]$ are expressed as in (5.38), (5.39), and (5.40) and the corresponding ranges for the global indexes i and j are taken from (5.41) and (5.42).

5.2.1 Domain Discretization

The three-dimensional simulation domain is discretized in the same way as for the scalar finite element method on tetrahedrons. Unfortunately this is not a simple problem, especially for arbitrary shaped regions and complicated field distributions [86, 87]. The mesh properties have considerable impact on the finite element analysis and strongly affect the solution quality and the calculation duration time. Generally these properties include geometry conformity, mesh density, and element quality. The geometry conformity requires that the area defined by the mesh elements should sufficiently good approximate the domain of the problem. As already mentioned in Subsection 4.1.1 the mesh density

Die approbierte gedruckte Originalversion dieser Dissertation ist an der TU Wien Bibliothek verfügbar.
The approved original version of this doctoral thesis is available in print at TU Wien Bibliothek.
TU Bibliothek WIEN Your knowledge hub

must be sufficiently high and the mesh size sufficiently small, respectively, to minimize the discretization error and to achieve accurate solutions. A good idea is to use denser mesh, which means smaller elements only in those regions, where a high spacial variation of the investigated fields is anticipated. Of course this can be realized only with unstructured meshes used in this work. Automatic mesh adaptation and improvement based on refinement in the regions presenting the highest error in the approximation procedure [88, 89, 90, 91] or on user expertise on the specific problem [92] are often used. Parallel mesh refinement algorithms can be applied to speed up this process [93, 94]. The finite element method leads to a linear equation system solved iteratively. As discussed in [95, 96] large element dihedral angles increase the discretization error in the finite element solution [97] and for a good condition number of the system matrix the discretization should avoid the generation of elements with a small inner solid angle or narrow elements [98, 99]. Unfortunately, if there are small solid angles predefined in the domain, the mesh generation software will likely produce bad elements at this place.

As an example a conducting inductor (Fig. <5.1>) placed in an insulating rectangular brick domain (Fig. <5.2>) is discretized and visualized. Similar structures will be used in the application part of this work, where the simulation results of the vector finite element algorithm are demonstrated. The inductor is colored bright and the insulator dark. Normally the inductance and the resistance of the inductor at different frequencies must be calculated, which requires the extraction of the magnetic field distribution and the current density distribution in the simulation domain. If the operating frequency is sufficiently high for the dimensions of the corresponding domain parts, skin effect is observed. The current is forced to flow only on or near the surface of the inductor wire. There is no current flow inside of the inductor wire. In such cases it is convenient to produce the finest mesh on the surface of the wire and in the area close to the boundary between the inductor and the insulating environment. Deep inside and far outside the wire coarser mesh elements can be used as shown in Fig. <5.3> and Fig. <5.4>.

5.2.2 Linear Vector Shape Functions on Tetrahedral Elements

Refer to the tetrahedron from Fig. <4.7>. The vector field in the tetrahedral element is interpolated by means of the Whitney 1-form basis function W_i^e associated to the element edge i [100]. For example along Edge 1 between Node 1 and Node 2 this function is given by

$$\vec{W}_1^e = \vec{W}_{12}^e = \lambda_1^e \vec{\nabla} \lambda_2^e - \lambda_2^e \vec{\nabla} \lambda_1^e.$$

This approach was introduced first by Whitney [101]. The functions λ_i^e are the barycentric coordinates from Subsection 4.2.2. If only one subscript index is used for the vector basis functions (for example $\vec{W}_1^e$), this index means an edge number (for example Edge 1). If two subscript indexes are used (for example $\vec{W}_{12}^e$), these indexes comply with the corresponding node numbers (for example Edge 1 belongs to the node pair Node 1 and Node 2). The edge indexes are associated to node pairs in Table 5.1.

Die approbierte gedruckte Originalversion dieser Dissertation ist an der TU Wien Bibliothek verfügbar.
The approved original version of this doctoral thesis is available in print at TU Wien Bibliothek.

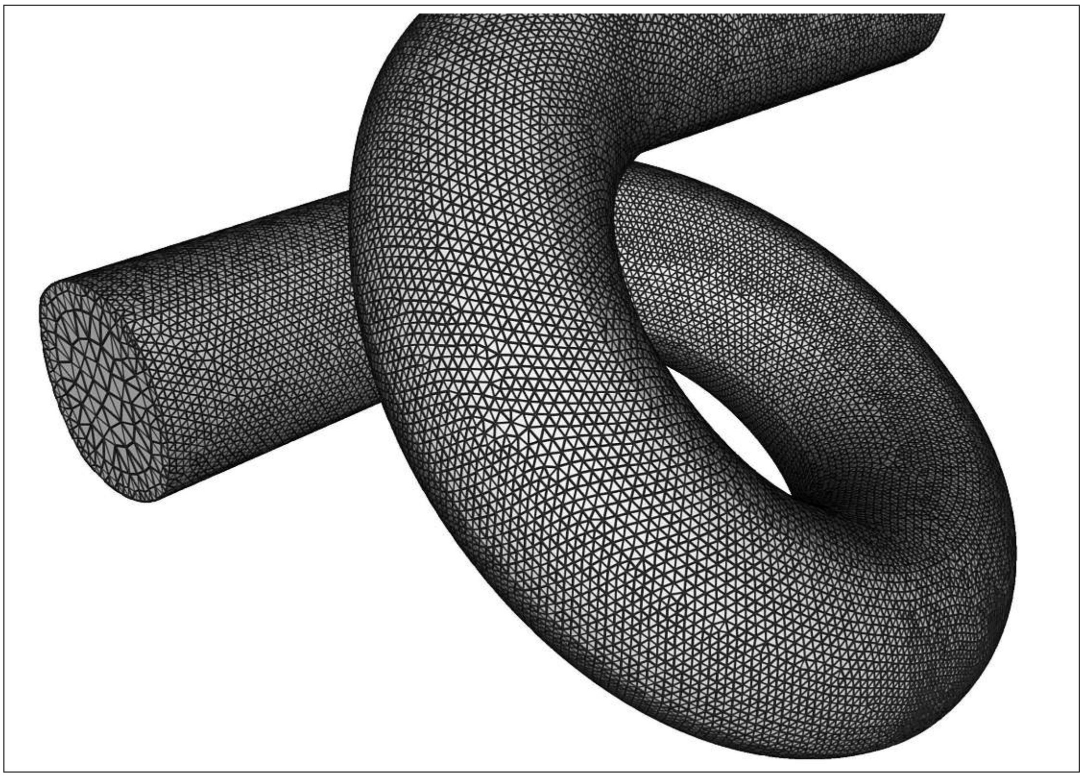

Figure 5.1: The inductor inside the simulation domain in Fig. <5.2>.

Furthermore the following notation is used

$$\vec{r}_1 = \vec{r}_{12},\ \vec{r}_2 = \vec{r}_{13},\ \vec{r}_3 = \vec{r}_{14},\ \vec{r}_4 = \vec{r}_{23},\ \vec{r}_5 = \vec{r}_{42},\ \vec{r}_6 = \vec{r}_{34}$$

and

$$l_1 = |\vec{r}_1|,\ l_2 = |\vec{r}_2|,\ l_3 = |\vec{r}_3|,\ l_4 = |\vec{r}_4|,\ l_5 = |\vec{r}_5|,\ l_6 = |\vec{r}_6|.$$

Since λ_1^e vanishes on the facet defined by $(2,3,4)$ and $\vec{\nabla}\lambda_1^e$ is perpendicular to that facet, $\vec{W}_1^e$ has no tangential component on this facet. Analogously it can be stated that $\vec{W}_1^e$ has no tangential component on the facet defined by $(1,3,4)$. Thus the edge function $\vec{W}_1^e$ has no tangential component along the edges different from the Edge 1 and it contributes only to their normal components. This is also valid for the Whitney vector basis functions $\vec{W}_i^e$ on the remaining element edges.

For the divergence and for the rotor of the Whitney function $\vec{W}_i^e$ it is written

$$\vec{\nabla} \cdot \vec{W}_1^e = \vec{\nabla}\lambda_1^e \cdot \vec{\nabla}\lambda_2^e - \vec{\nabla}\lambda_2^e \cdot \vec{\nabla}\lambda_1^e = 0$$

$$\vec{\nabla} \times \vec{W}_1^e = \vec{\nabla}\lambda_1^e \times \vec{\nabla}\lambda_2{}^e - \vec{\nabla}\lambda_2^e \times \vec{\nabla}\lambda_1^e = 2\vec{\nabla}\lambda_1^e \times \vec{\nabla}\lambda_2^e.$$

Die approbierte gedruckte Originalversion dieser Dissertation ist an der TU Wien Bibliothek verfügbar.
The approved original version of this doctoral thesis is available in print at TU Wien Bibliothek.

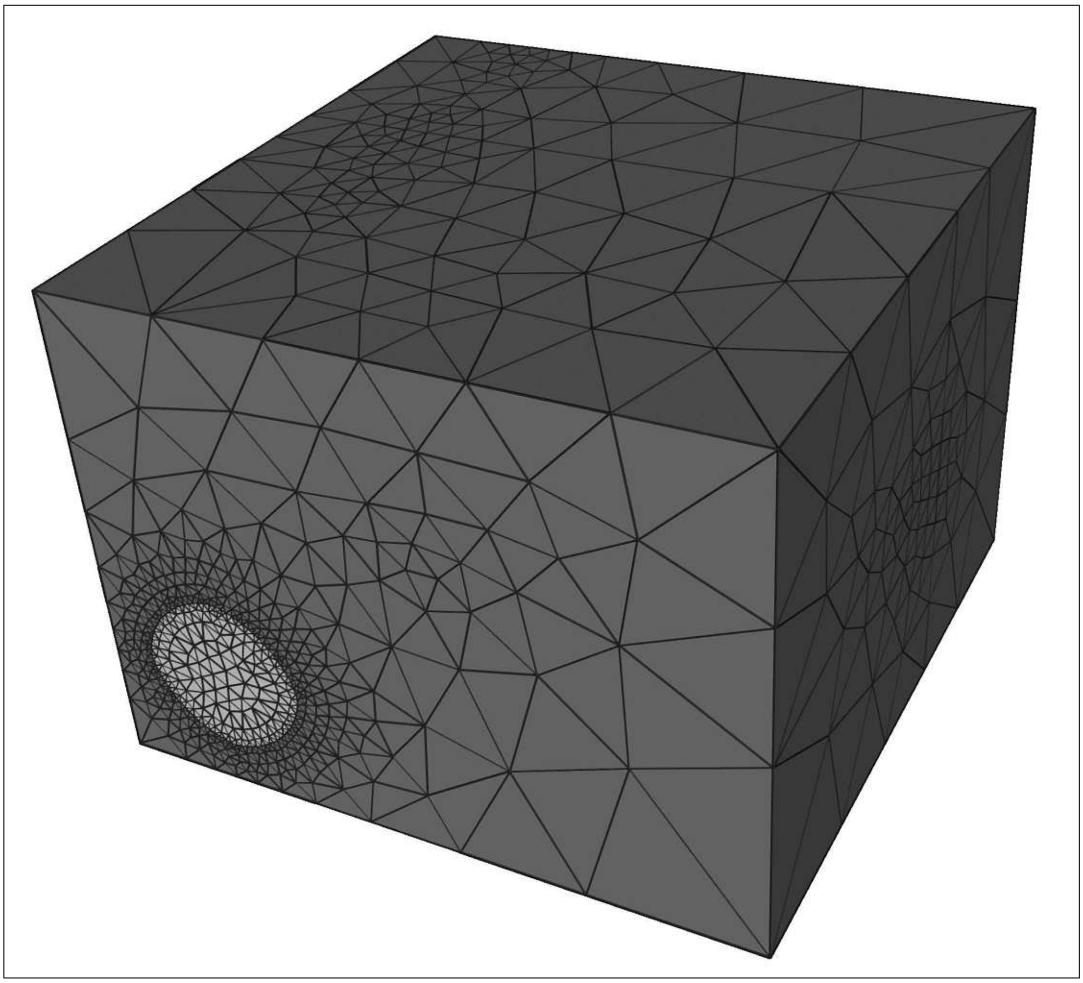

Figure 5.2: The entire simulation domain.

Along the direction of Edge i the Whitney function $\vec{W}_i^e$ has a constant tangential component. This will be demonstrated for $\vec{W}_1^e$.

$$\vec{W}_1 \cdot \frac{\vec{r}_1}{l_1} = \frac{1}{l_1}\left(\lambda_1 \frac{\vec{r}_2 \times \vec{r}_3}{6V^e} \cdot \vec{r}_1 - \lambda_2 \frac{\vec{r}_4 \times \vec{r}_5}{6V^e} \cdot \vec{r}_1\right) = \frac{1}{l_1}\left(\lambda_1 \frac{6V^e}{6V^e} - \lambda_2 \frac{-6V^e}{6V^e}\right) = \frac{\lambda_1 + \lambda_2}{l_1}.$$

In direction parallel to Edge 1 λ_3 and λ_4 are constant. On Edge 1 λ_3 and λ_4 are zero. With (4.76) $\lambda_1 + \lambda_2$ are also constant parallel to the edge 1. On Edge 1 $\lambda_1 + \lambda_2 = 1$. Consequently parallel to Edge 1

$$\vec{W}_1 \cdot \frac{\vec{r}_1}{l_1} = \frac{\lambda_1 + \lambda_2}{l_1} = const \tag{5.43}$$

and on Edge 1

$$\vec{W}_1 \cdot \frac{\vec{r}_1}{l_1} = \frac{1}{l_1}. \tag{5.44}$$

Die approbierte gedruckte Originalversion dieser Dissertation ist an der TU Wien Bibliothek verfügbar.
The approved original version of this doctoral thesis is available in print at TU Wien Bibliothek.

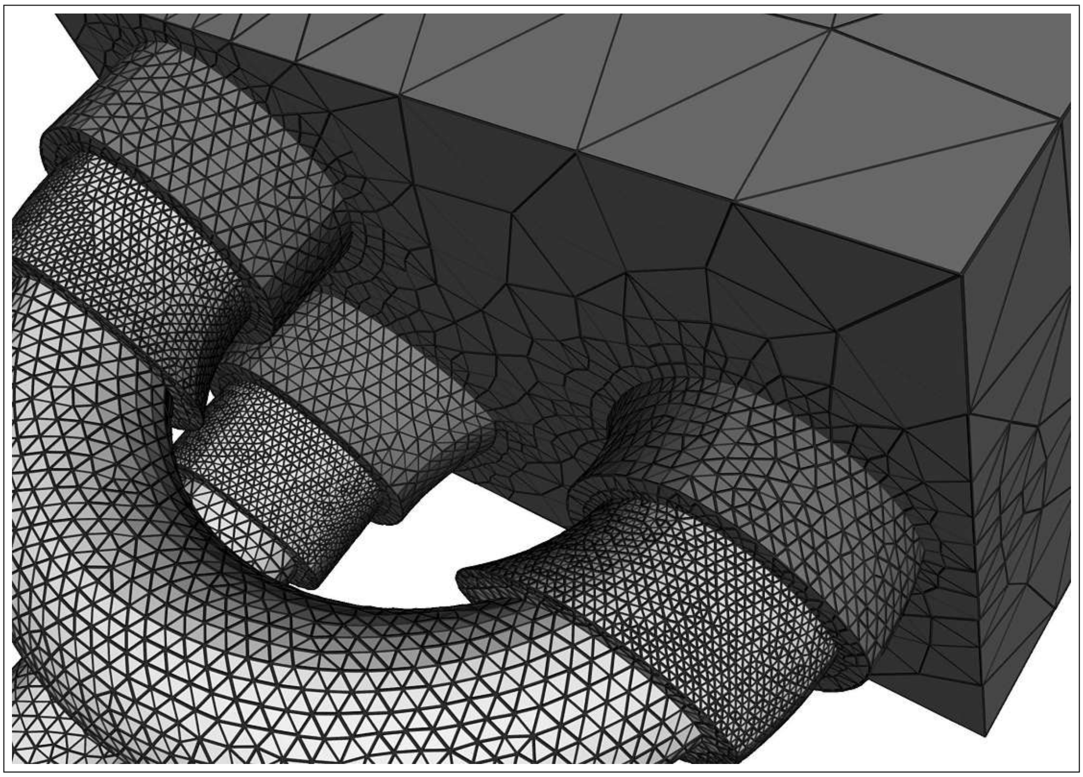

Figure 5.3: Inside view of the simulation domain in Fig. <5.2>.

Thus, the continuity of the tangential component along the element edge across the elements is guaranteed. Otherwise the normal component must not be continuous. Exactly this behavior is required for the fields $\vec{E}$ and $\vec{H}$ (if no surface current is available) and for the magnetic vector potential $\vec{A}$. Thus, the element vector basis functions for the field associated with the edges are given by the very well suited 1-form Whitney functions $\vec{W}_i^e$

$$\vec{N}_1^e = l_1 \vec{W}_1^e = l_1 (\lambda_1^e \vec{\nabla} \lambda_2^e - \lambda_2^e \vec{\nabla} \lambda_1^e) \tag{5.45}$$

$$\vec{N}_2^e = l_2 \vec{W}_2^e = l_2 (\lambda_1^e \vec{\nabla} \lambda_3^e - \lambda_3^e \vec{\nabla} \lambda_1^e) \tag{5.46}$$

$$\vec{N}_3^e = l_3 \vec{W}_3^e = l_3 (\lambda_1^e \vec{\nabla} \lambda_4^e - \lambda_4^e \vec{\nabla} \lambda_1^e) \tag{5.47}$$

$$\vec{N}_4^e = l_4 \vec{W}_4^e = l_4 (\lambda_2^e \vec{\nabla} \lambda_3^e - \lambda_3^e \vec{\nabla} \lambda_2^e) \tag{5.48}$$

$$\vec{N}_5^e = l_5 \vec{W}_5^e = l_5 (\lambda_4^e \vec{\nabla} \lambda_2^e - \lambda_2^e \vec{\nabla} \lambda_4^e) \tag{5.49}$$

$$\vec{N}_6^e = l_6 \vec{W}_6^e = l_6 (\lambda_3^e \vec{\nabla} \lambda_4^e - \lambda_4^e \vec{\nabla} \lambda_2^e). \tag{5.50}$$

Die approbierte gedruckte Originalversion dieser Dissertation ist an der TU Wien Bibliothek verfügbar.
The approved original version of this doctoral thesis is available in print at TU Wien Bibliothek.

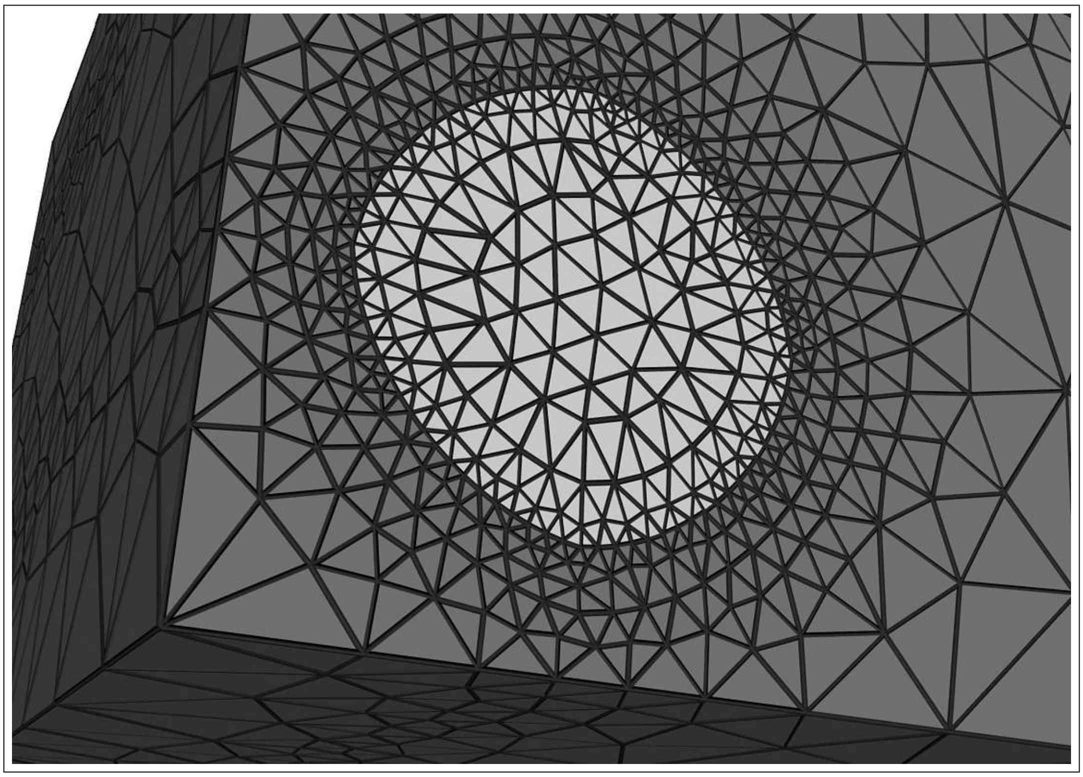

Figure 5.4: The conductor entry.

The performed multiplication with l_i delivers the normalized and dimensionless edge functions N_i.

The edge functions $\vec{N}_1^e$ and $\vec{N}_6^e$ are visualized in Fig. <5.5> and Fig. <5.6>, respectively.

If the field in the tetrahedral element (for instance the magnetic field $\vec{H}^e$) is given by

$$\vec{H}^e = \sum_{i=1}^{6} c_i \vec{N}_i^e, \tag{5.51}$$

the coefficient c_i corresponds to the tangential component of the field $\vec{H}^e$ on the Edge i. An example of the field in the element is depicted in Fig. <5.7> where all coefficients are set to 1.

5.2.3 Assembling

Similarly as presented in Section 4.1 the matrices $[A]$, $[B]$ and $[C]$ and the right hand side vector $\{b\}$ are assembled from the corresponding element matrices for each tetrahedron Fig. <4.7>. For the first term on the right hand side of (5.38) the rotor operator must

Die approbierte gedruckte Originalversion dieser Dissertation ist an der TU Wien Bibliothek verfügbar.
The approved original version of this doctoral thesis is available in print at TU Wien Bibliothek.

Table 5.1: Tetrahedral Element Edge Definition.

Edge	**Node 1**	**Node 2**
1	1	2
2	1	3
3	1	4
4	2	3
5	4	2
6	3	4

be applied to the element edge functions $\vec{N}_i^e$. For the first one, $\vec{N}_1^e$, it can be written

$$\begin{aligned}\vec{\nabla} \times \vec{N}_1^e &= 2l_1 \vec{\nabla}\lambda_1^e \times \vec{\nabla}\lambda_2^e = \\ &= 2l_1 \frac{\vec{r}_5 \times \vec{r}_6}{6V_e} \times \frac{\vec{r}_3 \times \vec{r}_6}{6V_e} = \frac{2l_1}{36{V_e}^2}\vec{r}_6 \left[\vec{r}_3 \cdot (\vec{r}_6 \times \vec{r}_5)\right] = \frac{2l_1}{36{V_e}^2}\vec{r}_6 6V_e = \frac{l_1}{3V_e}\vec{r}_6.\end{aligned}$$

Analogously the rotor operator of all element edge functions can be expressed by

$$\vec{\nabla} \times \vec{N}_i^e = \frac{l_i}{3V_e}\,\vec{r}_{7-i}, \quad i \in [1;6]. \tag{5.52}$$

Thus the element matrix of the first term on the right hand side of (5.38) can be given by the expression

$$\begin{aligned} S_{ij}^e &= \int\limits_{\mathcal{V}_e} \left(\vec{\nabla} \times \vec{N}_i^e\right) \cdot \left(\frac{1}{\gamma}\vec{\nabla} \times \vec{N}_j^e\right) \mathrm{d}V = \\ &= \frac{1}{\gamma}\left(\vec{\nabla} \times \vec{N}_i^e\right) \cdot \left(\vec{\nabla} \times \vec{N}_j^e\right) V_e = \frac{l_i\, l_j}{9\gamma V_e}\; \vec{r}_{7-i} \cdot \vec{r}_{7-j}, \quad i \in [1;6],\; j \in [1;6]. \end{aligned} \tag{5.53}$$

In (5.53) it is assumed that γ is scalar and constant at each element. A constant elemental γ is not an essential restriction, since the simulation domain is discretized sufficiently fine, which is anyway necessary for an accurate result. In regions, in which it is expected that $1/\gamma$ will seriously change, it can be required that a finer mesh is used.

For the second term of (5.38) the following elemental matrix is regarded

$$M_{ij}^e = \int\limits_{\mathcal{V}_e} \mu \vec{N}_i^e \cdot \vec{N}_j^e \,\mathrm{d}V. \tag{5.54}$$

Die approbierte gedruckte Originalversion dieser Dissertation ist an der TU Wien Bibliothek verfügbar.
The approved original version of this doctoral thesis is available in print at TU Wien Bibliothek.
TU WIEN Bibliothek Your knowledge hub

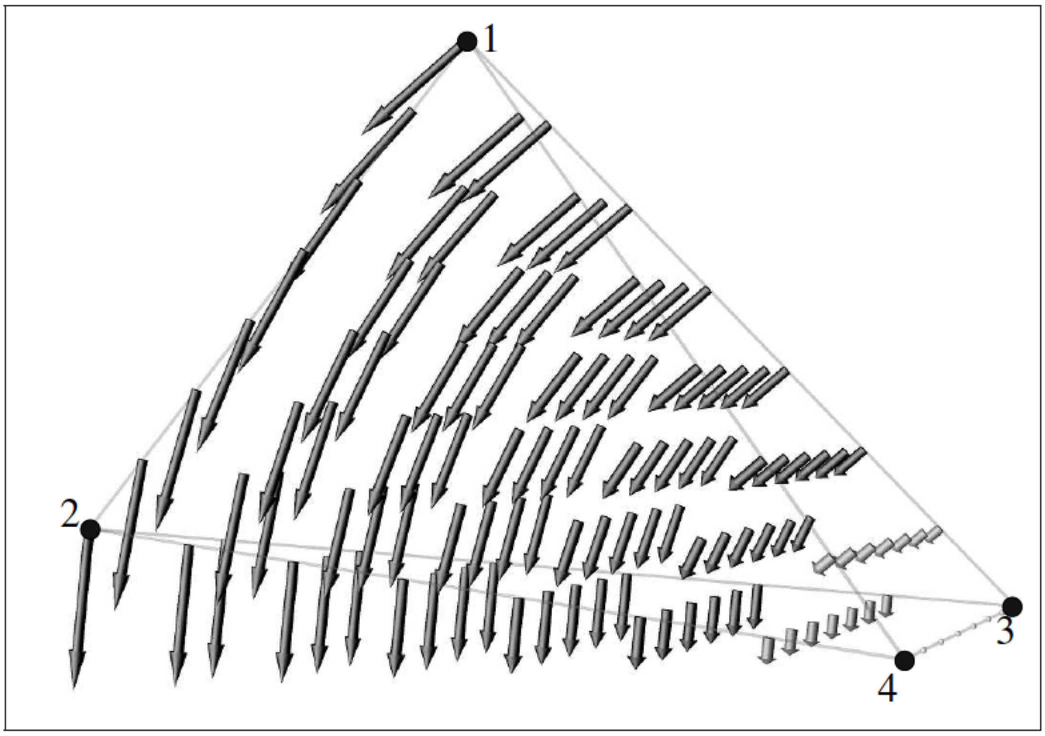

Figure 5.5: The shape function along Edge 12.

As an example the member with $i = 1$ and $j = 2$ of the elemental matrix $[M^e]$ is calculated to demonstrate the proceeding:

$$
\begin{aligned}
M^e_{12} &= \int\limits_{\mathcal{V}_e} \mu \vec{N}^e_1 \cdot \vec{N}^e_2 \,\mathrm{d}V = \mu\, l_1\, l_2 \int\limits_{\mathcal{V}_e} (\lambda^e_1 \vec{\nabla}\lambda^e_2 - \lambda^e_2 \vec{\nabla}\lambda^e_1) \cdot (\lambda^e_1 \vec{\nabla}\lambda^e_3 - \lambda^e_3 \vec{\nabla}\lambda^e_1) \,\mathrm{d}V \\
\frac{M^e_{12}}{\mu\, l_1\, l_2} &= \vec{\nabla}\lambda^e_2 \cdot \vec{\nabla}\lambda^e_3 \int\limits_{\mathcal{V}_e} (\lambda^e_1)^2 \,\mathrm{d}V - \vec{\nabla}\lambda^e_1 \cdot \vec{\nabla}\lambda^e_2 \int\limits_{\mathcal{V}_e} \lambda^e_1 \lambda^e_3 \,\mathrm{d}V - \\
&\quad - \vec{\nabla}\lambda^e_1 \cdot \vec{\nabla}\lambda^e_3 \int\limits_{\mathcal{V}_e} \lambda^e_1 \lambda^e_2 \,\mathrm{d}V + \left(\vec{\nabla}\lambda^e_1\right)^2 \int\limits_{\mathcal{V}_e} \lambda^e_2 \lambda^e_3 \,\mathrm{d}V.
\end{aligned}
\tag{5.55}
$$

For the evaluation of the above expression it is necessary to calculate the integral

$$
\int\limits_{\mathcal{V}_e} \lambda^e_i \lambda^e_j \,\mathrm{d}V, \; i \in [1;4] \; j \in [1;4].
$$

For this purpose the domain transformation (A.9) and (A.10) discussed in Appendix A is used

$$
\int\limits_{\mathcal{V}_e} \lambda^e_i \lambda^e_j \,\mathrm{d}V = \int\limits_0^1 \int\limits_0^{1-\lambda^e_1} \int\limits_0^{1-\lambda^e_1-\lambda^e_2} \lambda^e_i \lambda^e_j \, J \, d\lambda^e_3 \, d\lambda^e_2 \, d\lambda^e_1. \tag{5.56}
$$

Die approbierte gedruckte Originalversion dieser Dissertation ist an der TU Wien Bibliothek verfügbar.
The approved original version of this doctoral thesis is available in print at TU Wien Bibliothek.

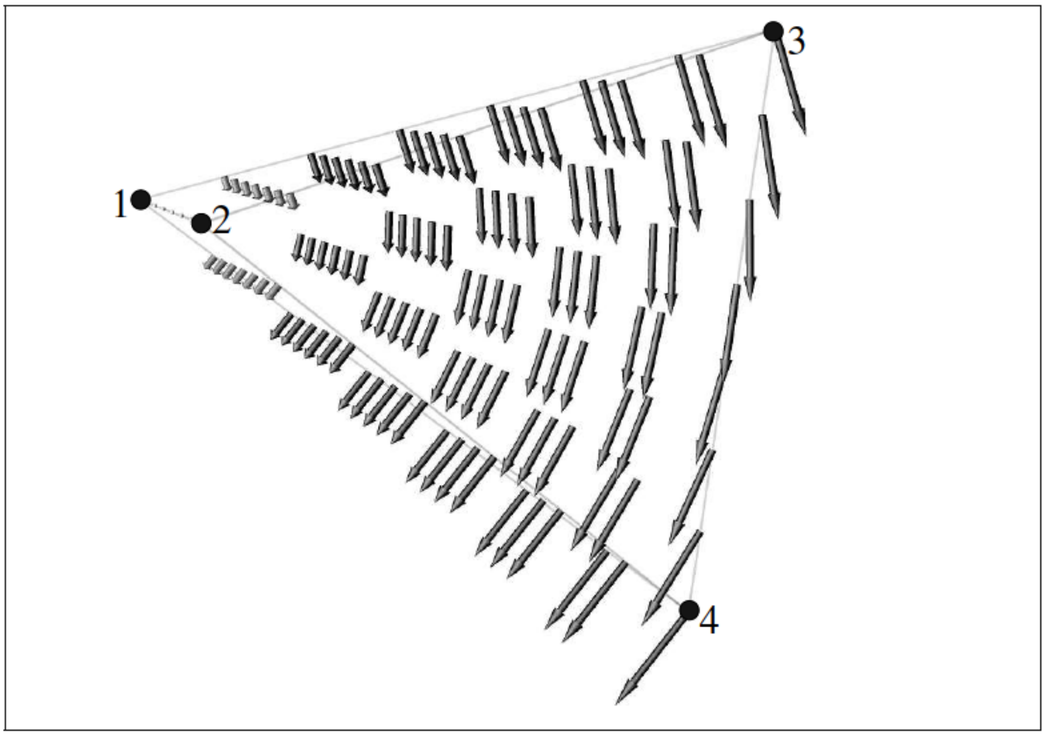

Figure 5.6: The shape function along Edge 34.

Using (4.79) the Jacobi matrix is given by the expression

$$J = \begin{vmatrix} \frac{\partial x}{\partial \lambda_1^e} & \frac{\partial x}{\partial \lambda_2^e} & \frac{\partial x}{\partial \lambda_3^e} \\ \frac{\partial y}{\partial \lambda_1^e} & \frac{\partial y}{\partial \lambda_2^e} & \frac{\partial y}{\partial \lambda_3^e} \\ \frac{\partial z}{\partial \lambda_1^e} & \frac{\partial z}{\partial \lambda_2^e} & \frac{\partial z}{\partial \lambda_3^e} \end{vmatrix} = 6V_e. \tag{5.57}$$

Thus the integral above results in

$$\int\limits_{\mathcal{V}_e} \lambda_i^e \lambda_j^e \, \mathrm{d}V = \left\{ \begin{array}{ll} \frac{V_e}{20}, & i \neq j \\ \frac{V_e}{10}, & i = j \end{array} \right. , \quad i \in [1;4], \; j \in [1;4] \tag{5.58}$$

and M_{12}^e can now be expressed as

$$M_{12}^e = \frac{\mu \, l_1 \, l_2 \, V_e}{20} (2\vec{\nabla}\lambda_2^e \cdot \vec{\nabla}\lambda_3^e - \vec{\nabla}\lambda_1^e \cdot \vec{\nabla}\lambda_2^e - \vec{\nabla}\lambda_1^e \cdot \vec{\nabla}\lambda_3^e + \vec{\nabla}\lambda_1^e \cdot \vec{\nabla}\lambda_1^e). \tag{5.59}$$

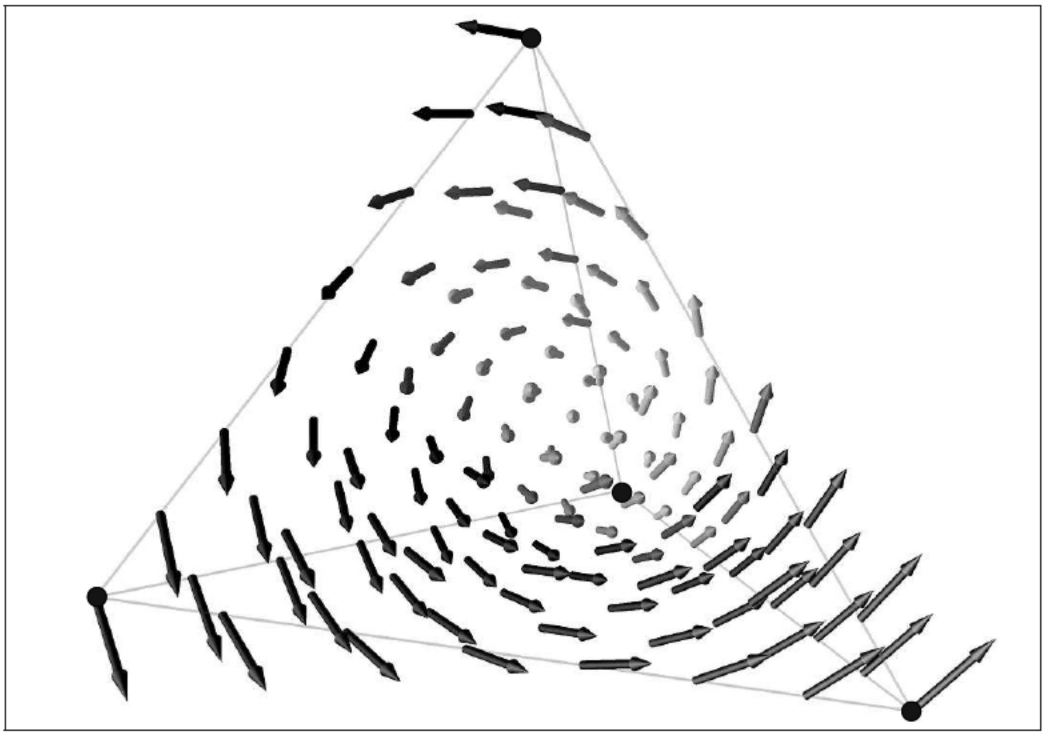

Figure 5.7: The sum of all shape functions in the tetrahedron.

Analogously the element matrix for the six linear edge functions is written as

$$
\begin{aligned}
M_{11}^e &= \frac{\mu\, l_1^2}{360\, V_e}(f_{11} - f_{12} + f_{22}) \\
M_{21}^e = M_{12}^e &= \frac{\mu\, l_1\, l_2}{720\, V_e}(2f_{23} - f_{12} - f_{13} + f_{11}) \\
M_{31}^e = M_{13}^e &= \frac{\mu\, l_1\, l_3}{720\, V_e}(2f_{24} - f_{12} - f_{14} + f_{11}) \\
M_{41}^e = M_{14}^e &= \frac{\mu\, l_1\, l_4}{720\, V_e}(f_{23} - f_{22} - 2f_{13} + f_{12}) \\
M_{51}^e = M_{15}^e &= \frac{\mu\, l_1\, l_5}{720\, V_e}(f_{22} - f_{24} - f_{12} + 2f_{14}) \\
M_{61}^e = M_{16}^e &= \frac{\mu\, l_1\, l_6}{720\, V_e}(f_{24} - f_{23} - f_{14} + f_{13})
\end{aligned}
\qquad (5.60)
$$

Die approbierte gedruckte Originalversion dieser Dissertation ist an der TU Wien Bibliothek verfügbar.
The approved original version of this doctoral thesis is available in print at TU Wien Bibliothek.
TU Bibliothek Your knowledge hub

Die approbierte gedruckte Originalversion dieser Dissertation ist an der TU Wien Bibliothek verfügbar.
The approved original version of this doctoral thesis is available in print at TU Wien Bibliothek.

$$\begin{aligned}
M^e_{22} &= \frac{\mu\, l_2^2}{360\, V_e}(f_{11} - f_{13} + f_{33}) \\
M^e_{32} = M^e_{23} &= \frac{\mu\, l_2\, l_3}{720\, V_e}(2f_{34} - f_{13} - f_{14} + f_{11}) \\
M^e_{42} = M^e_{24} &= \frac{\mu\, l_2\, l_4}{720\, V_e}(f_{33} - f_{23} - f_{13} + 2f_{12}) \\
M^e_{52} = M^e_{25} &= \frac{\mu\, l_2\, l_5}{720\, V_e}(f_{23} - f_{34} - f_{12} + f_{14}) \\
M^e_{62} = M^e_{26} &= \frac{\mu\, l_2\, l_6}{720\, V_e}(f_{34} - f_{33} - 2f_{14} + f_{13})
\end{aligned} \tag{5.61}$$

$$\begin{aligned}
M^e_{33} &= \frac{\mu\, l_3^2}{360\, V_e}(f_{11} - f_{14} + f_{44}) \\
M^e_{43} = M^e_{34} &= \frac{\mu\, l_3\, l_4}{720\, V_e}(f_{34} - f_{24} - f_{13} + f_{12}) \\
M^e_{53} = M^e_{35} &= \frac{\mu\, l_3\, l_5}{720\, V_e}(f_{24} - f_{44} - 2f_{12} + f_{14}) \\
M^e_{63} = M^e_{36} &= \frac{\mu\, l_3\, l_6}{720\, V_e}(f_{44} - f_{34} - f_{14} + 2f_{13})
\end{aligned} \tag{5.62}$$

$$\begin{aligned}
M^e_{44} &= \frac{\mu\, l_4^2}{360\, V_e}(f_{22} - f_{23} + f_{33}) \\
M^e_{54} = M^e_{45} &= \frac{\mu\, l_4\, l_5}{720\, V_e}(f_{23} - 2f_{34} - f_{22} + f_{24}) \\
M^e_{64} = M^e_{46} &= \frac{\mu\, l_4\, l_6}{720\, V_e}(f_{34} - f_{33} - 2f_{24} + f_{23})
\end{aligned} \tag{5.63}$$

$$\begin{aligned}
M^e_{55} &= \frac{\mu\, l_5^2}{360\, V_e}(f_{22} - f_{24} + f_{44}) \\
M^e_{65} = M^e_{56} &= \frac{\mu\, l_5\, l_6}{720\, V_e}(f_{24} - 2f_{23} - f_{44} + f_{34})
\end{aligned} \tag{5.64}$$

$$M^e_{66} = \frac{\mu\, l_6^2}{360\, V_e}(f_{33} - f_{34} + f_{44}) \tag{5.65}$$

with

$$\begin{aligned}
f_{11} &= \vec{r_4}^2\vec{r_6}^2 - (\vec{r_4}\cdot\vec{r_6})^2 \\
f_{21} = f_{12} &= (\vec{r_3}\cdot\vec{r_6})(\vec{r_4}\cdot\vec{r_6}) - (\vec{r_3}\cdot\vec{r_4})\vec{r_6}^2 \\
f_{31} = f_{13} &= (\vec{r_1}\cdot\vec{r_4})(\vec{r_3}\cdot\vec{r_6}) - (\vec{r_3}\cdot\vec{r_4})(\vec{r_1}\cdot\vec{r_6}) \\
f_{41} = f_{14} &= (\vec{r_1}\cdot\vec{r_6})\vec{r_4}^2 - (\vec{r_1}\cdot\vec{r_4})(\vec{r_4}\cdot\vec{r_6}) \\
f_{22} &= \vec{r_3}^2\vec{r_6}^2 - (\vec{r_3}\cdot\vec{r_6})^2 \\
f_{32} = f_{23} &= (\vec{r_1}\cdot\vec{r_6})\vec{r_3}^2 - (\vec{r_1}\cdot\vec{r_3})(\vec{r_3}\cdot\vec{r_6}) \\
f_{42} = f_{24} &= (\vec{r_1}\cdot\vec{r_3})(\vec{r_4}\cdot\vec{r_6}) - (\vec{r_3}\cdot\vec{r_4})(\vec{r_1}\cdot\vec{r_6}) \\
f_{33} &= \vec{r_1}^2\vec{r_3}^2 - (\vec{r_1}\cdot\vec{r_3})^2 \\
f_{43} = f_{34} &= (\vec{r_1}\cdot\vec{r_3})(\vec{r_1}\cdot\vec{r_4}) - \vec{r_1}^2(\vec{r_3}\cdot\vec{r_4}) \\
f_{44} &= \vec{r_1}^2\vec{r_4}^2 - (\vec{r_1}\cdot\vec{r_4})^2.
\end{aligned} \tag{5.66}$$

Thus the entries of the matrix $[A]$ are given by

$$A_{ij} = S_{ij} + \jmath\omega M_{ij}. \tag{5.67}$$

The matrix with the partial derivatives is usually called stiffness matrix and is notated with $[S]$. The matrix which does not contain any derivatives is the mass matrix $[M]$. However, the designations $[S]$ and $[M]$ come from the field of mechanics and bear on scalar fields. Analogously in (5.67) the same notations $[S]$ and $[M]$ are used for the derivative and non-derivative matrix, this time for the vector field $\vec{H}$.

For element wise assembling of the matrix $[B]$ from (5.39), it is also assumed that the magnetic permeability μ is constant in each element. The first entry is calculated in the following way

$$\begin{aligned}
B_{11}^e &= \mu \int\limits_{\mathcal{V}_e} \vec{N}_1^e \cdot \vec{\nabla}\lambda_1^e \,\mathrm{d}V = \mu \int\limits_{\mathcal{V}_e} l_1(\lambda_1^e\vec{\nabla}\lambda_2^e - \lambda_2^e\vec{\nabla}\lambda_1^e)\cdot\vec{\nabla}\lambda_1^e \,\mathrm{d}V = \\
&= \mu\, l_1 \left[\vec{\nabla}\lambda_1^e \cdot \vec{\nabla}\lambda_2^e \int\limits_{\mathcal{V}_e} \lambda_1^e \,\mathrm{d}V - \left(\vec{\nabla}\lambda_1^e\right)^2 \int\limits_{\mathcal{V}_e} \lambda_2^e \,\mathrm{d}V \right].
\end{aligned} \tag{5.68}$$

The remaining entries are obtained analogously. The integral expressions in (5.68) are computed using the integral domain transformation (A.9) and (A.10) from Appendix A, where the Jacobi matrix is calculated from (4.79) and given by (5.57)

$$\int\limits_{\mathcal{V}_e} \lambda_i^e \,\mathrm{d}V = 6V_e \int\limits_0^1 \int\limits_0^{1-\lambda_1^e} \int\limits_0^{1-\lambda_1^e-\lambda_2^e} \lambda_i^e \, d\lambda_3^e \, d\lambda_2^e \, d\lambda_1^e = \frac{V_e}{4},\ i \in [1;4]. \tag{5.69}$$

Die approbierte gedruckte Originalversion dieser Dissertation ist an der TU Wien Bibliothek verfügbar.
The approved original version of this doctoral thesis is available in print at TU Wien Bibliothek.
TU WIEN Bibliothek Your knowledge hub

Die approbierte gedruckte Originalversion dieser Dissertation ist an der TU Wien Bibliothek verfügbar.
The approved original version of this doctoral thesis is available in print at TU Wien Bibliothek.
TU WIEN Bibliothek Your knowledge hub

Now the entries of the element matrix B^e_{ij} can be expressed as

$$\begin{aligned}
B^e_{1j} &= \frac{\mu\, l_1}{144\, V_e}(f_{2j} - f_{1j}) \\
B^e_{2j} &= \frac{\mu\, l_2}{144\, V_e}(f_{3j} - f_{1j}) \\
B^e_{3j} &= \frac{\mu\, l_3}{144\, V_e}(f_{4j} - f_{1j}) \\
B^e_{4j} &= \frac{\mu\, l_4}{144\, V_e}(f_{3j} - f_{2j}) \\
B^e_{5j} &= \frac{\mu\, l_5}{144\, V_e}(f_{2j} - f_{4j}) \\
B^e_{6j} &= \frac{\mu\, l_6}{144\, V_e}(f_{4j} - f_{3j}), \quad j \in [1;4],
\end{aligned} \tag{5.70}$$

where f_{ij} are given by (5.66).

The matrix $[C]$ from (5.40) is assembled from the element matrix $[C]^e$. The entries of the element matrix C^e_{ij} are obtained from (5.40)

$$C^e_{ij} = \jmath\omega\mu\, \vec{\nabla}\lambda^e_i \cdot \vec{\nabla}\lambda^e_j\, V_e = \frac{\jmath\omega\mu}{36\, V_e} f_{ij}, \;\; i \in [1;4], \;\; j \in [1;4]. \tag{5.71}$$

5.3 Two-Dimensional Vector Finite Element Method

The two-dimensional case is, of course, very similar to the three-dimensional one. Equations (5.35) and (5.36) correspond to

$$\int\limits_{\mathcal{A}} \left(\vec{\nabla} \times \vec{N}_i\right) \cdot \left(\frac{1}{\gamma}\vec{\nabla} \times \vec{H}_1\right) \mathrm{d}A + \jmath\omega \int\limits_{\mathcal{A}} \mu\vec{N}_i \cdot \vec{H}_1\, \mathrm{d}A - \jmath\omega \int\limits_{\mathcal{A}} \mu\vec{N}_i \cdot \vec{\nabla}\psi\, \mathrm{d}A = 0 \tag{5.72}$$

$$\int\limits_{\mathcal{A}} \vec{\nabla}\lambda_i \cdot \left(\mu\vec{H}_1\right) \mathrm{d}A - \int\limits_{\mathcal{A}} \vec{\nabla}\lambda_i \cdot \left(\mu\vec{\nabla}\psi\right) \mathrm{d}A = 0. \tag{5.73}$$

The boundary $\partial\mathcal{A}$ of the two-dimensional domain $\mathcal{A}$ is divided into a Dirichlet boundary $\mathcal{C}_{D1}$ and a Neumann boundary $\mathcal{C}_{N1}$ for (5.72) and into a Dirichlet boundary $\mathcal{C}_{D2}$ and a Neumann boundary $\mathcal{C}_{N2}$ for (5.73)

$$\partial\mathcal{A} = \mathcal{C}_{D1} + \mathcal{C}_{N1}, \quad \partial\mathcal{A} = \mathcal{C}_{D2} + \mathcal{C}_{N2}.$$

The Dirichlet boundary conditions define values for ψ on the nodes belonging to the Dirichlet boundary $\mathcal{C}_{D2}$ or for the tangential component of $\vec{H}_1$ on the edges belonging to the Dirichlet boundary $\mathcal{C}_{D1}$. The finite element analysis is performed as for the three-dimensional case: The unknown functions in (5.72) and (5.73) are substituted by their approximations, the corresponding residua are weighted by vector and scalar trial

Die approbierte gedruckte Originalversion dieser Dissertation ist an der TU Wien Bibliothek verfügbar.
The approved original version of this doctoral thesis is available in print at TU Wien Bibliothek.
TU WIEN Bibliothek Your knowledge hub

functions, and the weak formulation (the law of Gauß) is applied. Thereby the boundary conditions on $\mathcal{C}_{N1}$ and $\mathcal{C}_{N2}$ arise analogously to (5.29) and (5.31) and read

$$f_{N1} = \int\limits_{\mathcal{C}_{N1}} \vec{n} \cdot \left[\vec{N}_i \times \left(\frac{1}{\gamma}\vec{\nabla} \times \vec{H}_1\right)\right] \mathrm{d}s = \int\limits_{\mathcal{C}_{N1}} \vec{N}_i \cdot \left(\vec{E} \times \vec{n}\right) \mathrm{d}s \quad \text{and} \tag{5.74}$$

$$f_{N2} = \int\limits_{\mathcal{C}_{N2}} \vec{n} \cdot \left\{\lambda_i \left[\mu(\vec{H}_1 - \vec{\nabla}\psi)\right]\right\} \mathrm{d}s = \int\limits_{\mathcal{C}_{N2}} \lambda_i \, \vec{n} \cdot \vec{B} \, \mathrm{d}s. \tag{5.75}$$

Often the shape and the dimensions of the simulation domain are chosen to assume the boundary conditions f_{N1} and f_{N2} are zero. For example this is the case, if the electric field $\vec{E}$ is normal to the Neumann boundary $\mathcal{C}_{N1}$ or if the magnetic flux $\vec{B}$ has no normal component to the Neumann boundary $\mathcal{C}_{N2}$, or if the simulation domain is sufficiently large to assume that $\vec{E} \times \vec{n}$ is zero on $\mathcal{C}_{N1}$ and $\vec{n} \cdot \vec{B}$ is zero on $\mathcal{C}_{N2}$. If the boundary conditions f_{N1} and f_{N2} have to be considered, for example to combine the finite element analysis with the boundary element method, the corresponding element matrices are calculated in the Appendix in Section B.1, Subsection B.2.1 and Subsection B.2.2.

The domain is discretized in triangular elements and the boundary in curves, respectively.

5.3.1 Linear Vector Shape Functions on a Triangular Elements

The following in this subsection refers to the triangular element from (Fig. <4.1>). The field in the element is interpolated similarly as for the three-dimensional case by edge functions. Since there are three edges in the triangular element three interpolation functions are given

$$\vec{N}^e_{12} = l_{12}(\lambda^e_1 \vec{\nabla}\lambda^e_2 - \lambda^e_2 \vec{\nabla}\lambda^e_1) \tag{5.76}$$

$$\vec{N}^e_{23} = l_{23}(\lambda^e_2 \vec{\nabla}\lambda^e_3 - \lambda^e_3 \vec{\nabla}\lambda^e_2) \tag{5.77}$$

$$\vec{N}^e_{31} = l_{31}(\lambda^e_3 \vec{\nabla}\lambda^e_1 - \lambda^e_1 \vec{\nabla}\lambda^e_3). \tag{5.78}$$

The same properties as for the three-dimensional vector element functions can be proved for the two-dimensional ones. Without loss of generality Edge 12 is used to prove the properties of the edge functions. The divergence of a vector edge function is zero, i.e.

$$\vec{\nabla} \cdot \vec{N}^e_{12} = l_{12}(\vec{\nabla}\lambda^e_1 \cdot \vec{\nabla}\lambda^e_2 - \vec{\nabla}\lambda^e_2 \cdot \vec{\nabla}\lambda^e_1) = 0. \tag{5.79}$$

For the rotor of a vector edge function it can be written

$$\vec{\nabla} \times \vec{N}^e_{12} = l_{12}(\vec{\nabla}\lambda^e_1 \times \vec{\nabla}\lambda^e_2 - \vec{\nabla}\lambda^e_2 \times \vec{\nabla}\lambda^e_1) = 2 l_{12} \vec{\nabla}\lambda^e_1 \times \vec{\nabla}\lambda^e_2. \tag{5.80}$$

Die approbierte gedruckte Originalversion dieser Dissertation ist an der TU Wien Bibliothek verfügbar.
The approved original version of this doctoral thesis is available in print at TU Wien Bibliothek.
TU Bibliothek
WIEN Your knowledge hub

The tangential component of $\vec{N}^e_{12}$ on Edge 23 can be obtained from

$$\vec{N}^e_{12} \cdot \vec{r}_{23} = (\lambda^e_1 \vec{r}_{23}) \cdot \vec{\nabla}\lambda^e_2 - \lambda^e_2(\vec{r}_{23} \cdot \vec{\nabla}\lambda^e_1). \tag{5.81}$$

Since λ^e_1 vanishes on the Edge 23 and $\vec{\nabla}\lambda^e_1$ is perpendicular to $\vec{r}_{23}$, the two terms on the right hand side of (5.81) are zero and $\vec{N}^e_{12}$ has no tangential component on the Edge 23:

$$\vec{N}^e_{12} \cdot \frac{\vec{r}_{23}}{l_{23}} = 0.$$

Analogously it can be shown that $\vec{N}^e_{12}$ has no tangential component on Edge 31 as well. For $\vec{N}^e_{12}$ along the direction of Edge 12 the following expression is applied

$$\begin{aligned}\vec{N}^e_{12} \cdot \frac{\vec{r}_{12}}{l_{12}} &= \lambda^e_1 \vec{r}_{12} \cdot \vec{\nabla}\lambda^e_2 - \lambda^e_2 \vec{r}_{12} \cdot \vec{\nabla}\lambda^e_1 = -\lambda^e_1 \vec{r}_{12} \cdot \frac{\vec{r}_{31} \times \vec{e}_z}{J} + \lambda^e_2 \vec{r}_{12} \cdot \frac{\vec{r}_{23} \times \vec{e}_z}{J} = \\ &= -\lambda^e_1 \frac{\vec{r}_{12} \times \vec{r}_{31}}{J} \cdot \vec{e}_z + \lambda^e_2 \frac{\vec{r}_{12} \times \vec{r}_{23}}{J} \cdot \vec{e}_z = \lambda^e_1 + \lambda^e_2.\end{aligned}$$

Since λ^e_3 is zero and therefore $\lambda^e_1+\lambda^e_2$ is one on Edge 12, the tangential component of $\vec{N}^e_{12}$ on Edge 12 is one. The vector function $\vec{H}_{12}$ has a constant tangential component $\lambda^e_1+\lambda^e_2$ only along its corresponding Edge 12. Along the remaining edges this function does not have a tangential component. Similarly this characteristics applies also to the remaining functions $\vec{H}_{23}$ and $\vec{H}_{31}$. Hence it follows that in an approach of the kind

$$\vec{f}(r) = c_1 \vec{N}^e_{12} + c_2 \vec{N}^e_{23} + c_3 \vec{N}^e_{31}$$

the arbitrary coefficients c_1, c_2 and c_3 are to be regarded as values of the projection of $\vec{f}(r)$ in the possible edge directions, respectively. This fact justifies the name edge function or edge element.

It is not simple to imagine, how the edge functions look like. The edge function $\vec{N}^e_{12}$ is visualized in Fig. <5.8>. Fig. <5.9> depicts function $\vec{f}(r)$ for all coefficients set to one.

5.3.2 Assembling

The two-dimensioanl case leads to a linear equation system similar to (5.37). The submatrix $[A]$ is written in the form (5.67). With γ constant in each element $[S]^e$ is given by

$$\begin{aligned}S^e_{ij} &= \frac{1}{\gamma} \int\limits_{\mathcal{A}_e} \left(\vec{\nabla} \times \vec{N}^e_i\right) \cdot \left(\vec{\nabla} \times \vec{N}^e_j\right) \mathrm{d}A = \frac{1}{\gamma} \left(\vec{\nabla} \times \vec{N}^e_i\right) \cdot \left(\vec{\nabla} \times \vec{N}^e_j\right) \int\limits_{\mathcal{A}_e} \mathrm{d}A = \\ &= \frac{1}{\gamma} \left(\vec{\nabla} \times \vec{N}^e_i\right) \cdot \left(\vec{\nabla} \times \vec{N}^e_j\right) F_e, \;\; i \in [1;3], \;\; j \in [1;3],\end{aligned} \tag{5.82}$$

Die approbierte gedruckte Originalversion dieser Dissertation ist an der TU Wien Bibliothek verfügbar.
The approved original version of this doctoral thesis is available in print at TU Wien Bibliothek.
TU WIEN Bibliothek Your knowledge hub

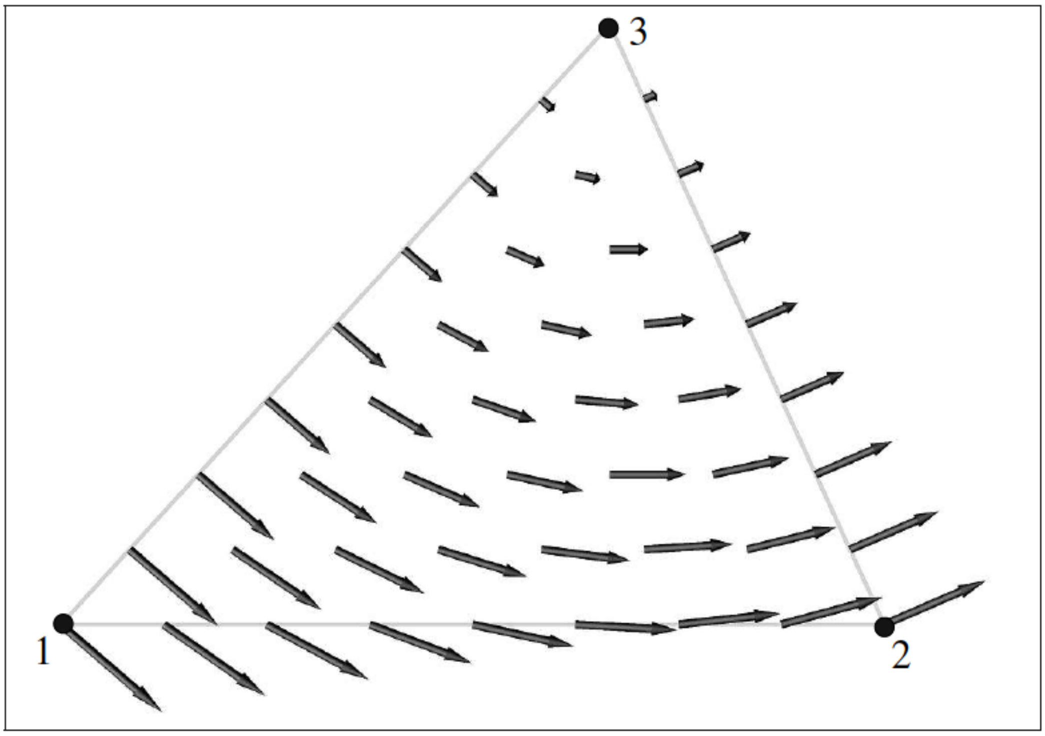

Figure 5.8: The shape function along Edge 12.

where the rotor terms are calculated in the following manner

$$\vec{\nabla} \times \vec{N}_1^e = 2l_{12}\left(\vec{\nabla}\lambda_1^e \times \vec{\nabla}\lambda_2^e\right) = 2l_{12}\frac{\vec{r}_{23} \times \vec{e}_z}{2F_e} \times \frac{\vec{r}_{31} \times \vec{e}_z}{2F_e} = \frac{l_{12}}{F_e}\vec{e}_z \tag{5.83}$$

$$\vec{\nabla} \times \vec{N}_2^e = \frac{l_{23}}{F_e}\vec{e}_z \qquad \vec{\nabla} \times \vec{N}_3^e = \frac{l_{31}}{F_e}\vec{e}_z. \tag{5.84}$$

Thus $[S]^e$ becomes

$$S_{11}^e = \frac{1}{\gamma}\left(\vec{\nabla} \times \vec{N}_1^e\right) \cdot \left(\vec{\nabla} \times \vec{N}_1^e\right) F_e = \frac{l_{12}^2}{\gamma F_e} \tag{5.85}$$

$$S_{21}^e = S_{12}^e = \frac{l_{12}l_{23}}{\gamma F_e} \tag{5.86}$$

$$S_{31}^e = S_{13}^e = \frac{l_{12}l_{31}}{\gamma F_e} \tag{5.87}$$

$$S_{22}^e = \frac{l_{23}^2}{\gamma F_e} \tag{5.88}$$

$$S_{32}^e = S_{23}^e = \frac{l_{23}l_{31}}{\gamma F_e} \tag{5.89}$$

$$S_{33}^e = \frac{l_{33}^2}{\gamma F_e}. \tag{5.90}$$

Die approbierte gedruckte Originalversion dieser Dissertation ist an der TU Wien Bibliothek verfügbar.
The approved original version of this doctoral thesis is available in print at TU Wien Bibliothek.
TU WIEN Bibliothek Your knowledge hub

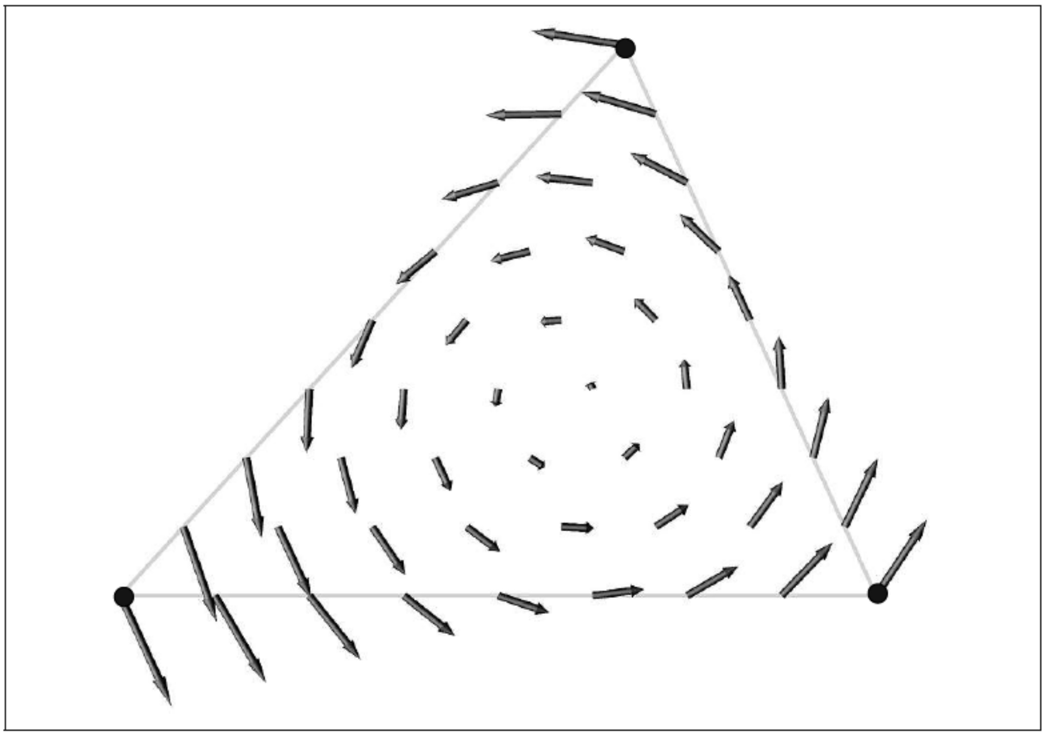

Figure 5.9: The sum of the shape functions in the triangle.

For element-wise constant μ the entries from $[M]^e$ are obtained from

$$M^e_{ij} = \mu \int\limits_{\mathcal{A}_e} \vec{N}^e_i \cdot \vec{N}^e_j \,\mathrm{d}A, \;\; i \in [1;3], \;\; j \in [1;3]. \tag{5.91}$$

One entry calculation is demonstrated in detail

$$M^e_{11} = \mu \int\limits_{\mathcal{A}_e} \vec{N}^e_1 \cdot \vec{N}^e_1 \,\mathrm{d}A = \mu \int\limits_{\mathcal{A}_e} \left[l_{12} \left(\lambda^e_1 \vec{\nabla} \lambda^e_2 - \lambda^e_2 \vec{\nabla} \lambda^e_1 \right) \right] \cdot \left[l_{12} \left(\lambda^e_1 \vec{\nabla} \lambda^e_2 - \lambda^e_2 \vec{\nabla} \lambda^e_1 \right) \right] \mathrm{d}A =$$

$$= \mu \, l_{12}^2 \left[\left(\vec{\nabla} \lambda^e_2 \right)^2 \int\limits_{\mathcal{A}_e} (\lambda^e_1)^2 \,\mathrm{d}A - 2 \vec{\nabla} \lambda^e_1 \cdot \vec{\nabla} \lambda^e_2 \int\limits_{\mathcal{A}_e} \lambda^e_1 \lambda^e_2 \,\mathrm{d}A + \left(\vec{\nabla} \lambda^e_1 \right)^2 \int\limits_{\mathcal{A}_e} (\lambda^e_2)^2 \,\mathrm{d}A \right].$$

The arrising integrals are solved as follows

$$\begin{aligned} \int\limits_{\mathcal{A}_e} (\lambda^e_1)^2 \,\mathrm{d}A &= 2F_e \int\limits_0^1 \int\limits_0^{1-\lambda^e_1} (\lambda^e_1)^2 \, d\lambda^e_2 \, d\lambda^e_1 = 2F_e \int\limits_0^1 (\lambda^e_1)^2 \int\limits_0^{1-\lambda^e_1} d\lambda^e_2 \, d\lambda^e_1 = \\ &= 2F_e \int\limits_0^1 (\lambda^e_1)^2 \left(1 - \lambda^e_1\right) \, d\lambda^e_1 = \frac{F_e}{6} \end{aligned} \tag{5.92}$$

Die approbierte gedruckte Originalversion dieser Dissertation ist an der TU Wien Bibliothek verfügbar.
The approved original version of this doctoral thesis is available in print at TU Wien Bibliothek.

$$\begin{aligned}\int_{\mathcal{A}_e} \lambda_1^e\lambda_2^e\,\mathrm{d}A &= 2F_e \int_0^1 \int_0^{1-\lambda_1^e} \lambda_1^e\lambda_2^e\, d\lambda_2^e\, d\lambda_1^e = 2F_e\int_0^1 \lambda_1^e \int_0^{1-\lambda_1^e} \lambda_2^e\, d\lambda_2^e\, d\lambda_1^e = \\ &= 2F_e \int_0^1 \lambda_1^e \frac{(1-\lambda_1^e)^2}{2}\, d\lambda_1^e = \frac{F_e}{12},\end{aligned} \tag{5.93}$$

using the integral domain transformation Appendix A. Generally it can be written

$$\int_{\mathcal{A}_e} \lambda_i^e\lambda_j^e\,\mathrm{d}A = \begin{cases} \frac{F_e}{6} & \text{for } i=j \\ \frac{F_e}{12} & \text{for } i\neq j \end{cases} \qquad j\in[1;3],\ j\in[1;3]. \tag{5.94}$$

In a similar manner all entries of $[M]^e$ are given

$$M_{11}^e = \frac{\mu\, l_{12}^2}{24\, F_e}\left(\vec{r}_{23}\cdot\vec{r}_{23} - \vec{r}_{23}\cdot\vec{r}_{31} + \vec{r}_{31}\cdot\vec{r}_{31}\right) \tag{5.95}$$

$$M_{21}^e = M_{12}^e = \frac{\mu\, l_{12}\, l_{23}}{48\, F_e}\left(\vec{r}_{31}\cdot\vec{r}_{12} - \vec{r}_{31}\cdot\vec{r}_{31} - 2\,\vec{r}_{23}\cdot\vec{r}_{12} + \vec{r}_{23}\cdot\vec{r}_{31}\right) \tag{5.96}$$

$$M_{31}^e = M_{13}^e = \frac{\mu\, l_{12}\, l_{31}}{48\, F_e}\left(\vec{r}_{23}\cdot\vec{r}_{31} - 2\,\vec{r}_{31}\cdot\vec{r}_{12} - \vec{r}_{23}\cdot\vec{r}_{23} + \vec{r}_{23}\cdot\vec{r}_{12}\right) \tag{5.97}$$

$$M_{22}^e = \frac{\mu\, l_{23}^2}{24\, F_e}\left(\vec{r}_{12}\cdot\vec{r}_{12} - \vec{r}_{12}\cdot\vec{r}_{31} + \vec{r}_{31}\cdot\vec{r}_{31}\right) \tag{5.98}$$

$$M_{32}^e = M_{23}^e = \frac{\mu\, l_{23}\, l_{31}}{48\, F_e}\left(\vec{r}_{23}\cdot\vec{r}_{12} - \vec{r}_{12}\cdot\vec{r}_{12} - 2\,\vec{r}_{23}\cdot\vec{r}_{31} + \vec{r}_{31}\cdot\vec{r}_{12}\right) \tag{5.99}$$

$$M_{33}^e = \frac{\mu\, l_{31}^2}{24\, F_e}\left(\vec{r}_{12}\cdot\vec{r}_{12} - \vec{r}_{12}\cdot\vec{r}_{23} + \vec{r}_{23}\cdot\vec{r}_{23}\right). \tag{5.100}$$

The entries of $[B]$ are expressed as

$$B_{ij}^e = -\jmath\omega\mu \int_{\mathcal{A}_e} \vec{N}_i^e\cdot\vec{\nabla}\lambda_j^e\,\mathrm{d}A,\ i\in[1;3],\ j\in[1;3]. \tag{5.101}$$

The entry B_{11}^e is calculated in detail as

$$\begin{aligned}B_{11}^e &= -\jmath\omega\mu \int_{\mathcal{A}_e} \vec{N}_1^e\cdot\vec{\nabla}\lambda_1^e\,\mathrm{d}A = -\jmath\omega\mu \int_{\mathcal{A}_e} \left[l_{12}\left(\lambda_1^e\vec{\nabla}\lambda_2^e - \lambda_2^e\vec{\nabla}\lambda_1^e\right)\right]\cdot\vec{\nabla}\lambda_1^e\,\mathrm{d}A = \\ &= -\jmath\omega\mu l_{12}\left(\vec{\nabla}\lambda_1^e\cdot\vec{\nabla}\lambda_2^e\int_{\mathcal{A}_e}\lambda_1^e\,\mathrm{d}A - \vec{\nabla}\lambda_1^e\cdot\vec{\nabla}\lambda_1^e\int_{\mathcal{A}_e}\lambda_2^e\,\mathrm{d}A\right).\end{aligned} \tag{5.102}$$

For the integral terms the integral domain transformation from Appendix A is used again to obtain

$$\int\limits_{\mathcal{A}_e} \lambda_i^e \, \mathrm{d}A = \frac{F_e}{3}, \; i \in [1;3]. \tag{5.103}$$

Thus $[B]^e$ is given by

$$B_{11}^e = -\jmath\omega\mu l_{12} \left(\frac{\vec{r}_{23} \times \vec{e}_z}{2F_e} \cdot \frac{\vec{r}_{31} \times \vec{e}_z}{2F_e} - \frac{\vec{r}_{23} \times \vec{e}_z}{2F_e} \cdot \frac{\vec{r}_{23} \times \vec{e}_z}{2F_e} \right) \frac{F_e}{3} = \tag{5.104}$$

$$= -\jmath\omega \frac{\mu l_{12}}{12F_e} \left(\vec{r}_{23} \cdot \vec{r}_{31} - \vec{r}_{23} \cdot \vec{r}_{23} \right)$$

$$B_{12}^e = -\jmath\omega \frac{\mu l_{12}}{12F_e} \left(\vec{r}_{31} \cdot \vec{r}_{31} - \vec{r}_{31} \cdot \vec{r}_{23} \right) \tag{5.105}$$

$$B_{13}^e = -\jmath\omega \frac{\mu l_{12}}{12F_e} \left(\vec{r}_{12} \cdot \vec{r}_{31} - \vec{r}_{12} \cdot \vec{r}_{23} \right) \tag{5.106}$$

$$B_{21}^e = -\jmath\omega \frac{\mu l_{23}}{12F_e} \left(\vec{r}_{23} \cdot \vec{r}_{12} - \vec{r}_{23} \cdot \vec{r}_{31} \right) \tag{5.107}$$

$$B_{22}^e = -\jmath\omega \frac{\mu l_{23}}{12F_e} \left(\vec{r}_{31} \cdot \vec{r}_{12} - \vec{r}_{31} \cdot \vec{r}_{31} \right) \tag{5.108}$$

$$B_{23}^e = -\jmath\omega \frac{\mu l_{23}}{12F_e} \left(\vec{r}_{12} \cdot \vec{r}_{12} - \vec{r}_{12} \cdot \vec{r}_{31} \right) \tag{5.109}$$

$$B_{31}^e = -\jmath\omega \frac{\mu l_{31}}{12F_e} \left(\vec{r}_{23} \cdot \vec{r}_{23} - \vec{r}_{23} \cdot \vec{r}_{12} \right) \tag{5.110}$$

$$B_{32}^e = -\jmath\omega \frac{\mu l_{31}}{12F_e} \left(\vec{r}_{31} \cdot \vec{r}_{23} - \vec{r}_{31} \cdot \vec{r}_{12} \right) \tag{5.111}$$

$$B_{33}^e = -\jmath\omega \frac{\mu l_{31}}{12F_e} \left(\vec{r}_{12} \cdot \vec{r}_{23} - \vec{r}_{12} \cdot \vec{r}_{12} \right). \tag{5.112}$$

Analogously to (4.49) for the element matrix $[C]^e$ one obtains:

$$C_{11}^e = -\jmath\omega \frac{\mu}{4F_e} \vec{r}_{23} \cdot \vec{r}_{23} \tag{5.113}$$

$$C_{12}^e = C_{21}^e = -\jmath\mu \frac{\mu}{4F_e} \vec{r}_{23} \cdot \vec{r}_{31} \tag{5.114}$$

$$C_{13}^e = C_{31}^e = -\jmath\mu \frac{\mu}{4F_e} \vec{r}_{23} \cdot \vec{r}_{12} \tag{5.115}$$

$$C_{22}^e = -\jmath\omega \frac{\mu}{4F_e} \vec{r}_{31} \cdot \vec{r}_{31} \tag{5.116}$$

$$C_{23}^e = C_{32}^e = -\jmath\omega \frac{\epsilon}{4F_e} \vec{r}_{31} \cdot \vec{r}_{12} \tag{5.117}$$

$$C_{33}^e = -\jmath\omega \frac{\mu}{4F_e} \vec{r}_{12} \cdot \vec{r}_{12}. \tag{5.118}$$

Die approbierte gedruckte Originalversion dieser Dissertation ist an der TU Wien Bibliothek verfügbar.
The approved original version of this doctoral thesis is available in print at TU Wien Bibliothek.
TU WIEN Bibliothek Your knowledge hub

Die approbierte gedruckte Originalversion dieser Dissertation ist an der TU Wien Bibliothek verfügbar.
The approved original version of this doctoral thesis is available in print at TU Wien Bibliothek.

Chapter 6

Applications

In this chapter different applications using scalar and vector finite element methods are presented. The first application is used to evaluate the numerical analysis performed by the combination of a vector and scalar finite element method from Section 5.2. The magnetic field and the current density distribution in a coaxial structure are numerically calculated for the quasi-magnetostatic case as discussed in Subsection (5.1.3). As consequence the inductance and the resistance of the structure are obtained. These parameters are calculated also analytically, since the intentionally chosen coaxial structure provides analytical solutions for them. The analytical results agree very precisely with the numerical ones.

The second application handles a structure, for which no analytical or only rough formulas can be given, an on-chip spiral inductor. Its main properties for further electromagnetical analysis, the resistance and the inductance, are obtained numerically. The field distributions are visualized to show the plausibility of the used method.

The third application shows the simplification of the simulation of periodic structures by applying the so called periodic boundary conditions.

6.1 Inductance and Resistance of a Coaxial Structure

The quasi-magnetostatic case from Section 5.2 is well suited for extraction of inductance and resistance of a given structure. Distributed phenomena like proximity and skin effect can also be analyzed. The finite element method on unstructured meshes allows to obtain these parameters in arbitrary regions with complex shape, for which no analytical procedures exist. This section handles intentionally a coaxial structure, for which analytical solutions for the inductance and for the resistance exist. It is interesting to obtain these parameters numerically and compare the results with the analytical calculations, or to evaluate the method from Section 5.2 at least for this special case.

The simulated coaxial structure is shown in Fig. <6.1>. The radius r of the inner conductor is a. The outer conductor has an inner radius b and an outer radius c. The conductor is assumed with $\mu_r = 1$ and $\gamma = 38{\cdot}10^6\ [\Omega m]^{-1}$. The dielectric material between the inner and the outer conductor ($a < r < b$) and outside the outer conductor ($r > c$) has $\mu_r = 1$ and $\gamma = 10^{-4}\ [\Omega m]^{-1}$. On the curve $\mathcal{C}_{in}$ around the inner conductor the magnetic field H_{in} is applied. This is managed by applying $\vec{H}_{in}$ to each edge which belongs to $\mathcal{C}_{in}$ and causes a current I in the inner inductor

$$I = \int\limits_{\mathcal{C}_{in}} \vec{H}_1 \,\mathrm{d}\vec{r} = \int\limits_{\mathcal{C}_{in}} \left(\vec{H} + \vec{\nabla}\psi\right) \mathrm{d}\vec{r} = \int\limits_{\mathcal{C}_{in}} \vec{H} \,\mathrm{d}\vec{r} = H_{in} \sum_i l_i. \tag{6.1}$$

In (6.1) l_i is the length of the i-th edge, which belongs to $\mathcal{C}_{in}$ and the sum applies to all edge lengths building $\mathcal{C}_{in}$. Along $\mathcal{C}_{out}$ (Fig. <6.1>) the magnetic field H_{out} is set consistently to zero. This requires that the current I in the inner conductor given by H_{in} on $\mathcal{C}_{in}$ flows back in the outer conductor. The resulting current density distribution is shown in Fig. <6.2> by directed cones placed in the nodes of the simulation domain. The size and the darkness of the cones correspond to the magnitude of the current density. Note that the current density in the inner conductor is not equal to the one in the outer one, because of the different cross sections of the conductors. The corresponding magnetic field distribution is similarly illustrated in Fig. <6.3>. It is not difficult to see that the curves $\mathcal{C}_{in}$ and $\mathcal{C}_{out}$ represent the Dirichlet boundary for $\vec{H}_1$. The magnetic field on the edges which belong to $\mathcal{C}_{in}$ is H_i and zero on $\mathcal{C}_{out}$, respectively. For the ψ field it is sufficient that a value of ψ is given on one node of the simulation domain. Since the gradient of ψ is determining and not ψ itself, this value can be chosen arbitrarily.

Such a coaxial structure is well suited for the comparison between simulation and analytical results, because analytical formulas can be given. Just homogeneous Neumann boundary conditions (5.30) and (5.32) are exactly satisfied also for finite dimensions (Refer to Fig. <6.3>). The field $\vec{H}$ has no normal component to the outer surface of the simulation domain. For isotropic materials in terms of the relative permeability μ_r the magnetic flux $\vec{B}$ will have the same direction as $\vec{H}$ and the Neumann boundary condition (5.30) is satisfied independently of the size of the simulation domain. Analogously the same can be considered for the electric field $\vec{E}$. Related to the electric conductivity γ the materials in the simulation domain are assumed isotropic. Because of the finite conductivity γ in the conducting parts the corresponding electric field $\vec{E}$ cannot be neglected. This is the reason why the dielectric layer (its thickness can be chosen arbitrarily) outside of the outer conductor is used. For the outer boundary, which lies on the dielectric, $\vec{E}$ is zero. For the remaining part of the outer boundary the current density distribution $\vec{J}$ is normal to the outer faces of the conducting regions, as demonstrated in Fig. <6.2>.

$$\int\limits_{\mathcal{C}_{in}} \vec{H}_1 \,\mathrm{d}\vec{r} = \int\limits_{\mathcal{A}} \vec{n} \cdot \left(\vec{\nabla} \times \vec{H}\right) \mathrm{d}A = \int\limits_{\mathcal{A}} \frac{J}{\gamma} \,\mathrm{d}A = \sum_i \frac{J_i}{\gamma_i} A_i. \tag{6.2}$$

$\mathcal{A}$ is the outer face enclosed from $\mathcal{C}_{in}$ and A_i is the i-th area of the triangular elements, in which this face is discretized. Thus $\vec{E}$ is either zero or perpendicular to the outer face and the homogeneous Neumann boundary condition (5.32) is satisfied, also for finite domain size.

Die approbierte gedruckte Originalversion dieser Dissertation ist an der TU Wien Bibliothek verfügbar.
The approved original version of this doctoral thesis is available in print at TU Wien Bibliothek.

Die approbierte gedruckte Originalversion dieser Dissertation ist an der TU Wien Bibliothek verfügbar.
The approved original version of this doctoral thesis is available in print at TU Wien Bibliothek.

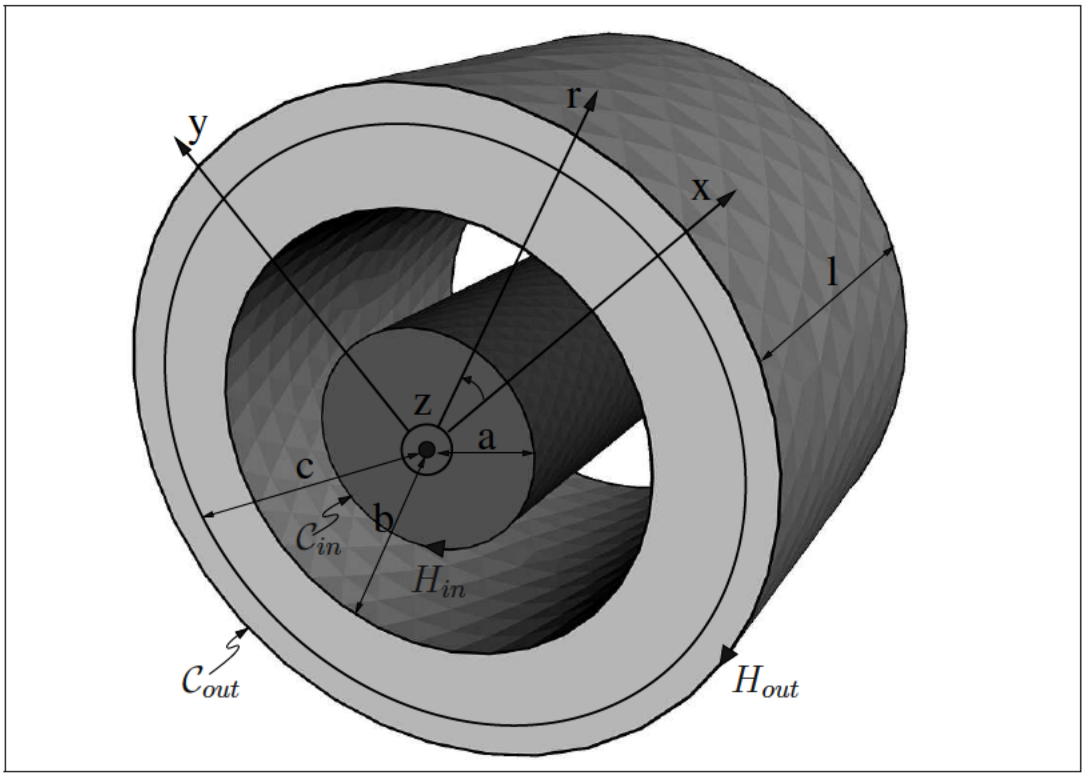

Figure 6.1: The simulated coaxial structure.

6.1.1 Analytical Inductance and Resistance Calculation

The analytical expression for the inductance L is obtained from the magnetic energy [102]

$$E_m = \int\limits_{\mathcal{V}} \frac{B^2}{2\mu}\,\mathrm{d}V = \frac{I^2 L}{2} \;\Rightarrow\; L = \frac{1}{I^2}\int\limits_{\mathcal{V}} \frac{B^2}{\mu}\,\mathrm{d}V = \frac{1}{I^2}\sum_{i=1}^{3}\int\limits_{\mathcal{V}_i} \frac{B^2}{\mu}\,\mathrm{d}V. \tag{6.3}$$

It must be distinguished between three regions: the inner conductor $\mathcal{V}_1$, the dielectric between the conductors $\mathcal{V}_2$, and the outer conductor $\mathcal{V}_3$.

For $\mathcal{V}_1 \mid r \in [0; a]$ the magnetic flux B and the integral are given by

$$B = \mu\frac{Ir}{2\pi a^2} \quad \text{and} \quad \int\limits_{\mathcal{V}_1} \frac{B^2}{\mu}\,\mathrm{d}V = \int\limits_0^a \mu\frac{I^2 r^2}{4\pi^2 a^4} l 2\pi r\,dr = \mu\frac{I^2 l}{8\pi}. \tag{6.4}$$

For $\mathcal{V}_2 \mid r \in [a; b]$

$$B = \mu\frac{I}{2\pi r} \quad \text{and} \quad \int\limits_{\mathcal{V}_2} \frac{B^2}{\mu}\,\mathrm{d}V = \int\limits_a^b \mu\frac{I^2}{4\pi^2 r^2} l 2\pi r\,dr = \mu\frac{I^2 l}{2\pi}\,\ln\frac{b}{a}. \tag{6.5}$$

Die approbierte gedruckte Originalversion dieser Dissertation ist an der TU Wien Bibliothek verfügbar.
The approved original version of this doctoral thesis is available in print at TU Wien Bibliothek.

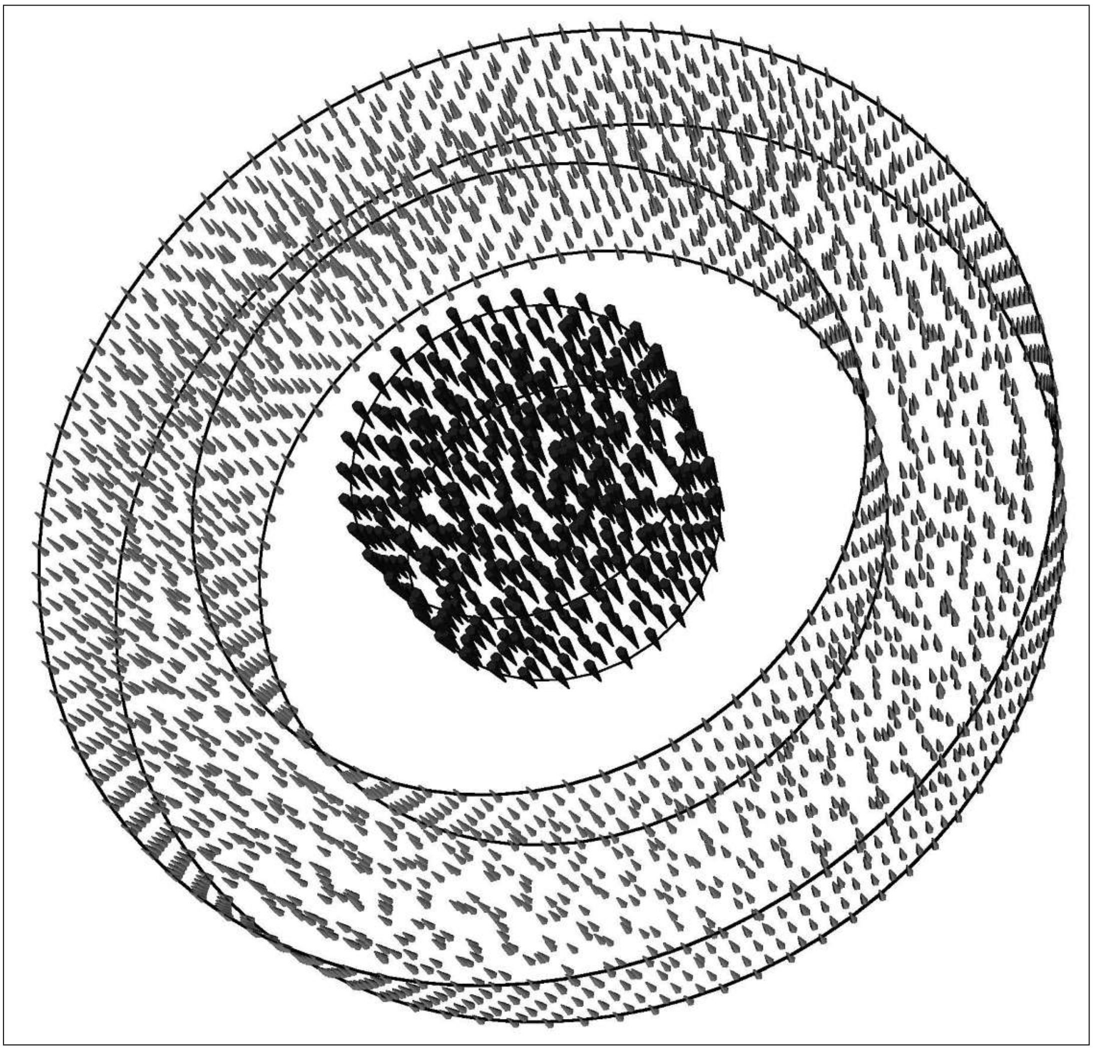

Figure 6.2: Current density distribution.

The current I flows along the inner conductor. The same current returns along the outer conductor flowing in the opposite direction. Similarly to (6.4), for $\mathcal{V}_3$ where $r \in [b;c]$, only the current through the circle inside the integration loop must be considered

$$I - \frac{I\left(\pi r^2 - \pi b^2\right)}{\pi c^2 - \pi b^2} = I\frac{c^2-r^2}{c^2-b^2} \quad \text{and} \quad B = \frac{\mu I}{2\pi r}\,\frac{c^2-r^2}{c^2-b^2}. \tag{6.6}$$

$$\begin{aligned}\int\limits_{\mathcal{V}_3} \frac{B^2}{\mu}\,\mathrm{d}V &= \int\limits_b^c \mu I^2 \left(\frac{c^2-r^2}{c^2-b^2}\right)^2 \frac{1}{4\pi^2 r^2} l 2\pi r\, dr = \\ &= \mu\frac{I^2 l}{2\pi\left(c^2-b^2\right)^2}\left[c^4 \ln\frac{c}{b} - \frac{1}{4}\left(c^2-b^2\right)\left(3c^2-b^2\right)\right].\end{aligned} \tag{6.7}$$

Die approbierte gedruckte Originalversion dieser Dissertation ist an der TU Wien Bibliothek verfügbar.
The approved original version of this doctoral thesis is available in print at TU Wien Bibliothek.

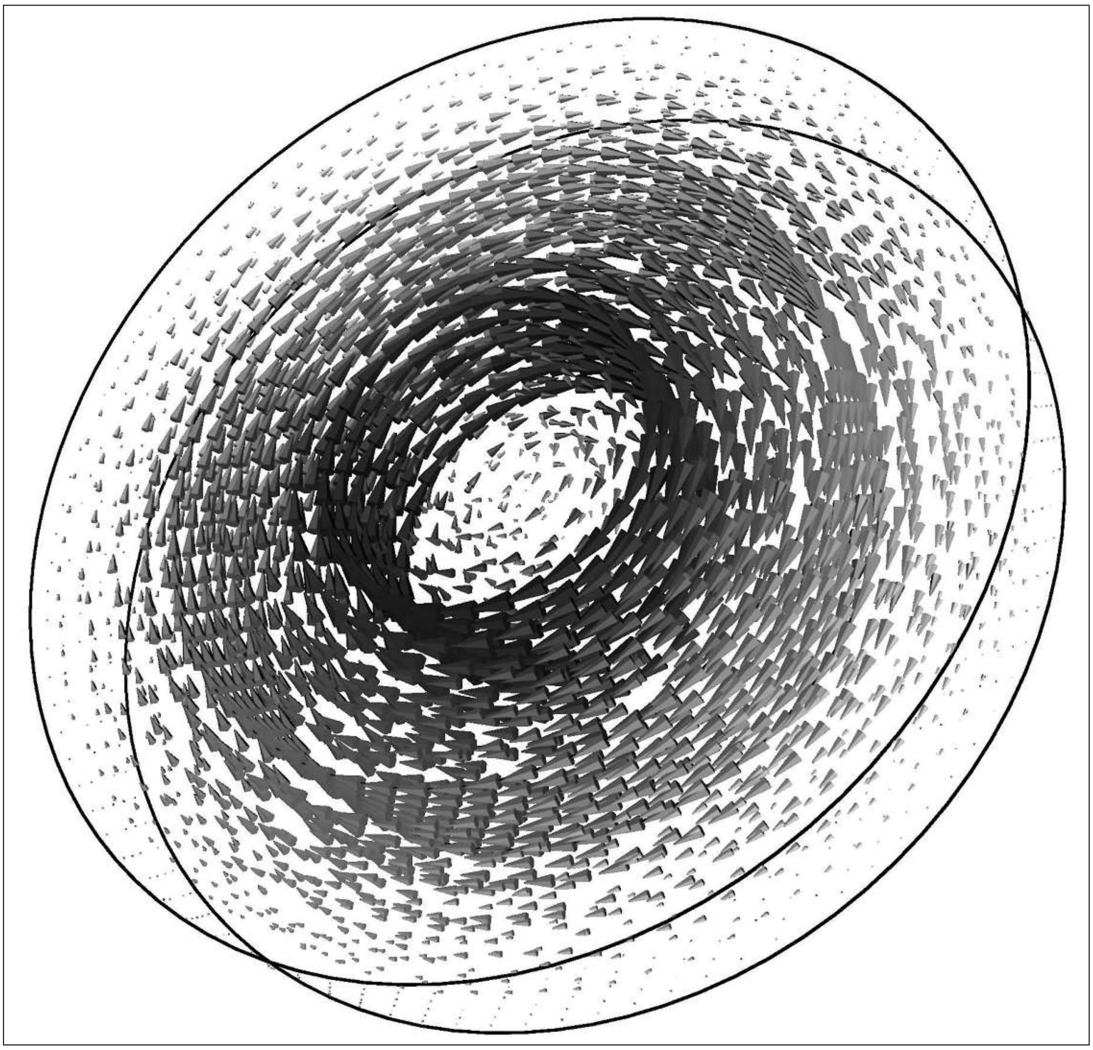

Figure 6.3: Magnetic field.

Now the inductance can be obtained from the integral over the entire domain

$$L = \frac{\mu l}{2\pi}\left\{\frac{1}{4\pi} + \ln\frac{b}{a} + \frac{1}{\left(c^2-b^2\right)^2}\left[c^4\ln\frac{c}{b} - \frac{1}{4}\left(c^2-b^2\right)\left(3c^2-b^2\right)\right]\right\}. \qquad (6.8)$$

The resistance R of the conductors is given by

$$R = R_{in} + R_{out}, \text{ where } \quad R_{in} = \frac{l}{\gamma\pi a^2} \quad \text{and} \quad R_{out} = \frac{l}{\gamma\pi\left(c^2-b^2\right)}. \qquad (6.9)$$

Equations (6.8) and (6.9) are obtained assuming a constant current density distribution in the conductors. This is true only for low frequencies. The distinction between low and high frequency is in terms of the skin effect. Thus, whether an operating frequency is considered as low or high depends also on the dimensions of the geometries, not only on the frequency itself. At high frequencies for which skin effect is not negligible L and R are modified to read [102]

$$L = \frac{\mu l}{2\pi} \left\{ \frac{\delta}{2a} + \ln\frac{b}{a} + \frac{\delta\left[\sinh\left(2\frac{d}{\delta}\right) - \sin\left(2\frac{d}{\delta}\right)\right]}{2b\left[\cosh\left(2\frac{d}{\delta}\right) - \cos\left(2\frac{d}{\delta}\right)\right]} \right\} \tag{6.10}$$

$$R = \frac{a}{2\delta} R_{in} + \frac{d\left[\sinh\left(2\frac{d}{\delta}\right) + \sin\left(2\frac{d}{\delta}\right)\right]}{\delta\left[\cosh\left(2\frac{d}{\delta}\right) - \cos\left(2\frac{d}{\delta}\right)\right]} R_{out}, \tag{6.11}$$

where R_{in} and R_{out} are taken from (6.9), d is the thickness of the outer conductor ($d = c - b$), and the skin depth δ is given by the expression

$$\delta = \sqrt{\frac{2}{\mu\gamma\omega}}. \tag{6.12}$$

Notice that (6.10) and (6.11) are valid only, if d is reasonably small compared to b ($d \ll b$).

6.1.2 Numerical Inductance and Resistance Extraction

The electro-magnetic power in the domain $\mathcal{V}$ can be expressed in two different ways. The first one is by volume integration over the power density distribution [103] in the region $\mathcal{V}$. The second one is by the current flowing trough the resulting resistance and inductance. As aforementioned, the quasi-magnetostatic case is considered

$$\int\limits_{\mathcal{V}} \left(\vec{J} \cdot \vec{E} + \vec{H} \cdot \partial_t \vec{B} \right) \mathrm{d}V = LI\frac{dI}{dt} + RI^2. \tag{6.13}$$

In the frequency domain using the constitutive relations (4.7) and (4.8) one obtains

$$\int\limits_{\mathcal{V}} \left(\frac{J^2}{\gamma} + \jmath\omega\mu H^2 \right) \mathrm{d}V = \jmath\omega L I^2 + RI^2. \tag{6.14}$$

The left hand side of (6.14) can be denoted in the following way:

$$P_1 = \int\limits_{\mathcal{V}} \frac{J^2}{\gamma}\,\mathrm{d}V, \quad P_2 = \jmath\omega \int\limits_{\mathcal{V}} \mu H^2\,\mathrm{d}V, \quad \text{and} \quad P = P_1 + P_2. \tag{6.15}$$

Consequently the resistance R and the inductance L arising in the domain $\mathcal{V}$ are calculated by

$$R = \frac{\mathcal{R}\mathrm{e}\{\mathrm{P}\}}{I^2}, \qquad L = \frac{\mathcal{I}\mathrm{m}\{\mathrm{P}\}}{\omega I^2}. \tag{6.16}$$

The domain $\mathcal{V}$ is discretized and the linear equation system (5.37) is assembled as described in Section 5.2 and solved to obtain the solution vector $\{c\}$. The indexes j of the

Die approbierte gedruckte Originalversion dieser Dissertation ist an der TU Wien Bibliothek verfügbar.
The approved original version of this doctoral thesis is available in print at TU Wien Bibliothek.

coefficients c_j are arranged as shown in Section 5.2. The fields $\vec{H}_1$ and ψ are constructed as in (5.27) and (5.28). $\vec{H}$ is obtained by (5.23). These quantities are used to determine P. Inserting (5.13) in the expression for P_1 from (6.15) gives

$$\begin{aligned} P_1 &= \int\limits_{\mathcal{V}} \frac{1}{\gamma} \left(\vec{\nabla} \times \vec{H}\right)^2 \mathrm{d}V = \int\limits_{\mathcal{V}} \frac{1}{\gamma} \left(\vec{\nabla} \times \vec{H}_1\right)^2 \mathrm{d}V = \\ &= \int\limits_{\mathcal{V}} \frac{1}{\gamma} \left[\sum_{j=1}^{m} c_j \left(\vec{\nabla} \times \vec{N}_j\right) + \sum_{j=n+1}^{M} c_j \left(\vec{\nabla} \times \vec{N}_j\right) \right]^2 \mathrm{d}V \end{aligned} \tag{6.17}$$

or

$$\begin{aligned} P_1 = & \sum_{i=1}^{m} c_i \sum_{j=1}^{m} \int\limits_{\mathcal{V}} \frac{1}{\gamma} \left(\vec{\nabla} \times \vec{N}_i\right) \left(\vec{\nabla} \times \vec{N}_j\right) \mathrm{d}V \, c_j + \\ & + 2 \left[\sum_{i=1}^{m} c_i \sum_{j=n+1}^{M} \int\limits_{\mathcal{V}} \frac{1}{\gamma} \left(\vec{\nabla} \times \vec{N}_i\right) \left(\vec{\nabla} \times \vec{N}_j\right) \mathrm{d}V \, c_j \right] + \\ & + \sum_{i=n+1}^{M} c_i \sum_{j=n+1}^{M} \int\limits_{\mathcal{V}} \frac{1}{\gamma} \left(\vec{\nabla} \times \vec{N}_i\right) \left(\vec{\nabla} \times \vec{N}_j\right) \mathrm{d}V \, c_j . \end{aligned} \tag{6.18}$$

With (5.23) P_2 is modified to read

$$P_2 = \jmath\omega \int\limits_{\mathcal{V}} \mu \left(\vec{H}_1 - \vec{\nabla}\psi\right)^2 \mathrm{d}V. \tag{6.19}$$

Expressing $\vec{H}_1$ from (5.27) and ψ from (5.28) one obtains

$$P_2 = \jmath\omega \int\limits_{\mathcal{V}} \mu \left(\sum_{j=1}^{m} c_j \vec{N}_j + \sum_{j=n+1}^{M} c_j \vec{N}_j - \sum_{j=m+1}^{n} c_j \vec{\nabla}\lambda_j - \sum_{j=M+1}^{N} c_j \vec{\nabla}\lambda_j \right)^2 \mathrm{d}V, \tag{6.20}$$

Die approbierte gedruckte Originalversion dieser Dissertation ist an der TU Wien Bibliothek verfügbar.
The approved original version of this doctoral thesis is available in print at TU Wien Bibliothek.
TU WIEN Bibliothek Your knowledge hub

Die approbierte gedruckte Originalversion dieser Dissertation ist an der TU Wien Bibliothek verfügbar.
The approved original version of this doctoral thesis is available in print at TU Wien Bibliothek.
TU WIEN Bibliothek Your knowledge hub

which is written in the more convenient form

$$\begin{aligned}\frac{P_2}{\jmath\omega} = &\sum_i c_i \sum_j \int_{\mathcal{V}} \mu \vec{N}_i \cdot \vec{N}_j \,\mathrm{d}V\, c_j \Bigg|_{i\in[1;m]\cup[n+1;M],\ j\in[1;m]\cup[n+1;M]} + \\ &+ \sum_i c_i \sum_j \int_{\mathcal{V}} \mu \vec{\nabla}\lambda_i \cdot \vec{N}_j \,\mathrm{d}V\, c_j \Bigg|_{i\in[m+1;n]\cup[M+1;N],\ j\in[1;m]\cup[n+1;M]} + \\ &+ \sum_i c_i \sum_j \int_{\mathcal{V}} \mu \vec{N}_i \cdot \vec{\nabla}\lambda_j \,\mathrm{d}V\, c_j \Bigg|_{i\in[1;m]\cup[n+1;M],\ j\in[m+1;n]\cup[M+1;N]} + \\ &+ \sum_i c_i \sum_j \int_{\mathcal{V}} \vec{\nabla}\lambda_i \cdot \vec{\nabla}\lambda_j \,\mathrm{d}V\, c_j \Bigg|_{i\in[m+1;n]\cup[M+1;N],\ j\in[m+1;n]\cup[M+1;N]} .\end{aligned} \tag{6.21}$$

Using (6.18) and (6.21) for P_1 and P_2 the very suitable form for the power P in the simulation domain is derived

$$P = P_1 + P_2 = \{c\}^T \begin{bmatrix} A_1 & B_1 & A_2 & B_2 \\ B_1^T & C_1 & B_2^T & C_2 \\ A_2 & B_2 & A_3 & B_3 \\ B_2^T & C_2 & B_3^T & C_3 \end{bmatrix} \{c\}\,, \tag{6.22}$$

where the sub-matrices A_k, B_k and C_k with $k \in [1;3]$ are calculated using the mathematical expressions given in (5.38), (5.39), and (5.40), respectively. The indexes k of A_k, B_k and C_k indicate the different ranges of the sub-matrix entries global indexes i and j. The associated global index ranges are specified in (6.18) and (6.21) and can be given more clearly as follows:

	$i \in [1; m]$	$i \in [m+1; n]$	$i \in [n+1; M]$	$i \in [M+1; N]$
$j \in [1; m]$	A_1	B_1	A_2	B_2
$j \in [m+1; n]$	B_1^T	C_1	B_2^T	C_2
$j \in [n+1; M]$	A_2	B_2	A_3	B_3
$j \in [M+1; N]$	B_2^T	C_2	B_3^T	C_3

In (5.37) only the $n \times n$ part of the matrix for the unknowns is used. The remaining part is assembled with the known Dirichlet values directly to right hand side vector $\{b\}$. For the power calculation (6.22) the whole $N \times N$ matrix is used. Expression (6.22) can be simplified by involving (5.37)

$$P = \{c_{n+1} \,...\, c_N\} \begin{vmatrix} A_2 & B_2 & A_3 & B_3 \\ B_2^T & C_2 & B_3^T & C_3 \end{vmatrix} \{c\}\,. \tag{6.23}$$

Die approbierte gedruckte Originalversion dieser Dissertation ist an der TU Wien Bibliothek verfügbar.
The approved original version of this doctoral thesis is available in print at TU Wien Bibliothek.

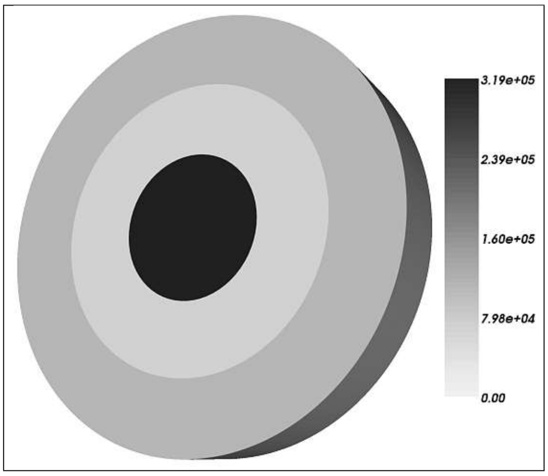

Figure 6.4: Current density distribution at low frequency.

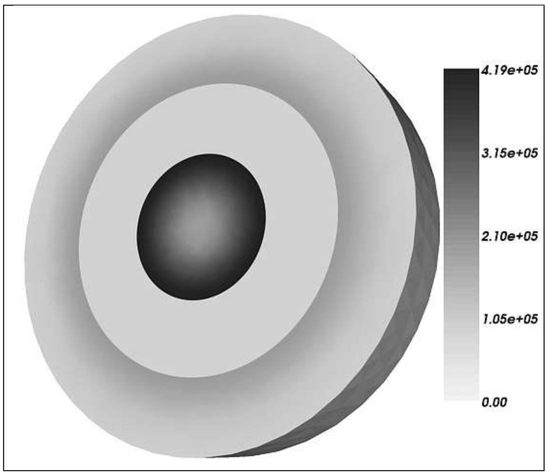

Figure 6.5: Current density distribution at 3 GHz.

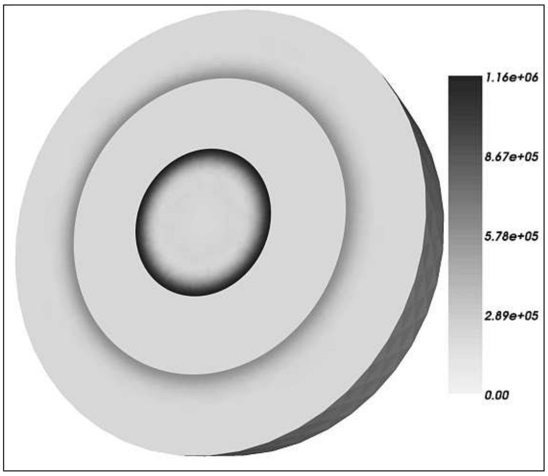

Figure 6.6: Current density distribution at 30 GHz.

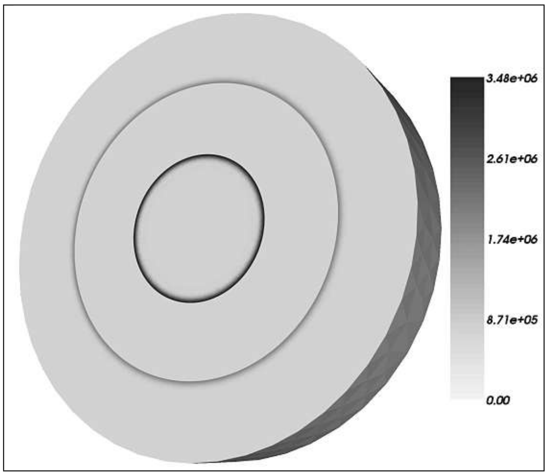

Figure 6.7: Current density distribution at 300 GHz.

6.1.3 Simulated Fields Visualization and Results Comparison

Now the simulation results are compared with the solutions of the analytical formulas (6.8) and (6.9) for low frequencies and (6.10) and (6.11) for high frequencies. The coaxial structure used is very well suited. It satisfies exactly the homogeneous Neumann boundary conditions.

The following dimensions are used: $a = 3\,\mu\text{m}$, $b = 6\,\mu\text{m}$, $c = 9\,\mu\text{m}$, and $l = 3\,\mu\text{m}$. These dimensions are typical for microelectronics applications. For these dimensions skin effect is observable at frequencies over 3 GHz. Of course it is a question of scaling, because, if larger dimensions are used, the same effects arise at lower frequencies. The outer dielectric layer is needed only for low frequencies, since for high frequencies there

Die approbierte gedruckte Originalversion dieser Dissertation ist an der TU Wien Bibliothek verfügbar.
The approved original version of this doctoral thesis is available in print at TU Wien Bibliothek.
TU WIEN Bibliothek Your knowledge hub

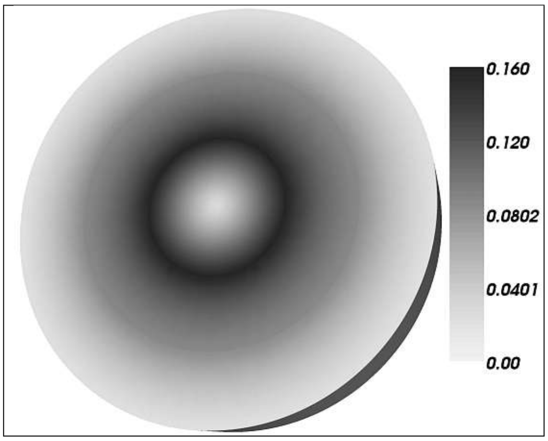

Figure 6.8: Magnetic field distribution at low frequency.

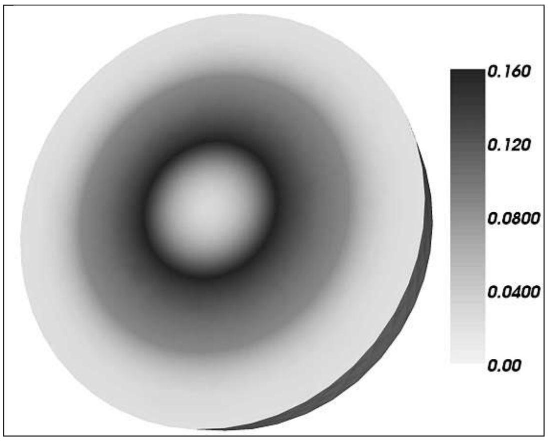

Figure 6.9: Magnetic field distribution at 3 GHz.

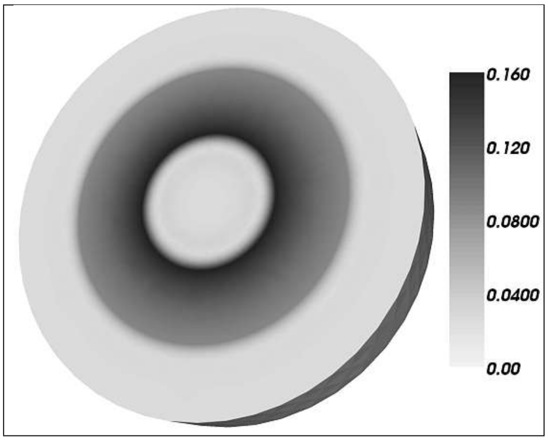

Figure 6.10: Magnetic field distribution at 30 GHz.

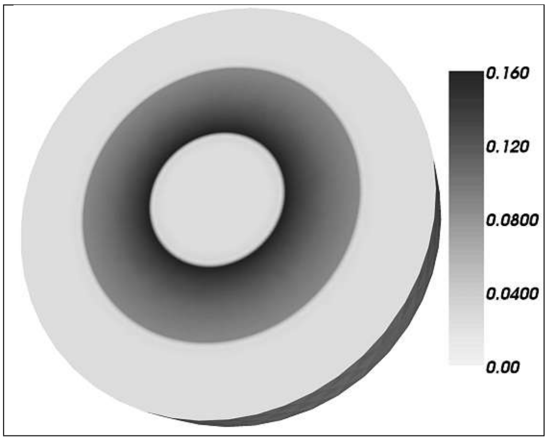

Figure 6.11: Magnetic field distribution at 300 GHz.

is no current density distribution on the outer face of the outer conductor. Then the homogeneous Neumann boundary conditions are also fulfilled without the outer dielectric layer. However, for low frequencies the homogeneous Neumann boundary conditions are fulfilled on the outer shell surface only using the outer dielectric cylinder. Its thickness can be chosen arbitrarily.

Numerical and analytical calculations are performed for different frequencies between 3 MHz and 300 GHz. The related results and skin depths are shown in Table 6.1. The field densities distributions in the region of interest are depicted in Fig. <6.4> – Fig. <6.11>. A remarkable short skin depth is observed at 300 GHz, which is a high frequency for the given dimensions. For 3 MHz the skin depth is much larger than the thickness of the conductors. For the given structure this is a low frequency case described analytically by (6.8) and (6.9). For this frequency the numerical results agree quite well with the analytical ones. For the remaining frequencies skin effect is observed

Table 6.1: Numerically simulated and analytically calculated R and L.

f [GHz]	δ [μm]	L [pH] **numeric**	L [pH] **analytic**	R [Ω] **numeric**	R [Ω] **analytic**
0.003	47.14	0.664398	0.664112	0.00335153	0.00335063
3	1.491	0.623599	0.639796	0.00479862	0.00387773
30	0.471	0.487201	0.486669	0.0137691	0.0128489
300	0.149	0.43899	0.438291	0.0426505	0.0416856

and the low frequency analytical formulas (6.8) and (6.9) are wrong. In this case (6.10) and (6.11) should be used. However the requirement $d \ll b$, which must be fulfilled for (6.10) and (6.11), is approximately provided only for the highest frequency at 300 GHz. At this frequency d is set to 3δ in (6.10) and (6.11) and the analytical results match the numerical ones very well. For 3 GHz and 30 GHz the condition $d \ll b$ is not satisfied and the numerical results differ strongerly from the analytical ones. In such cases the numerical method has to be used.

6.2 Inductance and Resistance of On-Chip Inductors

High frequencies in an integrated circuit (IC) affect both, the resistance and the inductance of the on-chip interconnects. These often as parasitics treated parameters cause longer signal rise, fall, and delay times and limit the maximum allowed frequency of modern ICs. However, as the operating frequencies increase, small inductors of high speed circuits can be also actively used. They can be even constructed on the chip. Thus the inductance of an on-chip interconnect line can be a disadvantage or very useful depending on the application. Of course the collateral resistance must also be considered. In each case it is necessary to investigate the structure of interest to obtain its inductance and resistance in order to estimate the impact on the entire electric circuit [104]. In the case of applications in radio frequency (RF) ICs such as voltage controlled oscillators or low noise amplifiers the inductance and the resistance of the on-chip inductors must be extensively investigated for the RF circuit design, performance optimization, and inductor quality factor. The frequency dependent inductance and resistance of wide on-chip interconnects must be captured to obtain the impact on power supply stability and signal delay.

Currently there are two major techniques for modeling of on-chip inductors: analytical compact modeling and numerical field calculation based modeling. In the case of a spiral inductor, where the models can be restricted to specific geometry classes, closed-form analytical models are very well suited for fast designs typical for the very early stage of the developing process [105, 106]. However, analytical modeling of arbitrarily shaped three-dimensional structures is very complicated, if possible at all. Thus, analytical parameter extraction methods have only limited applicability. For final analysis prior to fabrication and for irregular inductor geometries numerical simulation methods normally

Die approbierte gedruckte Originalversion dieser Dissertation ist an der TU Wien Bibliothek verfügbar.
The approved original version of this doctoral thesis is available in print at TU Wien Bibliothek.
TU WIEN Bibliothek Your knowledge hub

Die approbierte gedruckte Originalversion dieser Dissertation ist an der TU Wien Bibliothek verfügbar.
The approved original version of this doctoral thesis is available in print at TU Wien Bibliothek.
TU Bibliothek WIEN Your knowledge hub

based on solving the Maxwell equations provide the most accurate characterization. Moreover, the investigated interconnect structure can often be embedded in a small simulation region for which the optimized model of the dominant magnetic field can be used even at very high frequencies. The distributed vector and scalar fields must be extracted in structures which may consist of different inhomogeneous complex shaped three-dimensional regions, like splittings, widenings, and vertical connections. As a consequence, the vector and scalar finite element method for the qusi-magnetostatic case in the frequency domain on unstructured tetrahedral meshes [107, 108] as described in Section 5.2 needs to be addressed.

In this application an optimized model for inductance and resistance analysis of an on-chip inductor at different frequencies is proposed. The model describes the proximity effect and the skin effect typically arising at higher frequencies as well. The three-dimensional finite element simulation software **SAP** (**S**mart **A**nalysis **P**rograms) [109] was extended to implement the developed model. Simulation results demonstrate the physical plausibility of the applied model and numerical methods, as well as the necessity of three-dimensional simulations.

6.2.1 Boundary Conditions

The supplied total current in the inductor wire is considered by the following condition for $\vec{H}_1$:

$$I = \oint\limits_{\partial\mathcal{A}} \vec{H}_1 \cdot \mathrm{d}\vec{r} = \oint\limits_{\partial\mathcal{A}} \vec{H} \cdot \mathrm{d}\vec{r} \simeq H_t \sum_{i=1}^{p} l_i, \tag{6.24}$$

where $\partial\mathcal{A}$ is an arbitrary closed loop around the conducting wire, p is the number of edges, which build this loop, and l_i is the length of the i-th loop edge. The Dirichlet boundary part from (5.27) is expressed as

$$\vec{v} = \sum_{j=n+1}^{M} c_j \vec{N}_j \text{ with } c_j = H_t \text{ for } j \in [n+1; M] \text{ and } p = M - n.$$

Only the supply parts of the wire, which are used to force the electric current, lie directly on the outer bound of the simulation domain. The remaining parts of the wire are surrounded by dielectric material. The loop $\partial\mathcal{A}$ is chosen to lie on the outer face of the simulation domain. The Neumann boundary $\mathcal{A}_{N1}$ consists of all edges lying on the outer boundary of the simulation domain excluding the edges building $\partial\mathcal{A}$. In this work the dielectric environment enclosing the wire is assumed to be sufficiently thick so that $\vec{E}$ can be neglected on the dielectric part of $\mathcal{A}_{N1}$. On the other hand the electric current density is forced in a direction perpendicular to the conductor boundary faces. Thus, for isotropic materials with respect to σ, $\vec{E}$ will be also perpendicular to these faces and the homogeneous Neumann boundary condition (5.30) is used for the conductor surface parts.

For the calculations of ψ it is sufficient that one node of the simulation domain is set to an arbitrary value. Thus, the Dirichlet boundary part of (5.27) is modified to read

$$v = c_{M+1}\lambda_{M+1} \quad \text{with} \quad N = M + 1. \tag{6.25}$$

The Neumann boundary $\mathcal{A}_{N2}$ consists of all edges lying on the outer boundary of the simulation domain. The simulation domain is constructed sufficiently large to allow that the magnetic flux $\vec{B}$ can be neglected on the outer boundary $\mathcal{A}_{N2}$. Thus the homogeneous Neumann boundary condition (5.32) is applied.

6.2.2 Domain Discretization

The example inductor geometry presented in the next subsection and the coaxial geometry from Section 6.1 are discretized with the three-dimensional tetrahedron mesh generation software Netgen [110]. Netgen is able to combine the generation of very small elements in regions, where high resolution is needed with large elements, where the field does not change strongly. This advantage of Netgen makes high frequency simulations with pronounced skin effect possible at all. In the skin effect area a feasible field approximation can be guaranteed only if a very fine mesh is generated. Generating such a mesh in the entire simulation domain will push unnecessarily the memory limits. Thus it is very efficient to generate a coarse mesh in the remaining area.

Netgen uses different different geometry description formats. For the applications in this work the constructive solid geometry (CSG) format is preferred. It is very convenient for the description of small or medium size structures like the coaxial structure or the spiral inductor presented in the example section. The geometry is defined by Eulerian operations (union, intersection, and complement) from primitives. The primitives are generic volume elements like cubes, cylinders, spheres, or even half-spaces defined by an arbitrary point in the boundary plane and an outward normal vector. If CSG input is used, Netgen starts with the computation of the corner points. Then the edges are defined and meshed into segments. Next, the faces are generated by an advancing front algorithm [111]. After optimization of the surface mesh the volume inside is filled with tetrahedrons by a fast Delaunay algorithm [112]. Finally the volume mesh is optimized.

6.2.3 Examples and Results

As example a typical on-chip spiral inductor structure as discussed in [113] is investigated. The simulation domain consists of a transparent insulating rectangular brick over an opaque substrate brick as shown in Fig. <6.12>. The aluminum inductor is placed in the insulating environment about $5\,\mu$m above the substrate area. The substrate is modelled as region with a constant relative low resistivity of $10\,\Omega\,cm$. Thus the induced electric voltage in this region causes relative law electric current. The cross-section of the conductor is $20\,\mu\text{m} \times 1.2\,\mu$m. The horizontal distance between the winding wires is $10\,\mu$m. The outer dimensions of the inductor are $300\,\mu\text{m} \times 300\,\mu$m. The inductor is completely surrounded by the dielectric environment, except of the two small delimiting faces which lie directly in the boundary planes of the simulation domain. The conductor

Die approbierte gedruckte Originalversion dieser Dissertation ist an der TU Wien Bibliothek verfügbar.
The approved original version of this doctoral thesis is available in print at TU Wien Bibliothek.
TU WIEN Bibliothek Your knowledge hub

Table 6.2: Calculated inductance and resistance.

f [GHz]	L [nH] **without substrate**	L [nH] **with substrate**	R [Ω]
0.001	2.6887	2.6881	3.127
0.01	2.6887	2.6877	3.127
0.1	2.688	2.688	3.132
1	2.6516	2.6514	3.463
10	2.5501	2.5493	5.396
100	2.5458	2.5457	13.156

area, the dielectric, and the substrate area close to the conductor are discretized much finer then the remaining simulation domain. This is shown in Fig. <6.13> where a part of the dielectric environment is removed to visualize in detail the generated mesh inside the simulation domain. The variation of the fields in the finer discretized areas is expected to be much higher than in the coarser discretized domain. This special discretization reduces the number of generated nodes and edges, and the number of the linear equations respectively, even for big simulation environments which have to be used to satisfy the assumption of homogeneous Neumann boundary conditions (the tangential component of $\vec{E}$ on $\mathcal{A}_{N1}$ and normal component of $\vec{B}$ on $\mathcal{A}_{N2}$ are zero). Of coarse such a discretization is only possible, if an unstructured mesh is used.

The current density distribution depends heavily on the operating frequency in the analyzed frequency domain. It is unknown and arises from the simulation. At the beginning of the simulation only the total current in the inductor is known. As mentioned above it is set by the Dirichlet boundary condition for $\vec{H}_1$ which is given by the tangential component of the magnetic field H_t on the element edges, surrounding one of the conductor faces lying on the outer bound of the simulation domain.

The resistance and inductance values of the structure of interest are calculated numerically at different frequencies with and without the substrate influence. The corresponding results are presented in Table 6.2. While the inductance decreases slowly with increasing operating frequency, the resistance rises dramatically, which matches well the observed current density distribution and the skin effect, respectively. A surface view of the current density distribution in the conductor is shown in Fig. <6.14> and Fig. <6.15> for 100 MHz and 10 GHz, respectively. At 100 MHz the skin depth is about 6 μm and nearly the whole conductor cross-section is filled up by the current. At 10 GHz the skin depth is about 0.6 μm and the current is concentrated at the vertical side walls of the conductor. Fig. <6.16> shows the spatial current density distribution at 1 GHz as directed cones placed in the discretization nodes inside of the conductor area. The cone's size and darkness are proportional to the field strength. Fig. <6.17> depicts the corresponding spatial distribution of the magnetic field inside the dielectric environment around the inductor. Fig. <6.18> and Fig. <6.19> show the very different current density

Die approbierte gedruckte Originalversion dieser Dissertation ist an der TU Wien Bibliothek verfügbar.
The approved original version of this doctoral thesis is available in print at TU Wien Bibliothek.

distribution close to the small via for 100 MHz and 10 GHz, respectively. Fig. <6.20> and Fig. <6.21> show the current density distribution and the corresponding magnetic field in the substrate at 1 GHz. The underlying substrate does not influence the inductance and the resistance of the inductor, because of the relative high substrate resistivity. The values of the current density in the substrate (Fig. <6.20>) differ vastly to those in the inductor (Fig. <6.14> and Fig. <6.15>). As shown in Table 6.2 the calculated inductance taking into account the influence of the substrate does not differ from the inductance without substrate influence.

As the Q-factor of an inductor is inversely proportional to its resistance, making the inductor wire thicker might decrease the resistance and increase the Q-factor. However, as the examples show this is not the case for high frequencies at which the skin effect is noticeable. In these cases the current flows only in the area very close to the vertical surface and a wider transversal conductor cross section would not change the situation. For the visualization VTK [114, 115] is used.

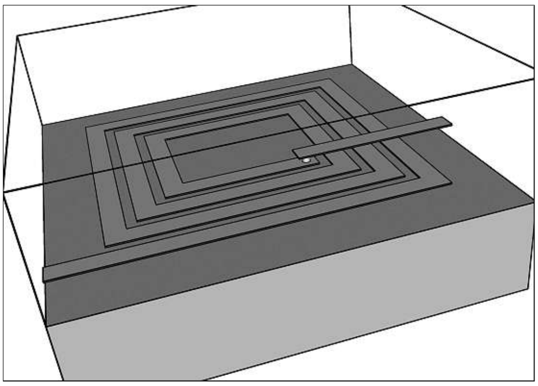

Figure 6.12: The simulation domain.

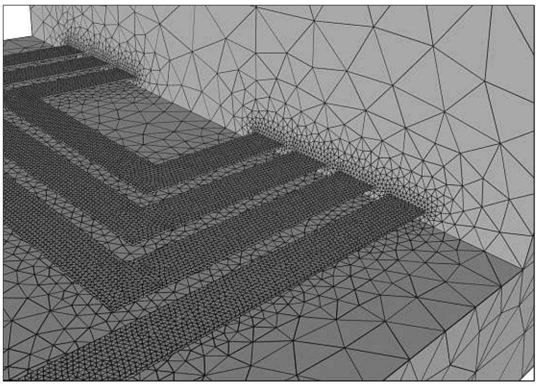

Figure 6.13: The generated mesh.

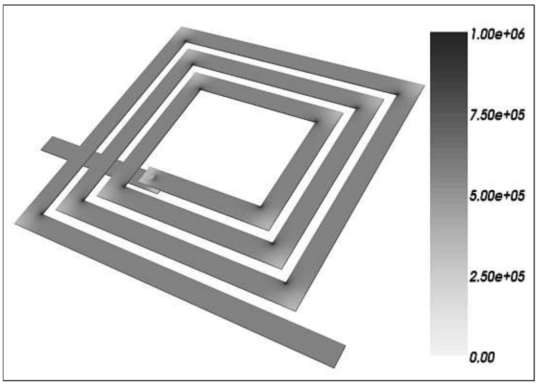

Figure 6.14: Surface view of the current density [A/m^2] distribution at 100 MHz.

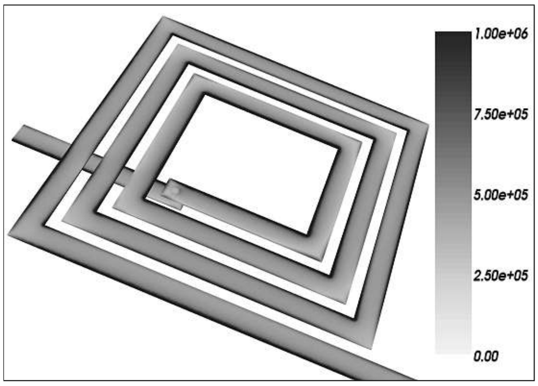

Figure 6.15: Surface view of the current density [A/m^2] distribution at 10 GHz.

Die approbierte gedruckte Originalversion dieser Dissertation ist an der TU Wien Bibliothek verfügbar.
The approved original version of this doctoral thesis is available in print at TU Wien Bibliothek.

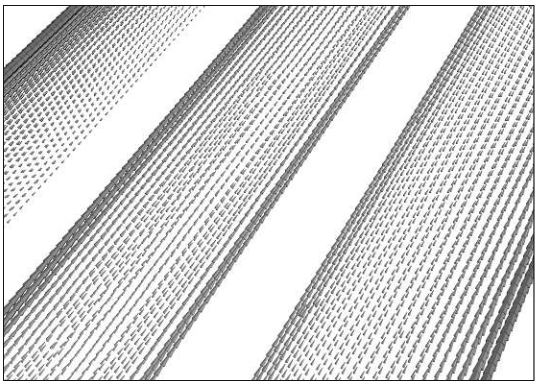

Figure 6.16: Current density distribution at 1 GHz.

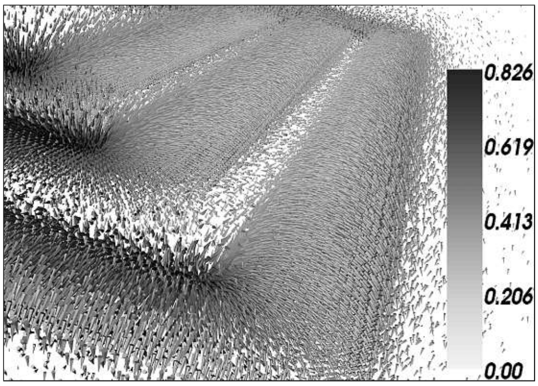

Figure 6.17: Magnetic field distribution [A/m] at 1 GHz.

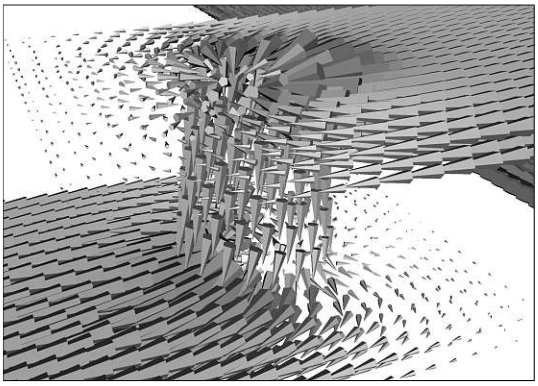

Figure 6.18: Current density distribution in the via at 100 MHz.

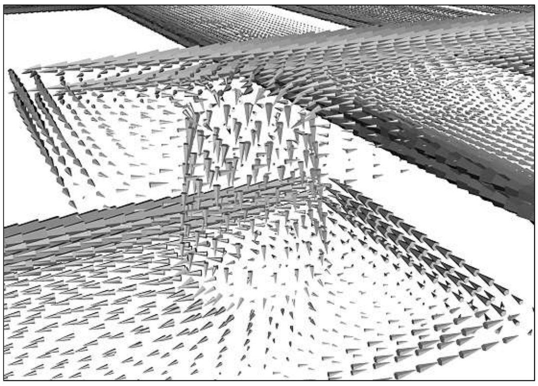

Figure 6.19: Current density distribution in the via at 10 GHz.

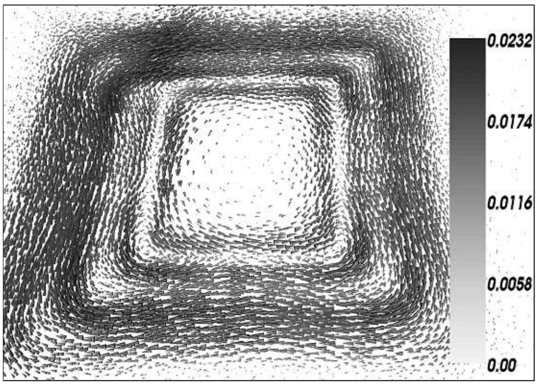

Figure 6.20: Current density [A/m^2] distribution in the substrate at 1 GHz.

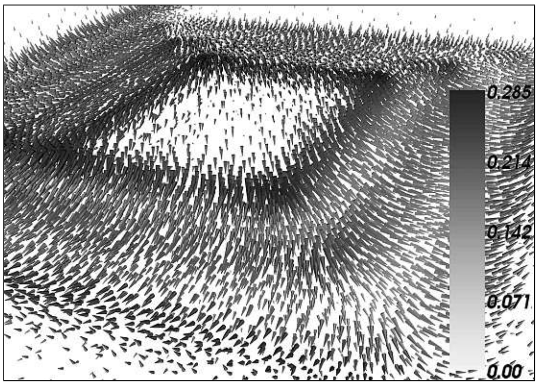

Figure 6.21: Magnetic field [A/m] in the substrate at 1 GHz.

Die approbierte gedruckte Originalversion dieser Dissertation ist an der TU Wien Bibliothek verfügbar.
The approved original version of this doctoral thesis is available in print at TU Wien Bibliothek.
TU WIEN Bibliothek Your knowledge hub

Die approbierte gedruckte Originalversion dieser Dissertation ist an der TU Wien Bibliothek verfügbar.
The approved original version of this doctoral thesis is available in print at TU Wien Bibliothek.
TU WIEN Bibliothek Your knowledge hub

6.3 Periodic Boundaries

Certain elements of integrated circuits like busses or memory cells make use of periodic structures [116, 117]. As example a part of an interconnect bus is shown in Fig. <6.22>. Often the capacitance between the wires must be extracted which requires the calculation of the electric field, where the wires are connected alternately to 0 V and to 1 V [118]. An appropriately fine resolution of the simulation area is important for the accuracy and leads unfortunately for such domains as in Fig. <6.22> to the generation of a huge number of nodes. Therefore the simulation process will demand a lot of memory, and the simulation duration can be unacceptably long. Considering the periodicity of the structure of Fig. <6.22> in direction of the x axis there is a smart way to solve the problem by investigating only one geometrical period of the structure. A possible geometrical period is the area shown in Fig. <6.23>. The electrodes for the capacitance extraction consist of one interconnect line connected to 1 V and two parts of the neighbor lines connected to 0 V, respectively, which can be seen in the top view in Fig. <6.24>. The interconnect bus of Fig. <6.22> can be created by periodic spatial continuation of the area of Fig. <6.23> along the x axis. Therefore it is not necessary to simulate the whole area of Fig. <6.22>. It is sufficient to simulate a single cell of periodicity as in Fig. <6.23>. The simulation has been performed by our software *Smart Analysis Programs* [119]. It is based on the finite element method using tetrahedral meshes. The algorithm for the linear algebraic equations arising from the finite element discretization is based on the iterative conjugate gradient method which uses an incomplete Cholesky pre-conditioning technique to speed up the iteration process [120, 121, 122, 123]. This application is a typical electro-static problem described by the Laplace equation (4.12) for the electric potential φ. The corresponding numerical analysis is based on scalar finite elements and was discussed in Chapter 4. The solution of the Laplace equation in the dielectric is completely extracted from the data defined on the dielectric boundary. Usually the electrodes are modeled by Dirichlet boundary conditions for the electrostatic potential and the outer boundary of the simulation domain by homogeneous Neumann conditions which can be implemented with the finite element method in a quite natural way. Homogeneous Neumann conditions on a planer surface effect the field in the simulation area in such way, as if the simulation area would be mirrored at the respective boundary face. Such “mirroring conditions” can be exploited for the simulation of symmetric structures and periodic structures which exhibit symmetry. However for general periodic structures proper boundary conditions must be implemented which require special treatment.

In this application two faces $\mathcal{A}_{1p} \subset \partial\mathcal{V}$ and $\mathcal{A}_{2p} \subset \partial\mathcal{V}$ are defined as periodic boundary, if:

- Each node from $\mathcal{A}_{1p}$ is uniquely mapped to another node from $\mathcal{A}_{2p}$ and vice versa.
- If $\vec{r}_{1i}$ is the position pointer to a simulation point of $\mathcal{A}_{1p}$ and $\vec{r}_{2i}$ is the position pointer to the corresponding simulation point of $\mathcal{A}_{2p}$ then $\varphi(\vec{r}_{1i}) = \varphi(\vec{r}_{2i})$ for each point of $\mathcal{A}_{1p}$ and $\mathcal{A}_{2p}$.
- Each node of $\mathcal{A}_{1p}$ has its own neighbor nodes and the neighbor nodes of the corresponding node from $\mathcal{A}_{2p}$.

Die approbierte gedruckte Originalversion dieser Dissertation ist an der TU Wien Bibliothek verfügbar.
The approved original version of this doctoral thesis is available in print at TU Wien Bibliothek.
TU WIEN Bibliothek Your knowledge hub

Although each two corresponding periodic points are separated in the space, due to the periodic condition, they should behave as if they were attached to each other.

If due to the discretization m points are created, the electric potential φ in dielectric $\mathcal{V}_D$ is approximated as (4.13) with (4.22) by the sum

$$\varphi \approx \tilde{\varphi} = \sum_{j=1}^{n} c_j \lambda_j(\vec{r}) + \sum_{j=n+1}^{m} c_j \lambda_j(\vec{r}). \tag{6.26}$$

In (6.26) the unknown nodes are numbered from 1 to n. The Dirichlet (known) nodes are numbered from $n{+}1$ to m. Thus the finite element method leads to a linear equation system for the first n coefficients c_j (the unknown ones with $j \in [1; n]$).

In general the mesh generation software does not order the simulation nodes as in (6.26). To implement the desired node ordering a supplemental auxiliary index array with the length m is allocated. This additional index array is used by the assembling procedure. The first n entries of this index array refer to the nodes in $\mathcal{V}_D$ without the nodes on the Dirichlet boundary. The remaining entries refer to the nodes on the Dirichlet boundary (from $n{+}1$ to m). The additional index assignment of the simulation nodes gives advantages to the implementation of the periodic boundary conditions. Each two corresponding points of the plains $\mathcal{A}_{1p}$ and $\mathcal{A}_{2p}$ get the same index in the additional index array. Thus, they are assembled to the same row in the linear equation system. Due to the element-by-element processing of the simulation volume each periodic point has not only its neighbor nodes but it is also connected to the neighbor nodes of the corresponding periodic point.

6.3.1 Mesh Generation

Although periodic boundary conditions can be applied to an arbitrary pair of faces with unique bidirectional node mapping, we will restrict this paragraph to parallelepiped structures for the sake of clarity. The periodic boundary conditions are applied at two opposite parallel faces. The mesh generated has to guarantee that the surface meshes on these faces are identical. Our interconnect simulation software *Smart Analysis Programs* uses two different three-dimensional mesh generation approaches. The first one is a layered approach which extends two-dimensional meshes [124] into the third dimension by means of linear extrusion. The second approach is a fully unstructured mesh generation method based on the program delink [107, 108]. Both approaches do not fulfill the above mentioned requirements for periodic boundaries a priori. To extend the mesh generation for periodic boundaries we use an iterative approach. In the first step the simulation domain is meshed without any special treatment for periodic boundaries. Afterwards the periodic boundary faces are checked for conformity. If they are not conform, they are merged and the newly generated points are fed into the mesh generator as additional input. After re-meshing of the geometry the periodic boundaries are again checked for conformity. These steps are repeated until conformity is reached. In the layer based meshing approach this iteration procedure must only be applied to the two-dimensional mesh generation process. The additional extrusion step preserves the conformity of the side walls. In the fully unstructured meshing method the conformity of the nodes on the periodic faces is not sufficient, because the same set of boundary nodes can lead to different boundary meshes (at least for cospherical points). Therefore also edge conformity has to be guaranteed during the iteration. Because of these additional difficulties the layer based mesh generation method is preferred for problems with periodic boundaries. Unfortunately, we were not able to prove theoretically that the iteration process necessary for fully unstructured meshes will always terminate, however we have not found any example so far, which took more than 11 iterations.

6.3.2 Simulation Results

The simulation results are evaluated by visualization of the electric field using VTK. In the presented example the simulation area consists of a SiO2 rectangular parallelepiped with the conductors inside as shown in Fig. <6.23>. The faces parallel to the yz plane are defined as periodic boundary. At the remaining outer faces homogeneous Neumann boundary conditions for the electrostatic potential are applied. The simulated potential and the corresponding iso faces with periodic boundary conditions are shown in Fig. <6.25> and Fig. <6.26>. The electric field is equivalent to the electric field in an inner single cell of the original interconnect bus structure. That is as if the simulation domain would be copied repeatedly in x and $-x$ direction by the length of its x dimension. The electric field looks like as if one boundary parallel to yz plane would be directly connected to the opposite one. The stamp of the electrodes which are lying on the one of the periodic faces can be seen on the other periodic face. In order to visualize the effect of the periodic boundary conditions, the same structure has been simulated with homogeneous Neumann boundary conditions (natural boundary conditions) for comparison. The obtained electric potential distribution is displayed in Fig. <6.27> and Fig. <6.28>. In this case the effect of the opposite electrodes is no longer seen on the side walls and the iso surfaces are now perpendicular to the boundary. The field in the simulation area is as if the simulation area would be mirrored with respect to these boundaries.

Originally the z dimension of the simulation region is longer than this one shown in the figures. For visualization the simulation area is cut off perpendicularly to the z axis and closely to the electrodes to minimize the mirronig effect of the homogeneous Neumann boundary conditions at the cutting planes, similarly to Subsection 4.1.5.

As expected the calculated capacitance between the electrodes in the small area from Fig. <6.23> is different for the different boundary conditions applied. The capacitance with the periodic boundary is 1.33 times the capacitance with homogeneous Neumann boundary. The capacitance of the whole area from Fig. <6.22> is the capacitance of the small simulation domain multiplied by the number of all small simulation domains needed to construct the complete structure.

Die approbierte gedruckte Originalversion dieser Dissertation ist an der TU Wien Bibliothek verfügbar.
The approved original version of this doctoral thesis is available in print at TU Wien Bibliothek.

Die approbierte gedruckte Originalversion dieser Dissertation ist an der TU Wien Bibliothek verfügbar.
The approved original version of this doctoral thesis is available in print at TU Wien Bibliothek.

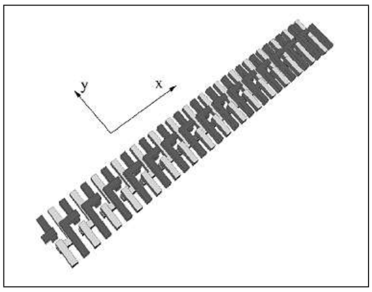

Figure 6.22:
An interconnect bus.

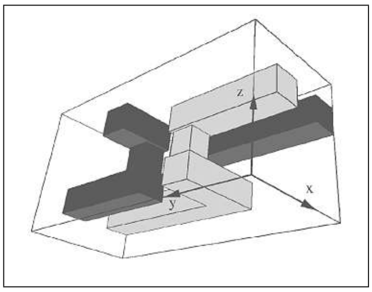

Figure 6.23:
The simulation area.

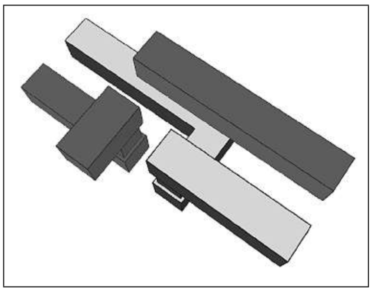

Figure 6.24: The electrodes in the simulation area.

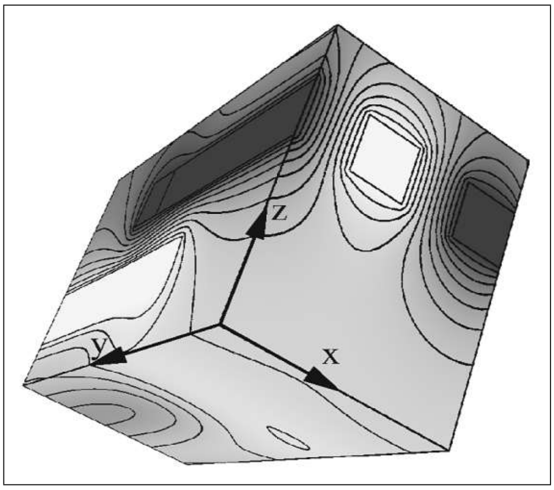

Figure 6.25: The electric potential distribution with x periodicity.

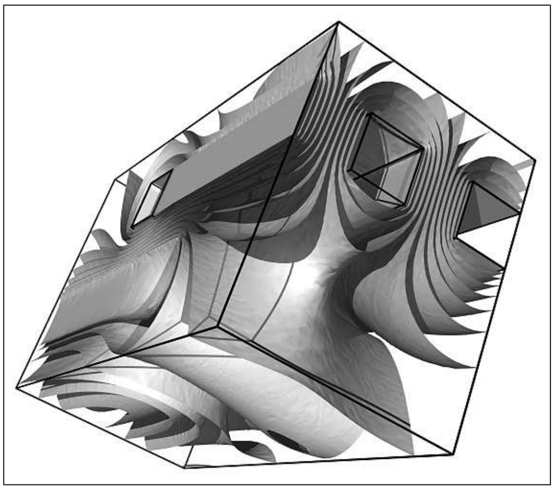

Figure 6.26: The iso faces of the electric potential distribution with x periodicity.

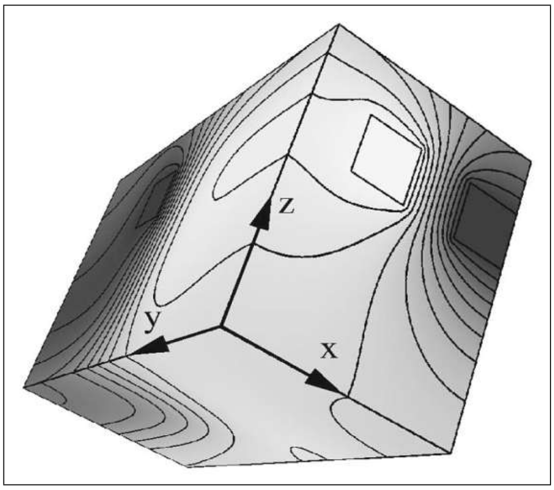

Figure 6.27: The electric potential distribution without periodicity.

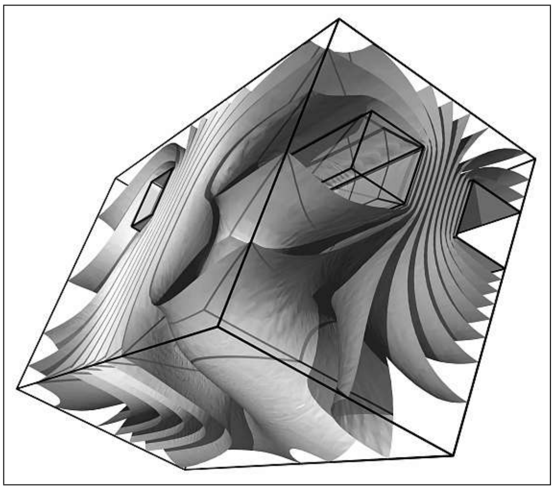

Figure 6.28: The iso faces of the electric potential distribution without periodicity.

Die approbierte gedruckte Originalversion dieser Dissertation ist an der TU Wien Bibliothek verfügbar.
The approved original version of this doctoral thesis is available in print at TU Wien Bibliothek.

Chapter 7

Outlook

This thesis elaborates electromagnetic numerical simulations in microelectronics for field calculations and parameter extraction in interconnect structures based on the finite element analysis with the special usage of edge elements. The method is demonstrated by the quasi-magnetostatic case, which is well suited for the small simulation domains typical for the interconnects in modern integrated circuits even at very high frequencies. In a similar way the proposed approach can be applied to the wave equation for the electric field or to the equations for the electrodynamic potentials in the frequency domain. It is not difficult to see, that the assembling formulas for the element matrices proposed can be used without any modifications, just the notation of the field variables and the constitutive parameters taking part are different. Of coarse, the way how to apply the boundary conditions and how to extract the corresponding parameters must be reconsidered.

The assembling of the approximation of the Neumann boundary conditions is given in the appendix for further implementation. This will allow inhomogeneous Neumann boundary conditions to be taken into account. It can be also used as a foundation for future integration of a combination of the finite element method with a boundary integral method for the analysis of open domains.

Another interesting area for further development and implementation represents the treatment of higher order vector finite elements to achieve efficiently better accuracy of the simulation results. In this case the efficiency bears on the computation, the research and adaptation of the method is much more difficult.

In spite of the fact that the simulation in the frequency domain meets the requirements for a large amount of applications, it is not sufficient, if nonlinear (field dependent) parameters are used. In such a case time domain edge finite element techniques must be addressed and the parameters have to be updated with each computational time step.

Die approbierte gedruckte Originalversion dieser Dissertation ist an der TU Wien Bibliothek verfügbar.
The approved original version of this doctoral thesis is available in print at TU Wien Bibliothek.

Appendix A

Integral Domain Transformation

It has been shown that the barycentric coordinates transform each triangular and tetrahedron element in the unit triangle and tetrahedron, respectively. (Refer to Fig. <4.3> and Fig. <4.8>.) This is used for the analytical calculation of the arising integral terms, when the element matrices are assembled.

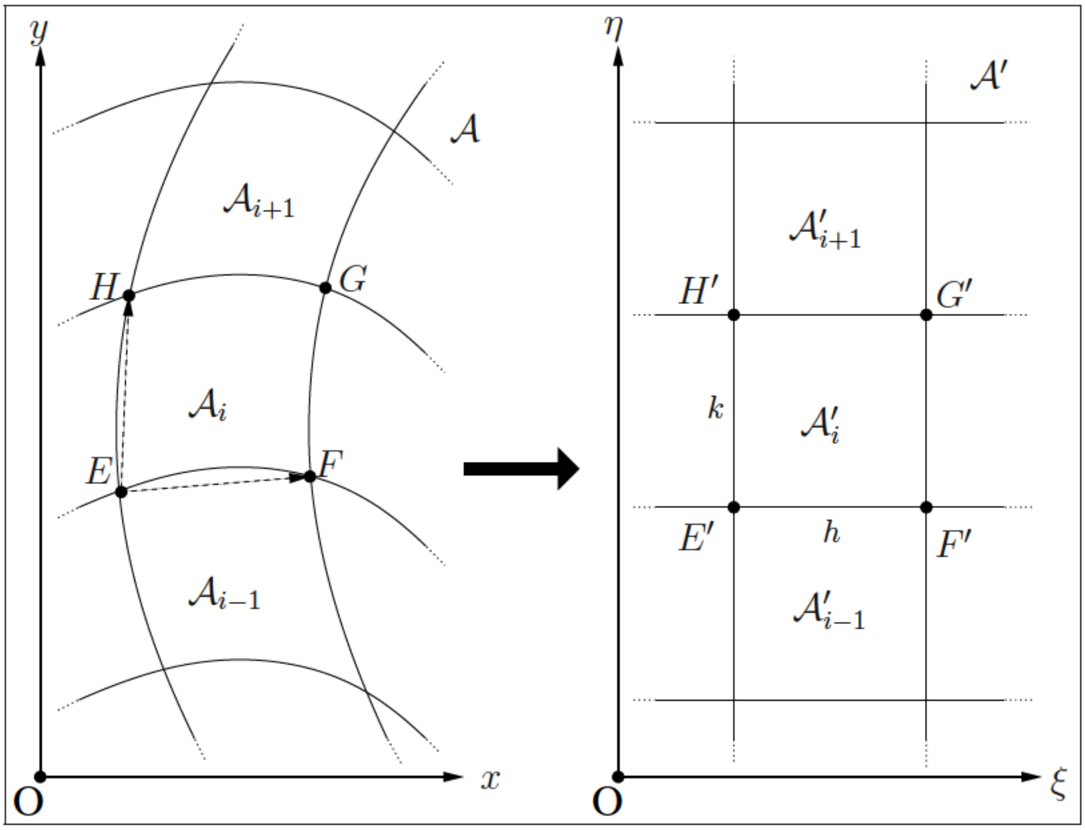

Figure A.1: Two-dimensional domain transformation.

The two-dimensional domain $\mathcal{A}'$ is transformed to $\mathcal{A}$ by the expressions

$$
\begin{aligned}
x &= x(\xi, \eta) \\
y &= y(\xi, \eta).
\end{aligned}
\tag{A.1}
$$

If (x_i, y_i) is a point in $\mathcal{A}_i$, (ξ_i, η_i) is a point in $\mathcal{A}'_i:\ x_i = x(\xi_i, \eta_i),\ y_i = y(\xi_i, \eta_i)$, and $\mathcal{A} = \sum_{i=1}^{n} \mathcal{A}_i,\ \mathcal{A}' = \sum_{i=1}^{n} \mathcal{A}'_i$.

$$
\begin{aligned}
&E'F'G'H' \rightarrow EFGH: \\
&E'(\xi, \eta),\ F'(\xi + h, \eta),\ G'(\xi + h, \eta + k),\ H'(\xi, \eta + k), \\
&E(\,x(\xi, \eta), y(\xi, \eta)\,),\ F(\,x(\xi + h, \eta), y(\xi + h, \eta)\,), \\
&G(\,x(\xi + h, \eta + k), y(\xi + h, \eta + k)\,),\ H(\,x(\xi, \eta + k), y(\xi, \eta + k)\,).
\end{aligned}
\tag{A.2}
$$

The area A_i of the i-th element $EFGH$ is approximately related by the vector product

$$
\vec{EF} \left\{
\begin{aligned}
x(\xi + h, \eta) - x(\xi, \eta) &= x_\xi(\tilde{\xi}, \eta)\, h \\
y(\xi + h, \eta) - y(\xi, \eta) &= y_\xi(\tilde{\tilde{\xi}}, \eta)\, h
\end{aligned}
\right.
\tag{A.3}
$$

and

$$
\vec{EH} \left\{
\begin{aligned}
x(\xi, \eta + k) - x(\xi, \eta) &= x_\eta(\xi, \tilde{\eta})\, k \\
y(\xi, \eta + k) - y(\xi, \eta) &= y_\eta(\xi, \tilde{\tilde{\eta}})\, k
\end{aligned}
\right. \quad ,
\tag{A.4}
$$

where

$$
\tilde{\xi} \in [\xi; \xi + h],\ \tilde{\tilde{\xi}} \in [\xi; \xi + h],\ \tilde{\eta} \in [\eta; \eta + k],\ \tilde{\tilde{\eta}} \in [\eta; \eta + k].
\tag{A.5}
$$

For sufficiently small h and k the face A_i is expressed as

$$
\begin{aligned}
A_i = |\vec{EF} \times \vec{EH}| &= [x_\xi(\tilde{\xi}, \eta) y_\eta(\xi, \tilde{\tilde{\eta}}) - x_\eta(\xi, \tilde{\eta}) y_\xi(\tilde{\tilde{\xi}}, \eta)]|hk| = \\
&= [x_\xi(\xi, \eta) y_\eta(\xi, \eta) - x_\eta(\xi, \eta) y_\xi(\xi, \eta)]|hk| = J(\xi, \eta)\ A'_i
\end{aligned}
\tag{A.6}
$$

with

$$
J(\xi, \eta) = \begin{vmatrix} x_\xi & x_\eta \\ y_\xi & y_\eta \end{vmatrix},\ A'_i = |hk|
\tag{A.7}
$$

Die approbierte gedruckte Originalversion dieser Dissertation ist an der TU Wien Bibliothek verfügbar.
The approved original version of this doctoral thesis is available in print at TU Wien Bibliothek.

and an integral is given by the Riemann sum

$$\begin{aligned}\int\limits_{\mathcal{A}} f(x,y)\,\mathrm{d}A = \sum_{i=1}^{n} f(x_i,y_i)A_i = \sum_{i=1}^{n} f(x(\xi_i,\eta_i),y(\xi_i,\eta_i))J(\xi_i,\eta_i)A'_i = \\ = \int\limits_{\mathcal{A}'} f(x(\xi,\eta),y(\xi,\eta))J(\xi,\eta)\,\mathrm{d}A'.\end{aligned} \tag{A.8}$$

Analogously the transformation for the three-dimensional case can be expressed by:

$$\int\limits_{\mathcal{A}} f(x,y,z)\,\mathrm{d}A = \int\limits_{\mathcal{A}'} f(x(\xi,\eta,\zeta),y(\xi,\eta,\zeta),z(\xi,\eta,\zeta))J(\xi,\eta,\zeta)\,\mathrm{d}A' \tag{A.9}$$

with

$$J(\xi,\eta,\zeta) = \begin{vmatrix} x_\xi & x_\eta & x_\zeta \\ y_\xi & y_\eta & y_\zeta \\ z_\xi & z_\eta & z_\zeta \end{vmatrix}. \tag{A.10}$$

Die approbierte gedruckte Originalversion dieser Dissertation ist an der TU Wien Bibliothek verfügbar.
The approved original version of this doctoral thesis is available in print at TU Wien Bibliothek.

Die approbierte gedruckte Originalversion dieser Dissertation ist an der TU Wien Bibliothek verfügbar.
The approved original version of this doctoral thesis is available in print at TU Wien Bibliothek.
TU WIEN Bibliothek Your knowledge hub

Appendix B

Two-Dimensional Neumann Boundary Term

As usual for the finite element method the assembling is performed element wise. Refer to the triangular element and its corresponding notations from Fig. <4.1>. Only elements which lie on the Neumann boundary (triangles with one or more edges as part of the Neumann boundary) are considered. The three edges in the triangle refer to as $\mathcal{C}^e_{12}$, $\mathcal{C}^e_{23}$ and $\mathcal{C}^e_{31}$, where the subscript indexes 1, 2, and 3 are the element nodes or to $\mathcal{C}^e_1$, $\mathcal{C}^e_2$ and $\mathcal{C}^e_3$, where the subscript indexes 1, 2, and 3 are the element edges.

B.1 Neumann Boundary for the Rotor-Rotor-Operator

The Neumann boundary integral from (5.74) is modified to read

$$\begin{aligned}\int\limits_{\mathcal{C}_{N1}} \vec{n}\cdot\left[\vec{N}_i\times\left(\frac{1}{\gamma}\vec{\nabla}\times\vec{H}_1\right)\right]\,\mathrm{d}s &= \sum_j c_j \int\limits_{\mathcal{C}_{N1}} \vec{n}\cdot\left[\vec{N}_i\times\left(\frac{1}{\gamma}\vec{\nabla}\times\vec{N}_j\right)\right]\,\mathrm{d}s = \\ &= [D]\,\{c\}\,.\end{aligned} \tag{B.1}$$

Three different cases for each of the three edges of every triangular element must be considered. γ is assumed to be a constant scalar in each element.

For the computation of the element matrix

$$\begin{aligned}D^e_{ij} &= \int\limits_{\mathcal{C}^e_k} \vec{n}_k\cdot\left[\vec{N}^e_i\times\left(\frac{1}{\gamma}\vec{\nabla}\times\vec{N}^e_j\right)\right]\,\mathrm{d}s = \int\limits_{\mathcal{C}^e_k}\left(\vec{n}_k\times\vec{N}^e_i\right)\cdot\left(\frac{1}{\gamma}\vec{\nabla}\times\vec{N}^e_j\right) = \\ &= \left[\int\limits_{\mathcal{C}^e_k}\left(\vec{n}_k\times\vec{N}^e_i\right)\,\mathrm{d}s\right]\cdot\left(\frac{1}{\gamma}\vec{\nabla}\times\vec{N}^e_j\right),\quad i\in[1;3],\quad j\in[1;3],\quad k\in[1;3]\end{aligned} \tag{B.2}$$

Die approbierte gedruckte Originalversion dieser Dissertation ist an der TU Wien Bibliothek verfügbar.
The approved original version of this doctoral thesis is available in print at TU Wien Bibliothek.
TU WIEN Bibliothek Your knowledge hub

the following expressions must be calculated

$$(l_{23}\vec{n}_1) \times \vec{\nabla}\lambda_1^e = -(l_{23}\vec{n}_1) \times \frac{l_{23}\vec{n}_1}{2F_e} = \vec{0} \tag{B.3}$$

$$\begin{aligned}(l_{23}\vec{n}_1) \times \vec{\nabla}\lambda_2^e &= -(\vec{r}_{23} \times \vec{e}_z) \times \frac{\vec{r}_{31} \times \vec{e}_z}{2F_e} = \frac{\vec{e}_z}{2F_e}\vec{r}_{31} \cdot (\vec{r}_{23} \times \vec{e}_z) = \\ &= \frac{\vec{e}_z}{2F_e} \underbrace{\vec{e}_z \cdot (\vec{r}_{31} \times \vec{r}_{23})}_{-2F_e} = -\vec{e}_z\end{aligned} \tag{B.4}$$

$$(l_{23}\vec{n}_1) \times \vec{\nabla}\lambda_3^e = \frac{\vec{e}_z}{2F_e} \underbrace{\vec{e}_z \cdot (\vec{r}_{12} \times \vec{r}_{23})}_{2F_e} = \vec{e}_z \tag{B.5}$$

$$(l_{31}\vec{n}_2) \times \vec{\nabla}\lambda_1^e = \vec{e}_z \qquad (l_{31}\vec{n}_2) \times \vec{\nabla}\lambda_2^e = \vec{0} \qquad (l_{31}\vec{n}_2) \times \vec{\nabla}\lambda_3^e = -\vec{e}_z \tag{B.6}$$

$$(l_{12}\vec{n}_3) \times \vec{\nabla}\lambda_1^e = -\vec{e}_z \qquad (l_{12}\vec{n}_3) \times \vec{\nabla}\lambda_2^e = \vec{e}_z \qquad (l_{12}\vec{n}_3) \times \vec{\nabla}\lambda_3^e = \vec{0} \tag{B.7}$$

$$\begin{aligned}\vec{\nabla} \times \vec{N}_1^e &= 2l_{12}\left(\vec{\nabla}\lambda_1^e \times \vec{\nabla}\lambda_2^e\right) = 2l_{12}\left(\frac{\vec{r_{23}} \times \vec{e}_z}{2F_e} \times \frac{\vec{r_{31}} \times \vec{e}_z}{2F_e}\right) = \\ &= -2l_{12}\frac{\vec{e}_z\left[\vec{r}_{31} \cdot (\vec{r_{23}} \times \vec{e}_z)\right]}{4F_e^2} = \frac{l_{12}}{2F_e^2}\vec{e}_z \underbrace{\left[\vec{e}_z \cdot (\vec{r_{23}} \times \vec{r}_{31})\right]}_{2F_e} = \frac{l_{12}}{F_e}\vec{e}_z\end{aligned} \tag{B.8}$$

$$\vec{\nabla} \times \vec{N}_2^e = \frac{l_{23}}{F_e}\vec{e}_z \tag{B.9}$$

$$\vec{\nabla} \times \vec{N}_3^e = \frac{l_{31}}{F_e}\vec{e}_z. \tag{B.10}$$

Along Edge 12:

$$\left.\begin{array}{l}\lambda_3^e = 0 \\ \lambda_2^e = 1 - \lambda_1^e\end{array}\right\} \Rightarrow \vec{r} = \sum_{i=1}^{n} \lambda_i^e \vec{r}_i = (\vec{r}_1 - \vec{r}_2)\lambda_1^e + \vec{r}_2 = \vec{r}_{21}\lambda_1^e + \vec{r}_2 \tag{B.11}$$

$$s = \vec{r} \cdot \vec{e}_{21} \quad \Rightarrow \quad \mathrm{d}s = \vec{r}_{21} \cdot \vec{e}_{21}\, d\lambda_1^e = l_{12}\, d\lambda_1^e \tag{B.12}$$

or for λ_2^e

$$\left.\begin{array}{l}\lambda_3^e = 0 \\ \lambda_1^e = 1 - \lambda_2^e\end{array}\right\} \Rightarrow \vec{r} = \sum_{i=1}^{n} \lambda_i^e \vec{r}_i = (\vec{r}_2 - \vec{r}_1)\lambda_2^e + \vec{r}_1 = \vec{r}_{12}\lambda_2^e + \vec{r}_2 \tag{B.13}$$

$$s = \vec{r} \cdot \vec{e}_{12} \quad \Rightarrow \quad \mathrm{d}s = \vec{r}_{12} \cdot \vec{e}_{12}\, d\lambda_2^e = l_{12}\, d\lambda_2^e \tag{B.14}$$

Die approbierte gedruckte Originalversion dieser Dissertation ist an der TU Wien Bibliothek verfügbar.
The approved original version of this doctoral thesis is available in print at TU Wien Bibliothek.
TU Bibliothek, WIEN Your knowledge hub

$$
\begin{aligned}
D_{ij}^e &= \frac{1}{\gamma}\int\limits_{\mathcal{C}_{12}^e} \vec{n}_3 \cdot \left[\vec{N}_i^e \times \left(\vec{\nabla}\times\vec{N}_j^e\right)\right] \,\mathrm{d}s = \frac{1}{\gamma}\int\limits_{\mathcal{C}_{12}^e} \left(\vec{n}_3\times\vec{N}_i^e\right)\cdot\left(\vec{\nabla}\times\vec{N}_j^e\right) = \\
&= \frac{1}{\gamma}\left[\int\limits_{\mathcal{C}_{12}^e}\left(\vec{n}_3\times\vec{N}_i^e\right)\mathrm{d}s\right]\cdot\left(\vec{\nabla}\times\vec{N}_j^e\right), \quad i\in[1;3], \quad j\in[1;3]
\end{aligned}
\tag{B.15}
$$

$$
\begin{aligned}
\int\limits_{\mathcal{C}_{12}^e}\left(\vec{n}_3\times\vec{N}_1^e\right)\mathrm{d}s &= \int\limits_{\mathcal{C}_{12}^e}\left\{\vec{n}_3\times\left[l_{12}\left(\lambda_1^e\vec{\nabla}\lambda_2^e-\lambda_2^e\vec{\nabla}\lambda_1^e\right)\right]\right\}\mathrm{d}s = \\
&= l_{12}\left\{\left[(l_{12}\vec{n}_3)\times\vec{\nabla}\lambda_2^e\right]\int\limits_0^1\lambda_1^e\,d\lambda_1^e-\left[(l_{12}\vec{n}_3)\times\vec{\nabla}\lambda_1^e\right]\int\limits_0^1\lambda_2^e\,d\lambda_2^e\right\} = \\
&= l_{12}\vec{e}_z
\end{aligned}
\tag{B.16}
$$

$$
\begin{aligned}
\int\limits_{\mathcal{C}_{12}^e}\left(\vec{n}_3\times\vec{N}_2^e\right)\mathrm{d}s &= \int\limits_{\mathcal{C}_{12}^e}\left\{\vec{n}_3\times\left[l_{23}\left(\lambda_2^e\vec{\nabla}\lambda_3^e-\lambda_3^e\vec{\nabla}\lambda_2^e\right)\right]\right\}\mathrm{d}s = \\
&= l_{23}\left\{\underbrace{\left[(l_{12}\vec{n}_3)\times\vec{\nabla}\lambda_3^e\right]}_{0}\int\limits_0^1\lambda_2^e\,d\lambda_2^e-\left(\vec{n}_3\times\vec{\nabla}\lambda_2^e\right)\underbrace{\int\limits_{\mathcal{C}_{12}^e}\lambda_3^e\,\mathrm{d}s}_{0}\right\} = \\
&= \vec{0}
\end{aligned}
\tag{B.17}
$$

$$
\begin{aligned}
\int\limits_{\mathcal{C}_{12}^e}\left(\vec{n}_3\times\vec{N}_3^e\right)\mathrm{d}s &= \int\limits_{\mathcal{C}_{12}^e}\left\{\vec{n}_3\times\left[l_{31}\left(\lambda_3^e\vec{\nabla}\lambda_1^e-\lambda_1^e\vec{\nabla}\lambda_3^e\right)\right]\right\}\mathrm{d}s = \\
&= l_{31}\left\{\left(\vec{n}_3\times\vec{\nabla}\lambda_1^e\right)\underbrace{\int\limits_{\mathcal{C}_{12}^e}\lambda_3^e\,\mathrm{d}s}_{0}-\underbrace{\left[(l_{12}\vec{n}_3)\times\vec{\nabla}\lambda_3^e\right]}_{0}\int\limits_0^1\lambda_1^e\,d\lambda_1^e\right\} = \\
&= \vec{0}
\end{aligned}
\tag{B.18}
$$

$$
[D]^e = \frac{1}{\gamma\,F_e}\begin{bmatrix} l_{12}l_{12} & l_{12}l_{23} & l_{12}l_{31} \\ 0 & 0 & 0 \\ 0 & 0 & 0 \end{bmatrix}.
\tag{B.19}
$$

Analogously the element matrices for the remaining edges are obtained.

Along Edge 23:

$$[D]^e = \frac{1}{\gamma\, F_e}\begin{bmatrix} 0 & 0 & 0 \\ l_{23}l_{12} & l_{23}l_{23} & l_{23}l_{31} \\ 0 & 0 & 0 \end{bmatrix}. \tag{B.20}$$

Along Edge 31:

$$[D]^e = \frac{1}{\gamma\, F_e}\begin{bmatrix} 0 & 0 & 0 \\ 0 & 0 & 0 \\ l_{31}l_{12} & l_{31}l_{23} & l_{31}l_{31} \end{bmatrix}. \tag{B.21}$$

B.2 Neumann Boundary for Gauß's Law of Magnetism

B.2.1 For the Scalar Function

The Neumann boundary integral for ψ from (5.75) is modified to read

$$\begin{aligned} \int\limits_{\mathcal{C}_{N2}} \lambda_i \vec{n} \cdot \left(\underset{\sim}{\mu} \cdot \vec{\nabla}\psi\right) \mathrm{d}s = \sum_j c_j \int\limits_{\mathcal{C}_{N2}} \lambda_i \vec{n} \cdot \left(\underset{\sim}{\mu} \cdot \vec{\nabla}\lambda_j\right) \mathrm{d}s = \\ = [D]\,\{c\} \end{aligned} \tag{B.22}$$

$$D^e_{ij} = \mu \left(\int\limits_{\mathcal{C}^e_k} \lambda^e_i \,\mathrm{d}s \right) \vec{n}_k \cdot \vec{\nabla}\lambda^e_j, \quad i \in [1;3],\ j \in [1;3],\ k \in [1;3]. \tag{B.23}$$

For the computation of $[D]$ the following expressions are obtained:

$$(l_{12}\vec{n}_3) \cdot \vec{\nabla}\lambda^e_1 = -\left(\vec{r}_{12} \times \vec{e}_z\right) \cdot \frac{\vec{r}_{23} \times \vec{e}_z}{2F_e} = -\frac{\vec{r}_{12} \cdot \vec{r}_{23}}{2F_e} \tag{B.24}$$

and analogously

$$(l_{12}\vec{n}_3) \cdot \vec{\nabla}\lambda^e_2 = -\frac{\vec{r}_{12} \cdot \vec{r}_{31}}{2F_e} \qquad (l_{12}\vec{n}_3) \cdot \vec{\nabla}\lambda^e_3 = -\frac{\vec{r}_{12} \cdot \vec{r}_{12}}{2F_e} \tag{B.25}$$

$$\begin{aligned} &(l_{23}\vec{n}_1) \cdot \vec{\nabla}\lambda^e_2 = -\frac{\vec{r}_{23} \cdot \vec{r}_{31}}{2F_e} \qquad (l_{23}\vec{n}_1) \cdot \vec{\nabla}\lambda^e_3 = -\frac{\vec{r}_{23} \cdot \vec{r}_{12}}{2F_e} \\ &(l_{23}\vec{n}_1) \cdot \vec{\nabla}\lambda^e_3 = -\frac{\vec{r}_{23} \cdot \vec{r}_{12}}{2F_e} \end{aligned} \tag{B.26}$$

Die approbierte gedruckte Originalversion dieser Dissertation ist an der TU Wien Bibliothek verfügbar.
The approved original version of this doctoral thesis is available in print at TU Wien Bibliothek.
TU WIEN Bibliothek Your knowledge hub

$$
\begin{aligned}
&(l_{31}\vec{n}_2)\cdot\vec{\nabla}\lambda_2^e = -\frac{\vec{r}_{31}\cdot\vec{r}_{31}}{2F_e} \qquad (l_{31}\vec{n}_2)\cdot\vec{\nabla}\lambda_3^e = -\frac{\vec{r}_{31}\cdot\vec{r}_{12}}{2F_e}\\
&(l_{31}\vec{n}_2)\cdot\vec{\nabla}\lambda_3^e = -\frac{\vec{r}_{31}\cdot\vec{r}_{12}}{2F_e}.
\end{aligned}
\tag{B.27}
$$

Along Edge 12:

$$
D_{1j}^e = \mu\left(\int_{\mathcal{C}_1^e}\lambda_1^e\,\mathrm{d}s\right)\vec{n}_3\cdot\vec{\nabla}\lambda_j^e = \mu\left(\int_0^1\lambda_1^e\,d\lambda_1\right)(l_{12}\vec{n}_3)\cdot\vec{\nabla}\lambda_j^e = \frac{\mu}{2}\,(l_{12}\vec{n}_3)\cdot\vec{\nabla}\lambda_j^e \tag{B.28}
$$

$$
D_{2j}^e = \mu\left(\int_{\mathcal{C}_1^e}\lambda_2^e\,\mathrm{d}s\right)\vec{n}_3\cdot\vec{\nabla}\lambda_j^e = \mu\left(\int_0^1\lambda_2^e\,d\lambda_2\right)(l_{12}\vec{n}_3)\cdot\vec{\nabla}\lambda_j^e = \frac{\mu}{2}\,(l_{12}\vec{n}_3)\cdot\vec{\nabla}\lambda_j^e \tag{B.29}
$$

$$
D_{3j}^e = \mu\left(\int_{\mathcal{C}_1^e}\lambda_3^e\,\mathrm{d}s\right)\vec{n}_3\cdot\vec{\nabla}\lambda_j^e = 0, \qquad \lambda_3^e = 0 \text{ on Edge 12} \tag{B.30}
$$

$$
[D]^e = -\frac{\mu}{4F_e}\begin{bmatrix}
\vec{r}_{12}\cdot\vec{r}_{23} & \vec{r}_{12}\cdot\vec{r}_{31} & \vec{r}_{12}\cdot\vec{r}_{12}\\
\vec{r}_{12}\cdot\vec{r}_{23} & \vec{r}_{12}\cdot\vec{r}_{31} & \vec{r}_{12}\cdot\vec{r}_{12}\\
0 & 0 & 0
\end{bmatrix}. \tag{B.31}
$$

Analogously for the remaining edges the following is calculated.

Along Edge 23:

$$
[D]^e = -\frac{\mu}{4F_e}\begin{bmatrix}
0 & 0 & 0\\
\vec{r}_{23}\cdot\vec{r}_{23} & \vec{r}_{23}\cdot\vec{r}_{31} & \vec{r}_{23}\cdot\vec{r}_{12}\\
\vec{r}_{23}\cdot\vec{r}_{23} & \vec{r}_{23}\cdot\vec{r}_{31} & \vec{r}_{23}\cdot\vec{r}_{12}
\end{bmatrix}. \tag{B.32}
$$

Along Edge 31:

$$
[D]^e = -\frac{\mu}{4F_e}\begin{bmatrix}
\vec{r}_{31}\cdot\vec{r}_{23} & \vec{r}_{31}\cdot\vec{r}_{31} & \vec{r}_{31}\cdot\vec{r}_{12}\\
0 & 0 & 0\\
\vec{r}_{31}\cdot\vec{r}_{23} & \vec{r}_{31}\cdot\vec{r}_{31} & \vec{r}_{31}\cdot\vec{r}_{12}
\end{bmatrix}. \tag{B.33}
$$

Die approbierte gedruckte Originalversion dieser Dissertation ist an der TU Wien Bibliothek verfügbar.
The approved original version of this doctoral thesis is available in print at TU Wien Bibliothek.

Die approbierte gedruckte Originalversion dieser Dissertation ist an der TU Wien Bibliothek verfügbar.
The approved original version of this doctoral thesis is available in print at TU Wien Bibliothek.

B.2.2 For the Vector Function

The Neumann boundary integral for $\vec{H}_1$ from (5.75) is written in the form

$$\begin{aligned}\int\limits_{\mathcal{C}_{N2}} \lambda_i \vec{n} \cdot \left(\underset{\sim}{\mu} \cdot \vec{H}_1 \right) \mathrm{d}s = \sum_j c_j \int\limits_{\mathcal{C}_{N2}} \lambda_i \vec{n} \cdot \left(\underset{\sim}{\mu} \cdot \vec{N}_j \right) \mathrm{d}s = \\ = [D]\,\{c\}\end{aligned} \tag{B.34}$$

$$D^e_{ij} = \mu \int\limits_{\mathcal{C}^e_k} \lambda^e_i \vec{n}_k \cdot \vec{N}^e_j \,\mathrm{d}s, \quad i \in [1;3],\; j \in [1;3],\; k \in [1;3]. \tag{B.35}$$

Along Edge 12:

$$\begin{aligned}
D^e_{11} &= \mu \int\limits_{\mathcal{C}^e_1} \lambda^e_1 \vec{n}_3 \cdot \vec{N}^e_1 \,\mathrm{d}s = \mu \int\limits_{\mathcal{C}^e_1} \lambda^e_1 \vec{n}_3 \cdot \left[l_{12} \left(\lambda^e_1 \vec{\nabla} \lambda^e_2 - \lambda^e_2 \vec{\nabla} \lambda^e_1 \right) \right] \mathrm{d}s = \\
&= \mu l_{12} \left(\vec{n}_3 \cdot \vec{\nabla} \lambda^e_2 \int\limits_{\mathcal{C}^e_1} \lambda^e_1 \lambda^e_1 \,\mathrm{d}s - \vec{n}_3 \cdot \vec{\nabla} \lambda^e_1 \int\limits_{\mathcal{C}^e_1} \lambda^e_1 \lambda^e_2 \,\mathrm{d}s \right) = \\
&= \mu l_{12} \left[\vec{n}_3 \cdot \vec{\nabla} \lambda^e_2 \int\limits_{\mathcal{C}^e_1} \lambda^e_1 \lambda^e_1 \,\mathrm{d}s - \vec{n}_3 \cdot \vec{\nabla} \lambda^e_1 \int\limits_{\mathcal{C}^e_1} \lambda^e_1 \left(1 - \lambda^e_1 \right) \mathrm{d}s \right] = \\
&= \mu l_{12} \left\{ (l_{12} \vec{n}_3) \cdot \vec{\nabla} \lambda^e_2 \int\limits_0^1 (\lambda^e_1)^2 \, d\lambda^e_1 - (l_{12} \vec{n}_3) \cdot \vec{\nabla} \lambda^e_1 \int\limits_0^1 \left[\lambda^e_1 - (\lambda^e_1)^2 \right] d\lambda^e_1 \right\} = \\
&= -\frac{\mu l_{12}}{12 F_e} \left(2\, \vec{r}_{12} \cdot \vec{r}_{31} - \vec{r}_{12} \cdot \vec{r}_{23} \right)
\end{aligned} \tag{B.36}$$

$$\begin{aligned}
D^e_{12} &= \mu \int\limits_{\mathcal{C}^e_1} \lambda^e_1 \vec{n}_3 \cdot \vec{N}^e_2 \,\mathrm{d}s = \mu \int\limits_{\mathcal{C}^e_1} \lambda^e_1 \vec{n}_3 \cdot \left[l_{23} \left(\lambda^e_2 \vec{\nabla} \lambda^e_3 - \lambda^e_3 \vec{\nabla} \lambda^e_2 \right) \right] \mathrm{d}s = \\
&= \mu l_{23} \left(\vec{n}_3 \cdot \vec{\nabla} \lambda^e_3 \int\limits_{\mathcal{C}^e_1} \lambda^e_1 \lambda^e_2 \,\mathrm{d}s - \vec{n}_3 \cdot \vec{\nabla} \lambda^e_2 \underbrace{\int\limits_{\mathcal{C}^e_1} \lambda^e_1 \lambda^e_3 \,\mathrm{d}s}_{0} \right) = \\
&= \mu l_{23}\, \vec{n}_3 \cdot \vec{\nabla} \lambda^e_3 \int\limits_{\mathcal{C}^e_1} \lambda^e_1 \lambda^e_2 \,\mathrm{d}s = \mu l_{23} \left(l_{12} \vec{n}_3 \right) \cdot \vec{\nabla} \lambda^e_3 \int\limits_0^1 \lambda^e_1 \lambda^e_2 \, d\lambda^e_1 = \\
&= -\frac{\mu l_{23}}{12 F_e}\, \vec{r}_{12} \cdot \vec{r}_{12}
\end{aligned} \tag{B.37}$$

Die approbierte gedruckte Originalversion dieser Dissertation ist an der TU Wien Bibliothek verfügbar.
The approved original version of this doctoral thesis is available in print at TU Wien Bibliothek.

$$\begin{aligned} D^e_{13} &= \mu \int\limits_{\mathcal{C}^e_1} \lambda^e_1 \vec{n}_3 \cdot \vec{N}^e_3 \,\mathrm{d}s = \mu \int\limits_{\mathcal{C}^e_1} \lambda^e_1 \vec{n}_3 \cdot \left[l_{31} \left(\lambda^e_3 \vec{\nabla} \lambda^e_1 - \lambda^e_1 \vec{\nabla} \lambda^e_3 \right) \right] \mathrm{d}s = \\ &= \mu l_{31} \left(\vec{n}_3 \cdot \vec{\nabla} \lambda^e_1 \underbrace{\int\limits_{\mathcal{C}^e_1} \lambda^e_1 \lambda^e_3 \,\mathrm{d}s}_{0} - \vec{n}_3 \cdot \vec{\nabla} \lambda^e_3 \int\limits_{\mathcal{C}^e_1} \lambda^e_1 \lambda^e_1 \,\mathrm{d}s \right) = \\ &= -\mu l_{31} \, \vec{n}_3 \cdot \vec{\nabla} \lambda^e_3 \int\limits_{\mathcal{C}^e_1} \lambda^e_1 \lambda^e_1 \,\mathrm{d}s = -\mu l_{31} \left(l_{12} \vec{n}_3 \right) \cdot \vec{\nabla} \lambda^e_3 \int\limits_0^1 \left(\lambda^e_1 \right)^2 \, d\lambda^e_1 = \\ &= \frac{\mu l_{31}}{6F_e} \, \vec{r}_{12} \cdot \vec{r}_{12} \end{aligned} \tag{B.38}$$

$$D^e_{21} = -\frac{\mu l_{12}}{12F_e} \left(\vec{r}_{12} \cdot \vec{r}_{31} - 2\, \vec{r}_{12} \cdot \vec{r}_{23} \right) \tag{B.39}$$

$$D^e_{22} = -\frac{\mu l_{23}}{6F_e} \, \vec{r}_{12} \cdot \vec{r}_{12} \tag{B.40}$$

$$D^e_{23} = \frac{\mu l_{31}}{12F_e} \, \vec{r}_{12} \cdot \vec{r}_{12} \tag{B.41}$$

$$D^e_{3j} = \mu \int\limits_{\mathcal{C}^e_1} \lambda^e_3 \, \vec{n}_3 \cdot \vec{N}^e_j \,\mathrm{d}s = 0, \;\; \lambda^e_3 = 0 \text{ on Edge 12.} \tag{B.42}$$

Along Edge 23:

$$D^e_{1j} = \mu \int\limits_{\mathcal{C}^e_2} \lambda^e_1 \, \vec{n}_1 \cdot \vec{N}^e_j \,\mathrm{d}s = 0, \;\; \lambda^e_1 = 0 \text{ on Edge 23} \tag{B.43}$$

$$
\begin{aligned}
D^e_{21} &= \mu \int\limits_{\mathcal{C}^e_2} \lambda^e_2 \vec{n}_1 \cdot \vec{N}^e_1 \, \mathrm{d}s = \mu \int\limits_{\mathcal{C}^e_2} \lambda^e_2 \vec{n}_1 \cdot \left[l_{12} \left(\lambda^e_1 \vec{\nabla} \lambda^e_2 - \lambda^e_2 \vec{\nabla} \lambda^e_1 \right) \right] \, \mathrm{d}s = \\
&= \mu l_{12} \left(\vec{n}_1 \cdot \vec{\nabla} \lambda^e_2 \underbrace{\int\limits_{\mathcal{C}^e_2} \lambda^e_2 \lambda^e_1 \, \mathrm{d}s}_{0} - \vec{n}_1 \cdot \vec{\nabla} \lambda^e_1 \int\limits_{\mathcal{C}^e_2} \lambda^e_2 \lambda^e_2 \, \mathrm{d}s \right) = \\
&= -\mu l_{12} \, \vec{n}_1 \cdot \vec{\nabla} \lambda^e_1 \int\limits_{\mathcal{C}^e_2} \lambda^e_2 \lambda^e_2 \, \mathrm{d}s = -\mu l_{12} \left(l_{23} \vec{n}_1 \right) \cdot \vec{\nabla} \lambda^e_1 \int\limits_0^1 \left(\lambda^e_2 \right)^2 \, d\lambda^e_2 = \\
&= \frac{\mu l_{12}}{6 F_e} \, \vec{r}_{23} \cdot \vec{r}_{23}
\end{aligned}
\tag{B.44}
$$

$$
\begin{aligned}
D^e_{22} &= \mu \int\limits_{\mathcal{C}^e_2} \lambda^e_2 \vec{n}_1 \cdot \vec{N}^e_2 \, \mathrm{d}s = \mu \int\limits_{\mathcal{C}^e_2} \lambda^e_2 \vec{n}_1 \cdot \left[l_{23} \left(\lambda^e_2 \vec{\nabla} \lambda^e_3 - \lambda^e_3 \vec{\nabla} \lambda^e_2 \right) \right] \, \mathrm{d}s = \\
&= \mu l_{23} \left(\vec{n}_1 \cdot \vec{\nabla} \lambda^e_3 \int\limits_{\mathcal{C}^e_2} \lambda^e_2 \lambda^e_2 \, \mathrm{d}s - \vec{n}_1 \cdot \vec{\nabla} \lambda^e_2 \int\limits_{\mathcal{C}^e_2} \lambda^e_2 \lambda^e_3 \, \mathrm{d}s \right) = \\
&= \mu l_{23} \left[\vec{n}_1 \cdot \vec{\nabla} \lambda^e_3 \int\limits_{\mathcal{C}^e_2} \lambda^e_2 \lambda^e_2 \, \mathrm{d}s - \vec{n}_1 \cdot \vec{\nabla} \lambda^e_2 \int\limits_{\mathcal{C}^e_2} \lambda^e_2 \left(1 - \lambda^e_2 \right) \, \mathrm{d}s \right] = \\
&= \mu l_{23} \left\{ \left(l_{23} \vec{n}_1 \right) \cdot \vec{\nabla} \lambda^e_3 \int\limits_0^1 \left(\lambda^e_2 \right)^2 \, d\lambda^e_2 - \left(l_{23} \vec{n}_1 \right) \cdot \vec{\nabla} \lambda^e_2 \int\limits_0^1 \left[\lambda^e_2 - \left(\lambda^e_2 \right)^2 \right] \, d\lambda^e_2 \right\} = \\
&= -\frac{\mu l_{23}}{12 F_e} \left(2 \, \vec{r}_{23} \cdot \vec{r}_{12} - \vec{r}_{23} \cdot \vec{r}_{31} \right)
\end{aligned}
\tag{B.45}
$$

Die approbierte gedruckte Originalversion dieser Dissertation ist an der TU Wien Bibliothek verfügbar.
The approved original version of this doctoral thesis is available in print at TU Wien Bibliothek.

$$\begin{aligned}
D^e_{23} &= \mu \int\limits_{\mathcal{C}^e_2} \lambda^e_2 \vec{n}_1 \cdot \vec{N}^e_3 \,\mathrm{d}s = \mu \int\limits_{\mathcal{C}^e_2} \lambda^e_2 \vec{n}_1 \cdot \left[l_{31} \left(\lambda^e_3 \vec{\nabla} \lambda^e_1 - \lambda^e_1 \vec{\nabla} \lambda^e_3 \right) \right] \,\mathrm{d}s = \\
&= \mu l_{31} \left(\vec{n}_1 \cdot \vec{\nabla} \lambda^e_1 \int\limits_{\mathcal{C}^e_2} \lambda^e_2 \lambda^e_3 \,\mathrm{d}s - \vec{n}_1 \cdot \vec{\nabla} \lambda^e_3 \underbrace{\int\limits_{\mathcal{C}^e_2} \lambda^e_2 \lambda^e_1 \,\mathrm{d}s}_{0} \right) = \\
&= \mu l_{31}\, \vec{n}_1 \cdot \vec{\nabla} \lambda^e_1 \int\limits_{\mathcal{C}^e_2} \lambda^e_2 \lambda^e_3 \,\mathrm{d}s = \mu l_{31} \left(l_{23} \vec{n}_1 \right) \cdot \vec{\nabla} \lambda^e_1 \int\limits_0^1 \lambda^e_2 \left(1 - \lambda^e_2 \right) \, d\lambda^e_2 = \\
&= -\frac{\mu l_{31}}{12 F_e}\, \vec{r}_{23} \cdot \vec{r}_{23}
\end{aligned} \tag{B.46}$$

$$D^e_{31} = \frac{\mu l_{12}}{12 F_e}\, \vec{r}_{23} \cdot \vec{r}_{23} \tag{B.47}$$

$$D^e_{32} = -\frac{\mu l_{23}}{12 F_e} \left(\vec{r}_{23} \cdot \vec{r}_{12} - 2\, \vec{r}_{23} \cdot \vec{r}_{31} \right) \tag{B.48}$$

$$D^e_{33} = -\frac{\mu l_{31}}{6 F_e}\, \vec{r}_{23} \cdot \vec{r}_{23}. \tag{B.49}$$

Along Edge 31:

$$\begin{aligned}
D^e_{11} &= \mu \int\limits_{\mathcal{C}^e_3} \lambda^e_1 \vec{n}_2 \cdot \vec{N}^e_1 \,\mathrm{d}s = \mu \int\limits_{\mathcal{C}^e_3} \lambda^e_1 \vec{n}_2 \cdot \left[l_{12} \left(\lambda^e_1 \vec{\nabla} \lambda^e_2 - \lambda^e_2 \vec{\nabla} \lambda^e_1 \right) \right] \,\mathrm{d}s = \\
&= \mu l_{12} \left(\vec{n}_2 \cdot \vec{\nabla} \lambda^e_2 \int\limits_{\mathcal{C}^e_3} \lambda^e_1 \lambda^e_1 \,\mathrm{d}s - \vec{n}_2 \cdot \vec{\nabla} \lambda^e_1 \underbrace{\int\limits_{\mathcal{C}^e_3} \lambda^e_1 \lambda^e_2 \,\mathrm{d}s}_{0} \right) = \\
&= \mu l_{12}\, \vec{n}_2 \cdot \vec{\nabla} \lambda^e_2 \int\limits_{\mathcal{C}^e_3} \lambda^e_1 \lambda^e_1 \,\mathrm{d}s = \mu l_{12} \left(l_{31} \vec{n}_2 \right) \cdot \vec{\nabla} \lambda^e_2 \int\limits_0^1 \left(\lambda^e_1 \right)^2 \, d\lambda^e_3 = \\
&= -\frac{\mu l_{12}}{6 F_e}\, \vec{r}_{31} \cdot \vec{r}_{31}
\end{aligned} \tag{B.50}$$

Die approbierte gedruckte Originalversion dieser Dissertation ist an der TU Wien Bibliothek verfügbar.
The approved original version of this doctoral thesis is available in print at TU Wien Bibliothek.

Die approbierte gedruckte Originalversion dieser Dissertation ist an der TU Wien Bibliothek verfügbar.
The approved original version of this doctoral thesis is available in print at TU Wien Bibliothek.

$$
\begin{aligned}
D_{12}^{e} &= \mu \int\limits_{\mathcal{C}_3^e} \lambda_1^e \vec{n}_2 \cdot \vec{N}_2^e \,\mathrm{d}s = \mu \int\limits_{\mathcal{C}_3^e} \lambda_1^e \vec{n}_2 \cdot \left[l_{23} \left(\lambda_2^e \vec{\nabla} \lambda_3^e - \lambda_3^e \vec{\nabla} \lambda_2^e \right) \right] \,\mathrm{d}s = \\
&= \mu l_{23} \left(\vec{n}_2 \cdot \vec{\nabla} \lambda_3^e \underbrace{\int\limits_{\mathcal{C}_3^e} \lambda_1^e \lambda_2^e \,\mathrm{d}s}_{0} - \vec{n}_2 \cdot \vec{\nabla} \lambda_2^e \int\limits_{\mathcal{C}_3^e} \lambda_1^e \lambda_3^e \,\mathrm{d}s \right) = \\
&= -\mu l_{23}\, \vec{n}_2 \cdot \vec{\nabla} \lambda_2^e \int\limits_{\mathcal{C}_3^e} \lambda_1^e \lambda_3^e \,\mathrm{d}s = -\mu l_{23} \left(l_{31} \vec{n}_2 \right) \cdot \vec{\nabla} \lambda_2^e \int\limits_0^1 \left(1 - \lambda_3^e \right) \lambda_3^e \, d\lambda_3^e = \\
&= \frac{\mu l_{23}}{12 F_e}\, \vec{r}_{31} \cdot \vec{r}_{31}
\end{aligned}
\tag{B.51}
$$

$$
\begin{aligned}
D_{13}^{e} &= \mu \int\limits_{\mathcal{C}_3^e} \lambda_1^e \vec{n}_2 \cdot \vec{N}_3^e \,\mathrm{d}s = \mu \int\limits_{\mathcal{C}_3^e} \lambda_1^e \vec{n}_1 \cdot \left[l_{31} \left(\lambda_3^e \vec{\nabla} \lambda_1^e - \lambda_1^e \vec{\nabla} \lambda_3^e \right) \right] \,\mathrm{d}s = \\
&= \mu l_{31} \left(\vec{n}_2 \cdot \vec{\nabla} \lambda_1^e \int\limits_{\mathcal{C}_3^e} \lambda_1^e \lambda_3^e \,\mathrm{d}s - \vec{n}_2 \cdot \vec{\nabla} \lambda_3^e \int\limits_{\mathcal{C}_3^e} \lambda_1^e \lambda_1^e \,\mathrm{d}s \right) = \\
&= \mu l_{31} \left[\vec{n}_2 \cdot \vec{\nabla} \lambda_1^e \int\limits_{\mathcal{C}_3^e} \lambda_1^e \left(1 - \lambda_1^e \right) \,\mathrm{d}s - \vec{n}_2 \cdot \vec{\nabla} \lambda_3^e \int\limits_{\mathcal{C}_3^e} \lambda_1^e \lambda_1^e \,\mathrm{d}s \right] = \\
&= \mu l_{31} \left\{ \left(l_{31} \vec{n}_2 \right) \cdot \vec{\nabla} \lambda_1^e \int\limits_0^1 \left[\lambda_1^e - \left(\lambda_1^e \right)^2 \right] \, d\lambda_1^e - \left(l_{31} \vec{n}_2 \right) \cdot \vec{\nabla} \lambda_3^e \int\limits_0^1 \left(\lambda_1^e \right)^2 \, d\lambda_1^e \right\} = \\
&= -\frac{\mu l_{31}}{12 F_e} \left(\vec{r}_{31} \cdot \vec{r}_{23} - 2\, \vec{r}_{31} \cdot \vec{r}_{12} \right)
\end{aligned}
\tag{B.52}
$$

$$
D_{2j}^{e} = \mu \int\limits_{\mathcal{C}_3^e} \lambda_2^e\, \vec{n}_2 \cdot \vec{N}_j^e \,\mathrm{d}s = 0, \;\; \lambda_2^e = 0 \text{ on Edge 31}
\tag{B.53}
$$

$$
D_{31}^{e} = -\frac{\mu l_{12}}{12 F_e}\, \vec{r}_{31} \cdot \vec{r}_{31}
\tag{B.54}
$$

$$
D_{32}^{e} = \frac{\mu l_{23}}{6 F_e}\, \vec{r}_{31} \cdot \vec{r}_{31}
\tag{B.55}
$$

$$
D_{33}^{e} = -\frac{\mu l_{31}}{12 F_e} \left(2\, \vec{r}_{31} \cdot \vec{r}_{23} - \vec{r}_{31} \cdot \vec{r}_{12} \right).
\tag{B.56}
$$

Die approbierte gedruckte Originalversion dieser Dissertation ist an der TU Wien Bibliothek verfügbar.
The approved original version of this doctoral thesis is available in print at TU Wien Bibliothek.
TU WIEN Bibliothek Your knowledge hub

Appendix C

Three-Dimensional Neumann Boundary Term Assembling

C.1 The Neumann Boundary for the Rotor-Rotor-Operator

The Neumann boundary integral (5.29) becomes

$$\int\limits_{\mathcal{A}_{N1}} \vec{n}\cdot\left[\vec{N}_i \times \left(\frac{1}{\gamma}\vec{\nabla}\times\vec{H}\right)\right]\,\mathrm{d}A = \sum_j c_j \int\limits_{\mathcal{A}_{N1}} \vec{n}\cdot\left[\vec{N}_i \times \left(\frac{1}{\gamma}\vec{\nabla}\times\vec{N}_j\right)\right]\,\mathrm{d}A = [D]\{c\}. \quad \text{(C.1)}$$

The assembly of the matrix $[D]$ with entries

$$D_{ij} = \int\limits_{\mathcal{A}_{N1}} \vec{n}\cdot\left[\vec{N}_i \times \left(\frac{1}{\gamma}\vec{\nabla}\times\vec{N}_j\right)\right]\,\mathrm{d}A \quad \text{(C.2)}$$

is performed element by element, whereby only the elements lying on the Neumann boundary are considered. The elements are tetrahedra and in each element $\vec{N}_i$ is represented by the vector edge functions (5.45) to (5.50).

The integral domain transformation for an arbitrary surface in the three-dimensional space is the same as in Appendix A and is derived in a similar manner. The integral is represented as a sum

$$\lim_{max(A_i)\to 0} \sum_i f(\vec{r}_i)A_i = \int\limits_{\mathcal{A}} f(\vec{r})\,\mathrm{d}A. \quad \text{(C.3)}$$

The surface $\mathcal{A}$ is subdivided into pieces $\mathcal{A}_i$ with areas A_i. $\vec{r}_i$ is point inside $\mathcal{A}_i$. The transformation is given by

$$\vec{r} = \vec{r}\,(x(\xi,\eta), y(\xi,\eta), z(\xi,\eta))\,. \quad \text{(C.4)}$$

An area A_i is calculated as

$$\begin{aligned} A_i &= \left|[\vec{r}(\xi+h,\eta)-\vec{r}(\xi,\eta)] \times [\vec{r}(\xi,\eta+k)-\vec{r}(\xi,\eta)]\right| = \\ &= \left|\left[\vec{r}_\xi(\tilde{\xi},\eta)h\right] \times [\vec{r}_\eta(\xi,\tilde{\eta})k]\right| \rightarrow \left|[\vec{r}_\xi(\xi,\eta) \times \vec{r}_\eta(\xi,\eta)]\, hk\right|, \end{aligned} \tag{C.5}$$

which leads again to (A.8) and (A.7).

Now the element matrix $[D]^e$ can be computed. As there are four outer triangular faces on each tetrahedral element, there will be four different element matrices for each face which lies on the Neumann boundary

$$\begin{aligned} D_{ij}^e &= \int\limits_{\mathcal{A}_k^e} \vec{n}_k \cdot \left[\vec{N}_i^e \times \left(\frac{1}{\gamma}\vec{\nabla} \times \vec{N}_j^e\right)\right] \mathrm{d}A = \int\limits_{\mathcal{A}_k^e} \left(\vec{n}_k \times \vec{N}_i^e\right) \cdot \left(\frac{1}{\gamma}\vec{\nabla} \times \vec{N}_j^e\right) \mathrm{d}A = \\ &= \left(\vec{n}_k \times \int\limits_{\mathcal{A}_k^e} \vec{N}_i^e \,\mathrm{d}A\right) \cdot \left(\frac{1}{\gamma}\vec{\nabla} \times \vec{N}_j^e\right), \quad k \in [1;4] \end{aligned} \tag{C.6}$$

and using (5.52)

$$D_{ij}^e = \frac{1}{3\gamma\, V_e} \left(\vec{n}_k \times \int\limits_{\mathcal{A}_k^e} \vec{N}_i^e \,\mathrm{d}A\right) \cdot \left(l_j\, \vec{r}_{7-j}\right), \quad k \in [1;4]. \tag{C.7}$$

$\mathcal{A}_k^e$ is the face opposite to the node k. $\vec{n}_k$ is a constant vector with the characteristic length 1, perpendicular to $\mathcal{A}_k^e$ and points outwards. γ is assumed to be constant in each element. Only the three $\vec{N}_i^e$ functions for the edges in the $\mathcal{A}_k^e$ plane are not perpendicular to A_k^e. The remaining three vector functions are perpendicular to A_k^e. Consequently these vectors are parallel to $\vec{n}_k$ and the corresponding vector product $\vec{n}_k \times \vec{N}_i^e$ becomes zero.

For the element face $\mathcal{A}_1^e$ the element matrix is given as follows

$$D_{1j}^e = D_{2j}^e = D_{3j}^e = 0 \tag{C.8}$$

$$D_{4j}^e = \frac{1}{3\gamma\, V_e} \left(\vec{n}_1 \times \int\limits_{\mathcal{A}_1^e} \vec{N}_4^e \,\mathrm{d}A\right) \cdot \left(l_j\, \vec{r}_{7-j}\right), \quad k \in [1;4]. \tag{C.9}$$

The integral is computed using the integral domain transformation discussed above.

$$\int\limits_{\mathcal{A}_1^e} \vec{N}_4^e \,\mathrm{d}A = 2A_1 \int\limits_0^1 \int\limits_0^{1-\lambda_2^e} l_4 \left(\lambda_2^e \vec{\nabla}\lambda_3^e - \lambda_3^e \vec{\nabla}\lambda_2^e\right) d\lambda_3^e\, d\lambda_2^e = \frac{l_4}{6}\, 2A_1 \left(\vec{\nabla}\lambda_3^e - \vec{\nabla}\lambda_2^e\right) \tag{C.10}$$

Die approbierte gedruckte Originalversion dieser Dissertation ist an der TU Wien Bibliothek verfügbar.
The approved original version of this doctoral thesis is available in print at TU Wien Bibliothek.
TU Wien Bibliothek Your knowledge hub

$$\begin{aligned}
\vec{n}_1 \times \int\limits_{\mathcal{A}_1^e} \vec{N}_4^e \,\mathrm{d}A &= \frac{l_4}{6}\,(2A_1\,\vec{n}_1) \times \left(\vec{\nabla}\lambda_3^e - \vec{\nabla}\lambda_2^e\right) = \\
&= \frac{l_4}{6}\,(\vec{r}_6 \times \vec{r}_5) \times \left(\frac{\vec{r}_3 \times \vec{r}_5}{6V_e} - \frac{\vec{r}_3 \times \vec{r}_6}{6V_e}\right) = \\
&= \frac{l_4}{6}\,\frac{1}{6V_e}\left\{-\vec{r}_5\,\underbrace{[(\vec{r}_6 \times \vec{r}_5)\cdot\vec{r}_3]}_{6V_e} + \vec{r}_6\,\underbrace{[(\vec{r}_6 \times \vec{r}_5)\cdot\vec{r}_3]}_{6V_e}\right\} = \\
&= \frac{l_4}{6}\,(\vec{r}_6 - \vec{r}_5)\,.
\end{aligned} \tag{C.11}$$

Thus the final solution for the fourth edge ($i = 4$) is given by the expression

$$D_{4j}^e = \frac{l_4\,l_j}{18\gamma\,V_e}\,(\vec{r}_6 - \vec{r}_5)\cdot\vec{r}_{7-j}. \tag{C.12}$$

The same procedure is used for remaining edges (with index i):

$$D_{5j}^e = \frac{l_4\,l_j}{18\gamma\,V_e}\,(\vec{r}_4 - \vec{r}_6)\cdot\vec{r}_{7-j} \tag{C.13}$$

$$D_{6j}^e = \frac{l_4\,l_j}{18\gamma\,V_e}\,(\vec{r}_5 - \vec{r}_4)\cdot\vec{r}_{7-j}. \tag{C.14}$$

Analogously it is proceeded for the remaining faces.

For the face $\mathcal{A}_2^e$:

$$D_{1j}^e = D_{4j}^e = D_{5j}^e = 0 \tag{C.15}$$

$$D_{2j}^e = -\frac{l_2\,l_j}{18\gamma\,V_e}\,(\vec{r}_6 + \vec{r}_3)\cdot\vec{r}_{7-j} \tag{C.16}$$

$$D_{3j}^e = \frac{l_3\,l_j}{18\gamma\,V_e}\,(\vec{r}_2 - \vec{r}_6)\cdot\vec{r}_{7-j} \tag{C.17}$$

$$D_{6j}^e = \frac{l_6\,l_j}{18\gamma\,V_e}\,(\vec{r}_2 + \vec{r}_3)\cdot\vec{r}_{7-j}. \tag{C.18}$$

For the face $\mathcal{A}_3^e$:

$$D_{2j}^e = D_{4j}^e = D_{6j}^e = 0 \tag{C.19}$$

$$D_{1j}^e = \frac{l_1\,l_j}{18\gamma\,V_e}\,(\vec{r}_3 - \vec{r}_5)\cdot\vec{r}_{7-j} \tag{C.20}$$

Die approbierte gedruckte Originalversion dieser Dissertation ist an der TU Wien Bibliothek verfügbar.
The approved original version of this doctoral thesis is available in print at TU Wien Bibliothek.

$$D^e_{3j} = -\frac{l_3\, l_j}{18\gamma\, V_e}\,(\vec{r}_1 + \vec{r}_5)\cdot\vec{r}_{7-j} \tag{C.21}$$

$$D^e_{5j} = \frac{l_5\, l_j}{18\gamma\, V_e}\,(\vec{r}_1 + \vec{r}_3)\cdot\vec{r}_{7-j}. \tag{C.22}$$

For the face $\mathcal{A}^e_4$:

$$D^e_{3j} = D^e_{5j} = D^e_{6j} = 0 \tag{C.23}$$

$$D^e_{1j} = -\frac{l_1\, l_j}{18\gamma\, V_e}\,(\vec{r}_2 + \vec{r}_4)\cdot\vec{r}_{7-j} \tag{C.24}$$

$$D^e_{2j} = \frac{l_2\, l_j}{18\gamma\, V_e}\,(\vec{r}_1 - \vec{r}_4)\cdot\vec{r}_{7-j} \tag{C.25}$$

$$D^e_{4j} = \frac{l_4\, l_j}{18\gamma\, V_e}\,(\vec{r}_1 + \vec{r}_2)\cdot\vec{r}_{7-j}. \tag{C.26}$$

C.2 Neumann Boundary for Gauß's Law of Magnetism

The goal in this section is to assemble the Neumann boundary term (5.31). The assembly could be made in one step for the vector edge functions $\vec{N}^e_i$ and for the scalar functions λ^e_i. However for the sake of clarity it is performed separately for the vector and for the scalar functions.

C.2.1 For the Scalar Function

Considering only the scalar functions ψ the Neumann boundary term (5.31) is written

$$\int\limits_{\mathcal{A}_{N2}} \lambda_i \vec{n}\cdot(\underset{\sim}{\mu}\cdot\vec{\nabla}\psi)\,\mathrm{d}A = \sum_j c_j \int\limits_{\mathcal{A}_{N2}} \lambda_i \vec{n}\cdot(\underset{\sim}{\mu}\cdot\vec{\nabla}\lambda_j)\,\mathrm{d}A = [D]\{c\}. \tag{C.27}$$

The matrix $[D]$ can be constructed by the element matrix $[D]^e$ with entries

$$D^e_{ij} = \mu \int\limits_{\partial\mathcal{A}^e_k} \lambda^e_i\,\vec{n}_k\cdot\vec{\nabla}\lambda^e_j\,\mathrm{d}A,\;\; k\in[i;4],\;\; i\in[1;4],\;\; j\in[1;4]. \tag{C.28}$$

$\mathcal{A}^e_k$ is the element face lying on the Neumann boundary $\mathcal{A}_{N2}$ and $\vec{n}_k$ is the corresponding normal vector pointing outwards. μ is assumed as constant scalar in each element. Again the element matrix is constructed for the four triangular faces (from $\mathcal{A}^e_1$ to $\mathcal{A}^e_4$) of the tetrahedron.

Die approbierte gedruckte Originalversion dieser Dissertation ist an der TU Wien Bibliothek verfügbar.
The approved original version of this doctoral thesis is available in print at TU Wien Bibliothek.

Die approbierte gedruckte Originalversion dieser Dissertation ist an der TU Wien Bibliothek verfügbar.
The approved original version of this doctoral thesis is available in print at TU Wien Bibliothek.
TU WIEN Bibliothek Your knowledge hub

For $\mathcal{A}_1^e$:

Since λ_1^e is 0 on $\mathcal{A}_1^e \Rightarrow$

$$D_{1j}^e = \mu \int\limits_{\partial \mathcal{A}_1^e} \lambda_1^e \, \vec{n}_1 \cdot \vec{\nabla} \lambda_j^e \, \mathrm{d}A = 0. \tag{C.29}$$

For the second row the following expression is obtained

$$\begin{aligned} D_{2j}^e &= \mu \int\limits_{\partial \mathcal{A}_1^e} \lambda_2^e \, \vec{n}_1 \cdot \vec{\nabla} \lambda_j^e \, \mathrm{d}A = \mu \, \vec{n}_1 \cdot \vec{\nabla} \lambda_j^e \int\limits_{\partial \mathcal{A}_1^e} \lambda_2^e \, \mathrm{d}A = \\ &= \mu \, (2A_1 \vec{n}_1) \cdot \vec{\nabla} \lambda_j^e \int\limits_0^1 \int\limits_0^{1-\lambda_2^e} \lambda_2^e \, d\lambda_3^e \, d\lambda_2^e = \frac{\mu}{6} \, (\vec{r}_5 \times \vec{r}_4) \cdot \vec{\nabla} \lambda_j^e = -\frac{\mu}{36 V_e} f_{1j}. \end{aligned} \tag{C.30}$$

Analogously the entries of the next rows are calculated

$$D_{2j}^e = D_{3j}^e = D_{4j}^e = -\frac{\mu}{36 V_e} f_{1j}. \tag{C.31}$$

The non-zero entries do not depend on the row index but on the face and column index. Consequently the non-zero rows are identical.

Similarly it is proceeded for the remaining element faces.

For $\mathcal{A}_2^e$:

$$D_{2j}^e = 0, \; D_{1j}^e = D_{3j}^e = D_{4j}^e = -\frac{\mu}{36 V_e} f_{2j}. \tag{C.32}$$

For $\mathcal{A}_3^e$:

$$D_{3j}^e = 0, \; D_{1j}^e = D_{2j}^e = D_{4j}^e = -\frac{\mu}{36 V_e} f_{3j}. \tag{C.33}$$

For $\mathcal{A}_4^e$:

$$D_{4j}^e = 0, \; D_{1j}^e = D_{2j}^e = D_{3j}^e = -\frac{\mu}{36 V_e} f_{4j}. \tag{C.34}$$

C.2.2 For the Vector Function

For the vector functions $\vec{H}_1$ the Neumann boundary term (5.31) is given by

$$\int\limits_{\mathcal{A}_{N2}} \lambda_i \vec{n} \cdot (\underset{\sim}{\mu} \cdot \vec{H}_1) \, \mathrm{d}A = \sum_j c_j \int\limits_{\mathcal{A}_{N2}} \lambda_i \, \vec{n} \cdot (\underset{\sim}{\mu} \cdot \vec{N}_j) \, \mathrm{d}A = [D]\{c\}. \tag{C.35}$$

Assuming that μ is a constant scalar in each element the corresponding element matrix is given by

$$D_{ij}^e = \mu \int\limits_{\mathcal{A}_k^e} \lambda_i^e \, \vec{n}_k \cdot \vec{N}_j^e \, \mathrm{d}A, \;\; k \in [1;4], \;\; i \in [1;4], \;\; j \in [1;6]. \tag{C.36}$$

For the face $\mathcal{A}_1^e$ opposite to the node 1 ($k = 1$):

The element function λ_1^e is 0 on the element face $\mathcal{A}_1^e$. Thus the first row of the element matrix is zero.

$$D_{1j}^e = \mu \int\limits_{\mathcal{A}_1^e} \lambda_1^e \, \vec{n}_1 \cdot \vec{N}_j^e \, \mathrm{d}A = 0. \tag{C.37}$$

The remaining entries can be calculated as follows

$$\begin{aligned}
D_{21}^e &= \mu \int\limits_{\mathcal{A}_1^e} \lambda_2^e \, \vec{n}_1 \cdot \vec{N}_1^e \, \mathrm{d}A = \mu \int\limits_{\mathcal{A}_1^e} \lambda_2^e \, \vec{n}_1 \cdot \left[l_1 \left(\lambda_1^e \vec{\nabla} \lambda_2^e - \lambda_2^e \vec{\nabla} \lambda_1^e \right) \right] \, \mathrm{d}A = \\
&= \mu l_1 \left[\vec{n}_1 \cdot \vec{\nabla} \lambda_2^e \underbrace{\int\limits_{\mathcal{A}_1^e} \lambda_1^e \lambda_2^e \, \mathrm{d}A}_{0} - \vec{n}_1 \cdot \vec{\nabla} \lambda_1^e \int\limits_{\mathcal{A}_1^e} (\lambda_2^e)^2 \, \mathrm{d}A \right] = \\
&= -\mu l_1 \, \vec{n}_1 \cdot \vec{\nabla} \lambda_1^e \int\limits_{\mathcal{A}_1^e} (\lambda_2^e)^2 \, \mathrm{d}A = -\mu l_1 \, (2 A_1 \vec{n}_1) \cdot \vec{\nabla} \lambda_1^e \int\limits_0^1 \int\limits_0^{1-\lambda_2^e} (\lambda_2^e)^2 \, d\lambda_3^e \, d\lambda_2^e = \\
&= -\frac{\mu l_1}{12} \, (\vec{r}_5 \times \vec{r}_4) \cdot \vec{\nabla} \lambda_1^e = \frac{\mu l_1}{72 V_e} \, f_{11}
\end{aligned} \tag{C.38}$$

$$\begin{aligned}
D_{22}^e &= \mu \int\limits_{\mathcal{A}_1^e} \lambda_2^e \, \vec{n}_1 \cdot \vec{N}_2^e \, \mathrm{d}A = \mu \int\limits_{\mathcal{A}_1^e} \lambda_2^e \, \vec{n}_1 \cdot \left[l_2 \left(\lambda_1^e \vec{\nabla} \lambda_3^e - \lambda_3^e \vec{\nabla} \lambda_1^e \right) \right] \, \mathrm{d}A = \\
&= \mu l_2 \left(\vec{n}_1 \cdot \vec{\nabla} \lambda_3^e \underbrace{\int\limits_{\mathcal{A}_1^e} \lambda_1^e \lambda_2^e \, \mathrm{d}A}_{0} - \vec{n}_1 \cdot \vec{\nabla} \lambda_1^e \int\limits_{\mathcal{A}_1^e} \lambda_2^e \lambda_3^e \, \mathrm{d}A \right) = \\
&= -\mu l_2 \, \vec{n}_1 \cdot \vec{\nabla} \lambda_1^e \int\limits_{\mathcal{A}_1^e} \lambda_2^e \lambda_3^e \, \mathrm{d}A = -\mu l_2 \, (2 A_1 \vec{n}_1) \cdot \vec{\nabla} \lambda_1^e \int\limits_0^1 \int\limits_0^{1-\lambda_2^e} \lambda_2^e \lambda_3^e \, d\lambda_3^e \, d\lambda_2^e = \\
&= -\frac{\mu l_2}{24} \, (\vec{r}_5 \times \vec{r}_4) \cdot \vec{\nabla} \lambda_1^e = \frac{\mu l_2}{144 V_e} \, f_{11}
\end{aligned} \tag{C.39}$$

Die approbierte gedruckte Originalversion dieser Dissertation ist an der TU Wien Bibliothek verfügbar.
The approved original version of this doctoral thesis is available in print at TU Wien Bibliothek.

$$D^e_{23} = \frac{\mu l_3}{144V_e}\, f_{11} \tag{C.40}$$

$$\begin{aligned} D^e_{24} &= \mu \int\limits_{\mathcal{A}^e_1} \lambda^e_2\, \vec{n}_1 \cdot \vec{N}^e_4 \,\mathrm{d}A = \mu \int\limits_{\mathcal{A}^e_1} \lambda^e_2\, \vec{n}_1 \cdot \left[l_4 \left(\lambda^e_2 \vec{\nabla} \lambda^e_3 - \lambda^e_3 \vec{\nabla} \lambda^e_2 \right) \right] \,\mathrm{d}A = \\ &= \mu l_4 \left[\vec{n}_1 \cdot \vec{\nabla} \lambda^e_3 \int\limits_{\mathcal{A}^e_1} (\lambda^e_2)^2 \,\mathrm{d}A - \vec{n}_1 \cdot \vec{\nabla} \lambda^e_2 \int\limits_{\mathcal{A}^e_1} \lambda^e_2 \lambda^e_3 \,\mathrm{d}A \right] = \frac{\mu l_4}{144V_e}(f_{12} - 2f_{13}) \end{aligned} \tag{C.41}$$

$$D^e_{25} = \frac{\mu l_5}{144V_e}(2f_{14} - f_{12}) \tag{C.42}$$

$$D^e_{26} = \frac{\mu l_6}{144V_e}(f_{13} - f_{14}) \tag{C.43}$$

$$\begin{aligned} &D^e_{31} = \frac{\mu l_1}{144V_e} f_{11} && D^e_{32} = \frac{\mu l_2}{72V_e} f_{11} && D^e_{33} = \frac{\mu l_3}{144V_e} f_{11} \\ &D^e_{34} = \frac{\mu l_4}{144V_e}(2f_{12} - f_{13}) && D^e_{35} = \frac{\mu l_5}{144V_e}(f_{14} - f_{12}) && D^e_{36} = \frac{\mu l_6}{144V_e}(f_{13} - 2f_{14}) \end{aligned} \tag{C.44}$$

$$\begin{aligned} &D^e_{41} = \frac{\mu l_1}{144V_e} f_{11} && D^e_{42} = \frac{\mu l_2}{144V_e} f_{11} && D^e_{43} = \frac{\mu l_3}{72V_e} f_{11} \\ &D^e_{44} = \frac{\mu l_4}{144V_e}(f_{12} - f_{13}) && D^e_{45} = \frac{\mu l_5}{144V_e}(f_{14} - 2f_{12}) && D^e_{46} = \frac{\mu l_6}{144V_e}(2f_{13} - f_{14}). \end{aligned} \tag{C.45}$$

For $\mathcal{A}^e_2$:

$$\begin{aligned} &D^e_{11} = -\frac{\mu l_1}{72V_e} f_{22} && D^e_{12} = \frac{\mu l_2}{144V_e}(f_{21} - 2f_{23}) && D^e_{13} = \frac{\mu l_3}{72V_e}(f_{21} - 2f_{24}) \\ &D^e_{14} = \frac{\mu l_4}{144V_e} f_{22} && D^e_{15} = -\frac{\mu l_5}{144V_e} f_{22} && D^e_{16} = \frac{\mu l_6}{144V_e}(f_{23} - f_{24}) \end{aligned} \tag{C.46}$$

$$D^e_{2\jmath} = 0, \ \ \jmath \in [1;6] \tag{C.47}$$

$$\begin{aligned} &D^e_{31} = -\frac{\mu l_1}{144V_e} f_{22} && D^e_{32} = \frac{\mu l_2}{144V_e}(2f_{21} - f_{23}) && D^e_{33} = \frac{\mu l_3}{72V_e}(f_{21} - 2f_{24}) \\ &D^e_{34} = \frac{\mu l_4}{72V_e} f_{22} && D^e_{35} = -\frac{\mu l_5}{144V_e} f_{22} && D^e_{36} = \frac{\mu l_6}{144V_e}(f_{23} - 2f_{24}) \end{aligned} \tag{C.48}$$

Die approbierte gedruckte Originalversion dieser Dissertation ist an der TU Wien Bibliothek verfügbar.
The approved original version of this doctoral thesis is available in print at TU Wien Bibliothek.
TU WIEN Bibliothek Your knowledge hub

$$\begin{aligned} D^e_{41} &= -\frac{\mu l_1}{144V_e} f_{22} & D^e_{42} &= \frac{\mu l_2}{144V_e}(f_{21} - f_{23}) & D^e_{43} &= \frac{\mu l_3}{72V_e}(2f_{21} - f_{24}) \\ D^e_{44} &= \frac{\mu l_4}{144V_e} f_{22} & D^e_{45} &= -\frac{\mu l_5}{72V_e} f_{22} & D^e_{46} &= \frac{\mu l_6}{144V_e}(2f_{23} - f_{24}). \end{aligned} \tag{C.49}$$

For $\mathcal{A}^e_3$:

$$\begin{aligned} D^e_{11} &= \frac{\mu l_1}{144V_e}(f_{31} - 2f_{32}) & D^e_{12} &= -\frac{\mu l_2}{72V_e} f_{33} & D^e_{13} &= \frac{\mu l_3}{144V_e}(f_{31} - 2f_{34}) \\ D^e_{14} &= -\frac{\mu l_4}{144V_e} f_{33} & D^e_{15} &= \frac{\mu l_6}{144V_e}(f_{34} - f_{32}) & D^e_{16} &= \frac{\mu l_5}{144V_e} f_{33} \end{aligned} \tag{C.50}$$

$$\begin{aligned} D^e_{21} &= \frac{\mu l_1}{144V_e}(2f_{31} - f_{32}) & D^e_{22} &= -\frac{\mu l_2}{144V_e} f_{33} & D^e_{23} &= \frac{\mu l_3}{144V_e}(f_{31} - f_{34}) \\ D^e_{24} &= -\frac{\mu l_4}{72V_e} f_{33} & D^e_{25} &= \frac{\mu l_6}{144V_e}(2f_{34} - f_{32}) & D^e_{26} &= \frac{\mu l_5}{144V_e} f_{33} \end{aligned} \tag{C.51}$$

$$D^e_{3j} = 0,\ \jmath \in [1;6] \tag{C.52}$$

$$\begin{aligned} D^e_{41} &= \frac{\mu l_1}{144V_e}(f_{31} - f_{32}) & D^e_{42} &= -\frac{\mu l_2}{144V_e} f_{33} & D^e_{43} &= \frac{\mu l_3}{144V_e}(4f_{31} - f_{34}) \\ D^e_{44} &= -\frac{\mu l_4}{144V_e} f_{33} & D^e_{45} &= \frac{\mu l_6}{144V_e}(f_{34} - 2f_{32}) & D^e_{46} &= \frac{\mu l_5}{72V_e} f_{33}. \end{aligned} \tag{C.53}$$

For $\mathcal{A}^e_4$:

$$\begin{aligned} D^e_{11} &= \frac{\mu l_1}{144V_e}(f_{41} - 2f_{42}) & D^e_{12} &= \frac{\mu l_2}{72V_e}(f_{41} - 2f_{43}) & D^e_{13} &= -\frac{\mu l_3}{72V_e} f_{44} \\ D^e_{14} &= \frac{\mu l_4}{144V_e}(f_{42} - f_{43}) & D^e_{15} &= \frac{\mu l_5}{144V_e} f_{44} & D^e_{16} &= -\frac{\mu l_6}{144V_e} f_{44} \end{aligned} \tag{C.54}$$

$$\begin{aligned} D^e_{21} &= \frac{\mu l_1}{144V_e}(2f_{41} - f_{42}) & D^e_{22} &= \frac{\mu l_2}{72V_e}(f_{41} - f_{43}) & D^e_{23} &= -\frac{\mu l_3}{144V_e} f_{44} \\ D^e_{24} &= \frac{\mu l_4}{144V_e}(f_{42} - 2f_{43}) & D^e_{25} &= \frac{\mu l_5}{72V_e} f_{44} & D^e_{26} &= -\frac{\mu l_6}{144V_e} f_{44} \end{aligned} \tag{C.55}$$

$$\begin{aligned} D^e_{31} &= \frac{\mu l_1}{144V_e}(f_{41} - f_{42}) & D^e_{32} &= \frac{\mu l_2}{72V_e}(2f_{41} - f_{43}) & D^e_{33} &= -\frac{\mu l_3}{144V_e} f_{44} \\ D^e_{34} &= \frac{\mu l_4}{144V_e}(2f_{42} - f_{43}) & D^e_{35} &= \frac{\mu l_5}{144V_e} f_{44} & D^e_{36} &= -\frac{\mu l_6}{72V_e} f_{44} \end{aligned} \tag{C.56}$$

$$D^e_{4j} = 0,\ j \in [1;6]. \tag{C.57}$$

Die approbierte gedruckte Originalversion dieser Dissertation ist an der TU Wien Bibliothek verfügbar.
The approved original version of this doctoral thesis is available in print at TU Wien Bibliothek.

Bibliography

[1] Ansoft. Simulation software for high-performance electronic design. http://www.ansoft.com.

[2] COMSOL. The unifying multiphysics simulation environment. http://www.comsol.com.

[3] CST. Comlete technology for 3D electromagnetic simulation. http://www.cst.com.

[4] Magwel. http://www.magwel.com.

[5] Remcom. http://www.remcom.com.

[6] Synopsys. Helping you design the chip inside. http://www.synopsys.com.

[7] R. B. Iverson and Y. L. LeCoz. A floating random-walk method for efficient RC extraction of complex IC-interconnect structures. In *Technical Proceedings of the 1998 Int. Conf. on Modeling and Simulation of Microsystems*, pages 117 – 121, 1998.

[8] K. Chatterjee and J. Poggie. A parallelized 3D floating random-walk algorithm for the solution of the nonlinear Poisson-Boltzmann equation. *Progress In Electromagnetics Research, PIER 57*, pages 237–252, 2006.

[9] R. Bauer. Numerische Berechnung von Kapazitäten in dreidimensionalen Verdrahtungsstrukturen. Dissertation, Technische Universität Wien, 1994.

[10] R. Sabelka. Dreidimensionale finite Elemente Simulation von Verdrahtungsstrukturen auf integrierten Schaltungen. Dissertation, Technische Universität Wien, 2001.

[11] Ch. Harlander. Numerische Berechnung von Induktivitäten in dreidimensionalen Verdrahtungsstrukturen. Dissertation, Technische Universität Wien, 2002.

[12] W. Wessner. Mesh refinement techniques for TCAD tools. Dissertation, Technische Universität Wien, 2006.

[13] H. J. Dirschmid. *Mathematische Grundlagen der Elektrotechnik*. Vieweg, Braunschweig;Wiesbaden, 1988.

Die approbierte gedruckte Originalversion dieser Dissertation ist an der TU Wien Bibliothek verfügbar.
The approved original version of this doctoral thesis is available in print at TU Wien Bibliothek.
TU WIEN Bibliothek Your knowledge hub

[14] S. J. Farlow. *Partial Differential Equations for Scientists and Engineers.* Dover Publications, September 1993.

[15] P. DuChateau and D. Zachmann. *Applied Partial Differential Equations.* Dover Publications, February 2002.

[16] Ch. Lang and N. Pucker. *Mathematische Methoden in der Physik.* Spektrum Akademischer Verlag, August 2005.

[17] S. Selberherr. *Analysis and Simulation of Semiconductor Devices.* Springer, Januar 1984.

[18] O. C. Zienkiewicz and R. L. Taylor. *The Finite Element Method for Solid and Structural Mechanics.* Butterworth-Heinemann, September 2005.

[19] K.-J. Bathe. *Finite-Elemente-Methoden.* Springer, 1990.

[20] C. Johnson. *Numerical Solution of Partial Differential Equations by the Finite Element Method.* Cambridge University Press, 1987.

[21] O.C. Zienkiewicz and R.L. Taylor. *The Finite Element Method.* Butterworth-Heinemann, 2000.

[22] P. Knabner and L. Angermann. *Numerik partieller Differentialgleichungen: Eine anwendungsorientierte Einführung.* Springer, May 2000.

[23] Ch. Grossmann, H.-G. Roos, and M. Stynes. *Numerical Treatment of Partial Differential Equations.* Springer, November 2007.

[24] S. Larsson and V. Thomée. *Partial Differential Equations with Numerical Methods.* Springer, December 2005.

[25] P. P. Silvester and R. L. Ferrari. *Finite Elements for Electrical Engineers.* Cambridge University Press, September 1996.

[26] R.E. White. *An Introduction to the Finite Element Method with Applications to Nonlinear Problems.* John Wiley & Sons, New York, 1985.

[27] J.L. Volakis, A. Chatterjee, and L.C. Kempel. *Finite Element Method for Electromagnetics.* IEEE Press, New York, 1998.

[28] T. R. Chandrupatla and A. D. Belegundu. *Introduction to Finite Elements in Engineering.* Prentice Hall, 2002.

[29] R.I. Mackie. *Object-Oriented Methods and Finite Element Analysis.* Saxe-Coburg Publications, 2001.

[30] M. Salazar-Palma, T. K. Sarkar, L. E. Garcia-Castillo, and T. Roy. *Iterative and Self-Adaptive Finite-Elements in Electromagnetic Modeling.* Artech House, 1998.

[31] I. Babuska and T. Strouboulis. *The Finite Element Method and its Reliability.* Oxford University Press, 2001.

Die approbierte gedruckte Originalversion dieser Dissertation ist an der TU Wien Bibliothek verfügbar.
The approved original version of this doctoral thesis is available in print at TU Wien Bibliothek.
TU WIEN Bibliothek Your knowledge hub

[32] I. Babuska, J. Chandra, and J.E. Flaherty. *Adaptive Computational Methods for Partial Differential Equations*. SIAM, Philadelphia, 1983.

[33] S. C. Brenner and L. R. Scott. *The Mathematical Theory of Finite Element Methods*. Springer, April 2002.

[34] K. H. Huebner, D. L. Dewhirst, D. E. Smith, and T. G. Byrom. *The Finite Element Method for Engineers*. Wiley-Interscience, September 2001.

[35] A. Kost. *Numerische Methoden in der Berechnung elektromagnetischer Felder*. Springer, Berlin, Februar 2007.

[36] Ch. Großman and H.-G. Roos. *Numerische Bechandlung partieller Differentialgleichungen*. Teubner, Wiesbaden, 2005.

[37] L. Badea and P. Daripa. A domain embedding/boundary control method to solve elliptic problems in arbitrary domains. In *Proceedings of the 41st IEEE Conference on Decision and Control*, volume 3, pages 3004 – 3009, December 2002.

[38] J. Jin. *The Finite Element Method in Electromagnetics*. John Wiley and Sons, New York, 2002.

[39] H. Haas. Numerische Berechnung elektromagnetischer Felder. Institut für Grundlagen und Theorie der Elektrotechnik, TU Wien, 2004.

[40] A. Prechtl. Vorlesungen über Theoretische Elektrotechnik. Institut für Grundlagen und Theorie der Elektrotechnik, TU Wien, 1996. Zweiter Teil: Elektrodynamik.

[41] J. C. Maxwell. *A Treatise on Electricity and Magnetism*. Oxford University Press, 1998.

[42] J. C. Maxwell. *An Elementary Treatise on Electricity: Second Edition*. Dover Publ. Inc., 2004.

[43] S. É. Umanskii and I. A. Duvidzon. Automatic subdivision of an arbitrary two-dimensional region into finite elements. *Strength of Materials*, 9(6):739–744, June 1977.

[44] I. A. Duvidzon and S. M. Begelman. Formation of a finite-element grid for an arbitrary two-dimensional region. *Strength of Materials*, 21(12):1734–1739, December 1989.

[45] K. Kpogli and A. Kost. Local error estimation and strategic mesh generation for time-dependent problems in electromagnetics coupled with heat conduction. *IEEE Trans. Magnetics*, 39(3):1701 – 1704, May 2003.

[46] S. Alfonzetti. Finite-element mesh adaptation of 2-D time-harmonic skin effect problems. In *IEEE Trans. Magnetics*, volume 36, pages 1592 – 1595, July 2000.

[47] S. Dufour, G. Vinsard, B. Laporte, and R. Moretti. Mesh improvement in 2-D eddy-current problems. In *IEEE Trans. Magnetics*, volume 38, pages 377 – 380, March 2002.

Die approbierte gedruckte Originalversion dieser Dissertation ist an der TU Wien Bibliothek verfügbar.
The approved original version of this doctoral thesis is available in print at TU Wien Bibliothek.

[48] H. R. Schwarz. *Methode der finiten Elemente*. Teubner, January 1991.

[49] M. V. K. Chari and Peter P. Silvester. *Finite Elements in Electrical and Magnetic Field Problems*. J. Wiley & Sons, New York, April 1980.

[50] K. Küpfmüller, W. Mathis, and A. Reibiger. *Theoretische Elektrotechnik*. Springer, Berlin, 2006.

[51] O. P. Gupta. *Finite and Boundary Element Methods in Engineering*. A.A. Balkema, Juli 1999.

[52] G. Beer and J. O. Watson. *Introduction to Finite and Boundary Element Methods for Engineers*. John Wiley and Sons, November 1992.

[53] D. Poljak and C. A. Brebbia. *Boundary Element Methods For Electrical Engineers*. WIT Press, August 2005.

[54] H. T. Yu, S. L. Ho, M. Q. Hu, and H. C. Wong. Edge-based FEM-BEM for wide-band electromagnetic computation. *IEEE Trans. Magnetics*, 42(4):771 – 774, April 2006.

[55] J. P. Webb. Edge elements and what they can do for you. *IEEE Trans. Magnetics*, 29(2):1460 – 1465, March 1993.

[56] N. Takahashi, T. Nakata, K. Fujiwara, and T. Imai. Investigation of effectiveness of edge elements. *IEEE Trans. Magnetics*, 28(2):1619 – 1622, March 1992.

[57] G. Mur. The fallacy of edge elements. *IEEE Trans. Magnetics*, 34(5):3244 – 3247, September 1998.

[58] A. Taflove. *Computational Electrodynamics*. Artech House, Boston, 1995.

[59] A. Taflove, editor. *Advances in Computational Electrodynamics*. Artech House, Boston, 1998.

[60] J. Schwinger, L.L. DeRaad Jr., K.A. Milton, and W. Tsai. *Classical Electrodynamics*. Perseus Books, 1998.

[61] R.C. Dorf, editor. *The Electrical Engineering Handbook*. CRC Press, 1997.

[62] J. van Bladel. *Electromagnetic Fields*. Springer, 1985.

[63] I. D. Mayergoyz. *Nonlinear Diffusion of Electromagnetic Fields: With Applications to Eddy Currents and Superconductivity*. Academic Press Inc., U.S., May 1998.

[64] H. Haas. Analytische Berechnung elektromagnetischer Felder. Institut für Grundlagen und Theorie der Elektrotechnik, TU Wien, 1998.

[65] A. Prechtl. *Vorlesungen über die Grundlagen der Elektrotechnik I*. Springer, Wien, January 1999.

[66] A. Prechtl. *Vorlesungen über die Grundlagen der Elektrotechnik II*. Springer, Wien, November 2007.

Die approbierte gedruckte Originalversion dieser Dissertation ist an der TU Wien Bibliothek verfügbar.
The approved original version of this doctoral thesis is available in print at TU Wien Bibliothek.
TU WIEN Bibliothek Your knowledge hub

[67] P. Meuris, W. Schoenmaker, and W. Magnus. Strategy for electromagnetic interconnect modeling. *IEEE Trans. Computer-Aided Design of Integrated Circuits and Systems*, 20(6):753–762, June 2001.

[68] W. Schoenmaker and P. Meuris. Electromagnetic interconnects and passives modeling: Software implementation issues. *IEEE Trans. on Computer-Aided Design of Integrated Circuits and Systems*, 21(5):534–543, May 2002.

[69] Roland Süße. *Theoretische Grundlagen der Elektrotechnik 2*. Teubner, 2006.

[70] R. Albanese and G. Rubinacci. Solution of three dimensional eddy current problems by integral and differential methods. *IEEE Trans. Magnetics*, 24(1):98 – 101, January 1988.

[71] T. Nakata, N. Takahashi, K. Fujiwara, and Y. Okada. Improvements of the $\mathrm{T} - \Omega$ method for 3-D eddy current analysis. *IEEE Trans. Magnetics*, 24(1):94 – 97, January 1988.

[72] O. Biro and K. Preis. Generating source field functions with limited support for edge finite-element eddy current analysis. *IEEE Trans. Magnetics*, 43(4):1165 – 1168, April 2007.

[73] T. Nakata, N. Takahashi, K. Fujiwara, T. Imai, and K. Muramatsu. Comparison of various methods of analysis and finite elements in 3-D magnetic field analysis. *IEEE Trans. Magnetics*, 27(5):4073 – 4076, September 1991.

[74] J. P. Webb and B. Forghani. DC current distributions and magnetic fields using the T-Omega edge-element method. *IEEE Trans. Magnetics*, 31(3):1444 – 1447, May 1995.

[75] T. Nakata, N. Takahashi, K. Fujiwara, and K. Muramatsu. Investigation of effectiveness of various methods with different unknown variables for 3-D eddy current analysis. *IEEE Trans. Magnetics*, 26(2):442 – 445, March 1990.

[76] T. Nakata, N. Takahashi, K. Fujiwara, and Y. Shiraki. Comparison of different finite elements for 3-D eddy current analysis. *IEEE Trans. Magnetics*, 26(2):434 – 437, March 1990.

[77] B. Boualem and F. Piriou. Hybrid formulation $\mathrm{A} - \Omega$ with finite element method to model in 3D electromagnetic systems. *IEEE Trans. Magnetics*, 32(3):59 – 662, May 1996.

[78] J. Wang and B. Tong. Calculation of 3D eddy current problems using a modified $\mathrm{T} - \Omega$ method. *IEEE Trans. Magnetics*, 24(1):114 – 117, January 1988.

[79] J. P. Webb and B. Forghani. The low-frequency performance of $\mathrm{H} - \phi$ and $\mathrm{T} - \Omega$ methods using edge elements for 3D eddy current problems. *IEEE Trans. Magnetics*, 29(6):2461 – 2463, November 1993.

[80] F. Bouillault, Z. Ren, and A. Razek. Calculation of 3D eddy current problems by an hybrid $\mathrm{T} - \Omega$ method. *IEEE Trans. Magnetics*, 26(2):478 – 481, March 1990.

Die approbierte gedruckte Originalversion dieser Dissertation ist an der TU Wien Bibliothek verfügbar.
The approved original version of this doctoral thesis is available in print at TU Wien Bibliothek.

[81] K. Iwata and H. Hirano. Magnetic field analysis by edge elements of magnetic components considering inhomogeneous current distribution within conductor windings. *IEEE Trans. Magnetics*, 42(5):1549 – 1554, May 2006.

[82] Z. Ren. T – Ω formulation for eddy-current problems in multiply connected regions. *IEEE Trans. Magnetics*, 38(2):557 – 560, March 2002.

[83] A. T. Phung, O. Chadebec, P. Labie, Y. Le Floch, and G. Meunier. Automatic cuts for magnetic scalar potential formulations. *IEEE Trans. Magnetics*, 41(5):1668 – 1671, May 2005.

[84] J. Simkin, S. C. Taylor, and E. X. Xu. An efficient algorithm for cutting multiply connected regions. *IEEE Trans. Magnetics*, 40(2):707 – 709, March 2004.

[85] P. R. Kotiuga. Toward an algorithm to make cuts for magnetic scalar potentials in finite element meshes. *Journal of Applied Physics*, 63:3357–3359, April 1988.

[86] J. M. Zhou, K. D. Zhou, and K. R. Shao. Automatic generation of 3D meshes for complicated solids. *IEEE Trans. Magnetics*, 28(2):1759 – 1762, March 1992.

[87] P. L. George, F. Hecht, and E. Saltel. Automatic 3D mesh generation with prescribed meshed boundaries. *IEEE Trans. Magnetics*, 26(2):771 – 774, March 1990.

[88] N. A. Golias and T. D. Tsiboukis. Three-dimensional automatic adaptive mesh generation. *IEEE Trans. Magnetics*, 28(2):1700 – 1703, March 1992.

[89] D. Dyck, D. A. Lowther, W. Mai, and G. Henneberger. Three-dimensional mesh improvement using self organizing feature maps. *IEEE Trans. Magnetics*, 35(3):1334 – 1337, May 1999.

[90] D. Korichi, B. Bandelier, and F. Rioux-Damidau. Adaptive 3D mesh refinement based on a two fields formulation of magnetodynamics. *IEEE Trans. Magnetics*, 36(4):1496 – 1500, July 2000.

[91] M. Dorica and D. Giannacopoulos. Impact of mesh quality improvement systems on the accuracy of adaptive finite-element electromagnetics with tetrahedra. *IEEE Trans. Magnetics*, 41(5):1692–1695, May 2005.

[92] S. Alfonzetti. A neural network generator for tetrahedral meshes. *IEEE Trans. Magnetics*, 39(3):1650 – 1653, May 2003.

[93] D. Q. Ren and D. D. Giannacopoulos. Parallel mesh refinement for 3-D finite element electromagnetics with tetrahedra: Strategies for optimizing system communication. *IEEE Trans. Magnetics*, 42(4):1251 – 1254, April 2006.

[94] D. D. Giannacopoulos and D. Q. Ren. Analysis and design of parallel 3-D mesh refinement dynamic load balancing algorithms for finite element electromagnetics with tetrahedra. *IEEE Trans. Magnetics*, 42(4):1235 – 1238, April 2006.

[95] L. Freitag and C. Ollivier-Gooch. A comparison of tetrahedral mesh improvement techniques. In *Proceedings of the Fifth International Meshing Roundtable*, pages 87–100, Sandia National Laboratories, 1996.

Die approbierte gedruckte Originalversion dieser Dissertation ist an der TU Wien Bibliothek verfügbar.
The approved original version of this doctoral thesis is available in print at TU Wien Bibliothek.

[96] L. Freitag and C. Ollivier-Gooch. Tetrahedral mesh improvement using swapping and smoothing. *Int. J. for Numerical Methods in Eng.*, 40(21):3979–4002, 1997.

[97] I. Babuska and A. K. Aziz. On the angle condition in the finite element method. *SIAM J. on Numerical Analysis*, 13(2):214–226, April 1976.

[98] I. Fried. Condition of finite element matrices generated from nonuniform meshes. *AIAA Journal*, 10:219–221, April 1972.

[99] K. Forsman and L. Kettunen. Tetrahedral mesh generation in convex primitives by maximizing solid angles. *IEEE Trans. Magnetics*, 30(5):3535 – 3538, September 1994.

[100] Alain Bossavit. Whitney forms: A class of finite elements for three-dimensional computations in electromagnetism. *IEE Proceedings*, 135, Part A(8):493–500, November 1988.

[101] H. Whitney. *Geometric Integration Theory*. Princeton, NJ:Princeton University Press, 1957.

[102] H. Kaden. *Wirbelströme und Schirmungen in der Nachrichtentechnik*. Springer, 1959.

[103] J. D. Jackson. *Classical Electrodynamics*. Wiley and Sons, January 1999.

[104] Y. Cao, X. Huang, D. Sylvester, T.-J. King, and C. Hu. Impact of on-chip interconnect frequency-dependent R(f)L(f) on digital and RF design. In *IEEE Int. ASIC-SoC Conference*, September 2002.

[105] A. Nieuwoudt and Y. Massoud. Variability-aware multilevel integrated spiral inductor synthesis. *IEEE Trans. Computer-Aided Design of Integrated Circuits and Systems*, 25(12):2613–2625, December 2006.

[106] F. Y. Huang, J. X. Lu, D. M. Jiang, X. C. Wang, and N. Jiang. A novel analytical approach to parameter extraction for on-chip spiral inductors taking into account high-order parasitic effect. *Solid-State Electronics*, 50(9-10):1557–1562, September-October 2006.

[107] P. Fleischmann and S. Selberherr. A new approach to fully unstructured three-dimensional Delaunay mesh generation with improved element quality. In *Simulation of Semiconductor Processes and Devices*, pages 129–130, 1996.

[108] P. Fleischmann, R. Sabelka, A. Stach, R. Strasser, and S. Selberherr. Grid generation for three-dimensional process and device simulation. In *Simulation of Semiconductor Processes and Devices*, pages 161–166, 1996.

[109] R. Sabelka and S. Selberherr. SAP — A program package for three-dimensional interconnect simulation. In *Proc. Intl. Interconnect Technology Conference*, pages 250–252, Burlingame, California, June 1998.

Die approbierte gedruckte Originalversion dieser Dissertation ist an der TU Wien Bibliothek verfügbar.
The approved original version of this doctoral thesis is available in print at TU Wien Bibliothek.
TU WIEN Bibliothek Your knowledge hub

Die approbierte gedruckte Originalversion dieser Dissertation ist an der TU Wien Bibliothek verfügbar.
The approved original version of this doctoral thesis is available in print at TU Wien Bibliothek.
TU WIEN Bibliothek Your knowledge hub

[110] J. Schöberl. NETGEN — automatic mesh generator. http://www.hpfem.jku.at/netgen/index.html.

[111] J. Schöberl. Netgen - An advancing front 2D/3D-mesh generator based on abstract rules. *Computing and Visualization in Science*, 1(1):41–52, July 1997.

[112] H. Borouchaki and S. H. Lo. Fast Delaunay triangulation in three dimensions. *Computer methods in applied mechanics and engineering*, 128(1):153–167, December 1995.

[113] Y. Zhan, R. Harjani, and S. Sapatnekar. On the selection of on-chip inductors for the optimal VCO design. In *Custom Integrated Circuits Conference*, pages 277–280, Oct. 2004.

[114] W. Schroeder, K. Martin, and B. Lorensen. *The Visualization Toolkit*. Kitware, Inc., USA, 2004.

[115] Kitware. *The VTK User's Guide*. Kitware, Inc., USA, 2004.

[116] N. Thepayasuwan and A. Doboli. Layout conscious bus architecture synthesis for deep submicron systems on chip. In *Proceedings of the Design, Automation and Test in Europe Conference and Exhibition*, volume 1, pages 108–113, Feb. 2004.

[117] I. Koren, Z. Koren, and D. K. Pradhan. Designing interconnection buses in VLSI and WSI for maximum yield and minimum delay. *IEEE J. Solid-State Circuits*, 23(3):859 – 866, Jun 1988.

[118] R. Sabelka, C. Harlander, and S. Selberherr. The state of the art in interconnect simulation. In *Simulation of Semiconductor Processes and Devices*, pages 6–11, 2000.

[119] R. Sabelka and S. Selberherr. A finite element simulator for three-dimensional analysis of interconnect structures. *Microelectronics J.*, 32(12):163–171, Jan 2001.

[120] R. Bauer and S. Selberherr. Preconditioned CG-solvers and finite element grids. In *Proceedings Colorado Conference on Iterative Methods*, volume 2, pages 1–5, Breckenridge, USA, April 1994.

[121] J. R. Shewchuk. An introduction to the conjugate gradient method without the agonizing pain. http://www.cs.cmu.edu/~jrs/jrspapers.html, Aug 1994.

[122] S. C. Eisenstat. Efficient implementation of a class of preconditioned conjugate gradient methods. *SIAM J.Sci.Stat.Comput.*, 2(1):1 – 4, 1981.

[123] T. A. Manteuffel. The shifted incomplete Cholesky factorization. In *Proceedings of the Symposium on Sparse Matrix Computation*, pages 41–61, Knoxville, TN, November 1978.

[124] J. R. Shewchuk. Triangle: Engineering a 2D quality mesh generator and Delaunay triangulator. In *WACG: 1st Workshop on Applied Computational Geometry: Towards Geometric Engineering, WACG*, pages 124–133. LNCS, May 1996.

Die approbierte gedruckte Originalversion dieser Dissertation ist an der TU Wien Bibliothek verfügbar.
The approved original version of this doctoral thesis is available in print at TU Wien Bibliothek.
TU WIEN Bibliothek Your knowledge hub

Own Publications

1. A. Nentchev, R. Sabelka, S. Selberherr: "Simplification of spacial structures by simulation with periodic boundary conditions"; VLSI Multilevel Interconnection Conference (VMIC), Fremont; 10-03-2005 – 10-06-2005; in: "2005 Proceedings Twenty Second International VLSI Multilevel Interconnection Conference", (2005), 547 – 552.
2. A. Nentchev, R. Sabelka, W. Wessner, S. Selberherr: "On chip interconnect simulation of parasitic capacitances in periodic structures"; European Simulation and Modeling Conference (ESMC), Porto; 10-24-2005 – 10-26-2005; in: "The 2005 European Simulation and Modelling Conference Proceedings", (2005), 420 – 424.
3. M. Movahhedi, A. Nentchev, H. Ceric, A. Abdipour, S. Selberherr: "A finite element time-domain algorithm based on the alternating-direction implicit method"; European Microwave Week (EUMW), Manchester; 09-10-2006 – 09-15-2006; in: "European Microwave Week 2006 Book of Abstracts", (2006), ISBN: 2-9600551-6-0; 1 – 4.
4. A. Nentchev, J. Cervenka, G. Marnaus, H. Enichlmair, S. Selberherr: "Heatring - smart investigation of temperature impact on integrated circuit devices"; Workshop on Thermal Investigations of ICs and Systems (THERMINIC), Nice; 09-27-2006 – 09-29-2006; in: "Collection of Papers Presented at the 12th International Workshop on Thermal Investigation of ICs and Systems", (2006), ISBN: 2-9161-8704-9; 235 – 238.
5. M. Movahhedi, A. Abdipour, A. Nentchev, M. Dehghan, S. Selberherr: "Alternating-direction implicit formulation of the finite-element time-domain method"; IEEE Transactions on Microwave Theory and Techniques, 55 (2007), 6; 1322 – 1331.
6. A. Nentchev, S. Selberherr: "Three-dimensional on-chip inductance and resistance extraction"; Sociedade Brasileira da Microeltronica 2007 (SBCCI 2007), Rio de Janeiro; 09-03-2007 – 09-06-2007; in: "20th Symposium on Integrated Circuits and Systems Design", (2007), ISBN: 978-1-59593-910-4; 218 – 223.
7. A. Nentchev, S. Selberherr: "On the magnetic field extraction for on-chip inductance calculation"; International Conference on the Simulation of Semiconductor Processes and Devices (SISPAD), Wien; 09-25-2007 – 09-27-2007; in: "International Conference on Simulation of Semiconductor Processes and Devices 2007", T. Grasser, S. Selberherr (ed.); Springer-Verlag Wien New York, 12 (2007), ISBN: 978-3-211-72860-4; 349 – 352.

8. H. Ceric, A. Nentchev, E. Langer, S. Selberherr: "Intrinsic stress build-up during Volmer-Weber crystal growth"; International Conference on the Simulation of Semiconductor Processes and Devices (SISPAD), Wien; 09-25-2007 – 09-27-2007; in: "International Conference on Simulation of Semiconductor Processes and Devices 2007", T. Grasser, S. Selberherr (ed.); Springer-Verlag Wien New York, 12 (2007), ISBN: 978-3-211-72860-4; 37 – 40.

9. A. Nentchev, J. Cervenka, S. Selberherr: "Three-dimensional on-chip inductance and resistance extraction"; Special Issue of the Analog Integrated Circuits and Signal Processing Journal by Springer. (Submitted for publication).

10. A. Nentchev, S. Selberherr: "Three-dimensional finite element frequency domain method for inductance calculation of small structures"; IEEE Trans. Magnetics. (Submitted for publication).

Die approbierte gedruckte Originalversion dieser Dissertation ist an der TU Wien Bibliothek verfügbar.
The approved original version of this doctoral thesis is available in print at TU Wien Bibliothek.
TU WIEN Bibliothek Your knowledge hub

Curriculum Vitae

since April 2004	Technical University of Vienna, Austria. Enrolled in a full Ph.D. program at the Institute for Microelectronics under the supervision of Prof. Siegfried Selberherr.
March 2004	Technical University of Vienna, Austria, master's degree, "Diplomingenieur", in Electrical Engineering with specialization in Computer Technology.
June 1990	High school graduation at the German secondary school in Sofia, Bulgaria.
May 15th, 1971	Born in Sofia, Bulgaria.

Die approbierte gedruckte Originalversion dieser Dissertation ist an der TU Wien Bibliothek verfügbar.
The approved original version of this doctoral thesis is available in print at TU Wien Bibliothek.
TU WIEN Bibliothek Your knowledge hub